CONTRACTOR REPORT

SAND82-7117
Unlimited Release
UC-63

Advanced Photovoltaic Trough Development

R. Spencer, K. Yasuda, B. Merson
Acurex Corporation
Alternate Energy Division
485 Clyde Avenue
Mountain View, California 94042

Prepared by Sandia National Laboratories Albuquerque, New Mexico 87185 and Livermore, California 94550 for the United States Department of Energy under Contract DE-AC04-76DP00789

Printed April 1982

When printing a copy of any digitized SAND Report, you are required to update the markings to current standards.

Issued by Sandia National Laboratories, operated for the United States Department of Energy by Sandia Corporation.

NOTICE: This report was prepared as an account of work sponsored by an agency of the United States Government. Neither the United States Government nor any agency thereof, nor any of their employees, nor any of their contractors, subcontractors, or their employees, makes any warranty, express or implied, or assumes any legal liability or responsibility for the accuracy, completeness, or usefulness of any information, apparatus, product, or process disclosed, or represents that its use would not infringe privately owned rights. Reference herein to any specific commercial product, process, or service by trade name, trademark, manufacturer, or otherwise, does not necessarily constitute or imply its endorsement, recommendation, or favoring by the United States Government, any agency thereof or any of their contractors or subcontractors. The views and opinions expressed herein do not necessarily state or reflect those of the United States Government, any agency thereof or any of their contractors or subcontractors.

Printed in the United States of America
Available from
National Technical Information Service
U.S. Department of Commerce
5285 Port Royal Road
Springfield, VA 22161

NTIS price codes
Printed copy: A11
Microfiche copy: A01

Distribution
Category UC-63

SAND82-7117
Unlimited Distribution
Printed April 1982

ADVANCED PHOTOVOLTAIC TROUGH DEVELOPMENT

R. Spencer, K. Yasuda and B. Merson
Acurex Corporation
Alternate Energy Division
485 Clyde Avenue
Mountain View, California 94042

ABSTRACT

This final report presents results of the Acurex advanced photovoltaic trough concentrator project funded through DOE through Sandia National Laboratories. The scope of the work includes analytical studies, hardware development, and component testing. Various aspects of the system have been optimized and improvements have been realized, particularly in the receiver and reflecting surface designs. An empirical system performance model has been developed that closely agrees with measured system performance. This in-depth study of single-axis reflecting linear focus photovoltaic concentrators will be very beneficial in the development of improved models for similar systems as well as other photovoltaic concentrator designs.

Prepared for Sandia National Laboratories under Contract #13-9493.

TABLE OF CONTENTS

Section		Page
1	EXECUTIVE SUMMARY	1-1
	1.1 PROJECT RESULTS	1-3
	1.1.1 Analytical Trough Optimization	1-3
	1.1.2 Glass Laminate Development	1-3
	1.1.3 Receiver Design and Fabrication	1-4
	1.1.4 Acurex 3001 Trough Improvement	1-4
	1.1.5 Test Activities	1-4
2	PHOTOVOLTAIC TROUGH OPTIMIZATION	2-1
	2.1 INTRODUCTION AND SUMMARY	2-1
	2.2 PERFORMANCE ANALYSIS	2-7
	2.2.1 Input Parameters	2-7
	2.2.2 Methodology	2-10
	2.2.3 Computer Code	2-12
	2.3 COST ANALYSIS METHODOLOGY	2-15
	2.4 OPTIMIZATION PROCEDURE	2-17
	2.4.1 Continuous Trough Optimization	2-17
	2.4.2 Slope Error Sensitivity	2-21
	2.4.3 Split Trough Optimization	2-27
	2.5 PERFORMANCE SENSITIVITY OF OPTIMUM DESIGN	2-31
3	FLEXIBLE GLASS LAMINATE REFLECTIVE PANEL DEVELOPMENT	3-1
	3.1 INTRODUCTION	3-1
	3.2 SCOPE	3-2
	3.3 PANEL DESIGN	3-2
	3.4 LAMINATE FABRICATION	3-3
	3.5 ACCELERATED ENVIRONMENTAL EXPOSURE	3-8
	3.6 INSTALLATION FEASIBILITY	3-12
	3.7 HAIL IMPACT SURVIVABILITY	3-14
	3.8 MINIMUM BEND RADII	3-15
	3.9 TASK SUMMARY	3-21
4	PV RECEIVER DESIGN	4-1
	4.1 INTRODUCTION	4-1
	4.2 RECEIVER DESIGN CONSIDERATIONS	4-2
	4.3 RECEIVER TUBE DESIGN	4-4
	4.4 CELL MODULE DESIGN	4-8
	4.5 WIRING HARNESS DESIGN	4-10

TABLE OF CONTENTS (Continued)

Section		Page
	4.6 RECEIVER SUPPORT AND FLUID COUPLING DESIGNS	4-11
5	PV TROUGH REFLECTOR QUALITY IMPROVEMENT	5-1
	5.1 INTRODUCTION	5-1
	5.2 OPTICAL ANALYSIS OF 3001 REFLECTOR	5-1
	5.3 REFLECTOR MODIFICAITON TO IMPROVE IMAGE QUALITY	5-6
6	TEST ACTIVITIES	6-1
	6.1 INTRODUCTION	6-1
	6.2 COLLECTOR PERFORMANCE MODEL	6-2
	6.3 TEST FIXTURE DEVELOPMENT	6-3
	6.4 PROTOTYPE RECEIVER PREPARATION	6-9
	6.5 TEST PLANS AND PROCEDURES	6-9
	6.5.1 Performance Tests	6-9
	6.5.2 Flux Mapping	6-13
	6.5.3 Single Cell Testing	6-17
	6.5.4 Environmental Testing	6-21
	6.5.5 Apex Angle Testing	6-25
	6.5.6 Glass Reflector Testing	6-27
	6.6 TEST RESULTS	6-28
	6.6.1 Concentrator Performance	6-28
	6.6.2 Intercept Factor and Image Uniformity	6-37
	6.6.3 Electrical Loss Factor	6-48
	6.6.4 Environmental Testing	6-69
	6.6.5 Apex Angle Testing	6-75
	6.6.6 Miscellaneous Testing Activities	6-77
	6.7 CONCLUSIONS	6-81
	6.7.1 Analytical Model of the Parabolic Trough Performance	6-91
	6.7.2 Empirical Model of the PV Parabolic Trough	6-94
	APPENDICES	
	A. Intensity Profiles for Different Reflector Rim Angles	A-1
	B. Intensity Profiles for Different Reflector Slope Errors	B-1
	C. Neutral Axis Calculation	C-1
	D. Cell Width Optimization Study	D-1
	E. Uncertainty Analysis	E-1

LIST OF ILLUSTRATIONS

Figure		Page
2-1	Current Collector Design	2-3
2-2	Module Geometry	2-6
2-3	Split Trough Concepts	2-9
2-4	Simplified Flow Chart	2-14
2-5	Optimization of Receiver Configuration for a Continuous Trough 90° Rim Angle	2-19
2-6	Receiver Intensity Distribution	2-20
2-7	Rim Angle Optimization -- Continuous Trough	2-22
2-8	Intensity Profile for Glass Sheet Edge Slope Error File	2-24
2-9	Integrated Energy Flux for Glass Sheet Edge Slope Error	2-25
2-10	Receiver Configuration Optimization for Glass Sheet Edge Slope Error	2-26
2-11	Performance Sensitivity to Cell Placement -- Split Trough	2-29
2-12	Receiver Configuration Optimization Split Trough Design	2-30
2-13	Comparison of Split and Continuous Trough Optimum Receiver Configuration	2-32
2-14	Performance Degradation with Receiver Misalignment	2-33
2-15	Performance Degradation with Tracking Error	2-35
3-1	Flexible Glass Laminate -- Full Size Panel	3-9
3-2	Flexible Glass Laminate -- Small-Scale Panel	3-10
3-3	Reflective Panel Installation Procedure	3-13
3-4	Load Versus Radius of Curvature for Small-Scale Laminate Panels	3-16
3-5	Load Versus Deflection for Flabeg Glass on 0.050-in. Thick Steel	3-17

LIST OF ILLUSTRATIONS (Continued)

Figure		Page
3-6	Load Versus Deflection for 0.40-in. Thick Glass on 0.050-in. Thick Steel	3-18
3-7	Load Versus Deflection for 0.60-in. Thick Glass on 0.050-in. Thick Steel	3-19
3-8	Load Versus Deflection for 0.60-in. Thick Glass on 0.062-in. Thick Steel	3-20
4-1	Receiver Tube Configuration	4-5
4-2	Cell Module Assembly	4-9
5-1	Acurex Laser Ray Test Facility	5-2
5-2	Sandia Laser Ray Trace Equipment	5-4
5-3	LRT Output for 3001 Coilzak Trough	5-5
5-4	Early 3001 Image	5-7
5-5	Improved 3001-P Image	5-9
5-6	3001-P Laser Ray Trace Results	5-12
6-1	Acurex Two-Axis Test Facility	6-5
6-2	Tracker Sensor Mounting Detail	6-7
6-3	Typical I-V Curve and Data Set	6-12
6-4	Acurex Flux Mapper	6-15
6-5	Single Cell Instrumented Module	6-19
6-6	Short Receiver Section for Environmental Testing	6-23
6-7	Apex Angle Test -- Receiver Support	6-26
6-8	Array Efficiency Versus Cell Temperature for ASEC Cells	6-29
6-9	Array Efficiency Versus Direct Normal Insolation for ASEC, SOLAREX, and SPIRE Cells	6-30
6-10	Array Versus Tracking Error -- ASEC Cells	6-31
6-11	Off-Normal Performance -- South Reflector	6-33

LIST OF ILLUSTRATIONS (Continued)

Figure		Page
6-12	Off-Normal Performance -- North Reflector	6-34
6-13	Acurex Inlet, Outlet, and Cell (39,40,42) Temperatures	6-35
6-14	Direct Normal and Total Horizontal Insolation	6-36
6-15	Acurex PRDA 35 VOC, ISC and Efficiency	6-37
6-16	Acurex EFF Versus Outlet Temperature for 0945 to 1215 Hours	6-38
6-17	One Dimensional Flux Map	6-40
6-18	Two-Dimensional Flux Map for 0° Incident Angle	6-41
6-19	Two-Dimensional Flux Map 10° Incident Angle	6-42
6-20	Two-Dimensional Flux Map 20° Incident Angle	6-43
6-21	Two-Dimensional Flux Map -- 30° Incident Angle	6-44
6-22	Two-Dimensional Flux Map -- 40° Incident Angle	6-45
6-23	Intercept Factor	6-47
6-24	Image Uniformity Factor	6-49
6-25	Receiver Electrical Schematic	6-50
6-26	10° Incident Angle Image	6-53
6-27	20° Incident Angle Image	6-55
6-28	30° Incident Angle Image	6-57
6-29	Diode Turn On Study "A" Face, South Module	6-59
6-30	Diode Turn On Study "B" Face, South Module	6-60
6-31	I-V Curve for 0° Incident Angle	6-62
6-32	I-V Curve for 17° Incident Angle	6-63
6-33	I-V Curve for 18° Incident Angle	6-64
6-34	I-V Curve for 20° Incident Angle	6-65

LIST OF ILLUSTRATIONS (Continued)

Figure		Page
6-35	Diode Turn On Study "A" Side, North Module.	6-67
6-36	Diode Turn On Study "B" Side North Module	6-68
6-37	Electrical Loss Factor	6-70
6-38	Spire Module Delaminated in Thermal Shock Cycling . . .	6-73
6-39	Lower Trough Half Apex Angle Optimizaton	6-76
6-40	Upper Trough Half Apex Angle Optimizaton	6-78
6-41	FEK Versus Glass Performance	6-80
6-42	Gap Effect in Glass Reflector	6-82
6-43	Flux Map -- South Face of Receiver Glass Trough	6-83
6-44	Flux Map -- First Gap on South Face -- Glass Trough . .	6-84
6-45	Flux Map -- Second Gap on South Face -- Glass Trough .	6-85
6-46	Flux Map -- Third Gap on South Face -- Glass Trough . .	6-86
6-47	Flux Map -- North Face of Receiver -- Glass Trough . .	6-87
6-48	Flux Map -- First Gap on North Face -- Glass Trough . .	6-88
6-49	Flux Map -- Second Gap on North Face -- Glass Trough .	6-89
6-50	Flux Map -- Third Gap on North Face -- Glass Trough . .	6-90
6-51	Schematic of Receiver Circuit	6-92

LIST OF TABLES

Table		Page
2-1	Comparison of Current and Optimized Designs	2-7
2-2	Computer Code Inputs	2-13
2-3	Cost Analysis Summary	2-16
2-4	Optical Efficiency for Various Slope Error Files . . .	2-23
2-5	Performance Comparison of Split and Continuous Trough	2-28
3-1	Properties of Glass -- Glaverbel	3-4
3-2	Properties of Glass -- Corning	3-5
3-3	Properties of Glass -- Flabeg	3-6
3-4	Description of Flexible Glass Laminate Panels	3-7
3-5	Glass Panel Dimensions and Uses	3-11
6-1	Model Evaluation	6-96

SECTION 1

EXECUTIVE SUMMARY

This document is the final report of the work performed for Sandia National Laboratories under Sandia Contract No. 13-9493.

The project objective was to develop a single axis photovoltaic trough concentrator which combined high efficiency, effective cell encapsulation, and improved array life.

The scope of the project included analytical studies, hardware development, and component testings in an interactive way. As a result, the designs of the receiver and reflective surface were substantially improved. Furthermore, an in-depth understanding of the single-axis tracking PV trough under various operating conditions was obtained. An empirical model was developed which encompasses all pertinent variables and adequately predicts the performance of the trough.

The project included the following tasks:

Task 1 -- Array Optimization. This task was an analytical study to optimize the array configuration including concentrator rim angle, split and continuous troughs, receiver apex angle, and cell size and position. This task is discussed in section 2 of this report.

Task 2 -- Advanced Reflector Development. The objectives of this task were: 1) to develop thin glass mirror laminates as reflective surface, 2) to characterize the performance of glass reflector, and 3) to

modify the existing trough for longitudinal FEK reflector and measure its performance. This task is discussed in section 3 of this report.

Task 3 -- Advanced Receiver Development. The objective of this task was to design and test advanced receivers with high efficiency and effective encapsulation. Concentrating cell modules of several manufacturers were to be evaluated. Section 4 is a description of the receiver optimization and design, section 5 is a description of concentrator design improvement efforts, and section 6 details testing and data reduction of the trough and receiver.

The above tasks were performed interactively with the results of analysis, design and testing of each task being fed back into the other tasks. Therefore, during the course of the program, the scope and approach of each task were modified to meet the overall project objectives most cost-effectively. Extensive testing of components and the concentrator module were performed under a wide range of environmental and operating conditions. The findings of the analytical and design efforts were used to define the test procedures and conditions.

A substantial portion of the test program was funded by Acurex. Specifically, Acurex funding was used for:

- Design and installation of a versatile test facility and data acquisition system
- Development of a flux mapping sensor to measure intensity distribution on the receiver
- Development of a single cell evaluation device to measure individual cell and diode characteristics in situ on the receiver

- Certain testing and data reduction effort not covered under the Sandia contract

1.1 PROJECT RESULTS

1.1.1 Analytical Trough Optimization

A computer model of trough performance was developed to trace rays into the aperture and map the resultant flux on the receiver. This program has the capability to map any reflector surface from slope error data produced by Sandia so as to simulate a reflector with perfect or any desired slope error characteristic. The receiver shape and position can be changed extensively as can many features of collector configuration. This program was used to optimize various trough and receiver design parameters. The results of this optimization are included in section 2 of this report. The principal results, however, were the discoveries that 1) a split trough design represents only a small improvement over a continuous parabola and would allow no cost-effective benefit, and 2) that slope error reduction in either case offers a much greater increase in performance. Reduction of slope error offers 6.1 percent performance benefit while alternate design offers only 1.9 percent improvement.

1.1.2 Glass Laminate Development

Acurex undertook to design and fabricate a laminate reflective surface of glass and shell which would offer low cost and long life at high reflectivity. The design was evaluated by production of several laminate panels of silvered microsheet glass on perforated sheet steel substrates. These panels exhibited 92 percent reflectivities and showed extended life at high reflectivity in chamber testing at Sandia. The design and evaluation of these panels is described in section 3 of this

report. This reflective laminate shows potential as a lower cost competitor to current FEK-244 surfaces.

1.1.3 Receiver Design and Fabrication

Acurex used several optimization studies to develop the design for a new vee-type receiver. All aspects of the configuration were carefully evaluated and optimized. In addition, we employed a radical departure from previous concentrator receiver designs in encapsulating the cells for environmental protection. The design was fabricated and some iteration performed in order to produce working products with cells from three different manufacturers. These products exhibit a significant improvement in performance over earlier designs. The receiver design effort is discussed in section 4.

1.1.4 Acurex 3001 Trough Improvement

The design of the concentrating trough used by Acurex for solar thermal collection installations proved to have too high a slope error to serve efficiently for photovoltaic concentrators. Acurex made several modifications to its trough design which have greatly lowered the slope error and hence improved efficiency in photovoltaic applications. The modifications made to the trough design are described in section 5 of this report. The changes described lowered the assembly cost of the concentrating trough sufficiently to justify inclusion of those design modifications in all future manufacturing operations. The improved model has now been used in three new installations, and a total of 18,000 ft^2 of collectors have been produced using the new design.

1.1.5 Test Activities

The testing was funded jointly by Acurex and Sandia. Acurex created a two-axis tracking test bed which is fully instrumented for

photovoltaic testing. The testing was performed at the Acurex Mountain View facility and at Sandia Laboratories in Albuquerque. Some duplication of the performance testing was performed in order to assure compatibility of results.

The performance testing was designed to evaluate the normal and off-normal efficiency of the newly designed photovoltaic collector. In addition, testing for installation tolerances and for effectiveness of certain design features was included. Active aperture efficiencies of greater than 11.6 percent have been observed with FEK-244 reflectors at 900 W/m^2 direct normal insolation and 28^oC cell temperature. Efficiencies of greater than 12.6 percent have been measured with a glass reflector at 800 W/m^2 and 28^oC. This is a significant improvement over 6.5 percent efficiency for the first generation parabolic trough collector design.

In environmental testing, the reflector and receiver test sections were submitted to a variety of accelerated exposure tests aimed at discovering life-limiting design flaws. The design of the receiver was improved based on the results of these tests. The environmental testing is described in section 6.6.4.

Acurex also developed two pieces of special test apparatus for the photovoltaic testing. The flux mapper is a device which quickly analyzes the distribution of irradiance in the concentrated field of the receiver surface. This is used to investigate intercept factor and image uniformity. In addition, it is invaluable as a cell design tool. The cell performance is optimized for a nonuniform illumination profile measured by the sensor. The testing performed by the flux mapper is described in sections 6.5.2 and 6.6.2. This sophisticated piece of test equipment is the first of its kind produced.

Acurex also funded the development of a special cell module which allows measurements of individual cell characteristics and diode characteristics while the module operates in a normal environment. The module provides accurate data on the effects of shading and off-normal nonuniformities in cell illumination. This testing is described in sections 6.5.3 and 6.6.3 of this report. The individual cell dynamics under the varying illumination of a single axis tracking concentrator is complex. It should, however, be understood in order to develop an accurate model of the collector performance.

Acurex combined all the results from testing to produce a mathematical model of the collector performance. Many terms had to be included to account for all of the dependent variables of trough performance. There are three independent variables: cell temperature, direct normal insolation, and incident angle. A thorough understanding of the linear focus photovoltaic concentrator has been achieved which will be beneficial in the development of improved models and photovoltaic concentrator designs in the future.

SECTION 2

PHOTOVOLTAIC TROUGH OPTIMIZATION

2.1 INTRODUCTION AND SUMMARY

The objective of this study was to review the parabolic trough reflector and receiver design parameters to optimize the optical performance of the concentrator. The selection of the optimum concentrator configuration was based on both cost and performance considerations. Alternatives to the baseline trough configuration included rim angles from 50° to 110° and split-trough design. In the split-trough design the two halves of the reflective surface are displaced to create two focal regions. Design options were limited to a parabolic concentrator with the same aperture size as Acurex 3001 trough, and a similar low cost production approach. Figure 2-1 illustrates the current trough design.

For each potential trough design, a variety of receiver design parameters were optimized. Sensitivity to change in field alignment of components was analyzed and the optimum configuration including manufacturing and field misalignment was charted. Receiver variables used in the optimization were:

- Cell leading edge distance from apex — .270 to .400 in.
- Receiver (vee type) included angle -- 10° to 180°
- Receiver location — vertical relative to the focal point -- .83 to 1.33 in.

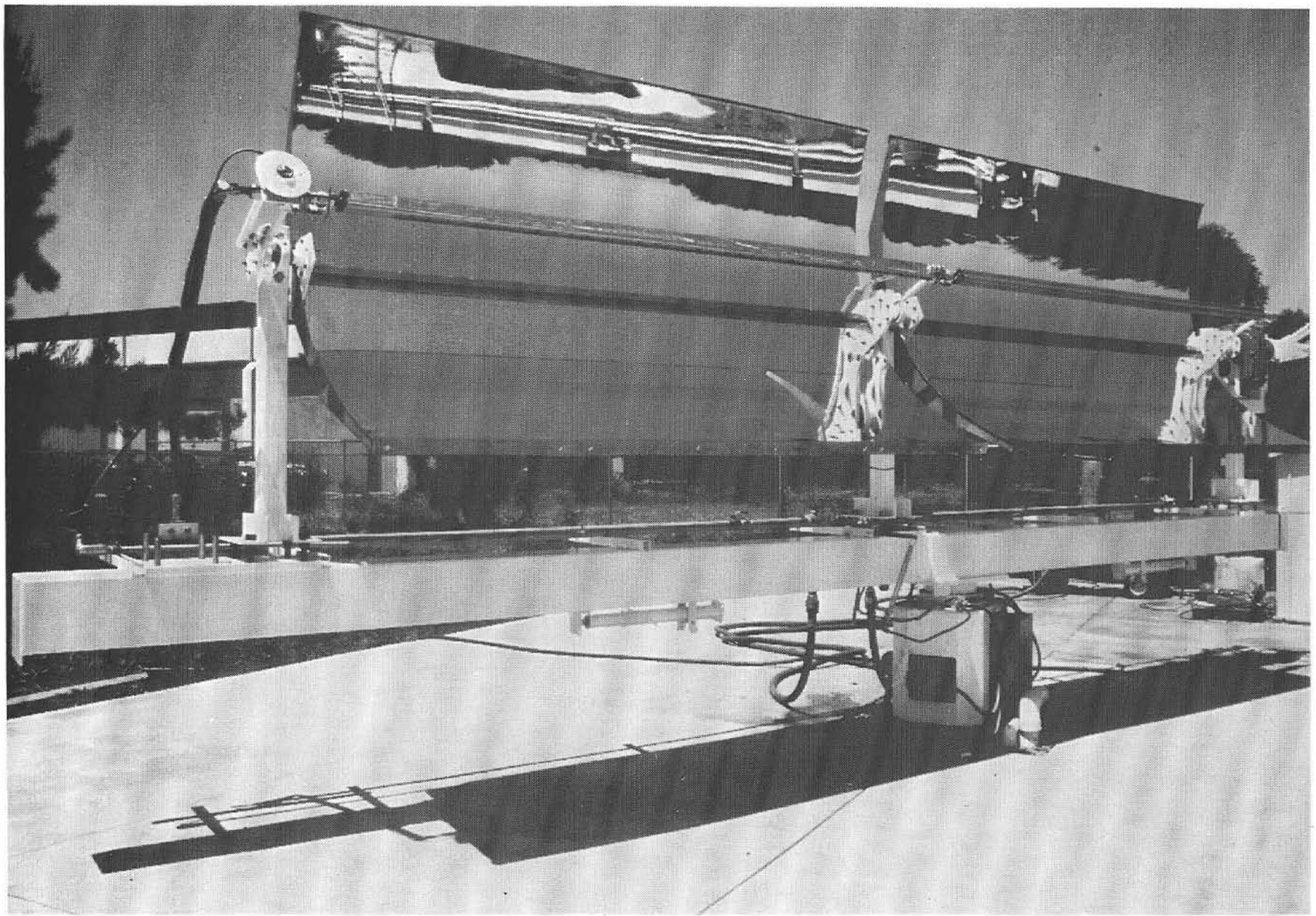

Figure 2-1. Current Collector Design

- Receiver mislocation -- lateral -- $\pm$ 0 to .5 in.
- Tracking error -- 0 to $.5^{o}$

The receiver variables are shown pictorially in figure 2-2. All other parameters were held constant during the optimization. The cell width was held at 1 in. (2.54 cm) based on the optimization study discussed in appendix D. For all plots contained in this section, the reported data is an optimized result in all variables except the one under discussion.

Finally, each trough design was optimized with three different sets of slope error data overlayed on the trough slope to assess the impact of reflector surface quality. The sets of data represent a bad slope error typical of sheet edges, a moderate slope error typical of mid-sheet and a perfect trough. The slope error analysis is detailed in section 2.4.2.

Results of the optimization summarized in table 2-1 show the current design to be very similar to the final design. The optimum concentrator rim angle is 95° versus the current 90°; nevertheless, the trough performance is virtually constant between 90° and 95° rim angles. A split trough design was found to result in improved performance and the optimum included receiver angle was 44°. The location of the receiver and cell changes slightly from the current design because the split trough design allows greater flexibility in receiver placement. The performance calculations of section 2.4 show that the optimized trough of table 2-1 results in 4.2 percent improvement over the current design.

Another important conclusion of this study was the dramatic effect of concentrator slope error on optical performance. Improvement in the slope error of the reflective surface could increase performance of the current design by 6.9 percent. The net effect of improving the design and slope error is a 10.7 percent performance increase.

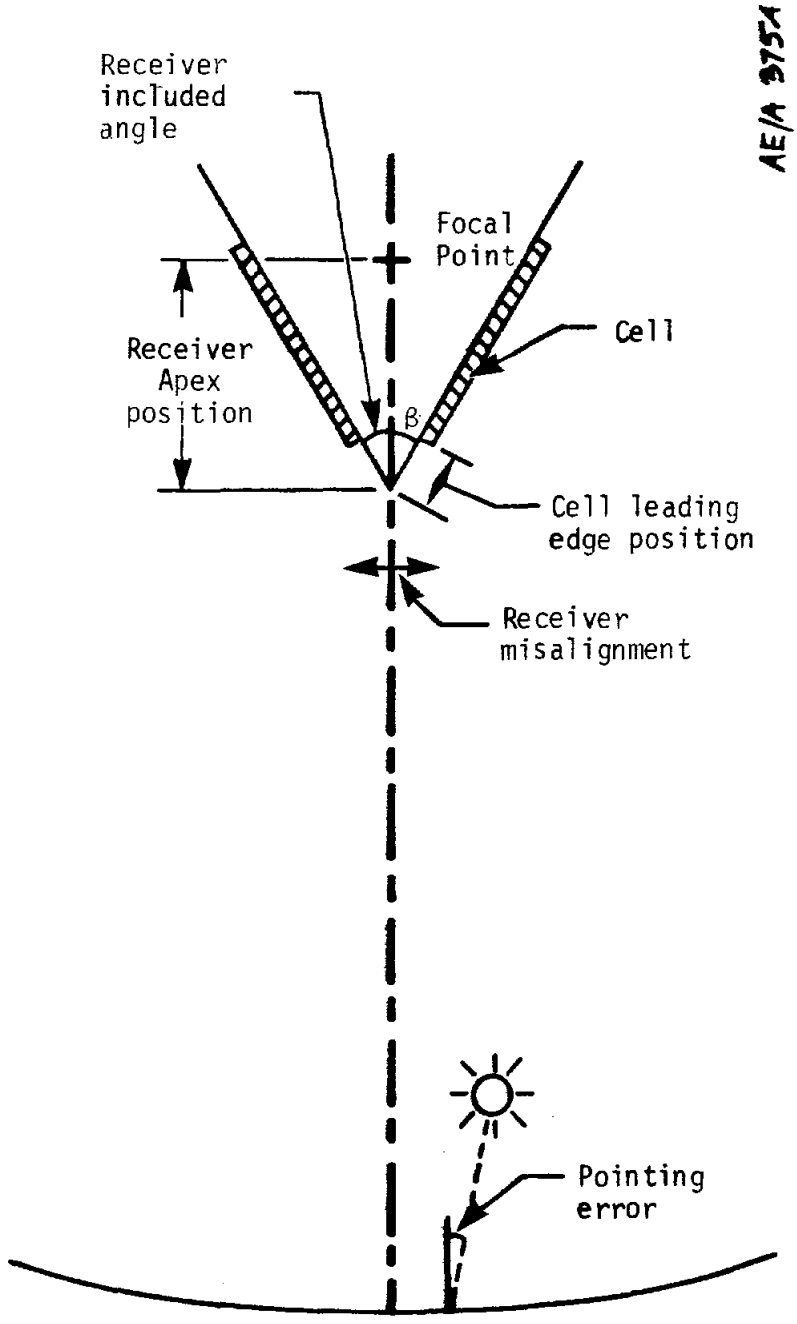

Figure 2-2. Module Geometry

Table 2-1. Comparison of Current and Optimized Designs

	Current	Optimized
Trough configuration	Continuous parabolic	Split trough displaced
Aperture length	10'	10'
Aperture width	6'	6'
Rim angle	90°	95°
Receiver included angle	60°	44°
Receiver apex position (from focal point)	.95"	1.02"
Cell location (from receiver apex)	.375"	.27"
Optical efficiency	89.1	90.8

This section describes in detail the work done to arrive at the optimum design. Section 2.2 describes how concentrator performance was evaluated and costing is described in section 2.3. Section 2.4 presents the optimization methodology and results, and section 2.5 discusses the sensitivity of the final design to various operating parameters, and summarizes the improvements over the current design.

2.2 PERFORMANCE ANALYSIS

2.2.1 Input Parameters

The objective of the performance analysis was to quantify the impact of the design variables upon concentrator performance. The performance analysis, together with cost and manufacturing considerations led to selection of the optimized design. The design variables included

both trough and receiver tube design parameters. The trough design was constrained to a reflector module with a 6-ft aperture and 10 ft in length. The trough dimensions were constrained because the extensive redesign and manufacturing tooling costs required to accommodate a different size trough were outside the scope of this program. The trough rim angle, however, was variable, and two split trough concepts were evaluated. Figure 2-3 illustrates the variation in rim angles considered and the split trough concepts.

The receiver tube design is characterized by three parameters: receiver included angle, receiver apex position, and cell leading edge position. These parameters together determine the location of the photovoltaic cell. All three parameters were variable for this study with the one constraint that the minimum leading edge position is 0.270 in. from the virtual apex of the receiver. The leading edge position is limited by manufacturing and stress limitations of the retaining lip, and the presence of the double bus. Cell position is illustrated in figure 2-2.

Other parameters which characterize concentrator design and performance were fixed. As mentioned previously, the trough aperture was 6 feet wide. Cell size was fixed at 2.5 cm wide using a double bus. Cell size optimization is discussed at greater length in section 4.4.

The sunshape was modeled as a one dimensional normal distribution with a root mean square width of σ_{ss} = 2.9 milliradians. The normal distribution is a good approximation of the actual sunshape. The actual σ_{ss} of the sun is 2.7 mrad. The slightly larger value of 2.9 mrad was used to account for atmospheric scattering. This corresponds to a more typical direct normal insolation value of 930 w/m^2.

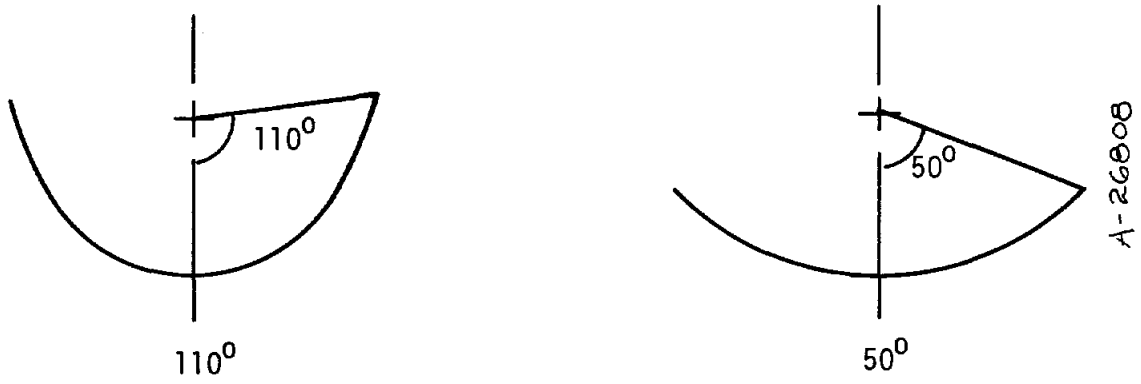

Rim angle variation

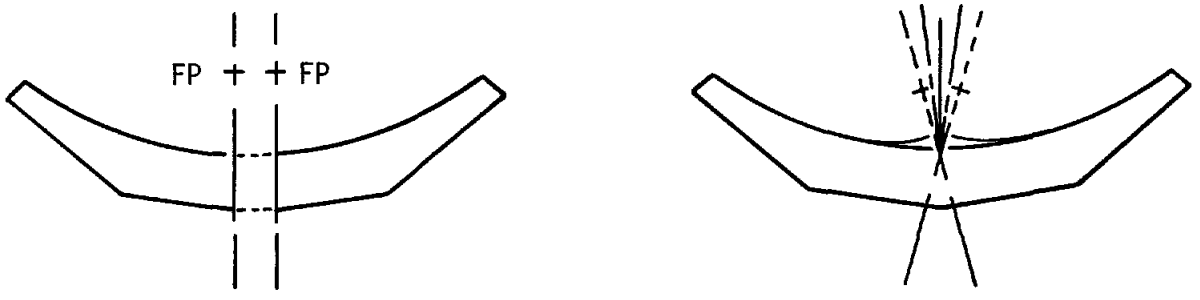

Split trough displaced

Split trough canted

Figure 2-3. Split Trough Concepts

The reflective surface was assumed to have a constant reflectivity (for simplicity a reflectivity of 1.0 was used), however this was subject to image spreading due to specularity and slope error. The effect of specularity was modeled as spreading the reflected image in a normal distribution. For the aluminized acrylic film (FEK 244) used on the Acurex trough collectors, the standard deviation is σ_{spec} = 0.85 mrad.

Slope errors result from the manufacturing process when the reflective surface does not conform to a parabolic shape. This results in the reflected image not being centered at the focal point. This error could be treated statistically with a characteristic σ. However, studies show that the slope errors are not random, and there is a definite pattern to the distribution of the errors. Therefore, actual slope error data taken at Sandia Laboratories on the Acurex Model 3001 concentrator were used to more accurately model concentrator performance. One file of typical slope errors was used for the entire optimization.

Other factors left constant for the optimization included tracking error (0°), incidence angle to collector aperture (0°), and receiver tube misalignment or deflection (none was assumed).

2.2.2 Methodology

Performance of the photovoltaic concentrator is characterized by its optical efficiency. The optical efficiency is defined as the percentage of solar energy striking the gross collector aperture which is reflected upon the photovoltaic cell active area. The optical efficiency (η_{opt}) is expressed by the following equation:

$$\eta_{opt} = F_S \, \rho\gamma\tau_{CG} \, F_{ECL}$$

where,

F_S = Receiver tube shading factor

ρ = Reflector surface reflectivity (assumed to be constant unity)

γ = Intercept factor

τ_{CG} = Cell cover glass transmissivity

F_{ECL} = Extrinsic cell loss factor[1]

The first step is to compute the amount of incident sunlight which strikes the reflector. Shading by the receiver tube is a function of the receiver included angle and the size of the cell module/receiver tube assembly. The energy not shaded by the receiver is reflected toward the cells. Since changes in trough reflectivity are not being considered here, the trough reflectivity is assumed to be unity to help isolate the other optical effects.

The intercept factor is the energy which strikes the photovoltaic cell active area divided by the energy reflected from the trough. It is influenced by cell placement, trough configuration, slope error, specularity, and sunshape. The sunshape and specularity are convolved analytically to obtain an "effective sunshape." This represents the distribution of the solar intensity broadened by the specularity effect. Since both are modeled as normal distributions, the effective sunshape is also a normal distribution with a standard deviation (σ_{ES}) of

$$\sigma_{ES} = \left(\sigma_{ss}^{2} + \sigma_{spec}^{2}\right)^{0.5}$$

---

[1]"Extrinsic Losses in Solar Cells for Linear Focus Systems," C. Michael Garner, SAND79-1781.

The effective sunshape is then reflected toward the focal point at an angle determined by the trough configuration and the slope error. The reflected energy from various parts of the trough combine to form a focused image at the receiver tube. For any given cell location, the distribution of optical energy striking the cell can be computed.

Also accounted for in this analysis are cover glass transmissivity and extrinsic cell losses. Since glass transmissivity only varies significantly for angles greater than 60 degrees off normal, this factor has a minor impact on concentrator performance.

Extrinsic cell loss is influenced by cell size, grid pattern, and single or double bus, however, these factors were all held constant for this analysis (except for the flat receiver). The variability in the extrinsic loss is due to the cell nonuniform illumination because of the concentrator optics.

2.2.3 Computer Code

A computer code was developed to execute the performance analysis described earlier. The first step is to input the details of the collector geometry, optical properties and sunshape to the code. Table 2-2 lists the code inputs required. From these inputs, the equation for the parabola and the focal plane are computed for use in later calculations.

The effective sunshape is computed next. The effective sunshape combines the distribution of energy from the sun with the randomly occurring optical errors such as specularity. With the Gaussian sunshape assumed for this analysis, the effective sunshape was computed analytically by combining the standard deviations of the components.

The effective sunshape is then projected toward the focal plane. The reflector is divided into 124 equal area segments with the slope of

Table 2-2. Computer Code Inputs

Parameter	Range of Variables
Trough	
Rim angle	50° to 110°
Surface slope error	0 - 14 mrad
Specularity (FEK)	0.85 mrad
Receiver	
Receiver included angle	20° to 90°
Receiver apex position	0.83 to 1.33 in.
Receiver misalignment	$\pm$0.25 in.
Receiver width	3.0 in.
Cell leading edge position	>0.270 in.
Sunshape	2.9 mrad
Tracking error	0 - 0.5^{o}

each segment computed from the equation of the parabola. The slope error of each segment and any tracking error is added. Given the slope and the position of the receiver tube, the effective sunshape is projected onto the focal plane of the receiver.

The focal plane is also divided into many equal segments, each 0.0675 in. wide. Knowing the energy distribution of the sunshape as a function of angle, the energy falling upon each focal plane segment can be computed. This is repeated for each reflector segment, with the results summed to obtain the energy distribution at the focal plane. A simplified flow chart of the code is shown in figure 2-4.

Two other optical effects are included during this computation. At some receiver angles, the energy from the outside edges or center of the trough can strike the focal plane at large incident angles. When this happens, some of the energy can be reflected off the cover glass. The

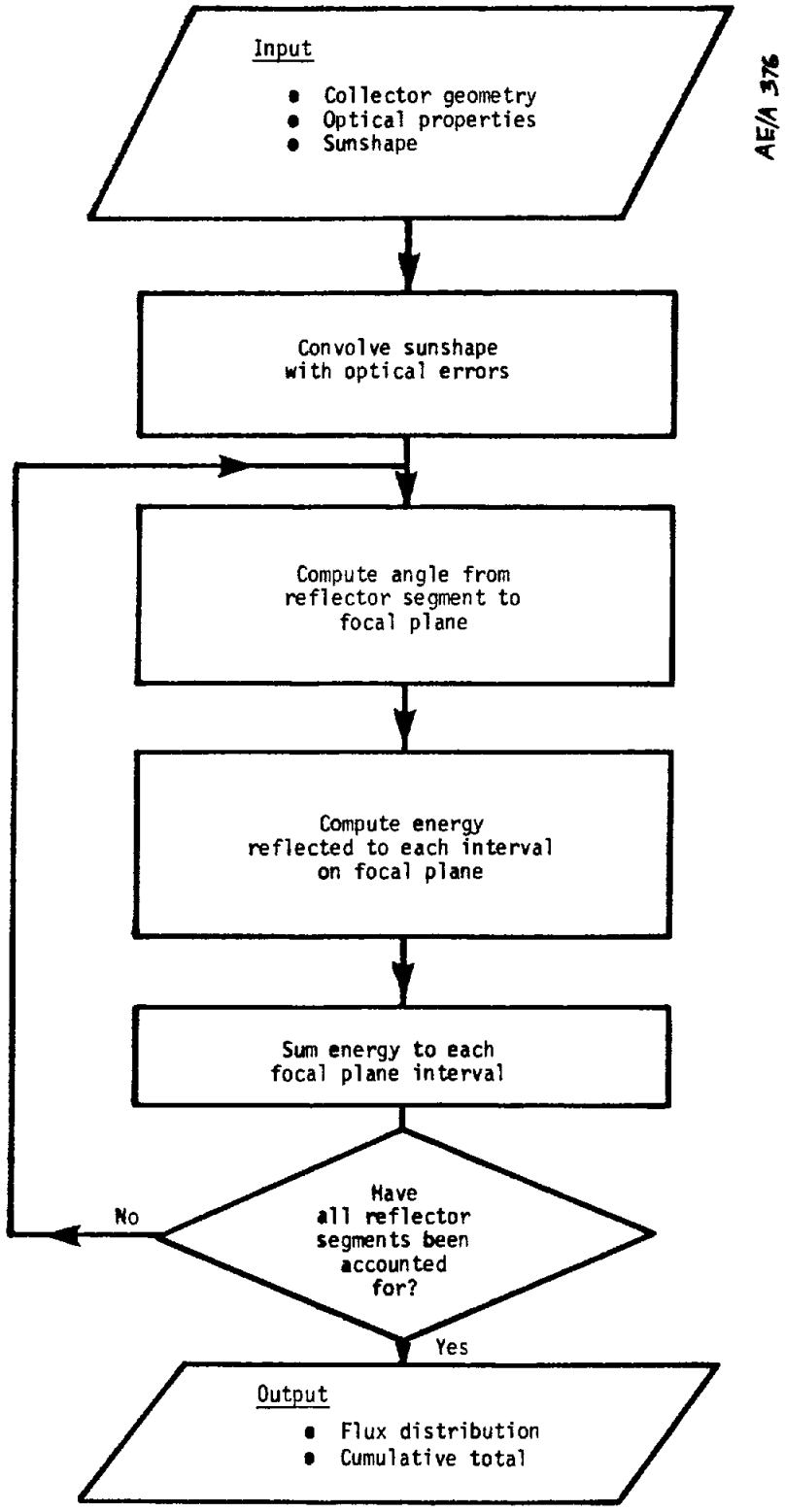

Figure 2-4. Simplified Flow Chart

code models this effect by assuming no reflection loss for angles up to 60° off normal. Beyond 60°, the reflection loss goes linearly from no loss at 60° to 100 percent loss at 90°. For the selected design, this factor accounted for a 0.3 percent performance degradation.

The other optical effect results from the slope errors. At the center of the trough, energy from one half of the trough can be reflected onto the cells facing the other half of the trough. This effect can become noticeable for shallow rim angle troughs ($\sim 50^{\circ}$) with large receiver included angles (up to 180°). As it turned out, the performance impact of this effect was not noticeable for the selected design.

In summary, accurate performance modeling is required to quantify the performance difference between various design options. The methodology outlined above has sufficient detail to account for all optical effects which influence concentrator performance in two dimensions.

2.3 COST ANALYSIS METHODOLOGY

The costing methodology used to compare one design to another is simply to project the manufactured cost of a 120 ft collector group (12 Acurex troughs with a center drive) and normalize it to the current design. For this analysis, only manufacturing costs at the current low capacity (400,000 ft^2/yr) were considered. No tooling or set-up costs are included, although they are shown in table 2-3. Once each candidate design was specified, design changes in components and assembly procedures could be evaluated in relation to current component cost and assembly labor costs.

The following common assumptions were made in the analysis: (1) 1-in. double-bus cells in identical encapsulation are used in all designs, (2) each collector contains the same number of cells, (3) the

Table 2-3. Cost Analysis Summary

Rim Angle	Receiver Configuration	Normalized Collector Cost	Tooling Cost
90°	Vee	1.000	-0-
110°	Vee	0.993	$37K
70°	Vee	1.006	$37K
50°	Vee or flat	1.008	$37K
90°	Split canted	1.000	$39K
90°	Split displaced	1.000	$32K

gross aperture area of the collector is 10 ft by 6 ft, (4) FEK 244 on Coilzak was used as the reflector, (5) stamped sheet metal ribs with torque tube design, (6) welded rib/flange/torque tube assembly.

For each angle of the rim angle study, the following changes were costed: 1) new reflector material total area, 2) new receiver support, 3) new rib stamping, 4) new receiver extrusion, 5) different length flex hose. Table 2-3 lists the overall cost impact of the various rim angles considered normalized to the 90° rim angle case. As indicated, the cost variations for the different rim angles are all less than 1 percent from the 90° case. The 50° and 70° rim angle cases have slightly higher costs than the 90° and 110° cases. This is due to the longer focal lengths which increase the cost of the receiver supports and flex hoses. This is countered by the fact that the lower rim angles require less reflector material.

The second set of inputs in table 2-3 are normalized manufacturing costs associated with the canted and displaced "split" version of the 90° rim angle collector. Neither of these designs has any significant impact on the manufacturing cost of collector. However, as with a change in rim angle, tooling changes would be required to produce either of these designs.

The components of the tooling cost for the split trough are as follows: new rib stamping die -- $7K, new rib/torque tube welding flange stamping die -- $2K, new weld fixture -- $30K.

These tooling costs do not include any engineering or design costs which would be required to implement any change from our current design. No estimate has been made of this effect.

2.4 OPTIMIZATION PROCEDURE

This section describes the procedures used to optimize the parabolic trough configuration for both the continuous reflector/Vee receiver and the split reflector/split receiver. Along with the selection of the optimum configurations, geometric sensitivity studies were done for both split and continuous trough. Sensitivity to reflector slope error was also studied for the continuous trough.

For both the continuous and split troughs, performance and manufactured costs were arrived at separately. These results were then combined to select optimum configurations in each category (maximum performance per cost) and finally to compare the split and continuous troughs.

2.4.1 Continuous Trough Optimization

The primary variable for the continuous trough is rim angle. The trough rim angle was varied from 50° to 110°. All other collector

geometric parameters were varied to maximize the optical efficiency at each rim angle. The basic procedure described in section 2.2 was used to determine the optimum geometric configuration.

Figure 2-5 shows a typical set of output curves generated by the rim angle study. These show the optical efficiency for various receiver apex positions and receiver included angles. For each point on these curves, the cell leading edge position was selected to yield the maximum intercept factor. Figure 2-5 shows a clear optimum receiver included angle of 34° with a receiver apex position of 1.08 in. The cell leading edge position was 0.270 in. Figure 2-6 shows the intensity profile across the receiver face for this geometry with the edges of the active cell area indicated along the distance axis. Intensity profiles for other rim angles are presented in appendix A. Figure 2-5 also shows the geometric sensitivity to a change in the receiver apex position by the change in optical efficiency for a given receiver angle. For this rim angle, there is only a 2.2 percent spread in optical efficiency between receiver apex positions of 1.21 in. and 0.96 in. Each curve also shows the sensitivity to receiver included angle for the given receiver apex position. The receiver included angle shows a clear optimum, which is easily achievable with an extruded substrate. The optimum receiver angle of 34° is influenced by several factors.

In order to maximize the intercept factor on the cell, the receiver/cell plane must be oriented to capture the reflected energy at the point where the ray bundle is the smallest. In order to do this, the receiver plane must be oriented normal to the "centroid" of that bundle. At first look, one might select a receiver angle of 72° to be normal to the ray coming from the center of the reflector. However, this angle is

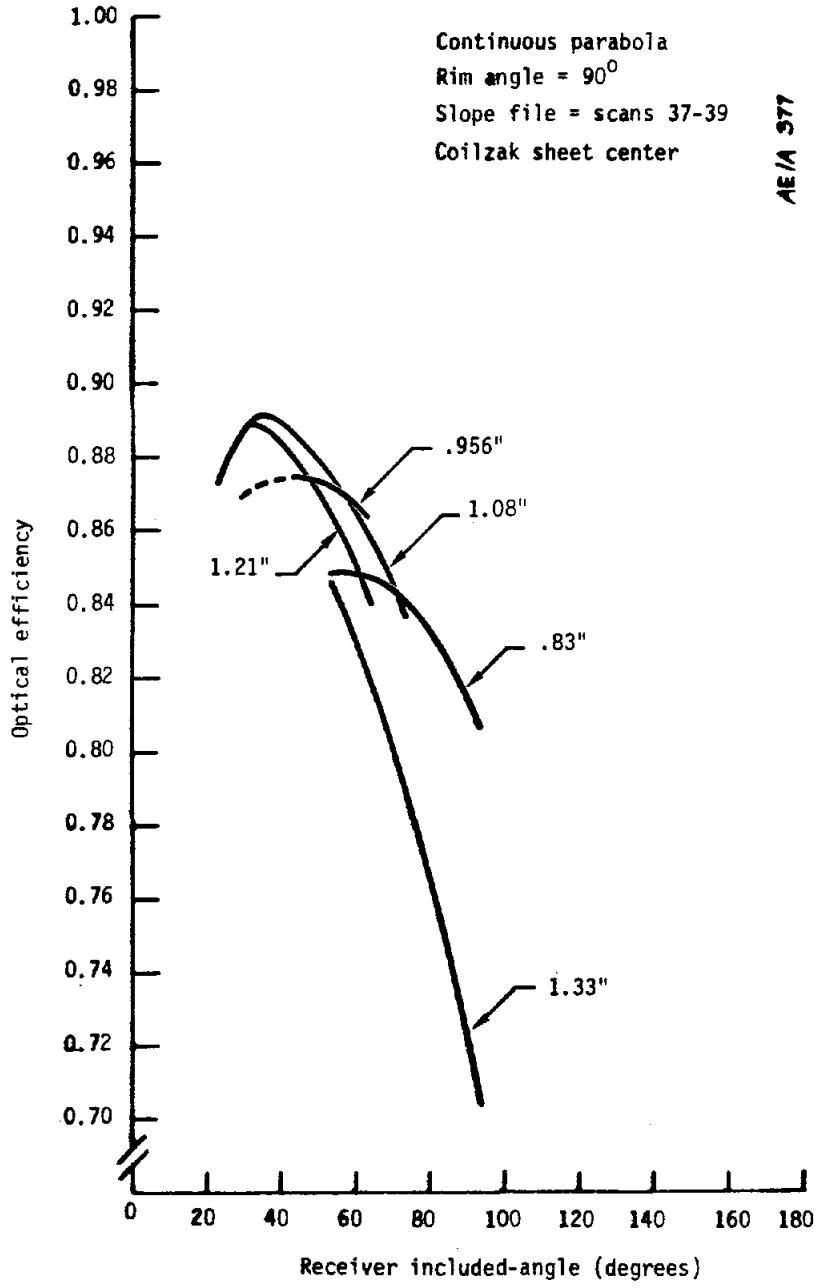

Figure 2-5. Optimization of Receiver Configuration for a Continuous Trough 90° Rim Angle

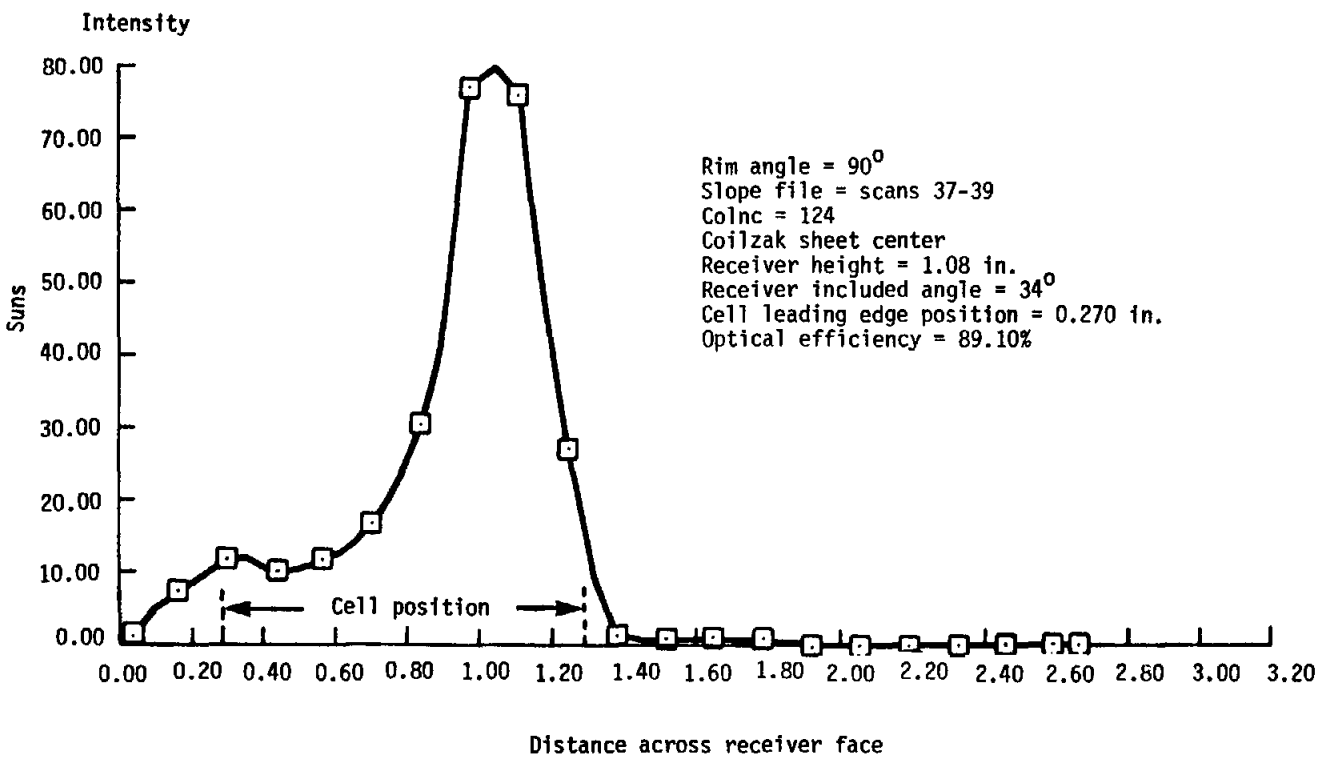

Figure 2-6. Receiver Intensity Distribution

driven to a smaller value because of receiver blockage, real slope error, and the nature of a parabolic trough combine to have the energy centroid reflected from a point about 3/4 of the way to the rim.

Figure 2-7 shows the results of the rim angle study as a single curve of optimum optical efficiency versus rim angle. A clear optimum occurs at around 95° with the current 90° rim angle trough only 0.3 percent lower in performance.

Two additional data points are shown for the special case of a 50° rim angle collector with a 180° apex angle or flat receiver. With a 2 in. wide double bus cell, the extrinsic losses are much higher than for a 1 in. wide cell. Although the intercept factor is 96 percent, the high extrinsic losses reduce the corrected optical efficiency to 81.9 percent. The double row of 1 in. cells has much lower extrinsic losses and the intercept factor is 91 percent for an optical efficiency is 83.4 percent.

2.4.2 Slope Error Sensitivity

In studying the rim angle sensitivity for the continuous trough, the significant performance variation with slope error became evident. As a result, a separate study was done to determine the effect on optical efficiency of varying the slope error. Slope error files generated in a like manner to the Coilzak file were selected and used as input to the computer code as described in section 2. The rim angle was fixed at 90° for all slope error files in this study. For each slope file, the receiver apex position, receiver included angle and the cell leading edge position were varied, as described in section 2.4.1, to yield a maximum optical efficiency. All other parameters were held constant. A perfect slope file, along with files for the center and edge of a microsheet glass

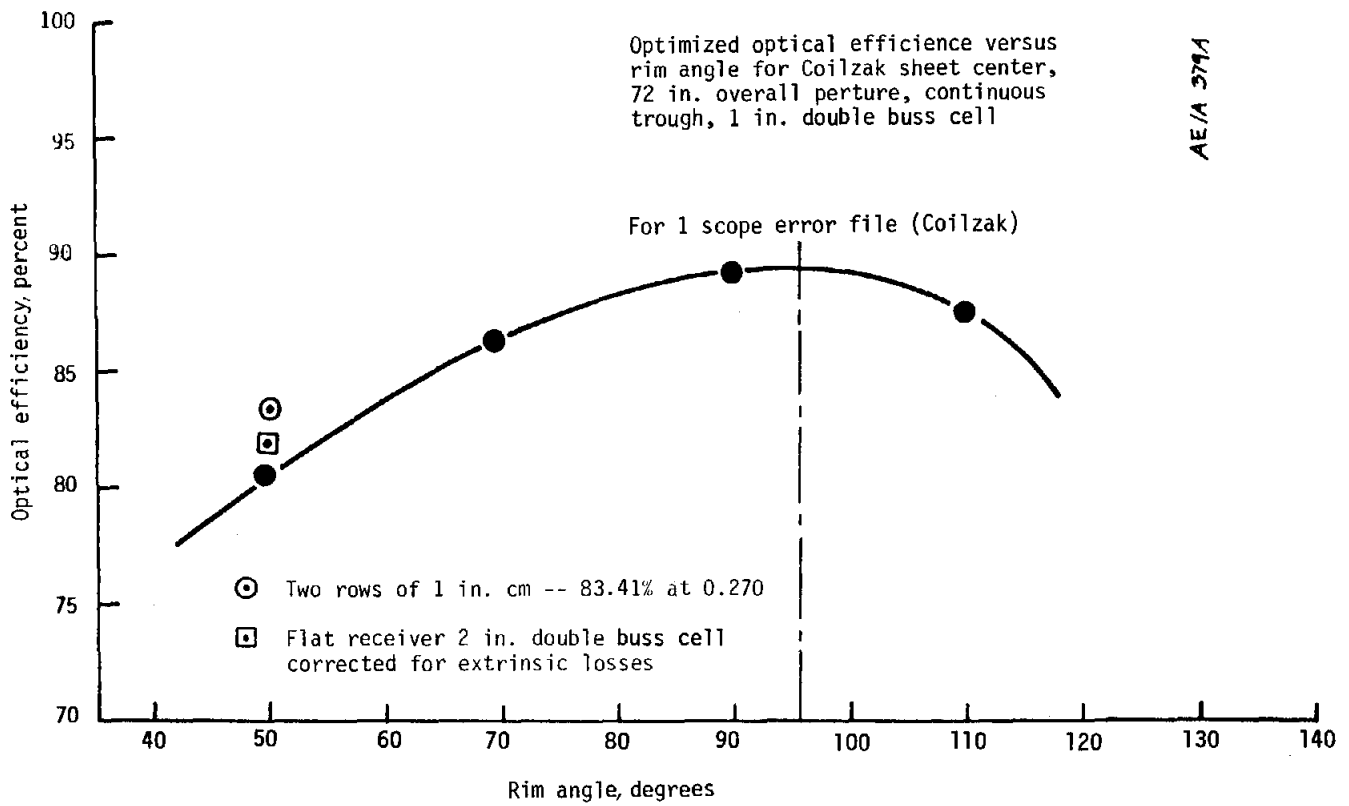

Figure 2-7. Rim Angle Optimization -- Continuous Trough

reflector were compared to the standard Coilzak file. Table 2-4 shows the variation in maximized optical efficiency for each of the four slope error files. As the wide variation (11 percent) in optical efficiency indicates, the trough performance is more sensitive to slope errors than to rim angle.

Figure 2-8 shows the intensity profile of a trough with glass edge slope error which is significantly more spread than the Coilzak trough in figure 2-6. Figure 2-9, shows energy integrated from the receiver apex. Eight percent of the reflected energy completely misses the cell. This accounts for the majority of the difference in optical efficiency between the Coilzak and glass sheet edge files, with the remainder due to a reduction in intercept factor for the energy which strikes the receiver.

Figure 2-10 shows the optical efficiency versus receiver included angle for the glass sheet edge file. The three curves illustrate the optimum receiver angle and receiver apex position, along with the sensitivities to each. The 24° optimum receiver angle is not practical

Table 2-4. Optical Efficiency for Various Slope Error Files

Maximized Optical Efficiency (Percent)	Slope Error File
93.49	No slope error
89.10	Scans 37-39, COLNC-124, Coilzak sheet center (standard)
92.50	Scans 26-28, glass sheet center
82.55	Scans 17-23, glass sheet edge

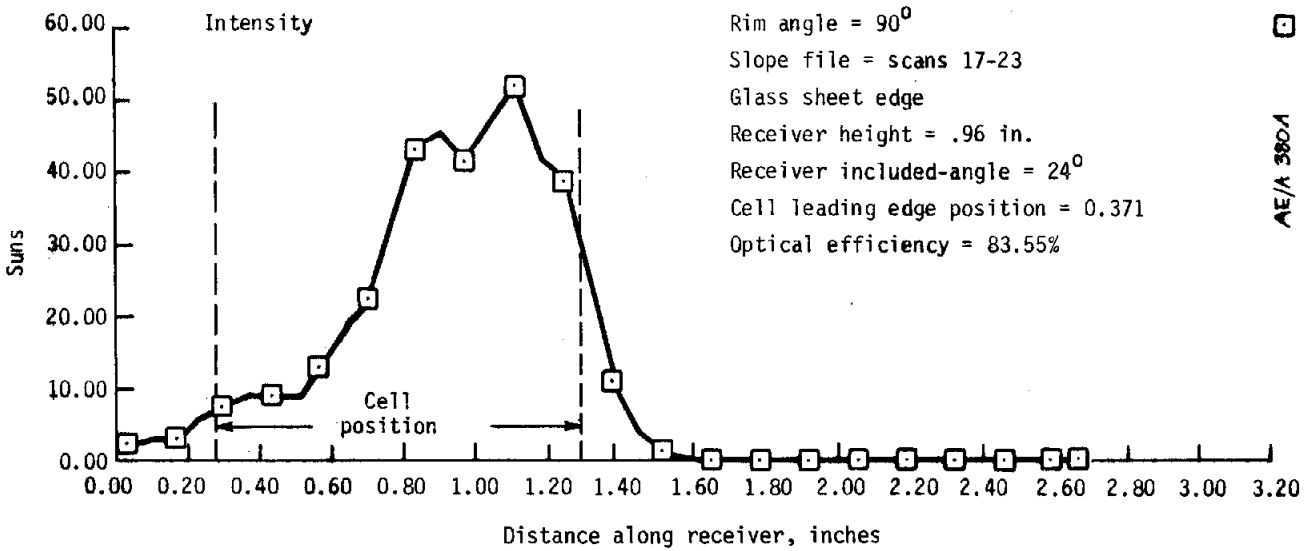

Figure 2-8. Intensity Profile for Glass Sheet Edge Slope Error File

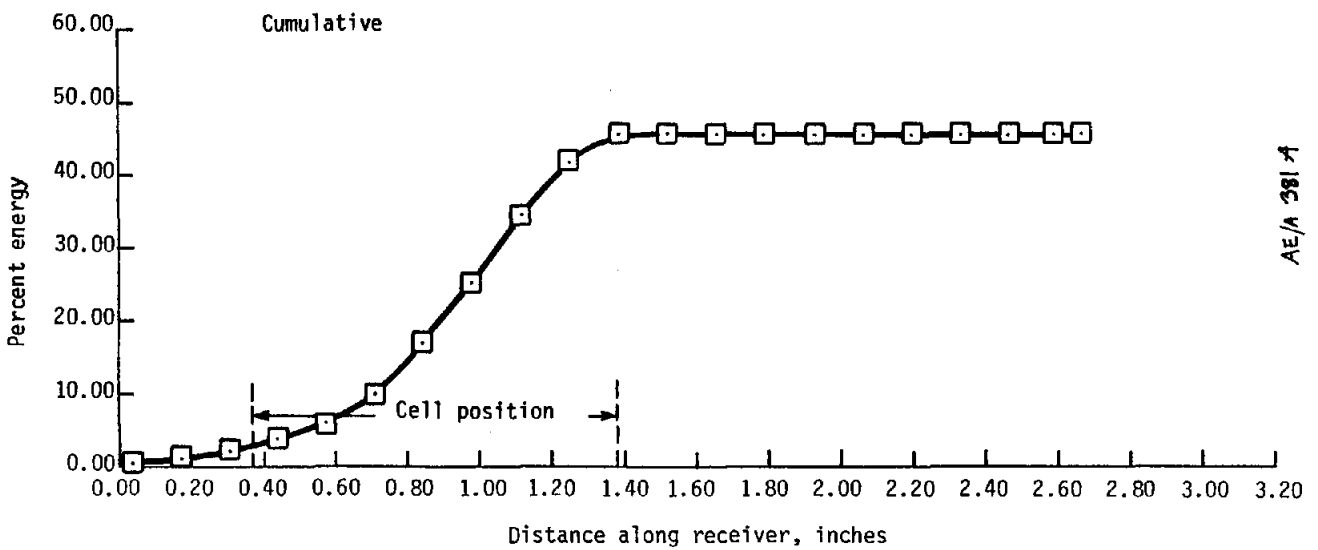

Figure 2-9. Integrated Energy Flux for Glass Sheet Edge Slope Error

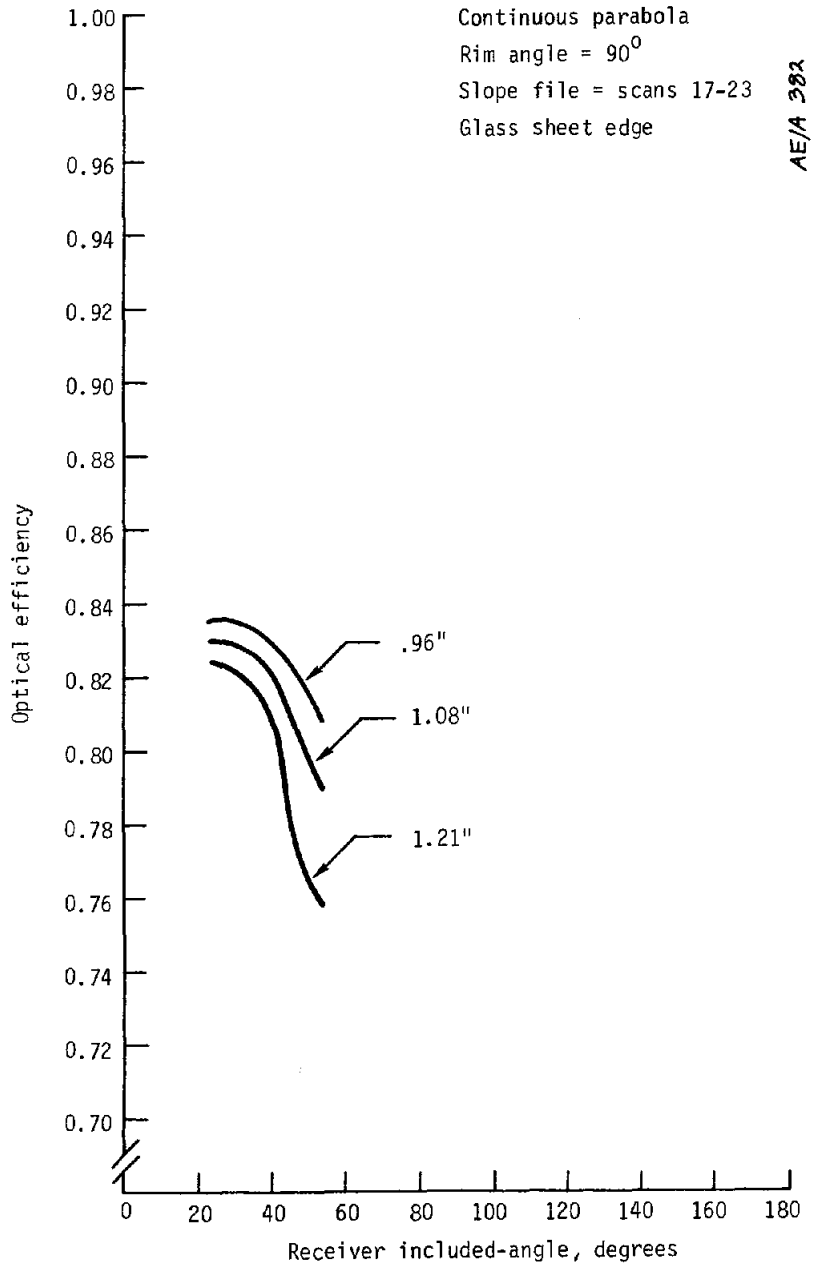

Figure 2-10. Receiver Configuration Optimization for Glass Sheet Edge Slope Error

because the heat cannot be effectively removed from the apex area without high coolant mass flowrate and corresponding high parasitic pumping power requirement. Yet the sensitivity to this parameter is weak enough that a more practical 44° can be selected with only a 3 percent reduction in optical efficiency. Appendix B contains the remaining optical efficiency and intensity profile curves for the slope error study.

2.4.3 Split Trough Optimization

One of the limitations of the continuous parabolic trough is that the cell location is constricted by the receiver design limitations. Figure 2-2 illustrates that the cell position cannot cross the centerline of the trough. The split trough results in two focal points for the trough, allowing greater flexibility in cell placement with the same receiver design (figure 2-3). The parabolic trough can be altered by two methods. One is to simply displace the two halves of the trough creating a "deadband" at the center. Alternatively, both halves can be canted away from each other to create two focal points.

Each split trough concept was optimized for best receiver location, included angle and cell position. A comparison of the split trough concepts with the continuous trough is presented in table 2-5. As expected, the split trough concepts exhibit a slightly higher optical efficiency because of better cell position. In fact, both split trough concepts have the same optical efficiency of 90.8. This is not surprising because both concepts have the effect of positioning the cell at any location relative to the focal point.

The performance increase is small (1.7 percent) for two reasons. First, the continuous trough focuses the incoming energy well enough that only 6.5 percent of the energy not blocked by the receiver tube misses the

Table 2-5. Performance Comparison of Split and Continuous Trough

Trough Configuration	Optical Efficiency	
	Coilzak Slope Error	Perfect Slope
Continuous parabolic	89.1	93.5
Split displaced	90.8	96.9
Split canted	90.8	96.9

1 in. cell. This leaves little room for improvement. Furthermore, the "spillover" of energy is off both sides of the cell; thus any gain in optical efficiency obtained by moving the cell closer to the apex is offset by the energy lost from the other end. This is illustrated in figure 2-11 which shows the sensitivity to cell placement for the split trough concept.

Both split trough concepts show the same improvement in optical efficiency with approximately the same cost increase. The displaced split trough was preferred to the canted trough because of manufacturing considerations. The canted design has a discontinuity of slope at the base of the trough. This requires a retaining strip down the center of the trough, and two sections of reflector instead of one. Despite the similarity in costs, the canted design has greater uncertainty in quality of the reflected image. Thus for the split trough designs, the displaced trough design was selected.

Looking at the displaced split concentrator, the trends for cell placement and receiver design, shown in figure 2-12, are similar to the

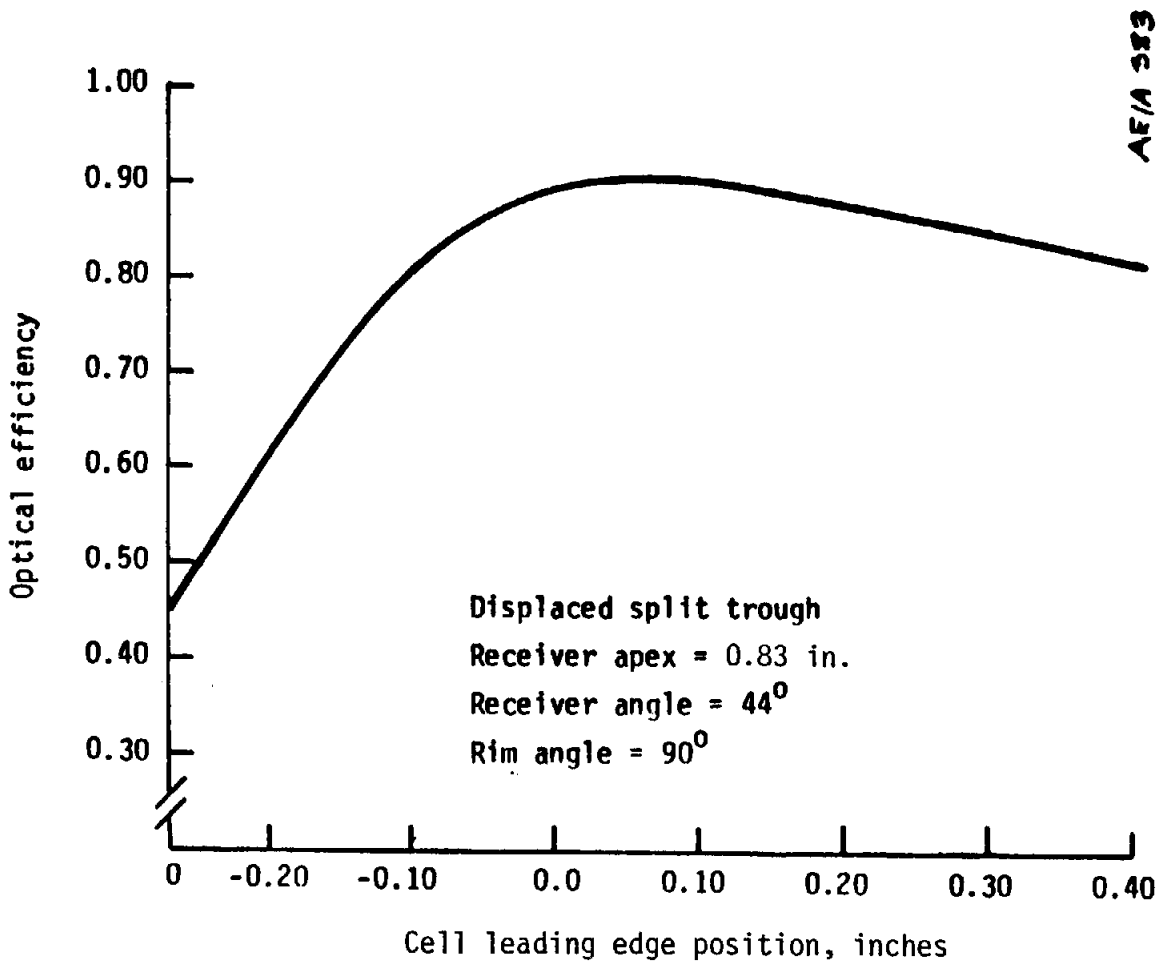

Figure 2-11. Performance Sensitivity to Cell Placement -- Split Trough

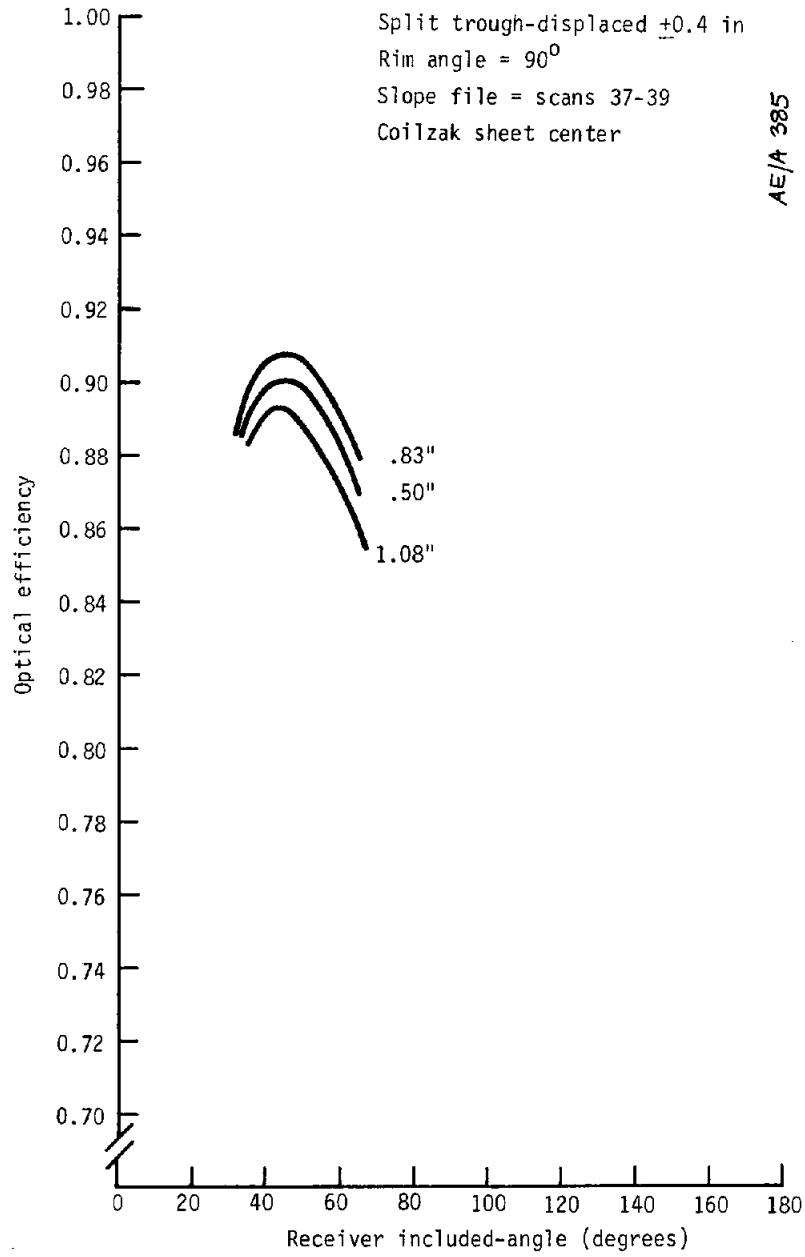

Figure 2-12. Receiver Configuration Optimization Split Trough Design

continuous parabola. The optimum receiver angle is well defined at 44°. There is also a clear optimum receiver apex position of 0.83 in. The cell position corresponding to these parameters was compared to the optimum cell position for the continuous trough, and they were found to be almost coincident (figure 2-13). This figure also shows how the split trough concept has a slightly larger view angle which accounts for the higher output.

The cost analysis from section 2.3 shows the manufacturing cost of both split trough concepts to be equivalent to the continuous parabola. The retooling cost for the displaced split trough design is $32,000. Including the additional engineering and design costs would bring the total redesign cost to about $80K. Amortized over an anticipated production run of 400,000 ft^2 of collectors, the additional cost is only 0.4 percent. Combined with the performance increase from 89.1 to 90.8 percent, the net result is an increase in cost effectiveness of 1.4 percent for the split trough design. Consequently, the displaced split trough was selected as the optimum design.

2.5 PERFORMANCE SENSITIVITY OF OPTIMUM DESIGN

Upon selection of the displaced split trough as the optimum design, a sensitivity study was performed to evaluate trough response to a variety of conditions. Receiver misalignment, both vertical and horizontal, were studied, as was sensitivity to pointing error. Another parameter was slope error, discussed in section 2.4.2

Figure 2-14 illustrates this degradation in performance with receiver misalignment. Within the expected alignment errors during assembly of $\pm 1/8$ in, the performance is off by no more than 2.7 percent.

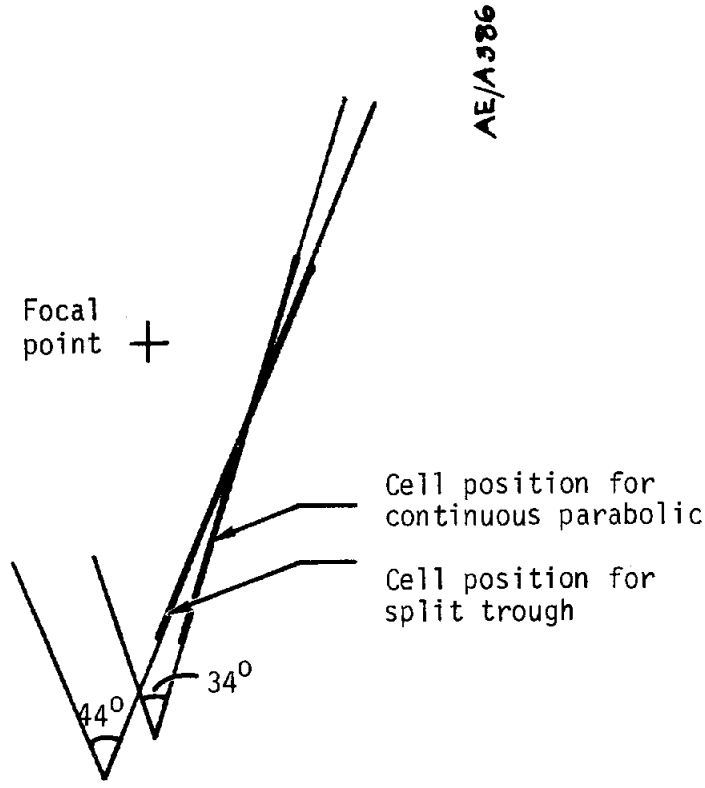

Figure 2-13. Comparison of Split and Continuous Trough Optimum Receiver Configuration

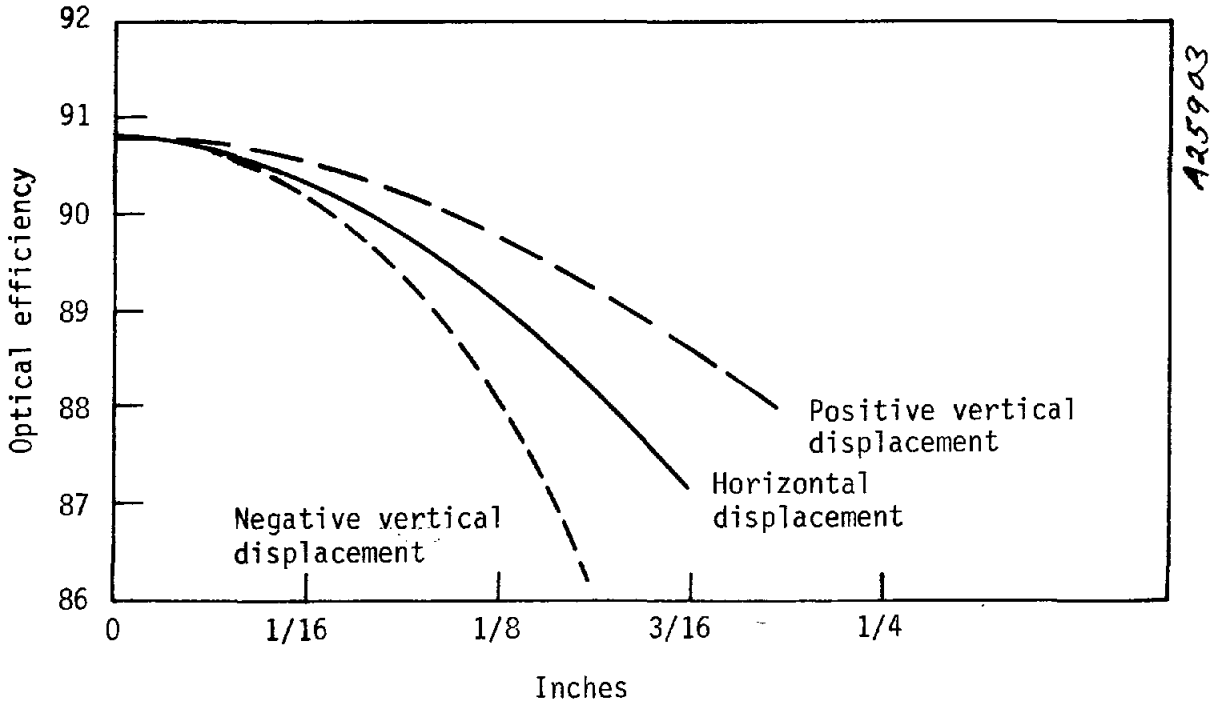

Figure 2-14. Performance Degradation with Receiver Misalignment

Accurate tracking of the sun is also required for maximum collector output. Acurex tracker can track the sun, including installation misalignment to within $\pm 1/8^{\circ}$. Most of the pointing error results from collector "windup." This occurs when the wind creates an overturning moment about the collector axis, causing misalignment in the modules farthest from the array drive unit. At the highest operating wind speed of 30 mph (survival wind speed is 80 mph) the maximum pointing error can be as high as 1° depending on wind orientation. For average wind conditions, however, of 10 mph, the average windup at the worst module is not expected to exceed $1/2^{\circ}$. Figure 2-15 shows that optical efficiency degrades to an average 86.5 percent at $\pm 0.125^{\circ}$ and 77.0 percent at $\pm 0.25^{\circ}$.

Note how the performance degradation is highly asymmetric at large pointing errors. This can be explained by referring to figure 2-6 which shows the image at the focal plane also to be highly asymmetric. The pointing error has the effect of moving the image across the cell. Since the trough has two halves, each a mirror image of the other, the receiver will see an optical efficiency corresponding to a positive pointing error on one side and a negative error on the other.

Optical efficiency varies widely with the slope error of the reflective surface as shown above with the continuous parabola. This is also true with the split trough. To see what performance improvements are possible, the computer code was run assuming a perfect parabola with no slope error. The results show that all the energy not blocked by the receiver, 97 percent, is intercepted by the cell. This represents a potential improvement of over 6 percent in optical efficiency.

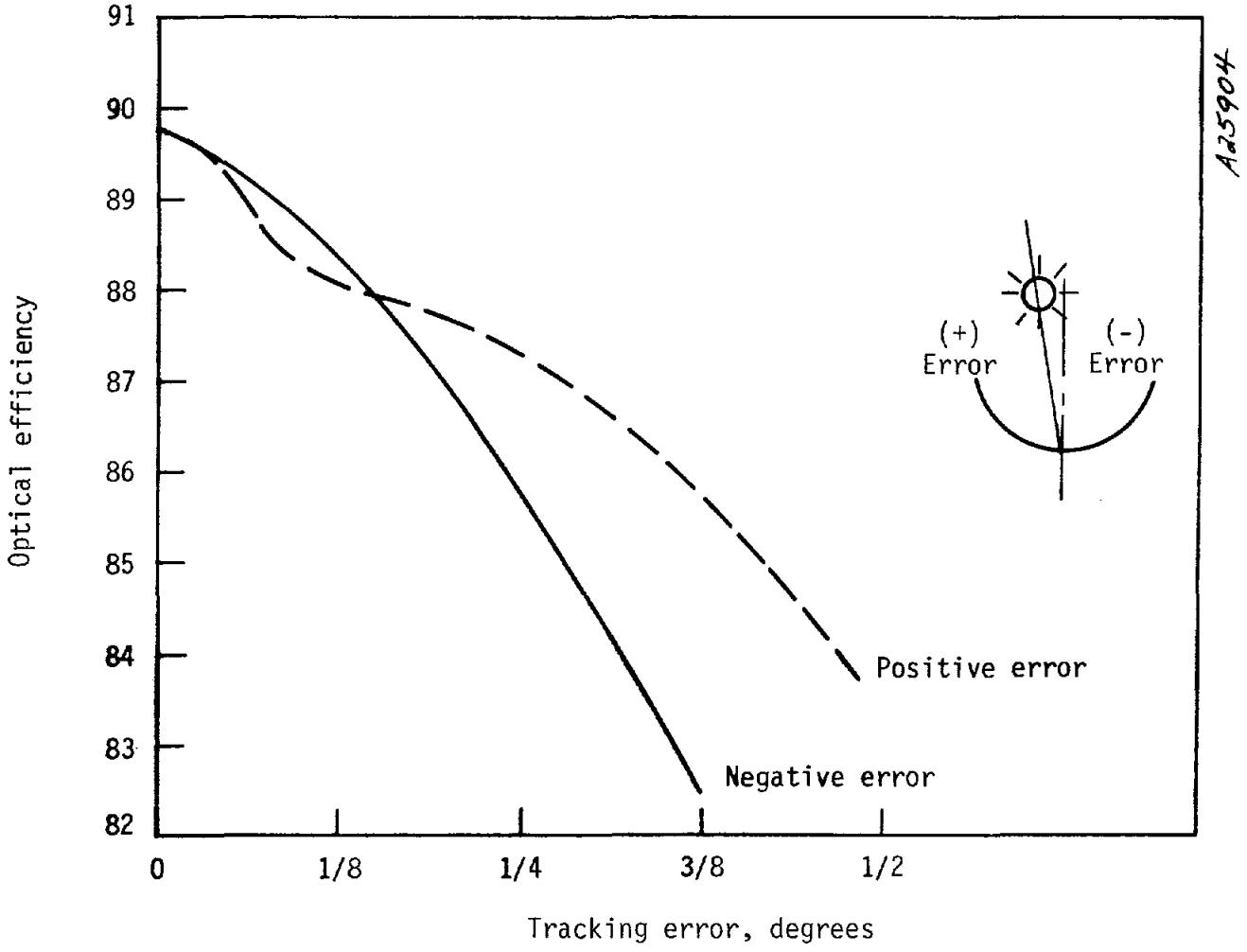

Figure 2-15. Performance Degradation with Tracking Error

In summary, the displaced split trough concept shows a modest increase in cost effectiveness over the continuous parabola. It also permits greater flexibility in design of the receiver tube/cell package assembly. The retooling costs, however, can only be justified if the production volumes assumed in the cost analysis are met. Alternatively, manufacturing changes to improve slope error could improve performance of the design continuous parabola from 89.1 to 93.5 percent. This indicates that the first area to pursue is not collector design, but methods of improving the manufacturing process to minimize slope error.

Collector redesign is not to be ignored, however, because the combined effect of improved design and slope error is to raise optical efficiency by 10.7 percent to 96.9 percent. If the collector is resdesigned, additional improvements should be considered. Acurex is currently designing larger trough modules 20 ft long and 7 ft wide for the next generation concentrator. A larger trough has the potential for reducing both the concentrator cost per square foot of reflector and the installation cost per square foot. It would not be prudent to change to a displaced split trough without also considering the 7 x 20 ft trough. The best arrangement would be to coordinate both redesign efforts and implement them at the same time.

SECTION 3

FLEXIBLE GLASS LAMINATE REFLECTIVE PANEL DEVELOPMENT

3.1 INTRODUCTION

The development of a reliable flexible glass laminate reflective panel has been undertaken by Acurex Corporation and Sandia Laboratories as a means of increasing performance and reducing maintenance of the photovoltaic Parabolic Trough Concentrating Collector.

The concept involves bonding thin, back surface-silvered glass to a metal backing sheet. The thickness of the glass and backing metal is specified such that the neutral axis (which separates regions of tension and compression loads during flexure) is located within the metal backing. Appendix C includes the details of the neutral axis calculation. This assures the glass will be subjected only to compressive stresses when the laminate panel is flexed into the parabolic profile. Glass has very low tensile strength but fairly high compression strength.

The advantages of flexible glass laminates over other currently used reflective surfaces are:

- Approaching maximum reflectivity of commercially available products
- Second surface silvering allows the use of less delicate cleaning techniques (i.e., no special personnel training or equipment required)

- Better durability (i.e., reflective silvering protected from degradation by the glass and adhesive/metal backing)
- Fabrication procedure could be adapted to automated production techniques
- Application to most parabolic concentrating collector structures is possible

3.2 SCOPE

Flexible glass laminate reflective panels developed and fabricated shall meet these critera:

- Compatible with the Acurex Model 3001 Parabolic Trough Concentrating Solar Collector
- Manufactured from commercially available raw materials
- Does not require exotic fabrication procedures
- Environmentally stable
- Fracture-resistant to hailstones

The work performed under this effort was an extension of flexible glass reflective panel development and fabrication work done by Acurex under interal programs and in support of the International Energy Agency 500 kWe Distributed Collector Field program.

3.3 PANEL DESIGN

Flexible glass laminate panels were designed and fabricated independently by both Acurex and Glaverbel of Belgium.

The Glaverbel design consists of back-silvered, chemically tempered, thin silicate glass bonded to thin, galvanized sheet steel. The panels provided were of two types, differing only in the adhesive system. The adhesives used by Glaverbel were: (1) epoxy, and (2) a polyester film

with double-sided acrylic adhesive. Properties of the glass used are shown in table 3-1.

The Acurex design uses perforated sheet metal as the backing material to prevent air entrapment in the adhesive bond region. An epoxy-Versamid adhesive was used as recommended by Sandia studies.* Two types of glass were used: (1) borosilicate fusion glass manufactured by Corning Glass Works and (2) chemically-tempered, machine-made silicate glass manufactured by Flabeg of West Germany. The properties of the Corning and Flabeg glass are given in tables 3-2 and 3-3, respectively.

The sheet metal backing material used had perforations of a large enough diameter (0.079 in.) and close enough spacing (0.216 in. staggered) to allow complete removal of air bubbles from the bond region. Excess epoxy adhesive was easily forced through the perforations resulting in a uniform bond thickness (approximately 0.003 in.). The specified backing material thickness is calculated to result in a laminate neutral axis located within the sheet metal backing. See appendix A for the calculation procedure.

Descriptions of the panel combinations of glass, adhesive, and backing steel fabricated by Acurex and Glaverbel are contained in table 3-4.

3.4 LAMINATE FABRICATION

The fabrication procedures used by Acurex and Glaverbel are not exotic and are most likely adaptable to large-scale, automated production techniques requiring only semiskilled labor.

---

*Marion, R. H. and R. C. Reuter Jr., "A Thin Glass Reflector Laminate for Solar Concentrators -- Design, Fabrication, and Testing," Sandia Laboratories, Albuquerque, New Mexico.

Table 3-1. Properties of Glass — Glaverbel

Dielectric Constant

At 20°C for 4×10^{10} Hz : 6.8

Hardness

A. Diamond-Vickers Scale, angle of 136°

600 to 650 kg/cm^2

B. Mohs' Scale

6 to 7

Resistance to Compression:	±9.00 K°/cm^2
Resistance to Traction:	±900 K°/cm^2
Specific Weight:	2.482744 (±0.00001)
Elasticity:	E = 7.000 kg/mm^2 (Young's modulus)

Thermal Conductivity:

At normal temperature:	0.7 to 0.8 Kcal/h/m^2/°C/m
At melting temperature:	1.5 to 2.0 Kcal/h/m^2/°C/m

Mean Coefficient of Expansion:

From 23° to 100°C	7.54×10^{-6}
From 23° to 400°C	8.14×10^{-6}
From 23° to 558°C	8.48×10^{-6}
From 23° to 585°C	9.02×10^{-6}

Specific Heat:

0.25 cal/kg/°c

Point of Littleton:	±700°C by 7.65 P
Softening point:	±600°C by log 11 P
Annealing point:	±530°C by log 13.2 P
Straing point:	±510°C by log 14.5 P

Refraction Index:

For λ = 589.3 nm (Sodium light): 1.5133
For λ = 546.0 nm (Mercury light): 1.5130

Light Transmission:

For 380 nm: 93.5 percent
For 1200 nm: 80 percent

Composition:

$SI\ O_2$	71.96 percent
Na_2O	14. percent
K_2O	0.70 percent
Ca O	7.14 percent
Mg O	3.99 percent
Fe_2O_3	0.1 percent
Al_2O_3	1.88 percent
SO_3	0.23 percent

Table 3-2. Properties of Glass -- Corning

Corning's Glass Reflector Substrate-Code 7809

Surface weatherability equivalent to that used in chemical laboratories.

Total hemispherical reflectivity weighted for the solar energy distribution up to 96%.

Reflective dispersion across the entire mirror area that is better than 2 milli radians.

Thickness from 0.040 to greater than 0.125 inches.

Widths to 52 inches and lengths to 10 feet.

Properties	7809
Softening Point, °C	750°
Annealing Point, °C	569°
Strain Point, °C	529°
Expansion, 0-300°C x 10^{-7}/°C	77
Poisson's Ratio	.20
Young's Modulus (psi)	11.1×10^6
Density, gm/cm³	2.44
Index of Refraction	1.509

Solar Transmission 1.5mm or less (Per Battelle Testing)	91.5%
Weather Resistance	Excellent

Based on prototype melt—may vary slightly with production melt.

Data provided by Battelle Pacific Northwest Laboratories
Richland, Washington

Solar Reflectivity

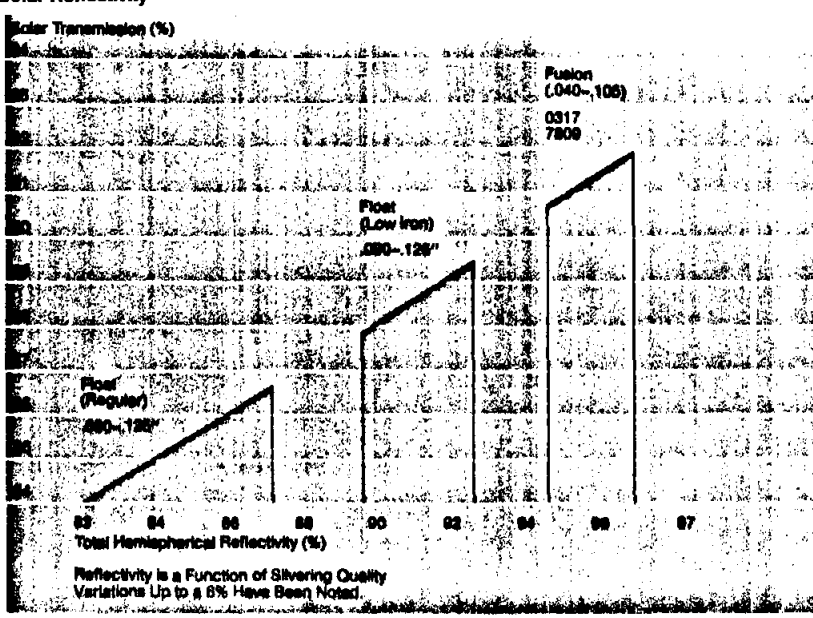

Solar Transmittance

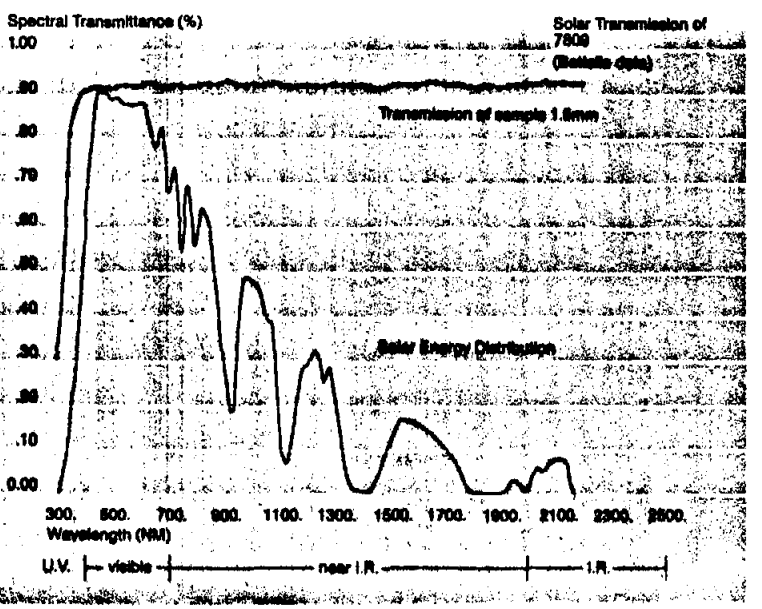

Table 3-3. Properties of Glass — Flabeg

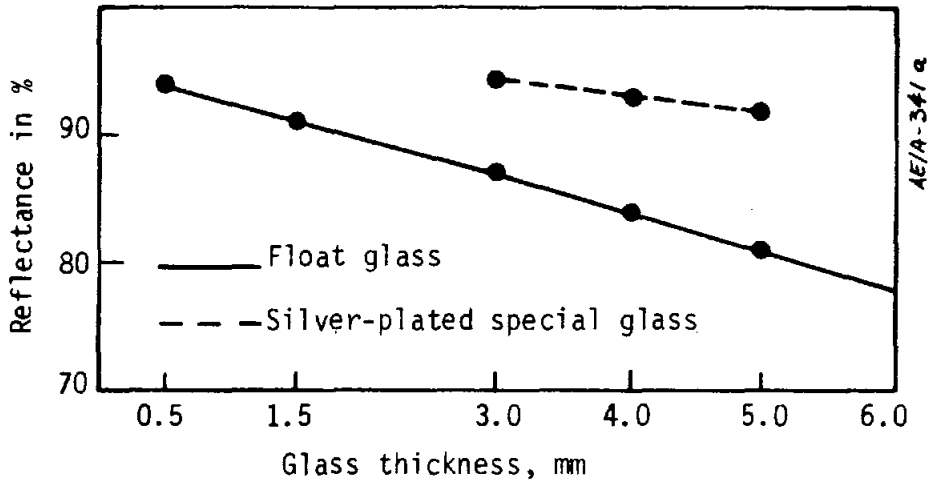

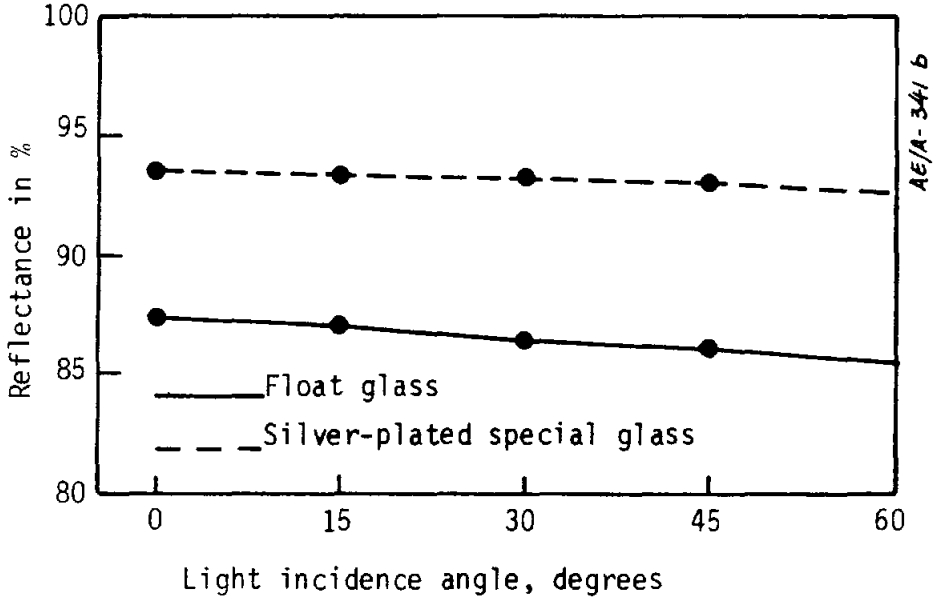

Physical Data of the Glass	
Specific weight	2.5 kg/mm m^2
Modulus of elasticity	750,000 kp/cm^2
Compressive strength	8,000-10,000 kp/cm^2
Coefficient of thermal linear expansion	$\simeq 9 \times 10^{-6}$ m/m°K (at 20 to 100°C)
Resistance to temperature variations	approximately $\pm$ 40°C
Mirror Structure	
Glass thickness	0.6 - 0.8 mm
Thickness of silver plating	0.8 $\pm$ 0.1 g/m^2
Thickness of copper layer	0.3 $\mp$ 0.05 g/m^2
Thickness of base lacquer	35 $\pm$ 10 μ
Thickness of cover lacquer	45 $\mp$ 10 μ
Structure of type of lacquer	annealing lacquer, highly solvent-resistant

Table 3-4. Description of Flexible Glass Laminate Panels

Number	Glass	Adhesive	Backing Steel
1	Corning code 7809, 0.060 in. thick	Epoxy-Versamid (70 wt percent Epon 828, 30 wt percent Versamid 140)	Perforated, cold-rolled sheet, 12.1 percent open, 0.062 in. thick
2	Corning code 7809, 0.060 in. thick	Epoxy-Versamid	Perforated, cold-rolled sheet, 12.1 percent open, 0.050 in. thick
3	Corning code 7809, 0.040 in. thick	Epoxy-Versamid	Perforated, cold-rolled sheet, 12.1 percent open, 0.050 in. thick
4	Flabeg, Chemically-tempered 0.040 in. thick	Epoxy-Versamid	Perforated, cold-rolled sheet, 12.1 percent open, 0.050 in. thick
5	Glaverbel, Chemically-tempered 0.024 in. thick	Epoxy	Galvanized steel, 0.030 in. thick
6	Glaverbel, Chemically tempered 0.024 in. thick	Polyester film with double-side acrylic adhesive	Galvanized steel, 0.030 in. thick

The procedures used by Glaverbel are considered proprietary and are not available for inclusion in this report.

The step-by-step fabrication procedure used by Acurex is detailed as follows:

1. Apply the epoxy adhesive liberally to the back of the glass mirror
2. Position the glass on backing metal with the perforation burr side down and secure with masking tape
3. Wrap the composite panel in successive layers of TX1040 Teflon and Trevarno silicone-treated porous glass release fabrics
4. Place the composite panel in a plastic breather bag, seal, and pull a vacuum on the bag (maximum 4 psia) for 30 min to apply a uniform bearing pressure over the panel surface
5. Remove the plastic bag and release fabric
6. Apply a uniform dead weight over the panel surface and allow the epoxy to cure (minimum 48 hr at room temperature)

Heavy application of epoxy near the glass edges results in an epoxy fillet along the edges providing protection of the silvering from weathering.

Two sizes of flexible glass laminate panels were fabricated. The dimensions and uses are given in table 3-5. Layouts of the glass on the backing metal are shown in figures 3-1 and 3-2.

3.5 ACCELERATED ENVIRONMENTAL EXPOSURE

Accelerated environmental exposure testing of the flexible glass laminates was performed by Sandia Laboratories, Albuquerque, New Mexico. The three tests performed and the test results are described in the following paragraphs.

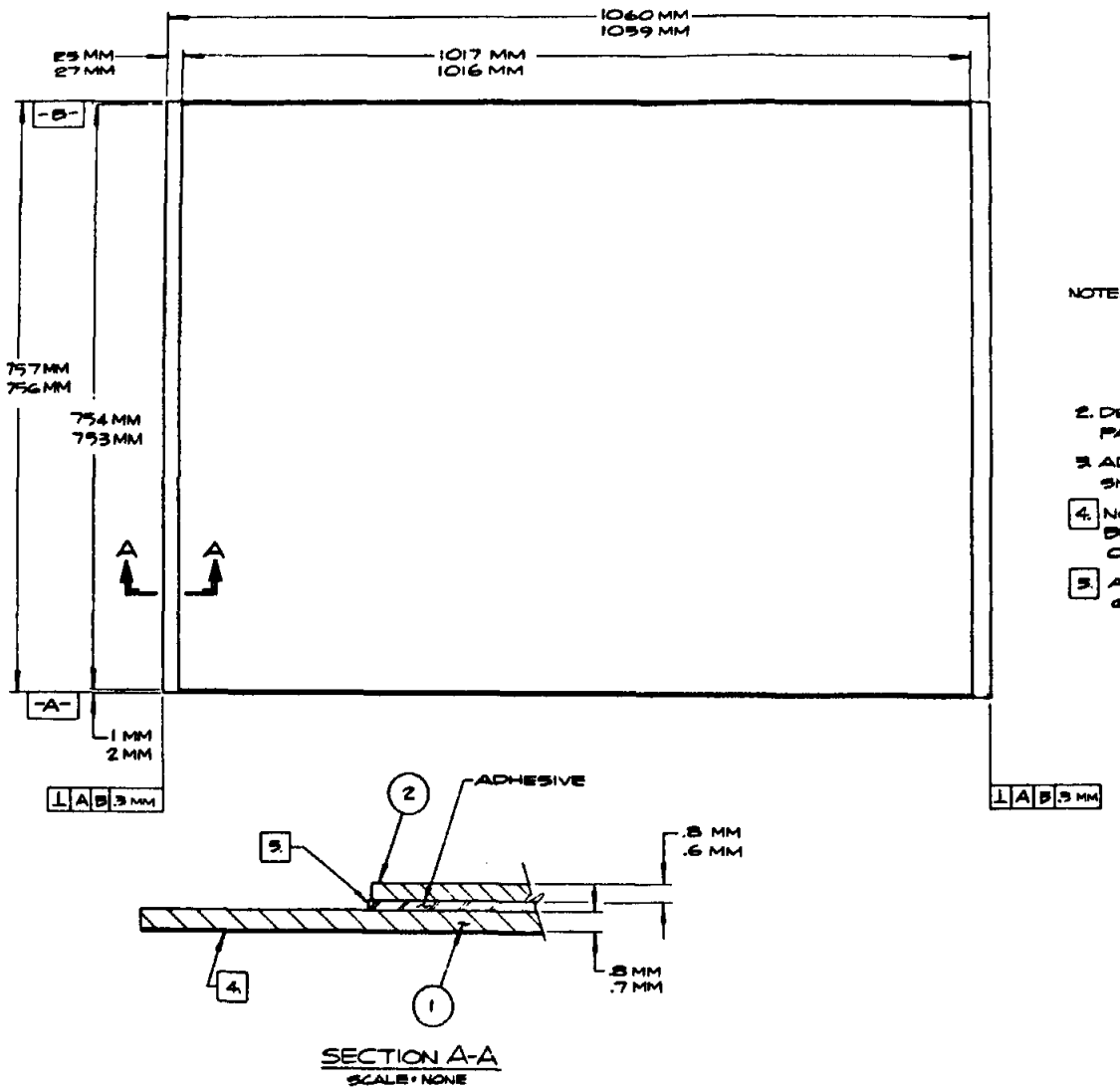

NOTES:

2. DEBURR SHEET METAL EDGES PRIOR TO PANEL ASSEMBLY.
3. ADHESIVE OR GLASS SHALL NOT OVERHANG SHEET METAL BACKING.
4. NON-REFLECTIVE SURFACES AND EDGES TO BE CORROSION PROTECTED BY SEALING OR SACRIFICIAL COATING.
5. ADHESIVE EXTENSION BEYOND EDGES OF GLASS NO MORE THAN 2 MM EACH END.

Figure 3-1. Flexible Glass Laminate — Full Size Panel

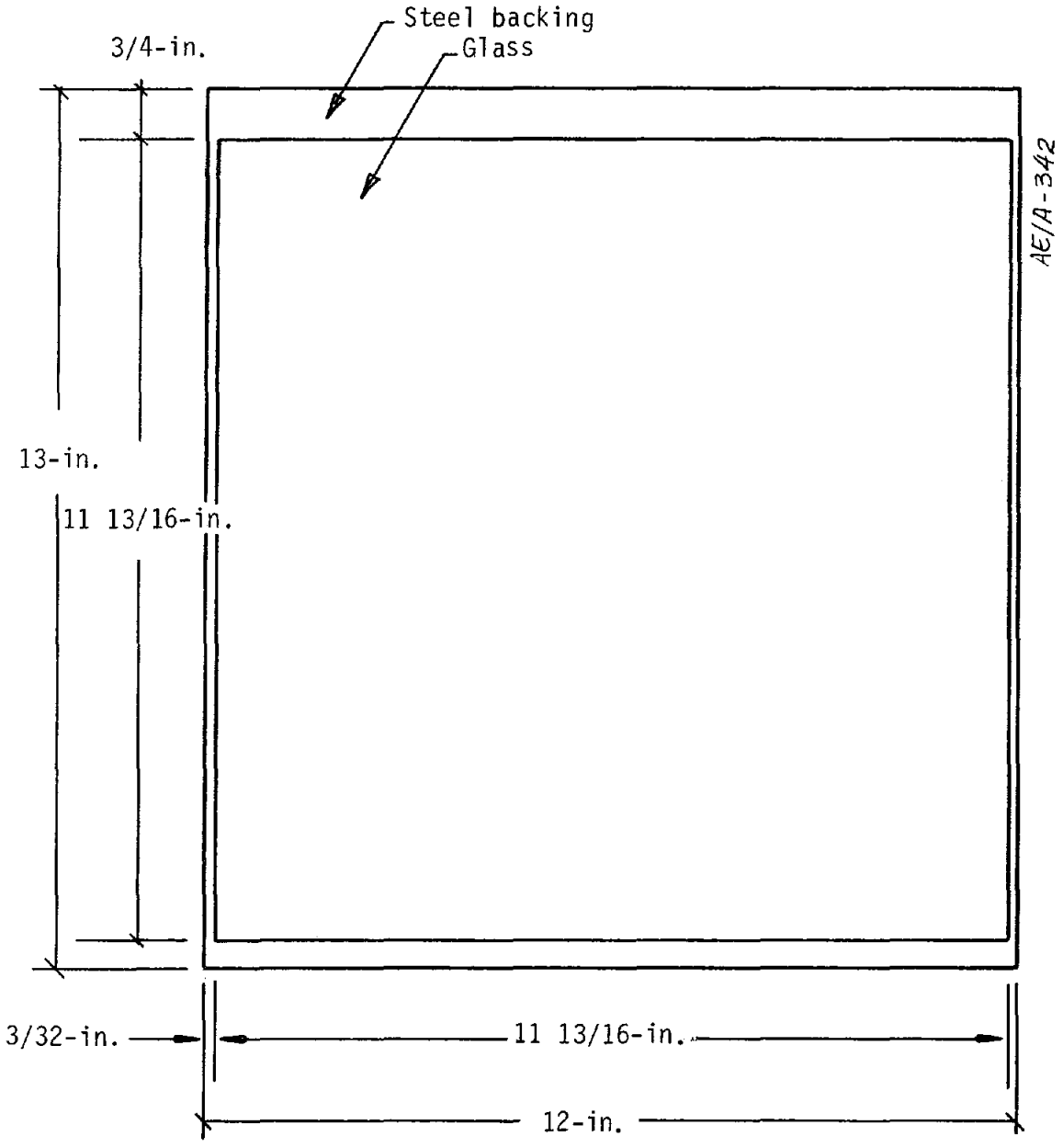

Figure 3-2. Flexible Glass Laminate -- Small-Scale Panel

Table 3-5. Glass Panel Dimensions and Uses

Dimensions (in.)		Use
Glass	Steel	
11-13/16 x 11-13/16	12 x 13	• Accelerated Environmental Exposure (section 3.5) • Minimum Bend Radii (section 3.8)
29-11/16 x 40	29-13/16 x 41-3/4	• Installation Feasibility (section 3.6) • Hail Impact Survivability (section 3.7)

Test 1 -- Temperature Cycles

The Laminate panels were subjected to temperature cycles from -6° to $120^{o}C$, 12 cycles per day for 4 weeks. The glass remained intact and the adhesive bond did not fail.

Test 2 -- Freeze/Thaw Cycle

Laminate panels were subjected to a freeze/thaw cycle between -10° and $60^{o}C$ with 100 percent humidity at $5^{o}C$, two cycles per day for four weeks. The glass and adhesive bond remained intact.

Test 3 -- Accelerated Corrosion

Laminate panels were subjected to a continuous saltwater spray at an elevated temperature for four weeks. The glass remained intact but the bond between the glass and metal backing failed at the copper and silver layers.

The laminate panels performed well under conditions of accelerated environmental exposure. The panels survived the temperature cycle and freeze/thaw cycles tests. The accelerated corrosion test represents an extremely harsh environment which would probably not be encountered by the panels in normal installation. Some attention should be paid, however, to the failure mode and developing some method of protecting that aspect of the panel.

3.6 INSTALLATION FEASIBILITY

Full size flexible glass laminate panels were installed on an Acurex Model 3001 Parabolic Trough Solar Concentrator located at the Acurex Solar Test Facility in Mountain View, California.

The reflective laminate panels listed in table 3-4 were installed in the collector module per the procedures given on Acurex drawing 7524M65109, figure 3-3, using these components:

- Collector Structure Subassembly (P/N 7524-264)
- Edge Clamp, Glass Reflector (P/N 7524-251)
- Panel Center Support (P/N 7524-253)
- Center Doubler (P/N 7524-255)
- End Doubler (P/N 7524-259)

The panels were installed and remained in the parabolic collector for 60 days. The observed panel failures (broken glass) were:

- One of the 0.060-in. thick Corning glass on 0.062-in thick backing steel failed during installation. The laminate failed at the silver/copper, and glass/silver bonds leading to glass breakage. Note that the epoxy adhesive bond was not the location of failure.

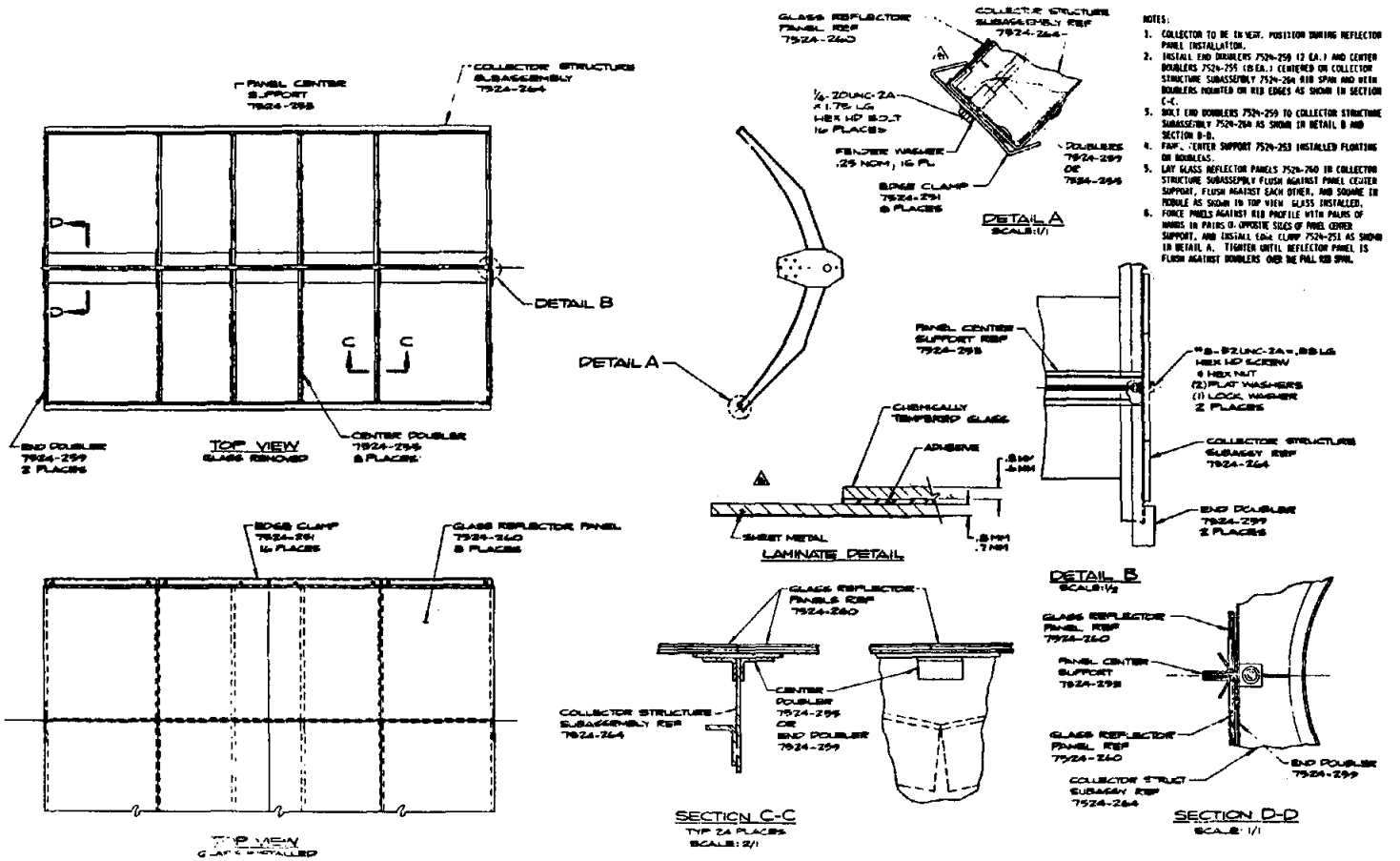

Figure 3-3. Reflective Panel Installation Procedure

- One of the 0.040-in. thick Corning glass on 0.050-in thick backing steel failed 8 days after installation. The failure mode was similar to the first failure.
- A technician accidently dropped a wrench on a 0.040-in. thick Corning glass on 0.050-in. thick backing steel causing a starcrack pattern with rays 2 to 3 in. long. The cracks did not propagate further over time.

It should be noted that the stiffer laminate panels were difficult to install using hands only to force the panels against the ribs. Installation ease is favored by more flexible panels.

3.7 HAIL IMPACT SURVIVABILITY

Typical collector field specifications require reflective panels to survive the impact of 3/4-in. diameter hailstones at terminal velocity (approximately 58 mph). The survivability of the flexible glass laminate panels was investigated by Acurex.

The testing was performed at the Acurex Solar Test Facility using the panels installed in the parabolic collector as part of the installation feasibility subtask, section 3-6.

Key elements of the test procedure were:

- 3/4-in. diameter iceballs propelled by a slingshot
- Iceball velocity monitored by a CMI Speed Gun 1 (radar)
- Iceball impact nearly normal to the reflective panel surface
- Impact distribution over the entire panel surface including the panel edges

The intact laminate panels sustained impacts with velocities in excess of 60 mph without any glass breakage.

Results of this and earlier testing indicate hail impact survivability is not a critical consideration. Typically, if a laminate panel can be installed into the parabolic structure without failure, the panel will also survive hail impact.

3.8 MINIMUM BEND RADII

The minimum possible bend radii of the laminate panels were investigated to determine the compatibility of the panels and the current collector design.

The test procedures and results follow:

1. Fabricate small-scale panels per section 3.4.
2. Position panel vertically in V-blocks mounted in screwjack press and drive V-blocks toward each other at constant rate.
3. Record load versus deflection off vertical of center-of-panel continuously until panel failure.
4. Plot load versus deflection, and load versus radius of curvature for the small-scale panels (see figures 3-4 through 3-8).

The Acurex collector module has a minimum bend radius of 36 in. The results of Step 4 indicate the Acurex-fabricated small panels No. 2, No. 3, and No. 4 (see table 3-4) were bent to radii of 9, 7, and 25 in. at failure, respectively. Panel 1 failed at a bend radius of approximately 80 in. Comparison of the results for the three Corning glass samples (Nos. 1, 2, and 3) indicates the bend radius limit (stress or failure limit) decreases with steel backing thickness and glass thickness. The required load to induce bending also decreases with glass and steel thickness. The Glaverbel panels (Nos. 5 and 6) are fabricated from thinner glass and steel than Nos. 1, 2, 3, or 4 and therefore should

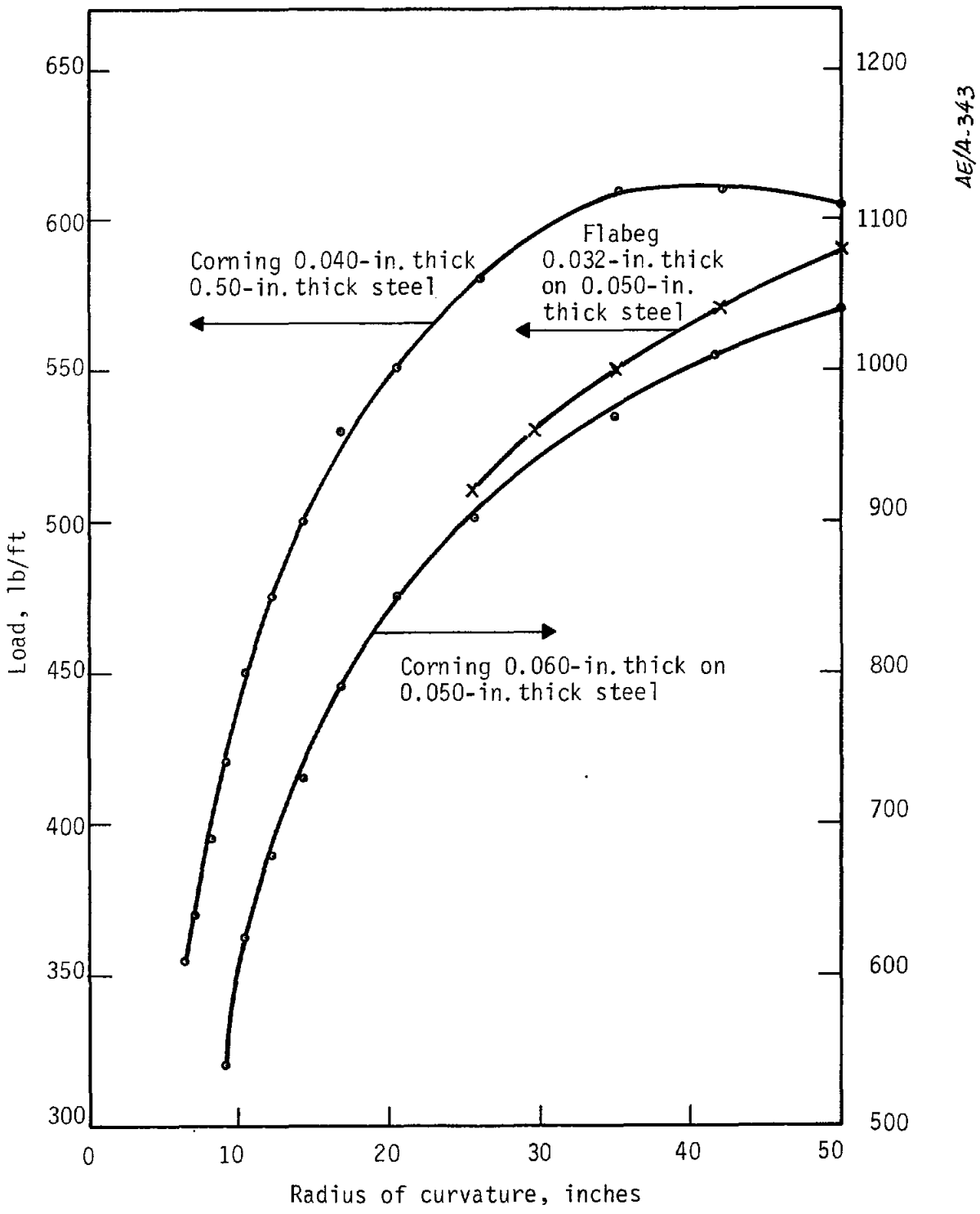

Figure 3-4. Load Versus Radius of Curvature for Small-Scale Laminate Panels

Flabeg 0.032-in on 18 gage

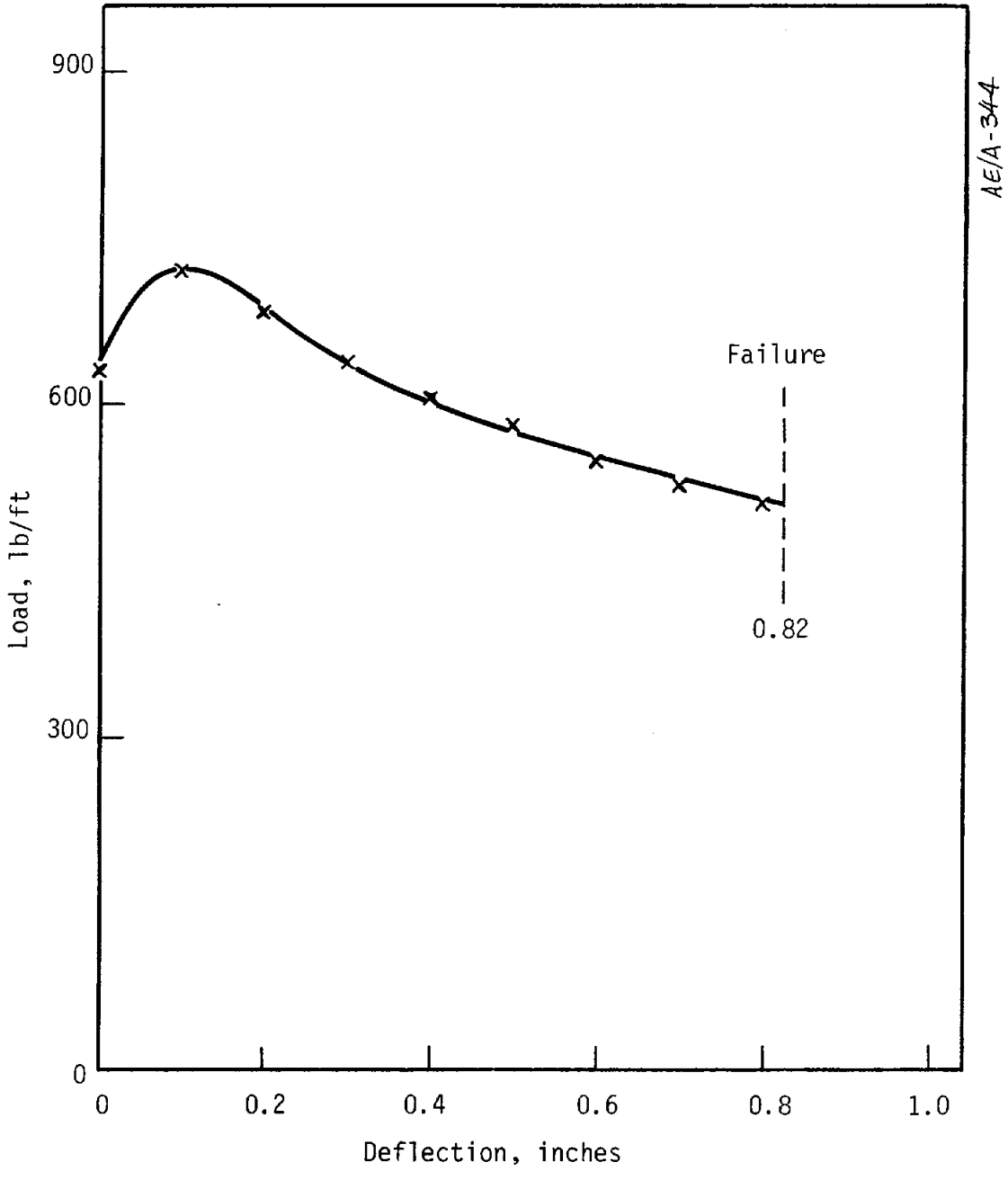

Figure 3-5. Load Versus Deflection for Flabeg Glass on 0.050-in. Thick Steel

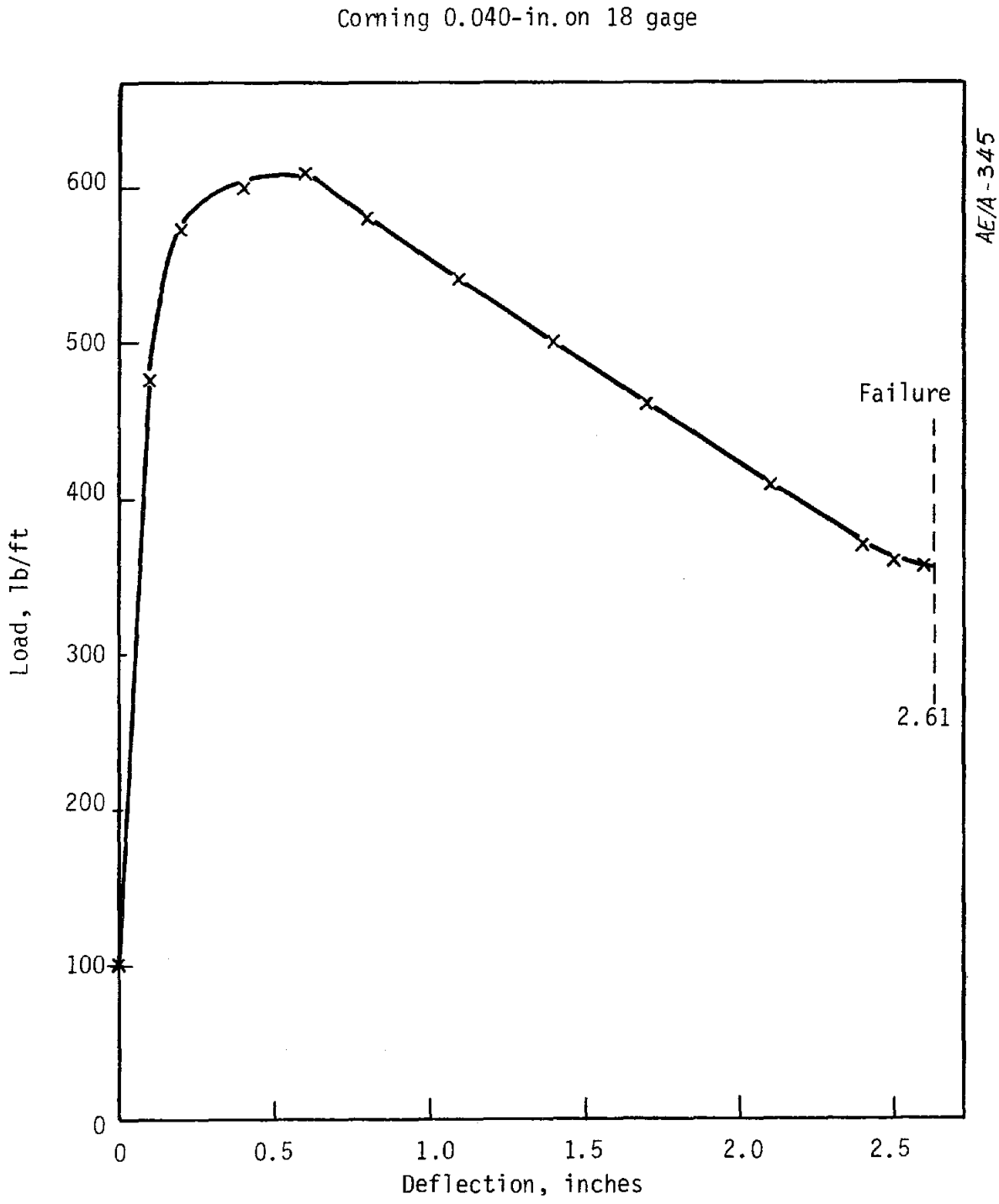

Figure 3-6. Load Versus Deflection for 0.40-in. Thick Glass on 0.050-in. Thick Steel

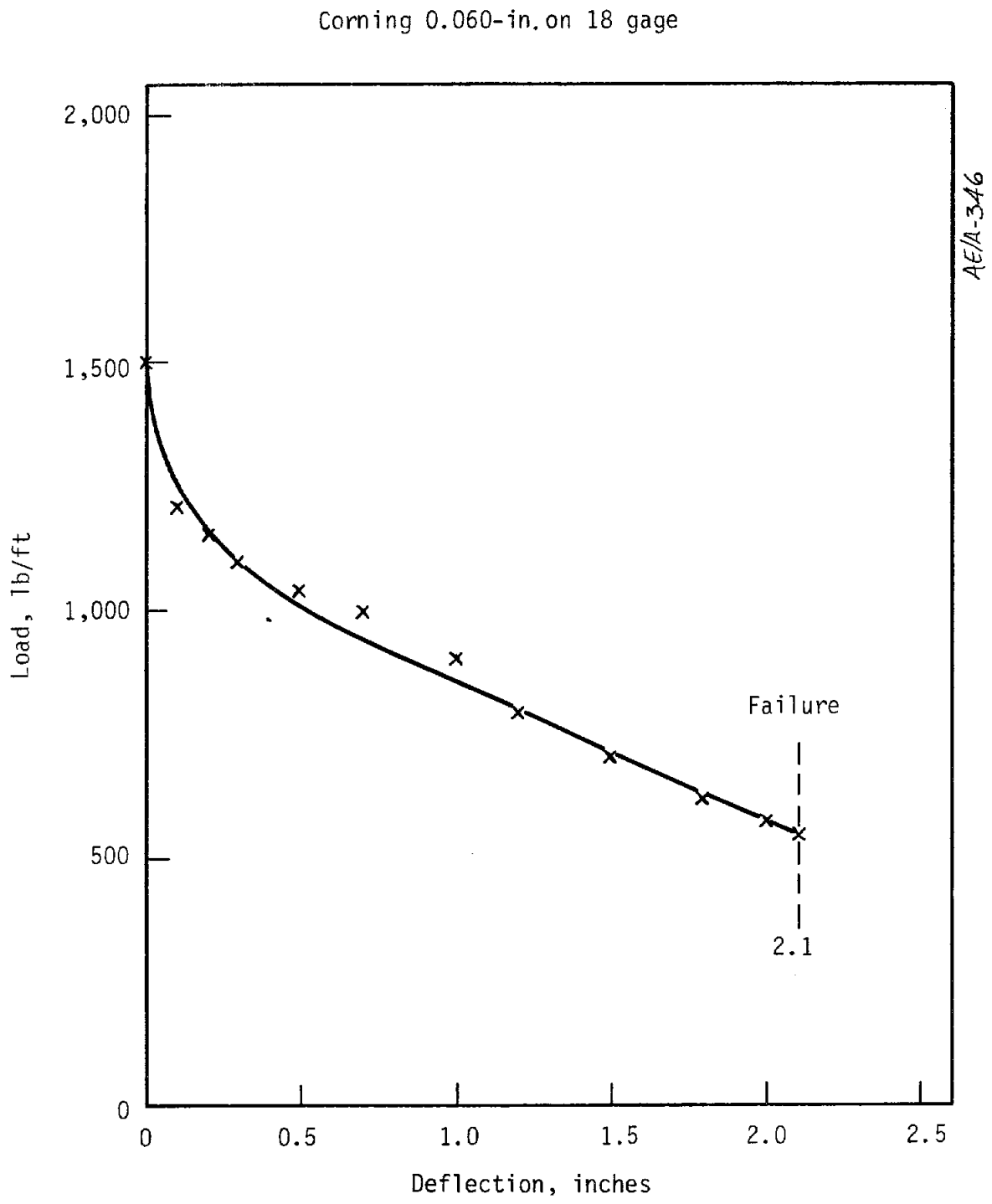

Figure 3-7. Load Versus Deflection for 0.60-in. Thick Glass on 0.050-in. Thick Steel

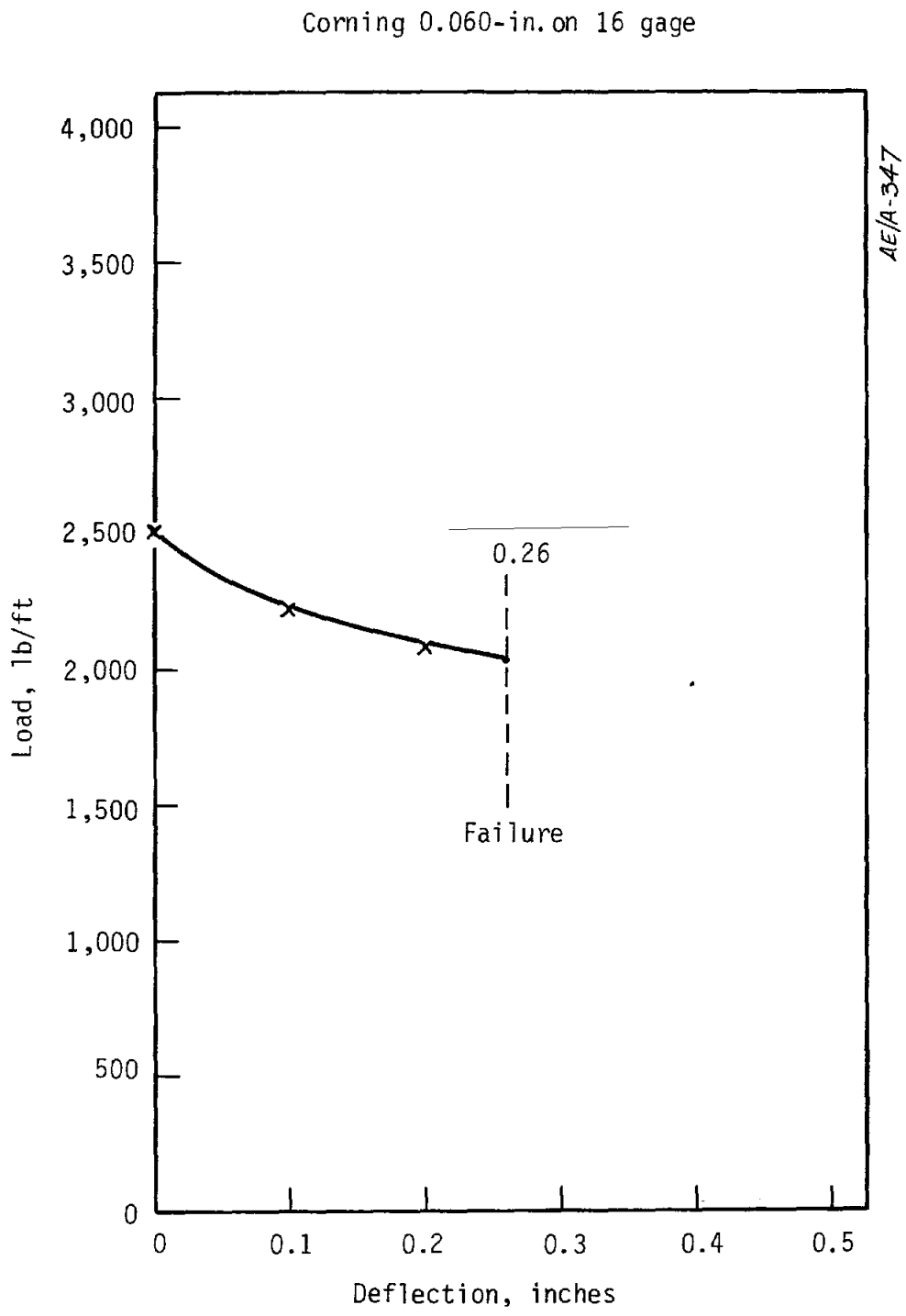

Figure 3-8. Load Versus Deflection for 0.60-in. Thick Glass on 0.062-in. Thick Steel

accommodate lower bend radii and require lower retaining loads than the samples tested.

3.9 TASK SUMMARY

Results of the flexible glass laminate reflective panel development have provided valuable information that will serve as a basis for future efforts.

Key results are:

- Use of perforated sheet metal backing sheet is a viable means of eliminating entrapped air from the adhesive bond region
- Laminate panels can be fabricated such that they are environmentally stable
- Hail impact survivability is not a major problem
- Ease of installation in a parabolic trough and the ability to bend to smaller radii favor thinner glass and a corresponding reduction in metal thickness

SECTION 4

PV RECEIVER DESIGN

4.1 INTRODUCTION

The Acurex advanced PV receiver design is the result of extensive analyses and prototype evaluation. The objectives of the receiver design were to improve performance, reliability and durability, while being suitable for large volume production with a low cost/ft^2 potential.

The goals were achieved through careful materials selection and utilizing sound, state-of-the-art engineering and manufacturing technology. Special considerations were given to:

- Corrosion protection
- Effective cell cooling (low ΔT between the cell and the coolant)
- Voltage isolation at the cell interface
- Allowance for differential thermal expansion of the receiver components
- Material compatibility of various materials and adhesives
- High-temperature continuous operation, and temperature cycling in a concentrated sunlight environment
- Allowance for differential thermal expansion between receiver and collector

The low cost potential through volume production goal was achieved by designing key components as modular units, using proven manufacturing

technology. The modular component design also helps minimize the field maintenance and replacement costs. The receiver consists of four major subcomponents:

- A hollow aluminum extrusion to provide the primary receiver structural component that will act as the cell module substrate, and the coolant tube. The receiver tube extrusion design included integrally molded features to interface with the cell modules, seals, spring clips, wiring harness and wiring cover.
- Cell modules consisting of interconnected cells bonded to a glass superstrate. The cell strings can be soldered in an existing automated machine that can stamp out interconnect material and solder cells in any desired series length.
- Prefabricated wiring harness with crimp connectors and plug-in interconnections which simplify wiring on the receiver and field installation
- Receiver support and fluid couplings

In the following subsections the receiver design considerations are outlined and the design of each subcomponent is described.

4.2 RECEIVER DESIGN CONSIDERATIONS

Several design studies were performed to characterize the receiver configuration for optimized performance. These studies included the characterization of the following parameters and their relationships:

- Cell width and number of current collecting buses, receiver vee angle, and active cell edge distance to the apex of the vee, for a 6-ft aperture parabolic trough. The details of these trade-off studies are given in appendix D (or Section 2).

- Cell length and receiver, array, and field output voltages, and the maximum area usage of a silicon wafer, are also described in appendix D
- Output degradation and diode placement during off-axis operation
- Differential thermal expansion betweeen the aluminum receiver and the steel reflector, which would influence the receiver support design and fluid coupling design

Following the receiver conceptual design, a number of design trade-offs were preformed to determine the detailed hardware design. The major elements of the design trade-offs are outlined here:

- Receiver tube material and construction: fabricated steel tubes were compared against aluminum extruded tubes. The factors which lead to the selection of the aluminum tubes were design flexibility with minimal finish machining operations, lighter weight, higher thermal conductivity, better corrosion resistance, and the potential for low-cost production at high volume.
- Cell module length: selection involved comparing the number of cells in series, and its relationship with the series and parallel circuit design of the receiver. A 12-in. cell module length was selected to facilitate assembly installation, and provide a large number of test points for fault isolation.
- Electrical circuit design: connections were designed for limited space envelopes, high temperature, and concentrated UV environments. I^2R losses were minimized through careful materials selection and sizing of the components.

- Cell encapsulation to the receiver substrate: the encapsulation method would have to satisfy the requirements of high thermal conductivity, and sufficient elasticity for thermal cycling and receiver loading. The encapsulant thickness is limited between 0.015 to 0.030 in. A direct bonding method of the cell module to receiver substrate was not selected because adhesive could not be found to adequately satisfy all the requirements. The selected method mechanically attaches the cell modules to the receiver substrate with spring clips. The cell modules are "floated" on a thin layer of thermally conductive grease. The edges are sealed with silicone foam gaskets and the ends are encapsulated with a silicone RTV.
- Other components: the designs of wiring harness, receiver supports, and fluid coupling were influenced by the results of the design trade studies discussed above.

4.3 RECEIVER TUBE DESIGN

The Acurex advanced receiver design is based on sound state-of-the-art engineering and manufacturing technology, which emphasized minimal machining and assembly steps. The main features of the design are shown in figure 4-1 and described below:

- Single piece 60^{0} vee-shaped hollow aluminum extrusion acting as the primary strucutral member, as well as the cell module substrate and coolant tube
- Aluminum alloy 6063 was selected because of its excellent extrudability, inherent corrosion resistance, and heat treatability. After subsequent welding operations, the

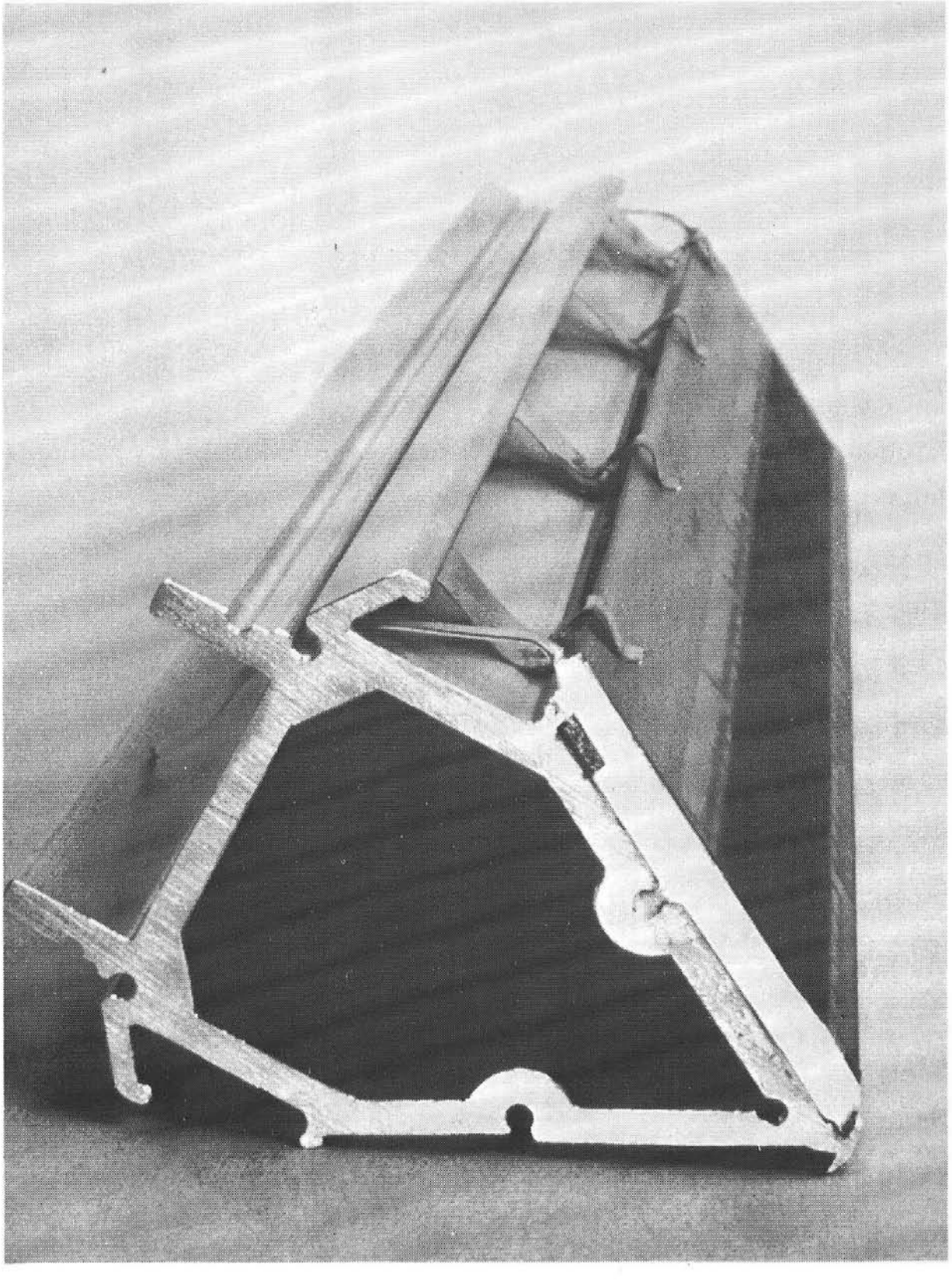

Figure 4-1. Receiver Tube Configuration

receiver tube is anodized to enhance its corrosion resistance and give it a hard surface coating.

- The aluminum extrusion incorporates in its profile all of the necessary features to mate with the cell modules, seals, spring clip, and electrical wiring harness. The cross-section and wall thickness were analyzed to minimize beam deflections under the weight and wind loading and to minimize wall deflections under hydrostatic pressure loading.
- The aluminum extrusion is designed to minimize the number of subsequent welding and drilling operations, while eliminating any finish machining operations. The end closure of the receiver tube assembly consists of a piece of stock aluminum tubing and a stamped aluminum plate that is welded to each end of the extrusion. The drilling operations were limited to drilling one hole for every three 12-in. cell modules for the electrical feedthrough of the cell module leads to the wiring harness.
- Voltage isolation was accomplished by applying a thin layer of Teflon tape to the cell module interface surface. This voltage isolation technique exceeds the required 1,750 VDC voltage isolation.
- A design requirement which affected both receiver extrusion design and cell module design was the requirement to optimize receiver performance by placing the leading edge of the cell as close as possible to the apex of the vee extrusion. This was accomplished by incorporating a ground bevel on an edge of the cell module glass superstrate, which is wedged into a mating

interface of the aluminum extrusion (figure 4-2). Spring clips are inserted to apply a load on the opposite edge of the cell module to hold and seal the beveled glass edge in place.

4.4 CELL MODULE DESIGN

The cell module configuration is the result of an extensive design effort to improve performance and minimize electrical and optical losses. The main features of the design are shown in figure 4-2 and described below:

- A 2.5 x 5.0 cm (nominal) double bus cell is used. The cell size selection was the result of an in-depth study of the relationship of receiver vee angle, reflector configuration, cell edge distance to the apex of the vee, desired output voltage of series string, series-parallel circuit of a receiver, field output, and maximum area usage of an existing silicon wafer. This study is presented in appendix D.
- Six cells are electrically connected in series for each cell module. Bypass diodes are connected in parallel to the circuit; one diode to every three cells. The number of diodes placed in the circuit was determined in an analysis which studied the relationship of offaxis shading on annual performance degradation. This work has been confirmed in separate analysis at Sandia by Mike Edenburn and C. Michael Garner.
- The cell interconnects are stamped from solder-plated soft-annealed OFHC copper sheets. Component reliability was assured by properly sizing the interconnects for current carrying capacity and heat dissipation, and by designing

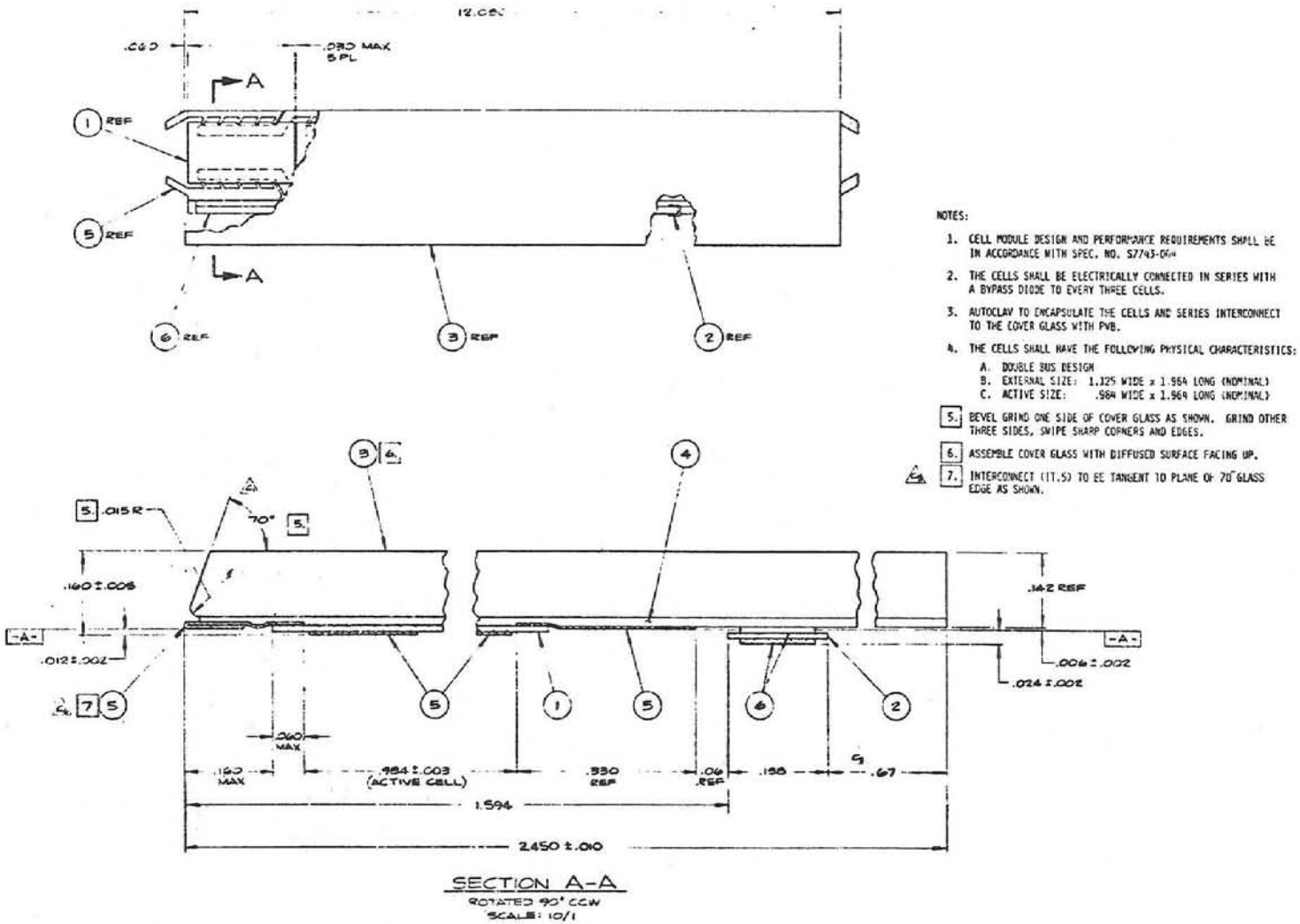

Figure 4-2. Cell Module Assembly

multiple fingerleaf tabs to provide redundant solder joints as well as strain relief between the cell and interconnect.

- The interconnected cell string is bonded to a glass superstrate with a transparent dry film encapsulant. The glass is a low iron, soda lime glass that is tempered after the edges are ground. The bonding material is polyvinyl butyral (PVB) which is widely used as one of the laminates in manufacturing automobile windshields.
- Copper leads are soldered to the interconnect ends of each cell modules, before assembly into an encapsulated three module string. A silicone RTV is applied between adjacent cell modules to provide a compliant seal.

The cell module assembly is manual and, thus, costly. A low cost production can be realized by utilizing an automated soldering machine of a type previously demonstrated by ASEC under Sandia Contract No. 13-2354. The machine has a system feeding solder-plated copper ribbon, a compound punching die to stamp out interconnects, an automatic cell dispenser, a solder station, and a final trimming operation to cut the cell assembly into any desired length.

4.5 WIRING HARNESS DESIGN

The preassembled wiring harness consists of a plug and a receptacle connector crimped to the output ends of the positive and negative power cables. At various intervals along the length of the power cables, there are branching leads terminated with crimp connectors. The branching lead wires are color coded to facilitate final assembly.

The wiring harness also incorporates the following features:

- Anchored at each end of the receiver to provide strain relief

- Main power cables will consist of a fine strand cable to provide high conductor flexibility, and a high temperature, concentrated UV resistant silicone rubber insulation
- Weatherproofing of the main power cable at the lead branch nodes was accomplished using a self-sealing heat-shrink tubing

4.6 RECEIVER SUPPORT AND FLUID COUPLING DESIGNS

A study was performed which suggested that the accuracy of receiver placement within the focus of a concentrator is of primary importance. In any concentrator application, the thermal expansion in large arrays can cause large displacements which could lead to a performance degradation of the system. The design of the receiver support and the selection of a fluid coupling had to be considered together in order to minimize any performance degradation.

A centerline receiver support was selected to preserve the receiver output without increasing blockage and shading loses. The receiver supports design requirements were as follows:

- One support for each end of a receiver assembly
- Must withstand combined dead and wind loading, loads due to temperature cycling, and loads due to hydrostatic pressure
- Must allow for height and lateral adjustments to locate the receiver in the concentrator focus
- Must minimize corrosion between the aluminum receiver components and the steel support interface

The fluid coupling selection was based on the following design requirements:

- Large angular alignment tolerance since the receiver assembly is aligned to the collector

- Axial thermal expansion cycling while maintaining pressure seal integrity
- High temperature seal material
- Corrosion resistance to the coolant and contact with aluminum receiver
- Capability to lock one end of the coupling to prevent "walking" of the coupling during temperature cycling

The receiver support configuration consists of a lightweight structural tube support and a sheet metal bracket to interface with the receiver assembly. Adjusting screws are incorporated into the design to provide the necessary height and lateral adjustment capability to align the receiver in the concentrator focus. A rubber material is applied to the surfaces where galvanic corrosion may occur between aluminum and steel components.

The fluid coupling consists of large BUNA-N seals and a stainless steel body and clamps. These couplings were selected because of their low cost, capability of 14° angular misalignment, and their capability to be thermally cycled from 0° to $200^{o}F$ at 80 psi without degredation in performance.

SECTION 5

PV TROUGH REFLECTOR QUALITY IMPROVEMENT

5.1 INTRODUCTION

The receiver design trade-offs of section 4 pointed to some design weaknesses in the existing Acurex trough reflector. Current PV troughs had been initially designed for thermal applications and no attention was paid to more stringent optical requirements of a PV concentrator. The results of optical analyses of Acurex 3001-01 reflectors are described in section 5.2. The analyses led to certain design improvements which are described in section 5.3.

5.2 OPTICAL ANALYSIS OF 3001 REFLECTOR

In performing the laser ray trace study for optimization of the second generation PV receiver we utilized two different laser ray trace (LRT) facilities. Each facility has unique capabilities.

The Acurex LRT facility is schematically described in figure 5-1. The reflector is positioned normal to the laser beam with a graduated "receiver" positioned appropriately in its focus. The laser is then traversed in two dimensions over the aperture and the return spot position is recorded. The operation and data acquisition is entirely manual. This facility was established to provide some measure of optical quality on manufactured reflectors. This tool is adequate for determining the intercept factor as a function of cell width and receiver placement.

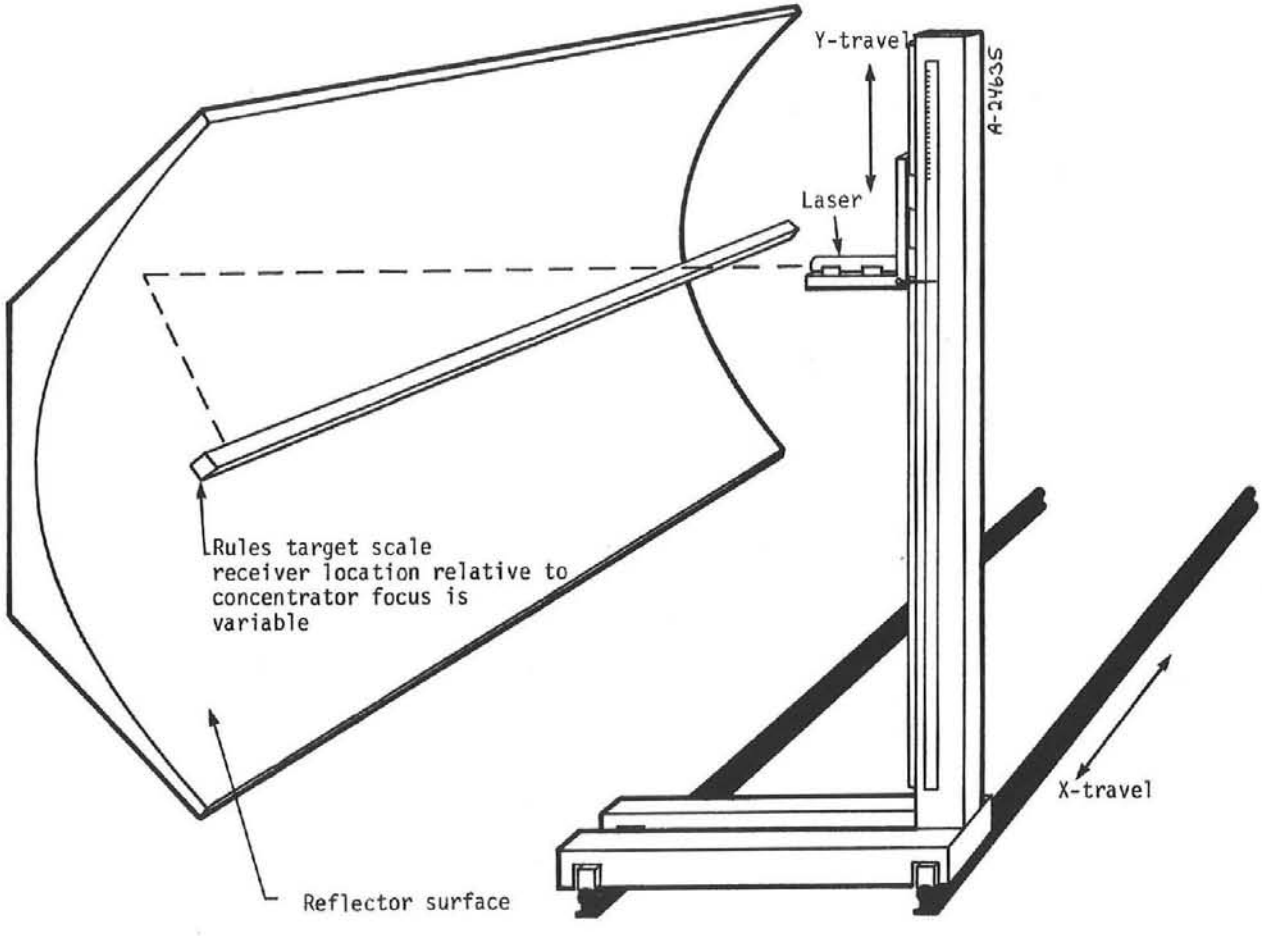

Figure 5-1. Acurex Laser Ray Test Facility

The measurement of longitudinal placement of the return spot cannot be easily accomplished on this tool, therefore, surface distortions which result in longitudinal displacement of the image cannot be measured easily.

The second laser ray trace facility used is at Sandia National Laboratories and is schematically pictured in figure 5-2. This facility offers two dimensional information on the return spot and is computer controlled. A much more complete data set is generated and can be utilized in locating systematic errors in the reflector optical properties. Figure 5-3 is part of the output from the laser ray trace analysis performed on an Acurex 3001 reflector as it was produced at the beginning of this program. There are obvious areas of high longitudinal slope error in bands across the reflector. The location of the worst of these bands corresponds to the juncture of the reflective sheets in the parabolic surface of the early 3001. The slightly less distorted bands in the LRT output correspond to the location of the supporting ribs in our design. The pressure of the reflective sheet on the ribs was sufficient to cause "print through" of the rib. This causes a local longitudinal distortion in image.

The effect of a longitudinal distortion in image is a "dark" region in the image surrounded by higher than normal intensity irradiation (nonuniform illumination). This has very little effect on the performance of a thermal receiver but has a large effect for photovoltaic applications. The cell in the "dark" region acts as a current limiting member in the series string of cells and forces the turn-on of a by-pass diode. This magnifies the effect of the relatively small distortion. For photovoltaic applications, therefore, this systematic slope error had to be reduced.

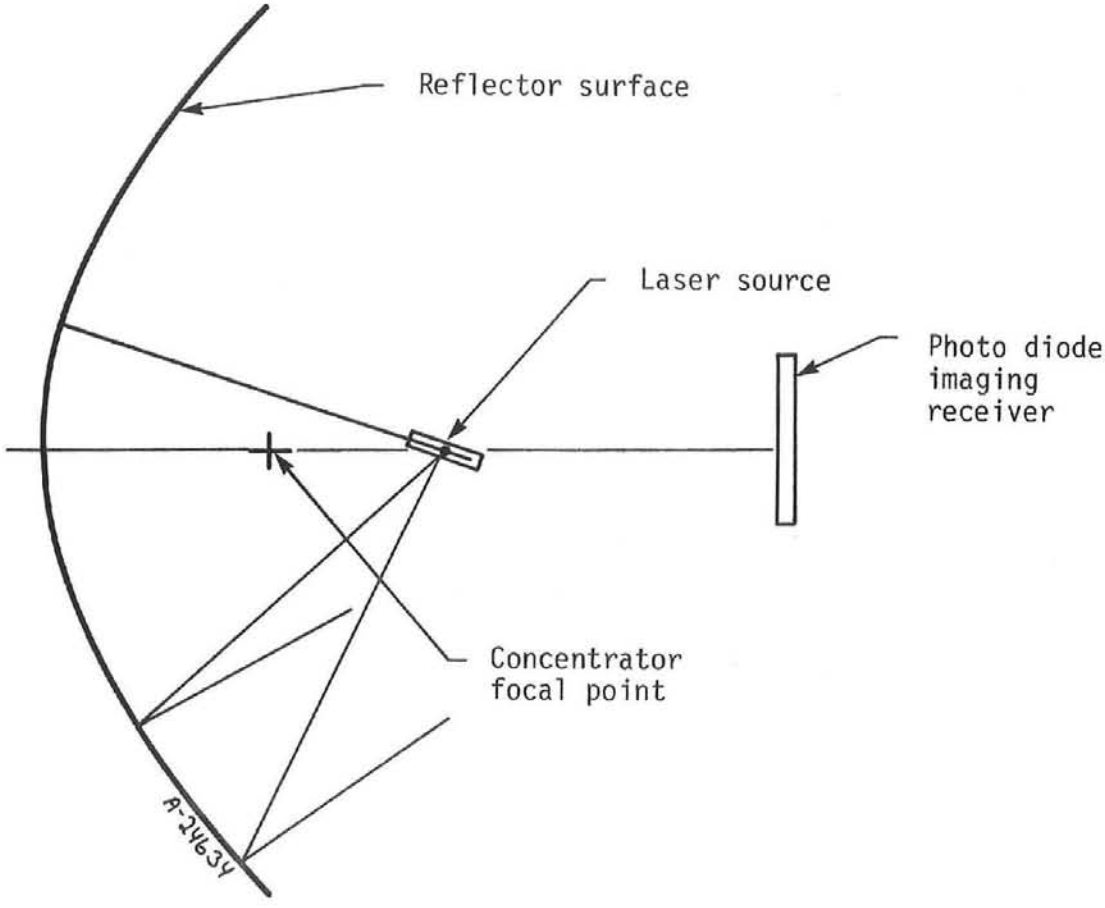

Figure 5-2. Sandia Laser Ray Trace Equipment

MIRROR NO. 44, YR,MO,DA,TEST NO: 791210000
SURFACE DATA WINDOW, M. = -5., -.04, .04, 5., FIRST, LAST SCAN= 1, 77
NOMINAL Z INCREMENT (M)=.04
SLOPE ERROR SCALE IS 20 MILLIRAD. PER Z INCREMENT

ACCUREX WITH COILZAK IN 851
LAST 4 SCANS, LASER MOVED DOWN SLIGHTLY.

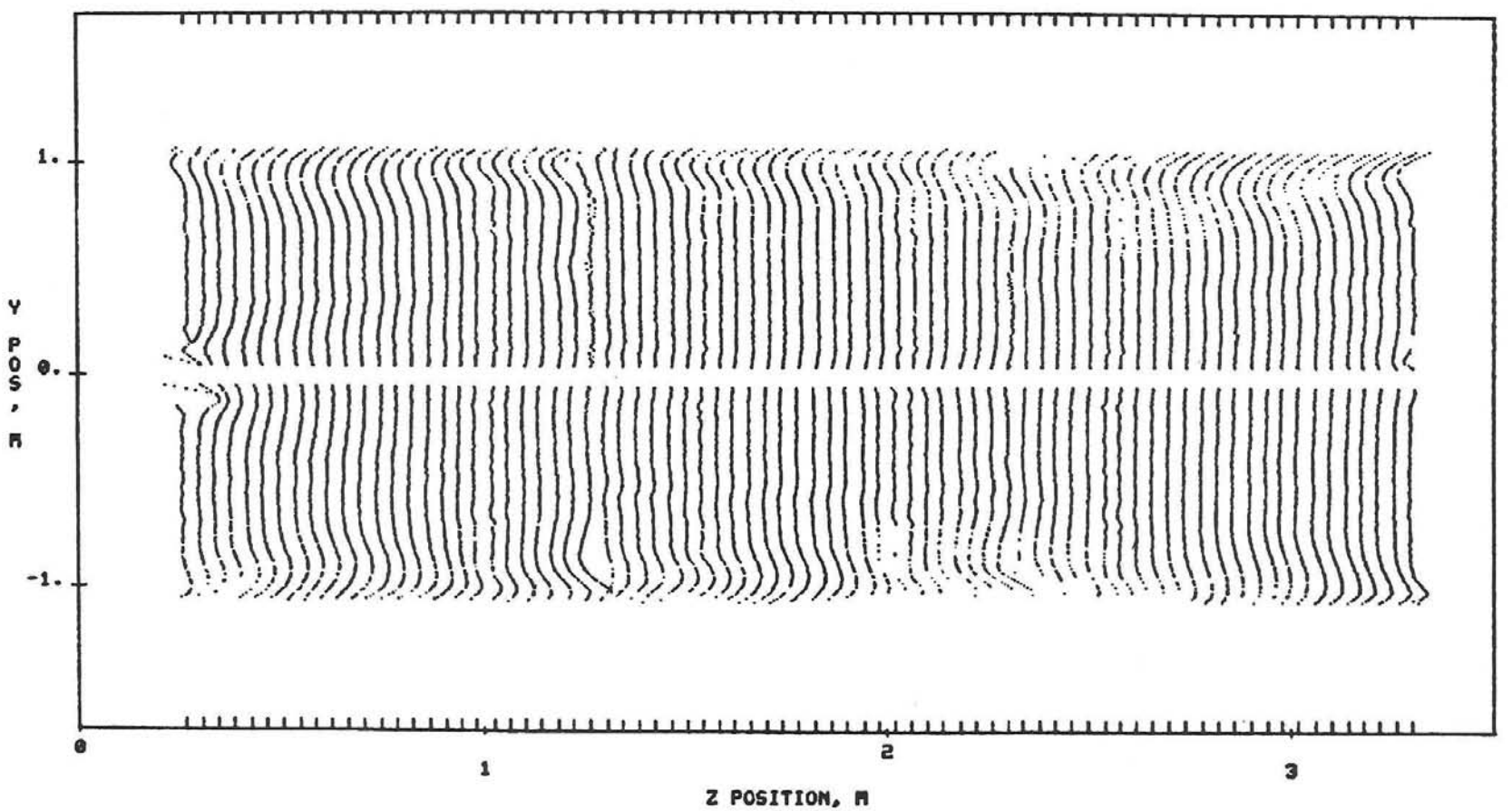

Figure 5-3. LRT Output for 3001 Coilzak Trough

5.3 REFLECTOR MODIFICATION TO IMPROVE IMAGE QUALITY

The causes of longitudinal distortions at the joints between reflective sheets are twofold: First, the sheets were not assembled to identical surface contours as there was no support directly under the sheet edges. This caused the sheet images to have different shapes. Second, independent clamps on each sheet were used to retain the sheet on the surface of the ribs. The poorer support of the lateral edges of the sheet caused stress concentration to occur at the adjoining sheet edges. The edges were not, therefore, driven to as low a parabolic profile as the rest of the sheet, resulting in a curvature which reflected the incoming light towards the center of the sheet. Although this was a very small effect, it was large enough to cause the longitudinal displacement of the image over the sheet joints. The rib print through caused a similar distortion in the reflective surface.

Therefore, the poor image uniformity along the receiver was caused by the orientation of the reflective sheets and the structural control of the edge retaining clamps. These areas were redesigned to reduce the severity of the problem. The following changes were incorporated:

- Reflective surface: Two sheets, 10 ft x 44 in. Sheet edges are controlled in a doubler assembly in the vertex of the trough. There are no lateral joints between sheets in the illuminated area of the reflector.
- The edge clamp and retainer assembly were redesigned to unify the clamp and increase its stiffness. This improves the support of the reflective sheet and limits the rib print through

Figures 5-4 and 5-5 demonstrate the effect of the changes. Both photos are taken looking into the reflector at the reflection of the

Figure 5-4. Early 3001 Image

Figure 5-5. Improved 3001-P Image

receiver. Any distortion in that image is indicative of slope error which would cause nonuniform illumination on the receiver. In figure 5-4 (the original 3001 design) the image of the receiver is heavily distorted in the region of sheet edge and ribs. In figure 5-5 the image of the receiver is relatively free from distortion. The effect of this improvement on collector performance is discussed in section 6.

The necessary components were designed and fabricated to manufacture two prototype modules. The prototypes were tested at Acurex and Sandia. The performance results are reported in section 6. The prototypes were also evaluated mechanically at Sandia and Acurex and were determined to exceed the structural integrity of the earlier 3001 designs exposed to the same test procedure. Finally, the prototype module at Sandia was laser ray traced. The results (figure 5-6) demonstrate the improvement realized through the design change.

MIRROR NO. 0 DATE (YYYYMMDD) 81 527 TEST NO. 0
SURFACE WINDOW, M. -5.000 0.000 0.000 5.000 FIRST,LAST SCAN 1 60
Z INCREMENT (M) 0.05
SLOPE ERROR SCALE 20.0 MILLIRAD PER INCREMENT
ACCUREX ON GREEN CART IN 851, FOR PHOTOVOLTAICS.

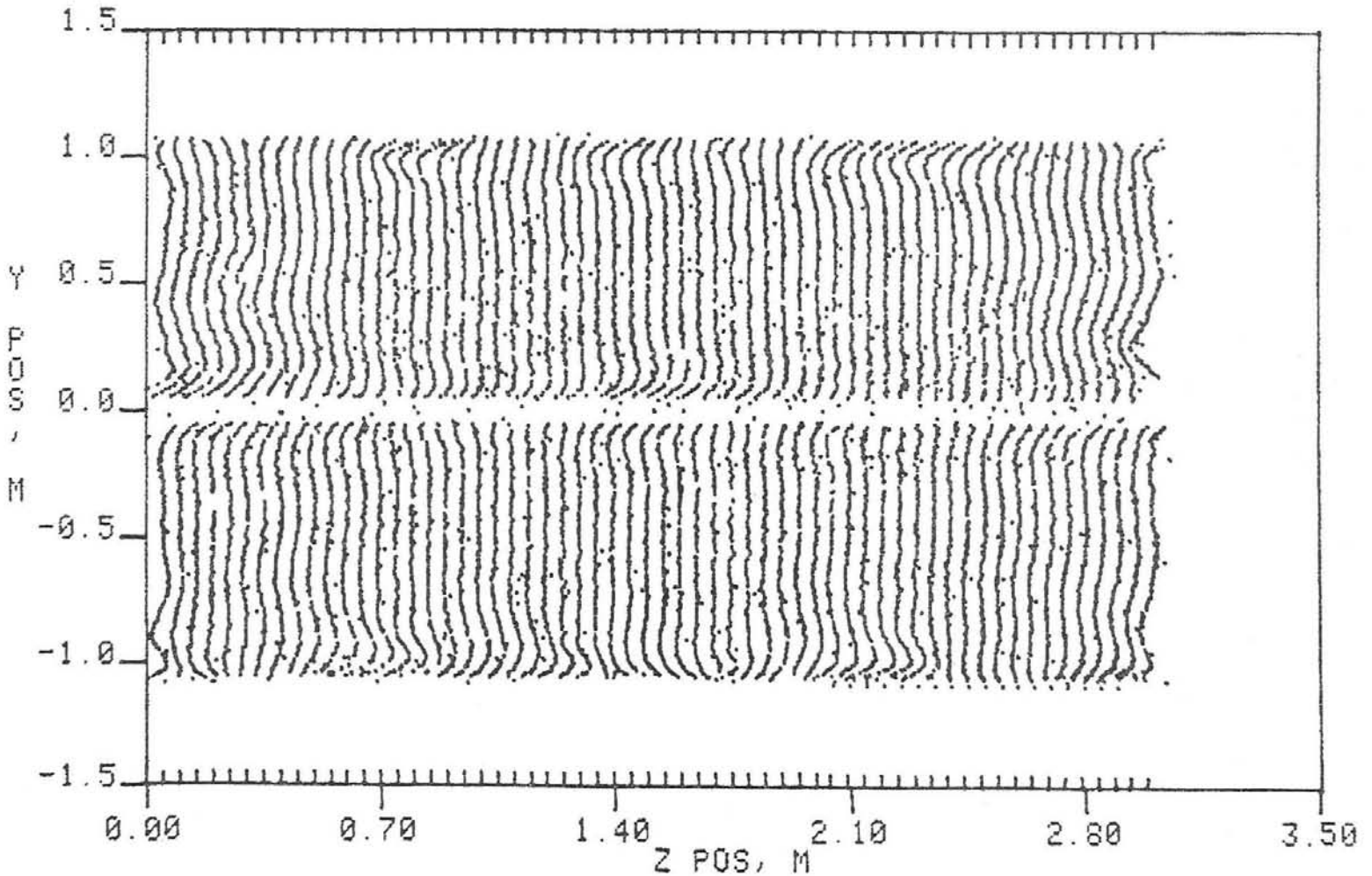

Figure 5-6. 3001-P Laser Ray Trace Results

SECTION 6

TEST ACTIVITIES

6.1 INTRODUCTION

The objective of the test program was to evaluate empirically the concentrator performance and characterize component design features, durability, and performance degradation. A great deal of theoretical data have been generated by Sandia and others. These data have been used in the development of the second generation PV trough described in previous sections. The testing activities were intended to complement and verify the theoretical results and guide the development of a comprehensive trough performance model.

In addition to the Sandia funds, Acurex funds were invested in the test facility and equipment such as a two-axis tracking structure, flux mapping sensor, and data acquisition system. Most of the test activities which were accomplished at Acurex were performed on internal funds. The accelerated life and some performance testing was performed at Sandia. The remainder of the tests, including extensive performance characterization of the PV concentrator, were carried out at Acurex. Receivers with cell modules from three manufacturers were tested; Applied Solar Energy Corporation (ASEC), Solarex, and Spire Corporation. They all used the same cell module design.

In the following sections the collector performance model is presented and then the test fixtures and prototype receiver features are described. The remainder of this chapter is dedicated to detailed description of the test plan, analysis of results and development of the empirical model of collector performance.

6.2 COLLECTOR PERFORMANCE MODEL

Based on our extensive evaluation of the available empirical and theoretical data, we felt that collector performance could be modeled as:

$$P_{array} = H_i \cos(\beta) A F_B F_{RL} \rho \gamma(\beta) F_{iu}(\beta) \eta_{cell}(T, H_i) M E(\beta) \qquad (6\text{-}1)$$

where,

P_{array}	=	Output power of the array, W
H_i	=	Direct Normal insolation, W/m^2
β	=	Incident angle to the collector aperture, degrees
A	=	Array gross aperture area, m^2
F_B	=	Blockage factor -- fraction of reflector area not blocked by receiver
F_{RL}	=	Receiver active fraction (the ratio of active length of cells mounted on the receiver to its total length; $\leq$.887 in current design)
ρ	=	Surface reflectivity
$\gamma(\beta)$	=	Average intercept factor (fraction of the reflected energy that reaches that active cell area)
$F_{iu}(\beta)$	=	Image uniformity factor, a measure of the effect of variability in axial flux distribution
$\eta_{cell}(T,H_i)$	=	Cell efficiency
T	=	Cell temperature, ^oC
M	=	Cell matching factor

$E(\beta)$ = Electrical loss factor (diode losses)

A primary objective of the testing was to evaluate the model and determine the functions empirically.

6.3 TEST FIXTURE DEVELOPMENT

At the onset of the test program it became apparant that existing Acurex facilities were inadequate to carry out the ambitious and comprehensive experiments that were planned. One of the first efforts was therefore, to design and construct a new test fixture with expanded capabilities.

Figure 6-1 shows the new test bed at the Acurex Test Park in Mountain View. The two-axis tracking structure utilizes the normal single axis capability of Acurex 3001 trough design for elevation tracking and adds an azimuth tracking base and support structure. The tracker sensor mounting brackets in the upper right-hand corner of figure 6-1 are shown in more detail in figure 6-2. The lower sensor controls the azimuth tracker and can be adjusted directly for any incident angle. The elevation (upper) sensor can be adjusted to simulate pointing error. The test bed can accommodate two complete modules with the capability of evaluating the two receivers independently or in combination. Both receivers are cooled using a self-contained fluid loop.

The data acquisition system is equipped to handle up to 30 channels of thermocouple temperature data and 20 channels of voltage or current data. Pyranometer, pyrheliometer, and all important weather data are also available through the Acurex Test Park data system.

All information is fed to an Autodata Nine data logger and stored on magnetic tape cassettes for computer data reduction. A variable

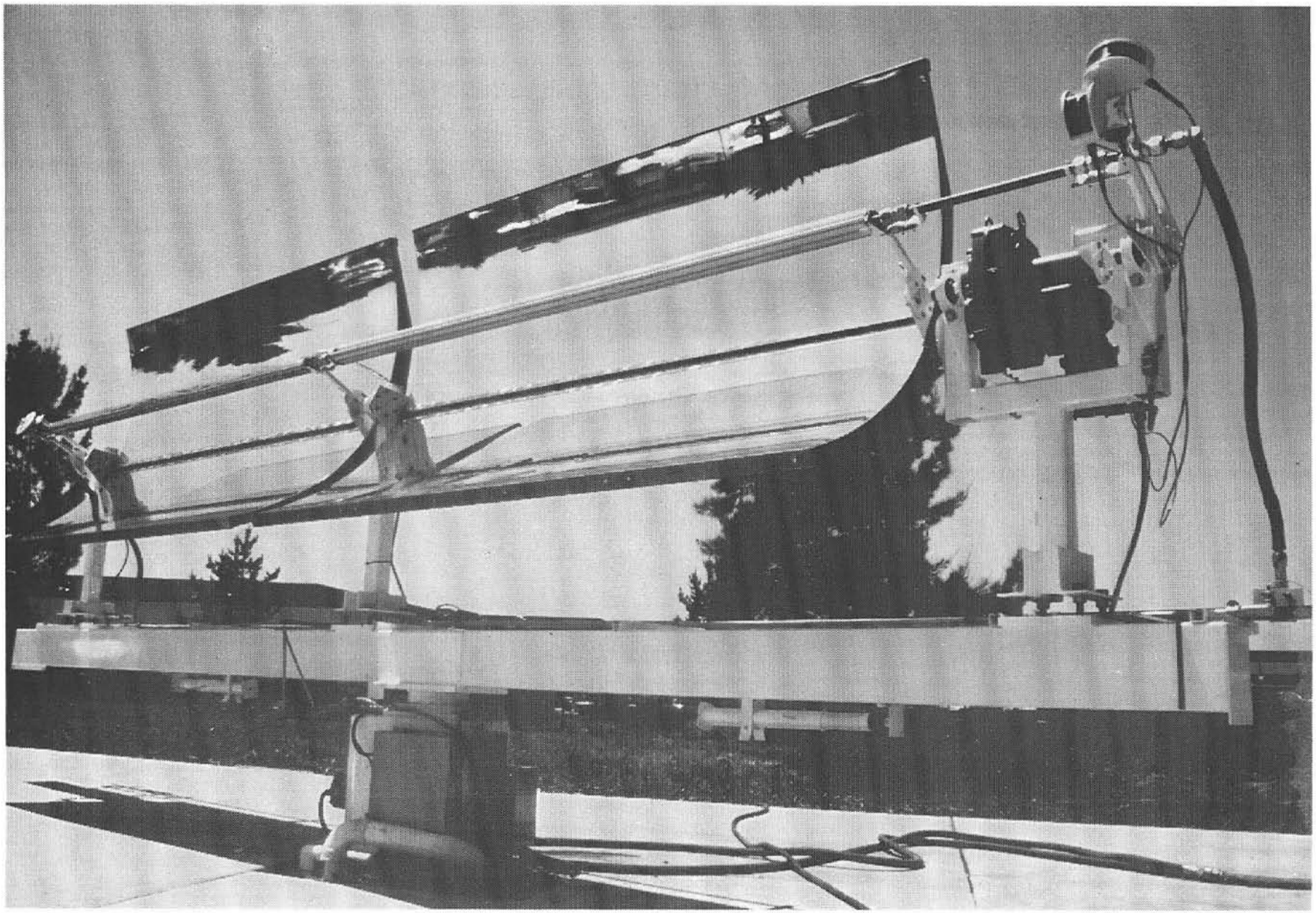

Figure 6-1. Acurex Two-Axis Test Facility

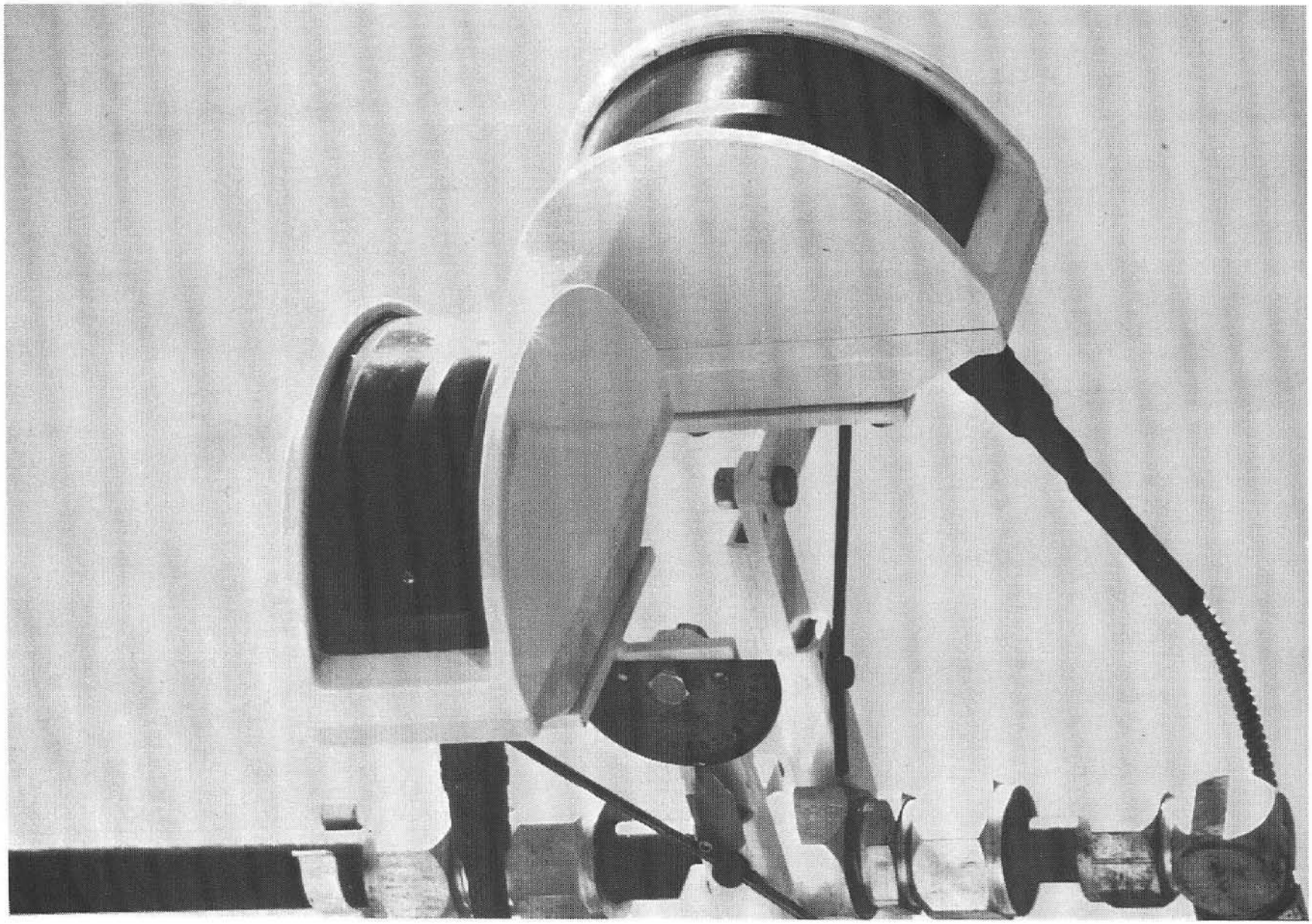

Figure 6-2. Tracker Sensor Mounting Detail

resistive load controls the PV output and an analog x-y plotter is used to record I-V curves.

With the development of some specialized test equipment such as a flux mapping sensor, this fixture allowed us to perform all of the desired tests. The flux mapping sensor is described in section 6.5.2. The tracking accuracy is $\pm 1/8^{0}$ in both axes, but no effect on performance was observable due to the dead band.

6.4 PROTOTYPE RECEIVER PREPARATION

The design of the test receiver was identical to that of section 4 except for the addition of some thermocouples. Seventeen theromcouples were spot-welded to the back of four cells spaced out on the receiver. Five thermocouples were arrayed longitudinally on one cell to measure the temperature profile along the cell. On three cells, four thermocouples each were spaced laterally to measure image (irradiation) related temperature profiles. These three cells were distributed at both ends and the middle of the receiver to allow evaluation of the ΔT variability between all modules.

6.5 TEST PLANS AND PROCEDURES

This section lists the tests that were performed to characterize the PV trough module and discern individual functions of the performance equation. For each test, the objective of the test equipment and test procedure are described.

6.5.1 Performance Tests

The objective of these tests was to characterize the array output, η_{array}, and cell module efficiency, η_{cell} $(T_1 H_i)$. The independent variables are fluid temperature, insolation, and incident angle.

Receivers populated with cell modules manufactured by ASEC, Solarex, and Spire were tested. The first test was to determine the effect of temperature on performance. The test procedure was as follows:

- Assemble the test fixture, modules, and receiver at normal incidence and with fluid at 112 $\pm 3^{o}$F.
- Adjust elevation tracker to center focus on receiver moving the receiver vertically in 0.1 in. increments.
- Determine the optimal response and readjust the elevation tracker to optimize performance.
- Run several I-V curves at each fluid temperature increment of 10°F from 90°F to 160°F and return to 90°F. Insolation shall not vary greater than ± 50 W/m^2 from nominal 800 W/m^2.
- Run several I-V curves at T_{fluid} = 112 $\pm 3^{o}$F and evaluate degredation in module performance.

The second test determined the effect of insolation on performance. The test consisted of taking normal performance data (I-V curve) at as wide a range of insolation readings attainable. Fluid temperature was held constant at 112 $\pm 3^{o}$F for all candidate test points.

Each test point for both tests included an I-V curve with data scan at start, midpoint, and end of curve plotting. The data scan included:

- Direct normal insolation
- Total normal insolation
- Cell temperatures (17 original)
- Inlet and outlet fluid temperatures
- Ambient temperature
- Wind speed and direction
- Output current and voltage

A typical I-V curve is shown in figure 6-3 along with the data scans for that curve. The data is in unreduced format as recorded on magnetic tape. Note that the number of cell temperatures recorded in figure 6-3 is less than 17 due to themocouple failures.

Once a full range of normal incidence performance data had been gathered, off-normal performance tests were carried out. Data were collected for a range of off-normal incidences in both axes. Off-normal incidence in the elevation axis is equivalent to pointing error and can be used to establish field installation tolerances. Off normal incidence in the azimuth axis equates directly to angle of incidence to the collector apperture due to solar declination.

Data were taken in 1/4 degree increments, $\pm 5^{o}$ from normal in the elevation off-normal test. In the azimuth off-normal test, data was taken from 10° north to 60° south in 10° increments. Similar to the normal incidence tests, the fluid temperature was held at 112 $\pm 3^{o}$F and insolation at 800 ± 50 W/m^{2}. In all cases, several I-V curve scans were taken at each increment. At the completion of each test, several scans were made at normal incidence and the receiver was inspected visually for damage.

Throughout all testing at Acurex, the receiver performance and physical condition remained unchanged. This was not the case at Sandia where the insolation level is generally higher than at Mountain View. The results of the tests at Acurex and Sandia are described in section 6.6. Performance testing at Sandia was primarily restricted to normal incidence. Fluid temperature and flow rate were varied and data was taken at various insolation levels. Insolation at Sandia would appear to vary from 850 to

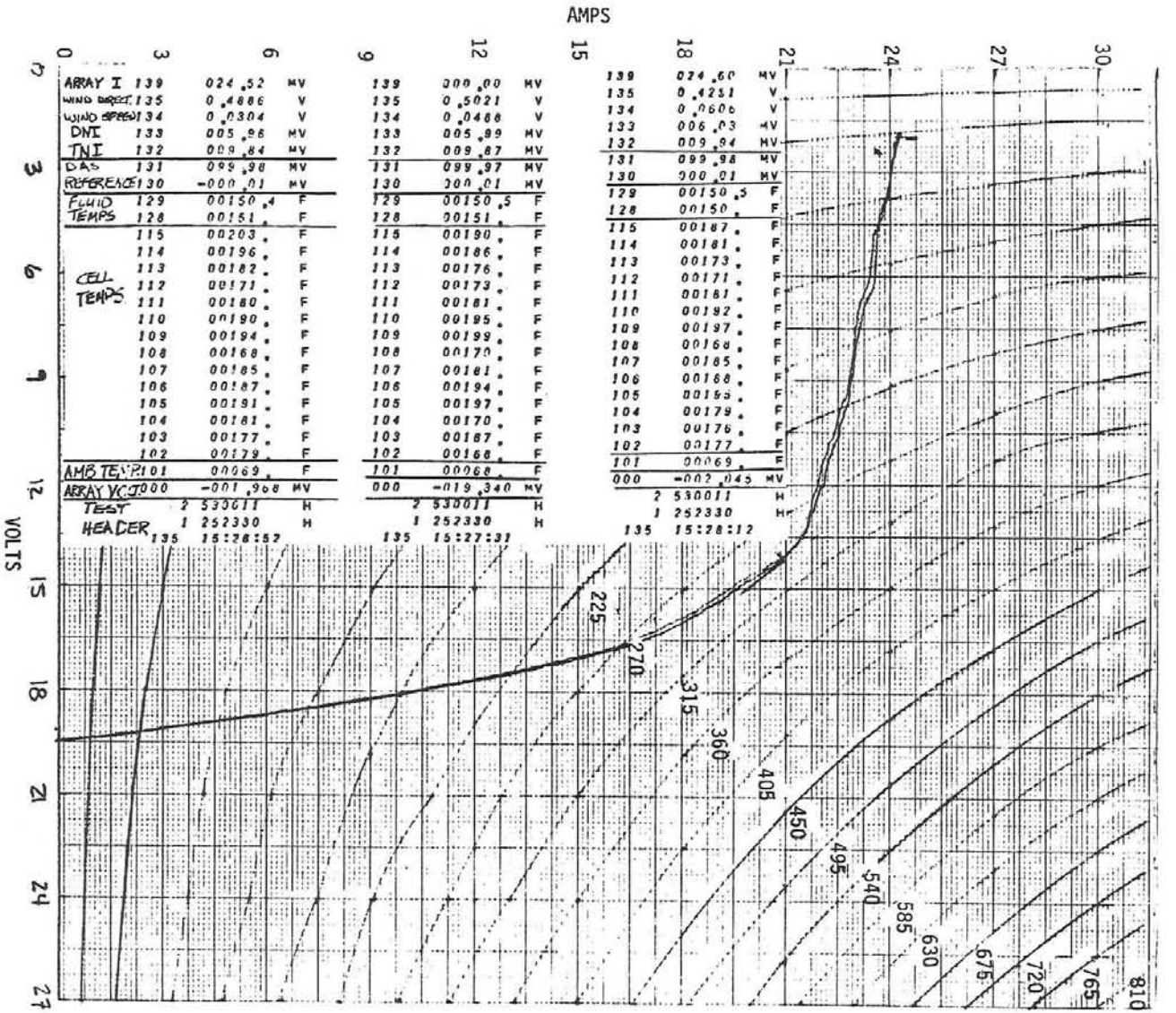

Figure 6-3. Typical I-V Curve and Data Set

1,050 W/m^2 with occasional excursions to 1,100 W/m^2. Very few data were collected at lower values.

6.5.2 Flux Mapping

The objective of these tests was to evaluate the array intercept factor, $\gamma(\beta)$, and image uniformity factor, $F_{iu}(\beta)$, of the performance equation. A sensor was designed and constructed which could directly measure the luminous flux distribution across the cells at any receiver location. By integrating the flux over the cell width, we can determine the fraction of reflected light which is incident on the cell (γ). The variation in intercept factor along the receiver will provide a measure of the image uniformity.

The flux mapping sensor is shown in figure 6-4. The sensor elements are small (0.040 in. x 0.025 in.) segments of concentrator cell material. These elements are hard soldered to a common Invar substrate on a 0.050 in. grid, and form a 2.50 in. wide measuring surface. Each sensor element is individually wired to a current shunt on an input card of an Autodata Nine data logger. Each element has a calibration curve of current versus incident irradiance. The calibration curves were determined through six-point approximation on a calibrated source at ASEC. The active area of the flux sensor extends out 2.5 in. from the virtual apex of the Vee receiver. This arrangement covers the entire surface of the cell and provides full coverage of the concentrated image. The flux sensor also includes a solenoid operated shutter mechanism. The sensor elements were only exposed to the concentrated light for the 1.2 seconds necessary to gather the flux data. In this way, the sensors remain at ambient temperature and do not lose calibration due to thermal transient.

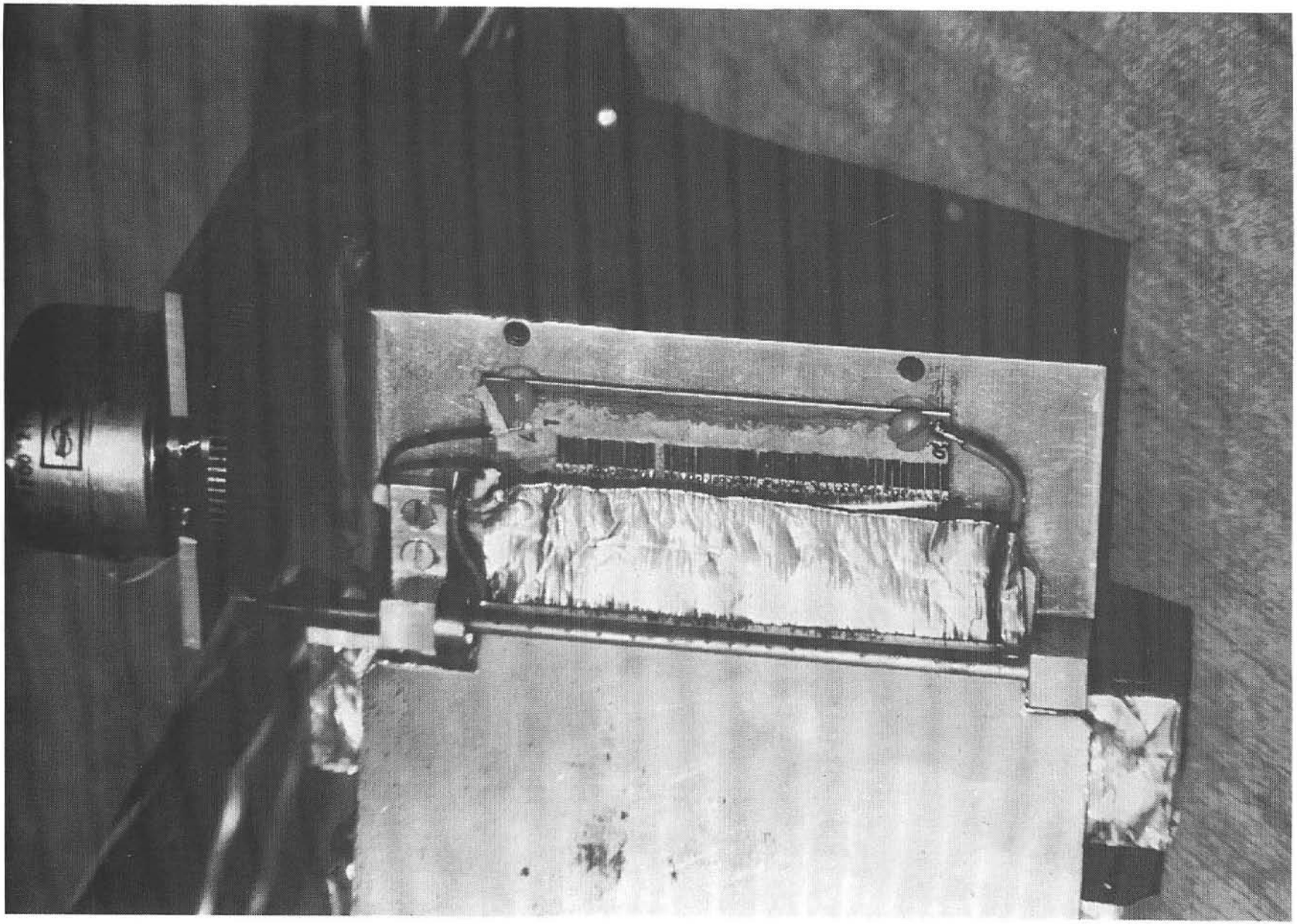

Figure 6-4. Acurex Flux Mapper

The flux mapper was mounted on a receiver extrusion without cell modules attached. Fluid flow was established in the receiver at $80^{o}F$. The data scan at each receiver location included the 49* sensor outputs, direct normal, and total normal insolation. When the shutter was opened, the cells were given 600 ms to stabilize. All of the data were taken in 1.2 s and the shutter closed. The mapper was then moved to the next position.

For each incident angle, data were taken at 6-inch intervals on both sides of the receiver. In all, 40 stations were mapped. The incident angle was varied from normal to 50° South in 10 degree increments. A total of 1,440 data scans were made on FEK modules, and an additional 80 scans were made on an Acurex 3001 glass reflector trough to determine its compatibility with the photovoltaic receiver. All of the data were reduced by computer and the results are discussed in section 6.6.

6.5.3 Single Cell Testing

The last function which we needed to evaluate for the model is $E(\beta)$, the electrical loss factor. This has to do with diode turn-on and, I^2R losses in the cell string. A cell module was modified in which we could monitor the voltage of each cell and diode and the current in each substring. Figure 6-5 shows the arrangment of this cell module on the receiver set up for testing.

The purpose of the tests was to determine the effect of diode turn-on on receiver performance. The incident angle was varied in 1 degree increments from 15° through 45°. For each increment, the

---

*One element was damaged in soldering and therefore not used.

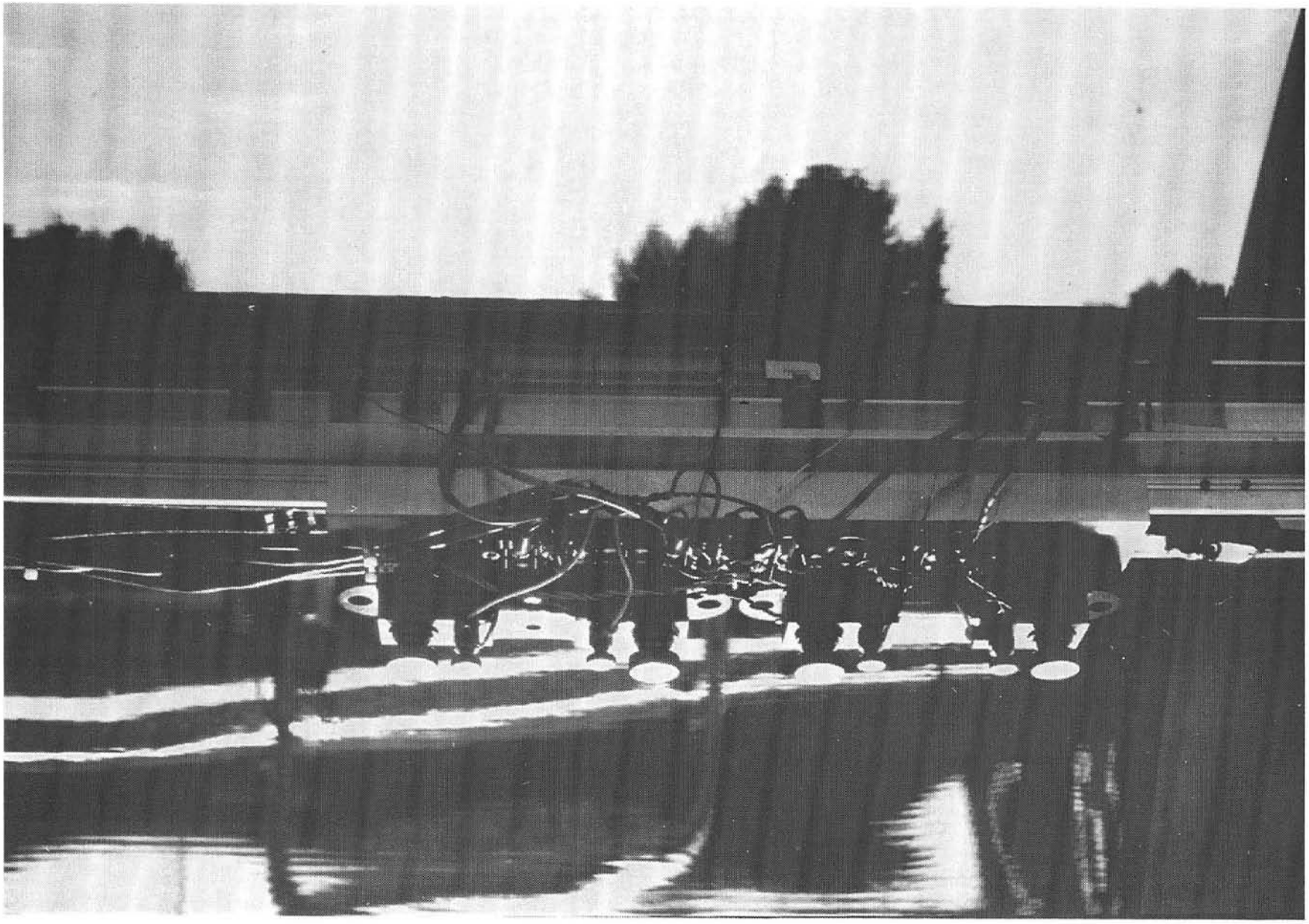

Figure 6-5. Single Cell Instrumented Module

string was adjusted to peak power with normal coolant flow and temperature and within the normal insolation range. The I-V curve was scanned and then, other data were measured. These included the single cell measurements, DNI, TNI, weather data, cell and fluid temperatures. The results of this study are discussed in section 6.6.

6.5.4 Environmental Testing

In addition to the performance tests described above, accelerated life tests were carried out at Sandia. The test samples were short receiver sections and were built up exactly as the full length receivers were, except there was only one module per side. Figure 6-6 is a photograph of one of the ASEC cell short sections delivered. In all, seven short sections were sent to Sandia for testing:

Short Section ID Number		
Acurex	Sandia	Description
ASEC 0001	347-348	Untempered glass, ASEC cells
ASEC 0002	345-346	Untempered glass, ASEC cells
SPIRE 0005	362	Untempered glass, SPIRE cells
SPIRE 0006	380-381	Untempered glass, SPIRE cells
SOLAREX 1	375-376	Untempered glass, SOLAREX cells
SOLAREX 2	377-378	Untempered glass, SOLAREX cells
ASEC 0009	382-383	Tempered glass, ASEC cells

These were evaluated for one sun performance and voltage isolation at 1,750 VDC. The sections were then exposed in several different accelerated life testing chambers:

- UV exposure -- extremely harsh UV irradiation at elevated temperature

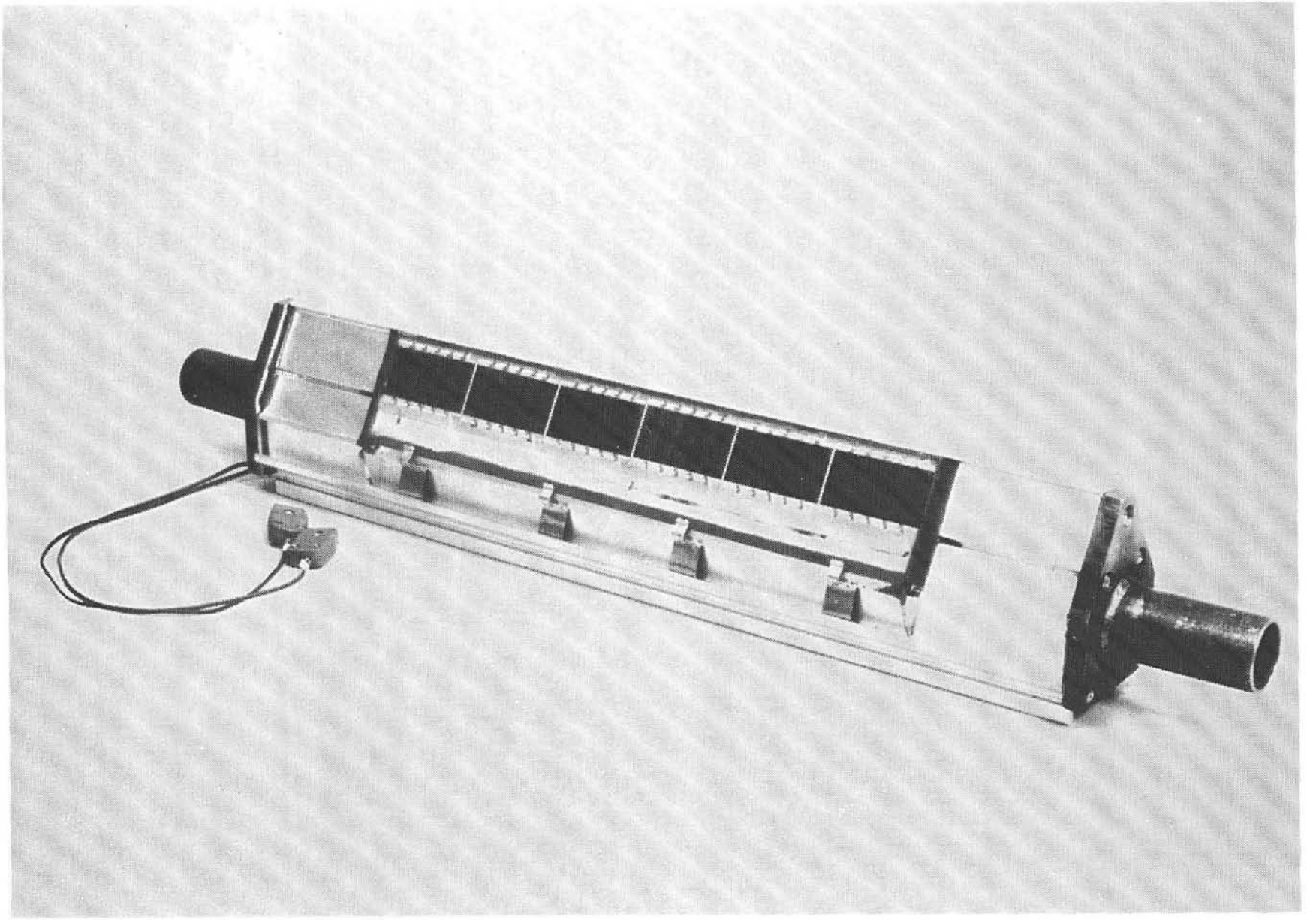

Figure 6-6. Short Receiver Section for Environmental Testing

- Thermal shock -- twelve excursions/day of $-6^{o}C$ to $+120^{o}C$, dry air
- Freeze thaw cycling -- three excursions/day of $-6^{o}C$ to $+55^{o}C$ with 100 percent relative humidty below $+5^{o}C$

The exposures were typically completed after 4 weeks.

After each test, the module performance was remeasured at one sun irradiance and the voltage isolation was checked. The modules were also inspected visually for degradation as a result of the accelerated exposure.

6.5.5 Apex Angle Testing

The qualification tests described so far were carried out on Acurex second generation receiver described in section 4. The apex angle of this receiver is 60° and was selected on the basis of then available analytical studies. The theoretical trade-offs of section 2, which were performed in parallel with the receiver design, indicated that the optimum apex angle is 44°. Therefore, it was necessary to verify the findings of optimum apex angle for the Vee receiver.

For this experimental study we fabricated some special receiver support brackets which allowed the receiver to be rotated about its virtual apex without affecting receiver height. Figure 6-7 illustrates how this was achieved. The receiver wiring was also modified so that only one side of the receiver was active at a time. Apex angle tests were run at different receiver heights and over four different reflector surfaces (all FEK). For each test the apex half angle was varied from 0° to 90° (vertical cell surface to horizontal). At each data scan we produced an I-V curve and recorded the following data:

- String voltage
- String current

} at peak power

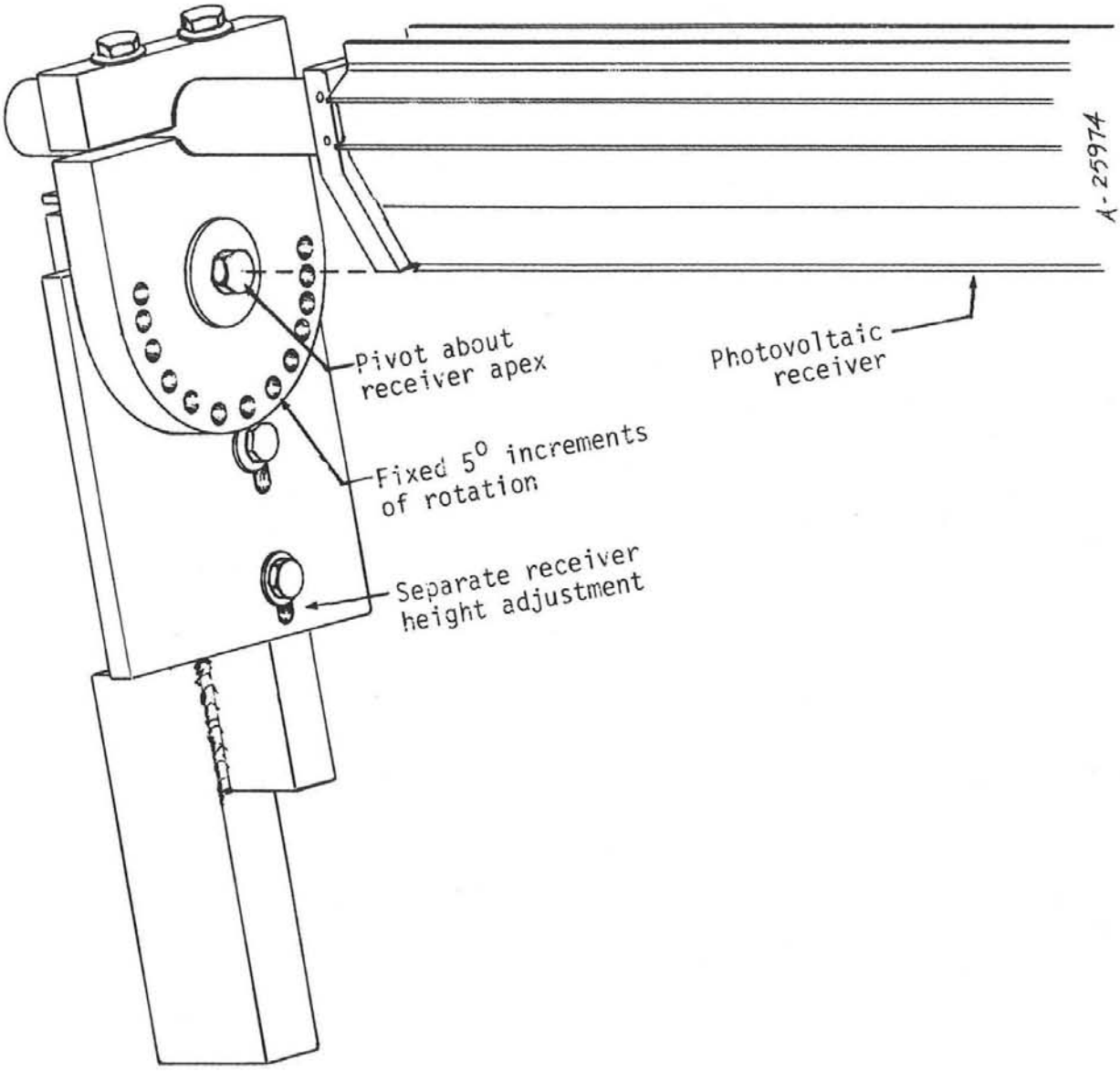

Figure 6-7. Apex Angle Test -- Receiver Support

- Direct normal insolation
- Total normal insolation
- Fluid outlet temperature
- Ambient temperature
- Receiver height above the reflective surface
- Reflector surface (glass, FEK-244, etc.)
- Apparent apex angle

The data was recorded on magnetic tape and data reduction was done by computer.

6.5.6 Glass Reflector Testing

Acurex manufactures a version of its 3001 trough with silvered microsheet glass reflective laminates similar to those described in section 3 of this report. The thin glass is manufactured by Glaverbel, Inc. (Belgium) and is silvered and laminated by Mirordan of Belgium. The reflectivity is 0.92 (FEK-244 is 0.84). The objective of the test was to evaluate the performance of the glass collector as a photovoltaic concentrator.

A standard photovoltaic receiver was used to evaluate the normal performance of the glass reflector. Several data scans and I-V curves were generated at 112 $\pm 3^{o}$F fluid temperatures and 900 ± 50 W/m^2 insolation levels. The flux profile was mapped using the flux mapper described in section 6.5.2. Special attention was paid to the image gaps caused by the non-reflective regions at reflector sheet edges. Data scans were taken at 6-in. increments along both sides of the receiver. In the region of the image gaps, data scans were taken at 1/2-in. increments for a 6-in. span.

6.6 TEST RESULTS

6.6.1 Concentrator Performance

The performance testing at normal incidence was intended to measure η_{array} and determine the term η cell(T,H_i) for the performance model. Figure 6-8 shows η_{array} as a function of T_i at constant insolation, for an ASEC receiver. The cells exhibit the expected performance degration with temperature, i.e., $-\frac{1}{\eta}\frac{d\eta}{dT} = 0.0048$. Figure 6-8 also shows the error bands calculated for that data in appendix E.

The graphs of η_{array} against H_i normalized to 50^oC are shown in figure 6-9. None of the three vendors designed their cells for high enough peak concentration. Since the flux profile was not known at the time of procurement, the cells were designed for a uniform 35 sun (geometric) concentration. All of the cells are well past their peak performance under the actual conditions of operation.

The performance of the trough in off-normal incidence in the elevation axis is equivalent to performance with a pointing error or a receiver mislocation due to improper installation. The data is presented as the normalized aperture efficiency, $\overline{\eta}_{array}$ which is normalized to 50^oC cell temperature and no cosine loss. $\overline{\eta}_{array}$ is defined as:

$$\overline{\eta}_{array} = \frac{P_{array}\left[1 + 0.0048\left(T_{cell} - 50\right)\right]}{DNI * A * \cos\beta} \qquad (6\text{-}2)$$

The variation of η_{array} with tracking error shown in figure 6-10 demonstrates the tracking sensitivity of the photovoltaic trough. It also demonstrates the difficulty in correctly aligning the receiver. Although a careful visual alignment was made during setup, we still had a built in $1/4^o$ tracking error. This error was removed before other tests were done. It should be pointed out that Acurex tracker can track the sun

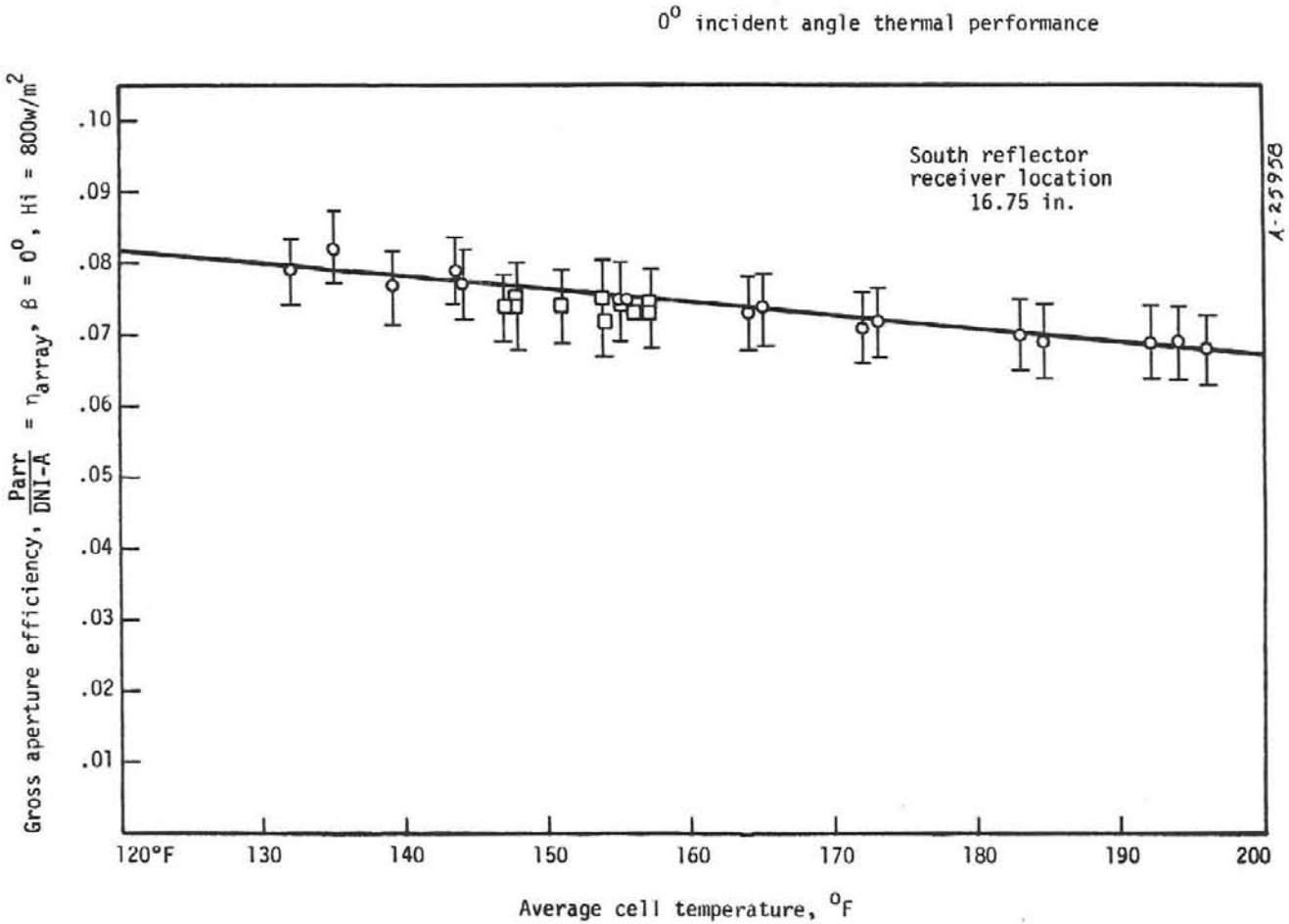

Figure 6-8. Array Efficiency Versus Cell Temperature for ASEC Cells

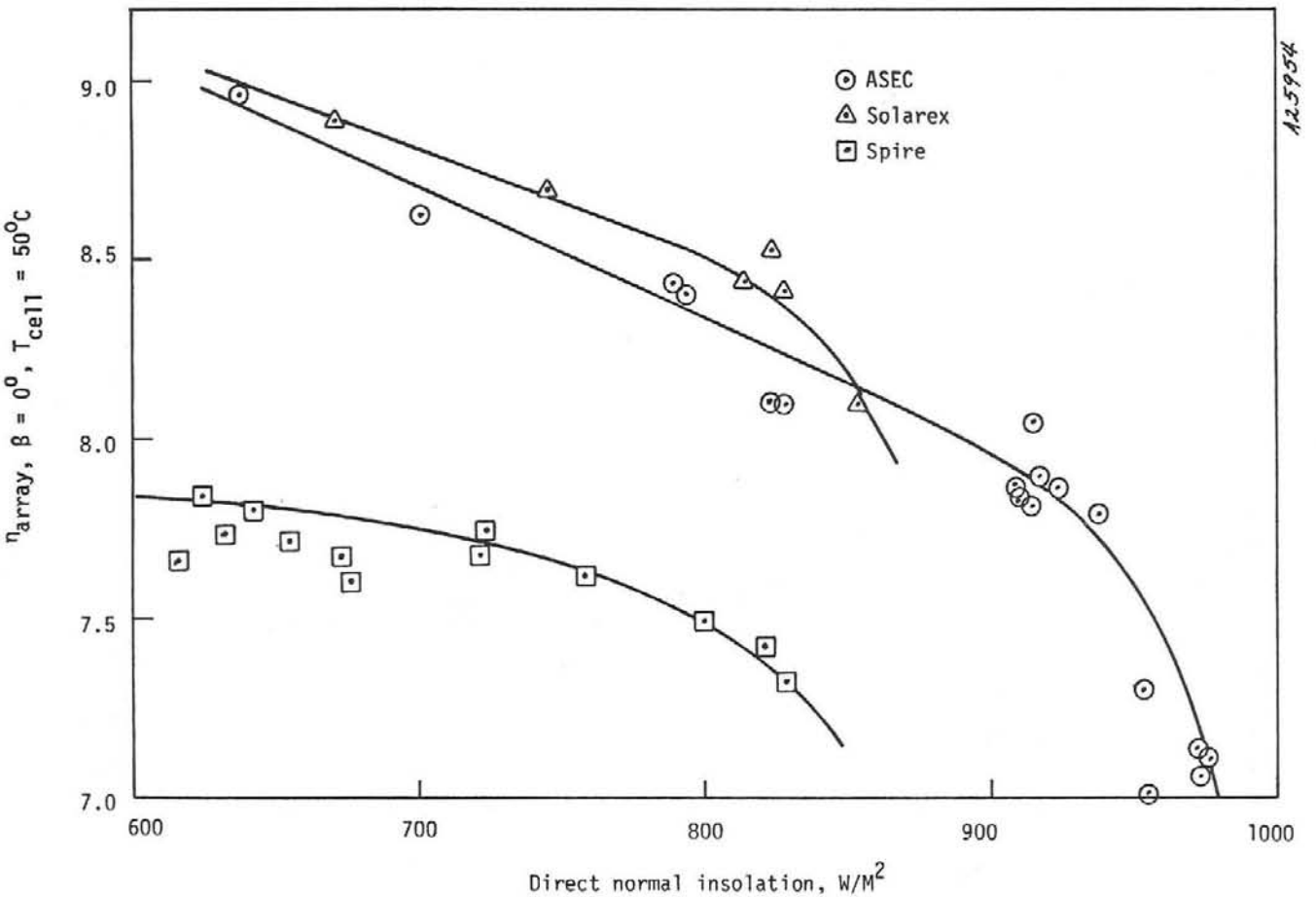

Figure 6-9. Array Efficiency Versus Direct Normal Insolation for ASEC, SOLAREX, and SPIRE Cells

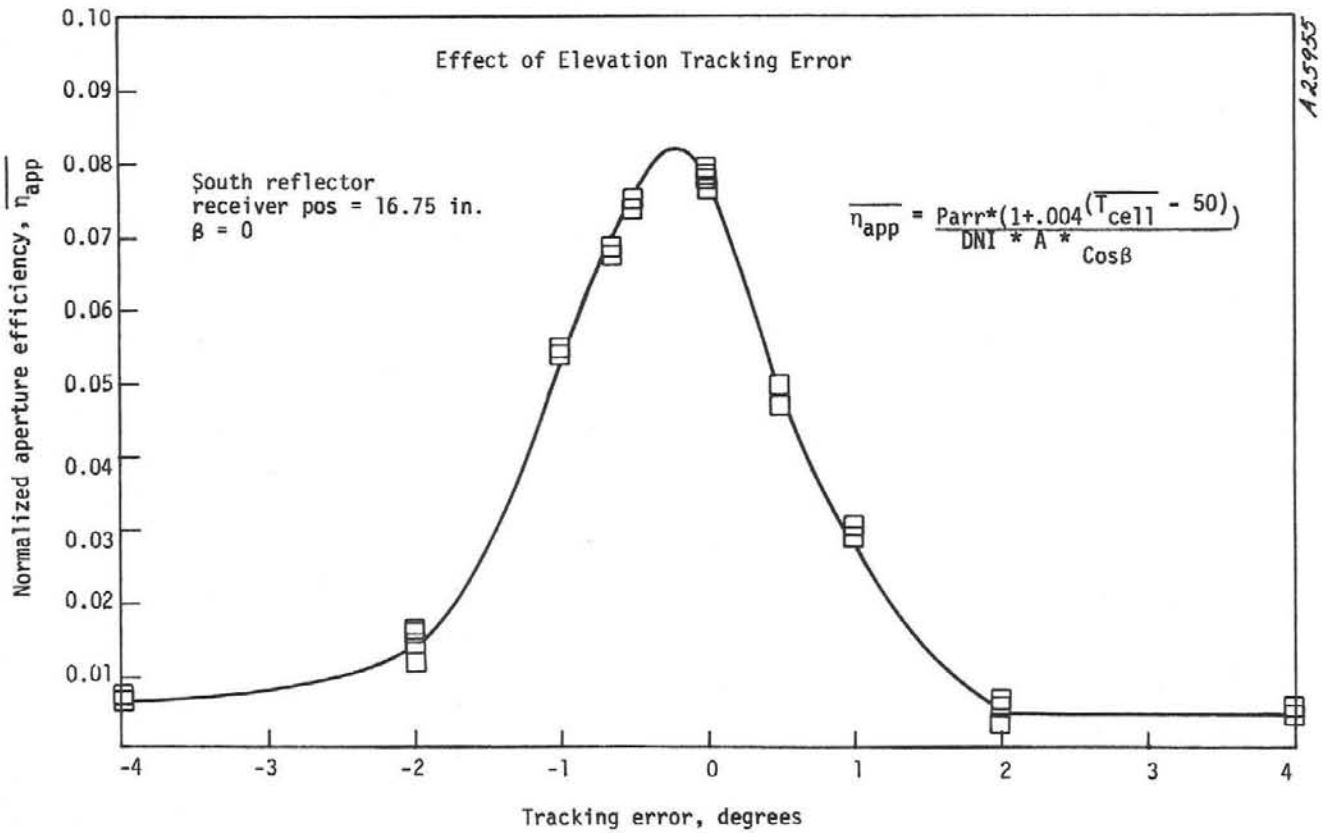

Figure 6-10. η Array Versus Tracking Error — ASEC Cells

within $\pm 0.125^{o}$; hence, the error was in alignment, not the electronics. The performance degradation due to a tracking error of $\pm 0.125^{o}$ will be less than 2 percent.

The performance at off-normal incidence in the azimuth axis (i.e., due to solar declination) is presented in figures 6-11 and 6-12. There is a significant difference in performance depending on whether there is an adjacent reflector to the south of the module being evaluated. Figure 6-11 shows the data for a module without adjacent module and figure 6-12 shows the same function with adjoining reflector. The curve with adjacent reflector is skewed and peaks at a lower incident angle than the nonadjacent reflector curve. The 0° incident angle and peak values from the two curves are not equal due to slope error differences between them.

The performance data generated by testing at Sandia support the data generated at Acurex. The data presented in figures 6-13 through 6-16 were generated on a typical day at Sandia. All data are at normal incidence and with a coolant rate of 4 gpm.

All testing at Acurex was performed with a flowrate of 8 gpm. The lower flowrate leads to higher cell to fluid temperature differentials. The efficiencies, referenced to standard conditions for most of the day are on the order of 7.9 through 8.0 which is equivalent to Acurex data for the observed 930 W/m^2 direct normal insolation.

Figure 6-13 illustrates the cell to fluid temperature drop as well as the distribution of temperatures across the cell. The center of the cell in the brightest illumination is the hottest. The apex of the cell is cooler due to lower irradiation level, but not as cool as the outer edge due to the poorer fluid circulation in the Vee of the apex. Figure 6-14 covers a much larger span of time and details the total and

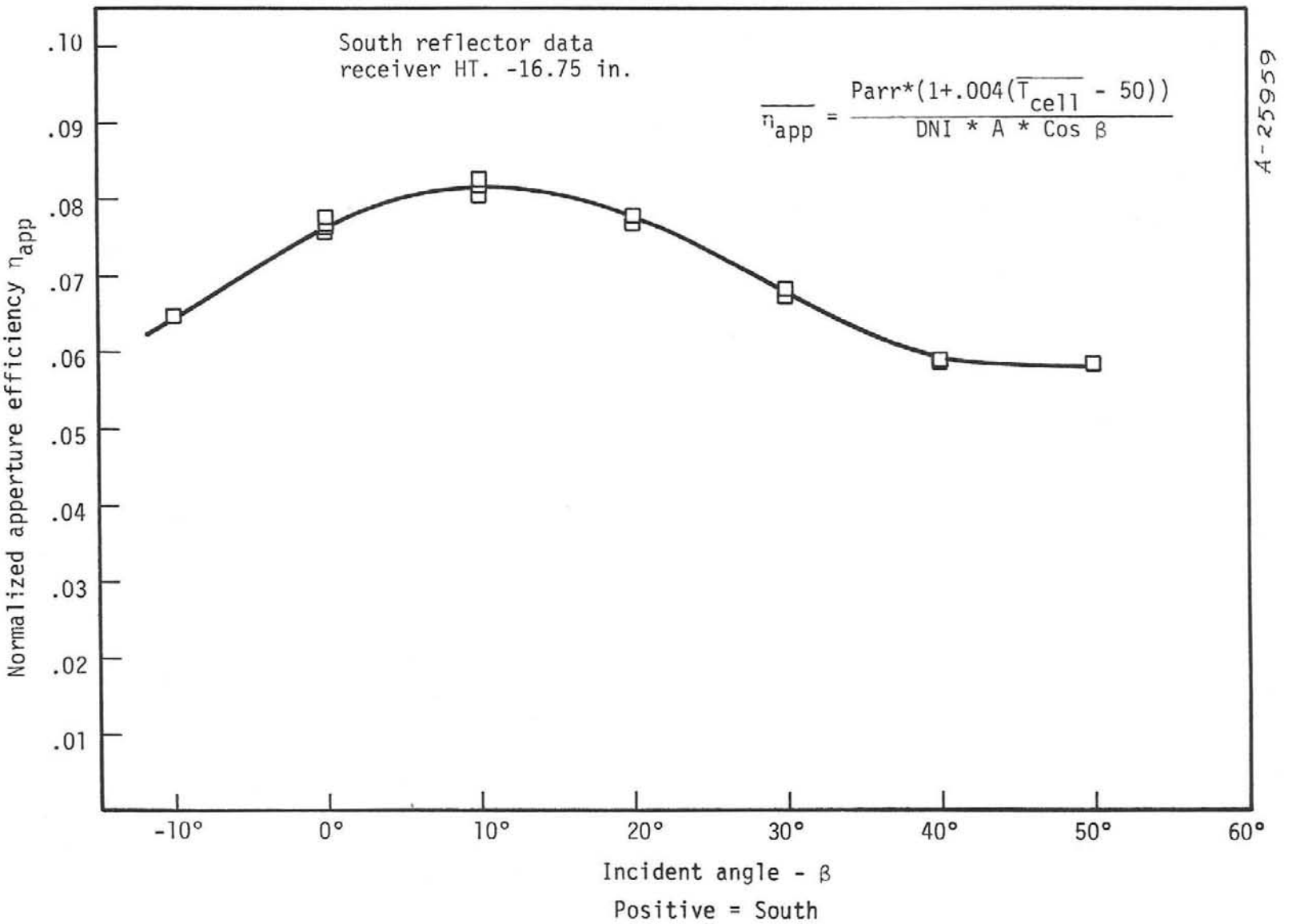

Figure 6-11. Off-Normal Performance -- South Reflector

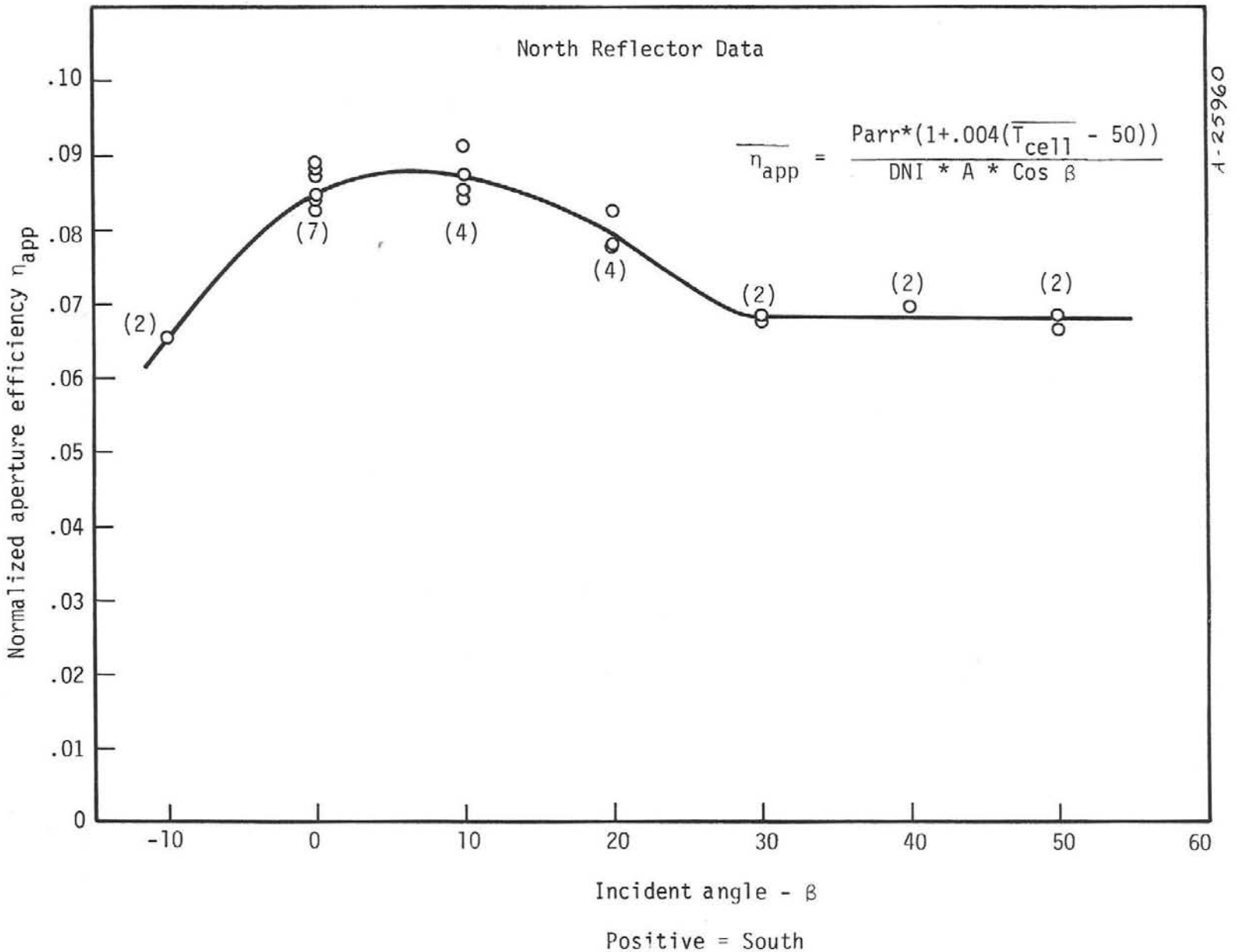

Figure 6-12. Off-Normal Performance — North Reflector

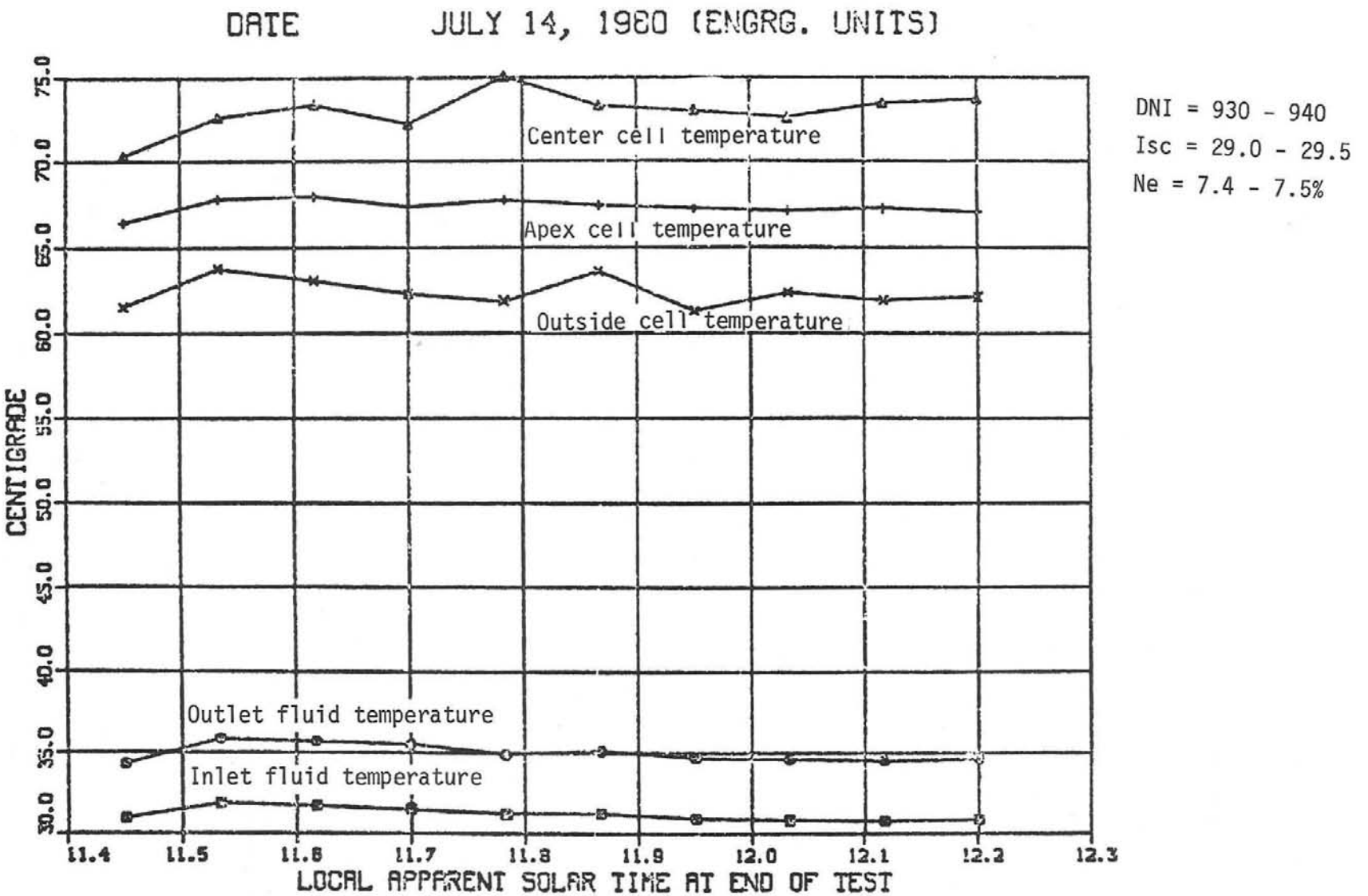

Figure 6-13. Acurex Inlet, Outlet, and Cell (39,40,42) Temperatures

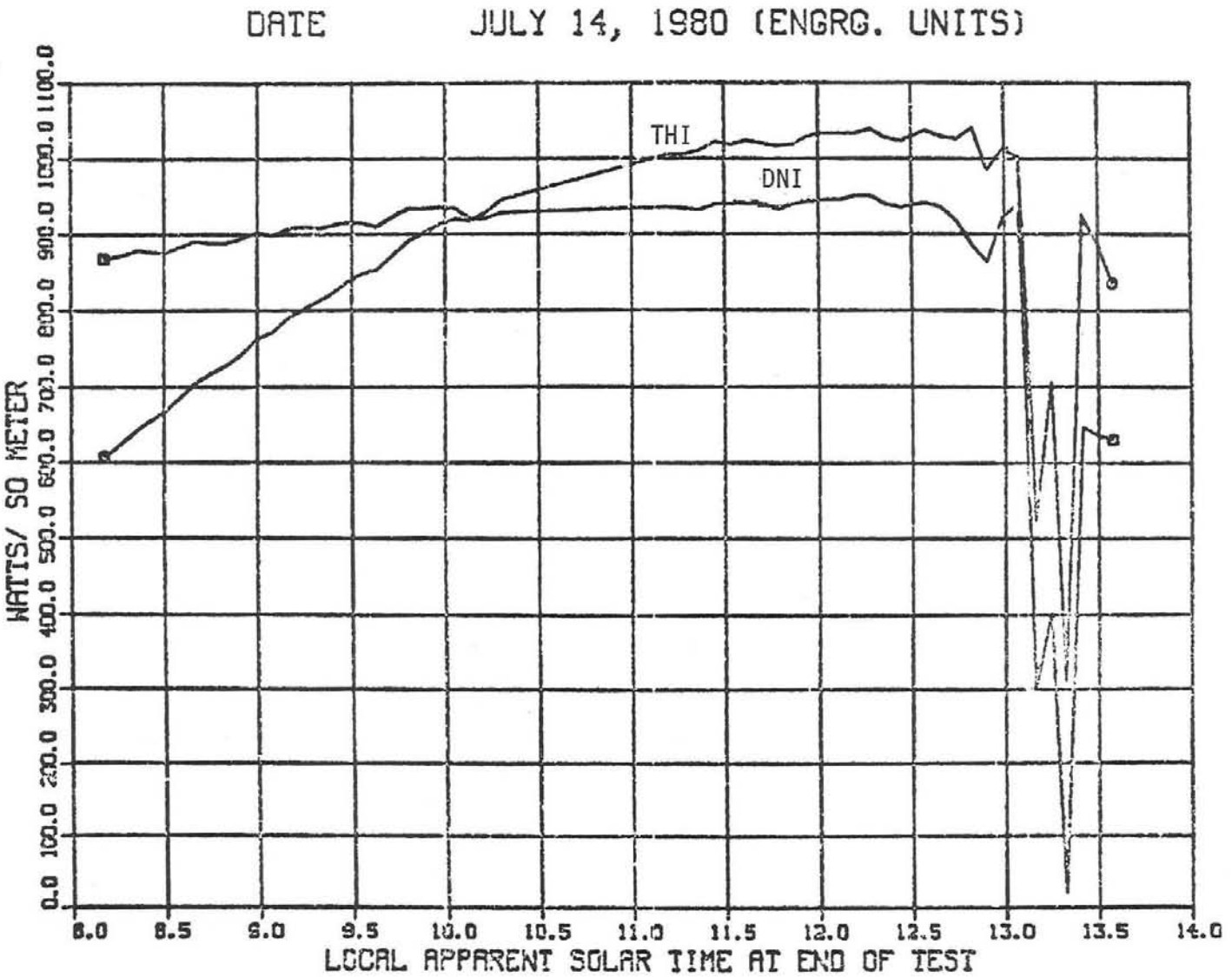

Figure 6-14. Direct Normal and Total Horizontal Insolation

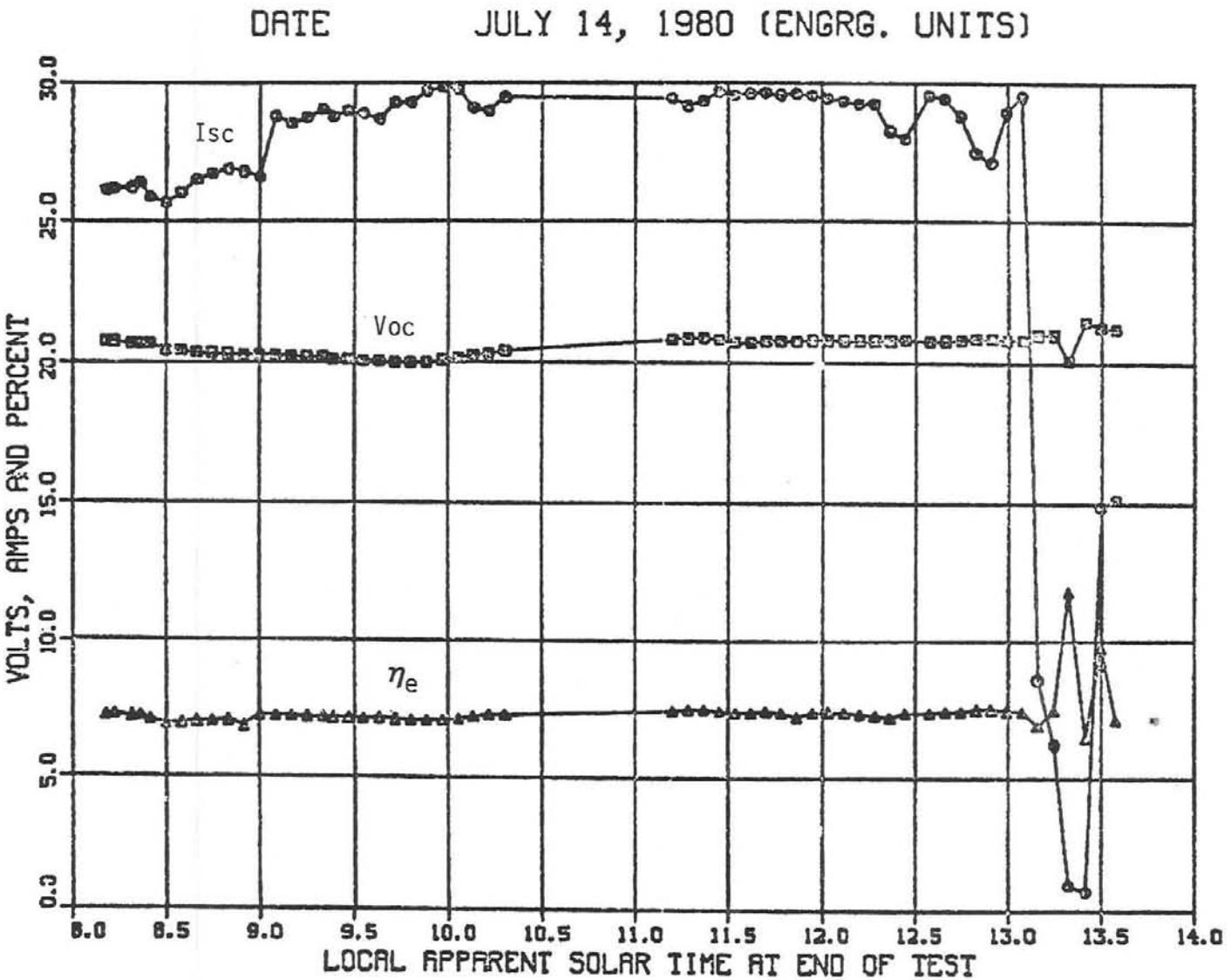

Figure 6-15. Acurex PRDA 35 VOC, ISC and Efficiency

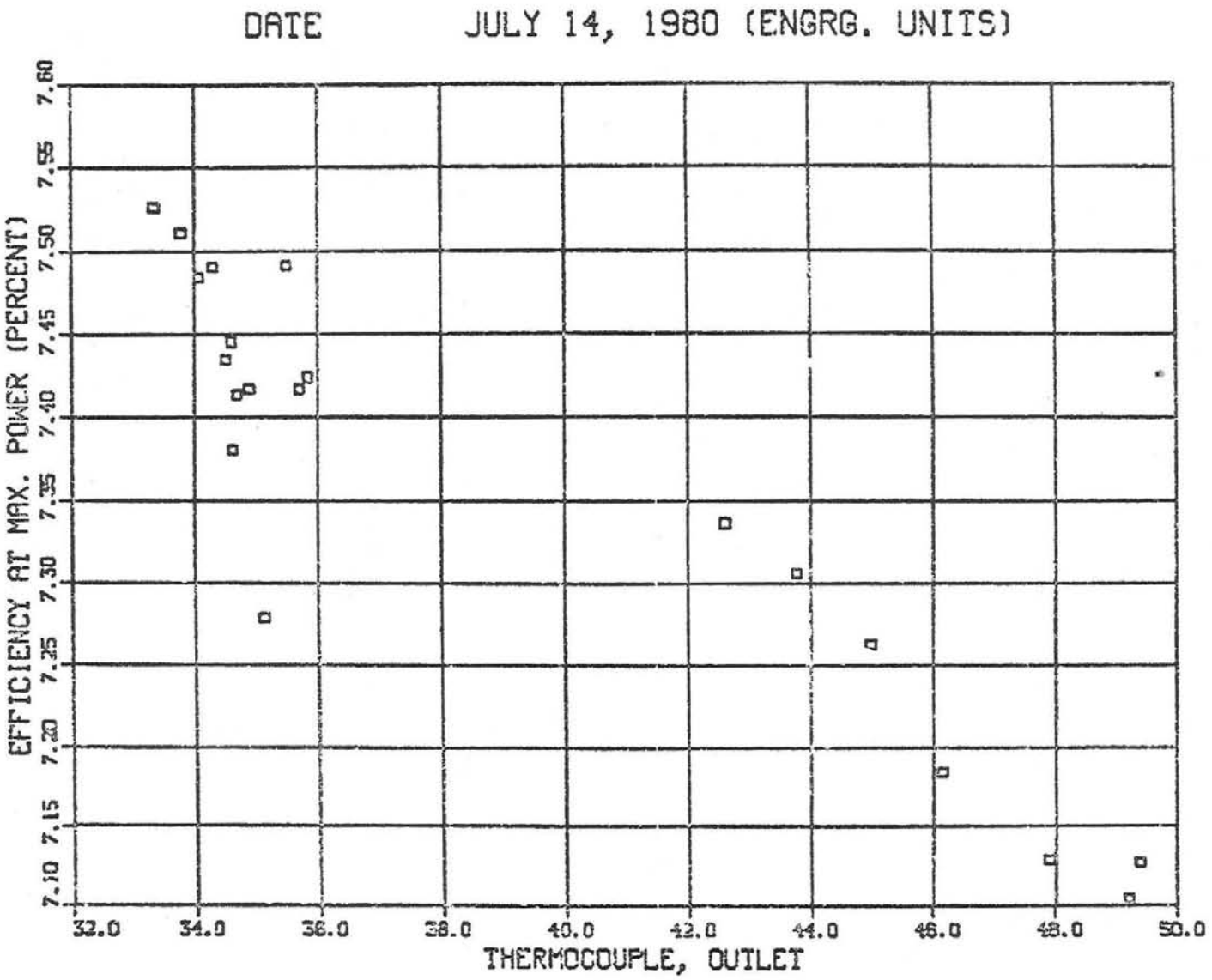

Figure 6-16. Acurex EFF Versus Outlet Temperature for 0945 to 1215 Hours

direct insolation values for the day. Figure 6-14 shows the effect of changing DNI on module performance. In the early morning, with low insolation and low temperatures, the short circuit current (Isc) is low and the open circuit voltage (Voc) is high. The Voc drops with increasing cell temperature and the Isc increases with insolation. The net result is virtually no change in module efficiency (ηe). The plot of efficiency versus otulet fluid temperature (figure 6-16) demonstrates an interesting characteristic. The best fit in the rather scattered data corresponds to a cell thermal coefficient $-\frac{1}{\eta}\frac{d\eta}{dT} = 0.0032$. This low a value is relatively unheard of and is not repeated in any data at Acurex.

6.6.2 Intercept Factor and Image Uniformity

The output of the flux mapper are 50 voltage readings which correspond directly to the local intensity of light on the 0.040 in. x 0.200 in. active surface of the sensors. Since the family of data points corresponds to a particular physical array of sensor elements, the computer can plot out the "flux map" for the slice of receiver represented by the mapping device. Figure 6-17 is such a map. The virtual apex of the V-receiver and the cell active width are also shown. Note the peak intensity of 60 suns at this receiver location.

Twenty locations along each side of the receiver were scanned. These data are combined to produce two-dimensional flux profiles as shown in figures 6-18 through 6-22. These flux maps demonstrate the changes in the image with increasing incident angle. The images represent the east face of the receiver with the apex on the left. The south end of the receiver is in the foreground and it represents data for the northernmost reflector so there is additional radiation from an adjacent reflector which can be seen in the 30° and 40° incident angle views. The

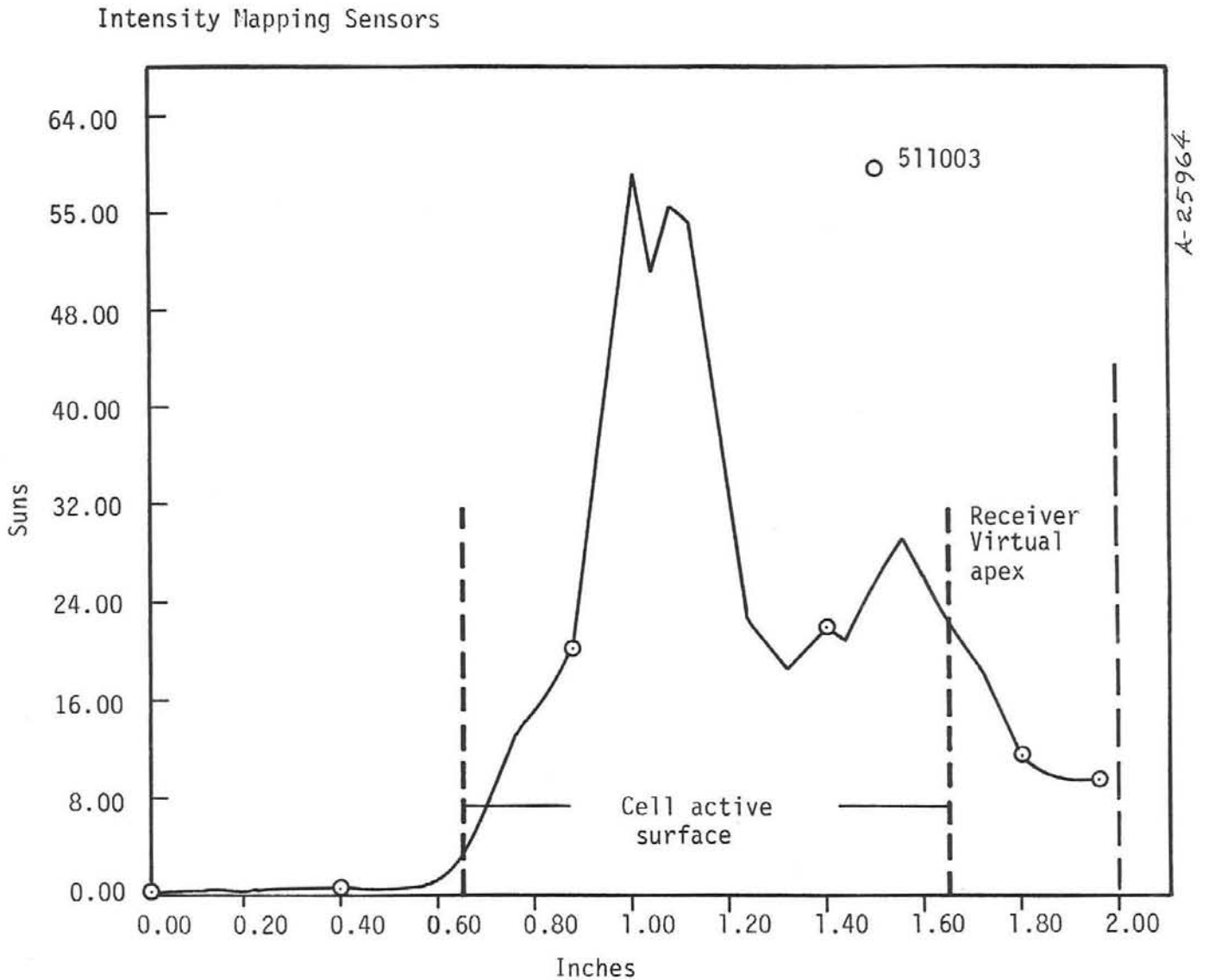

Figure 6-17. One Dimensional Flux Map

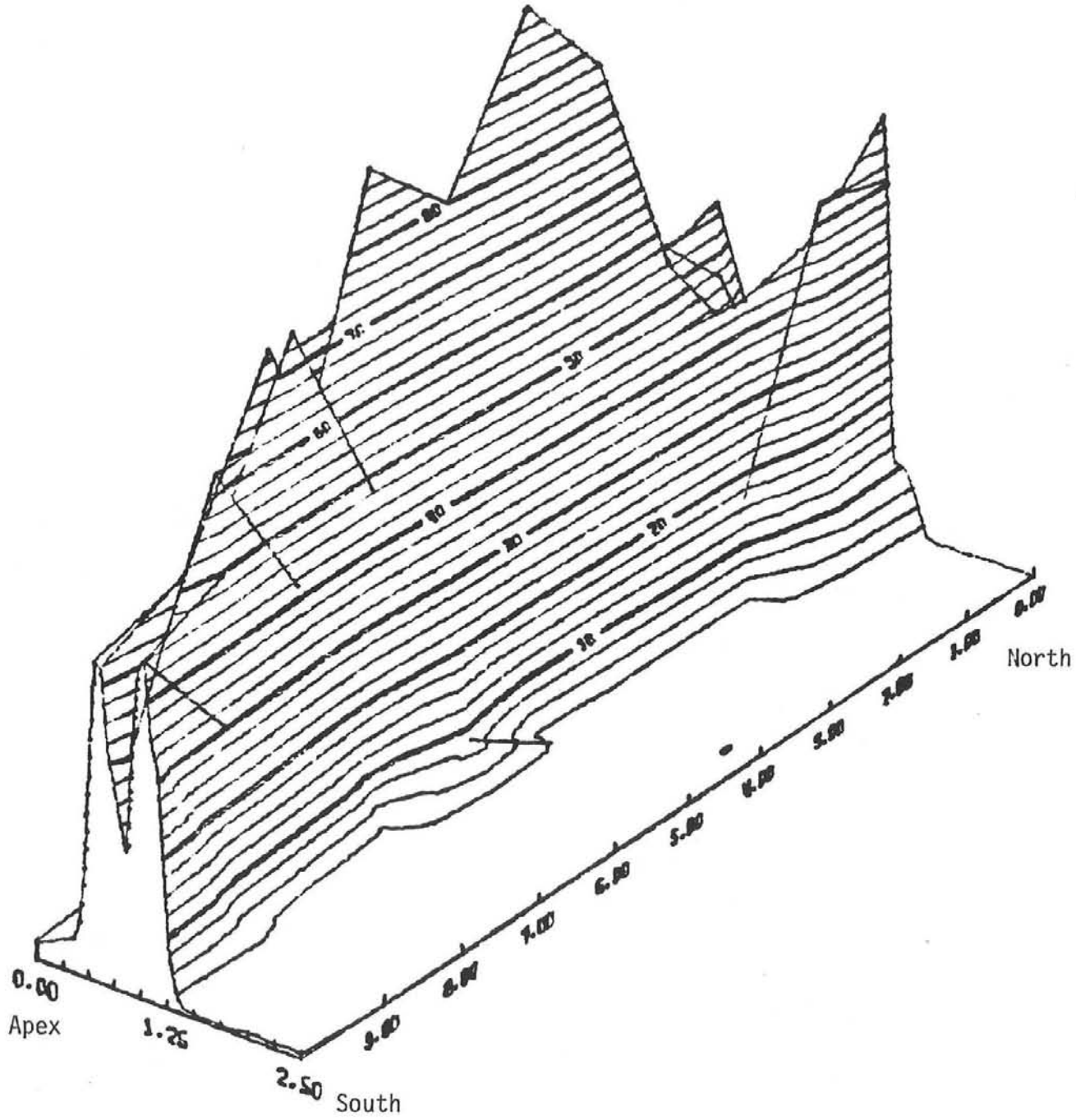

NORTH.UPSIDE 0.

Figure 6-18. Two-Dimensional Flux Map for 0° Incident Angle

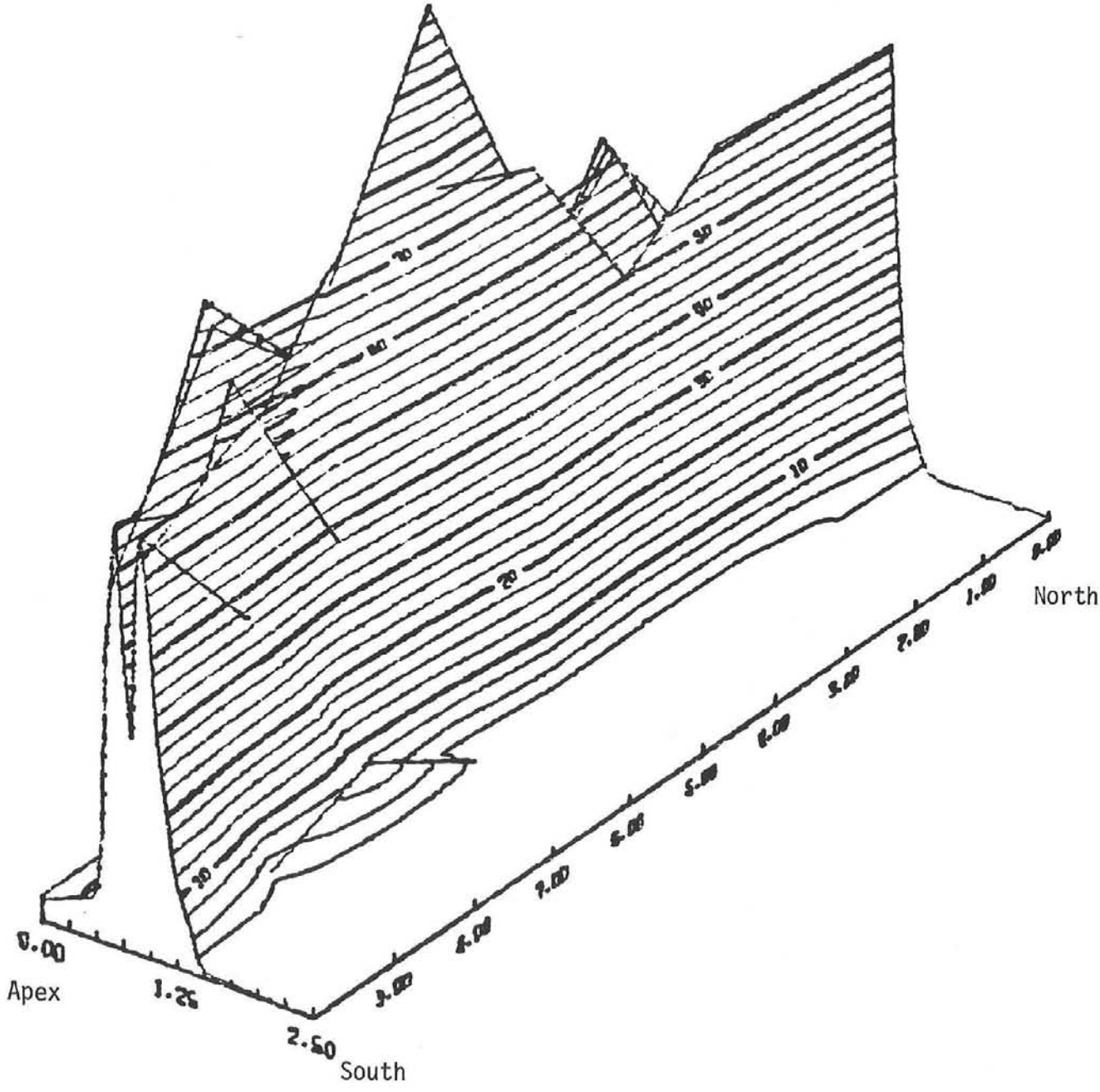

NORTH.UPSIDE.10.

Figure 6-19. Two-Dimensional Flux Map 10° Incident Angle

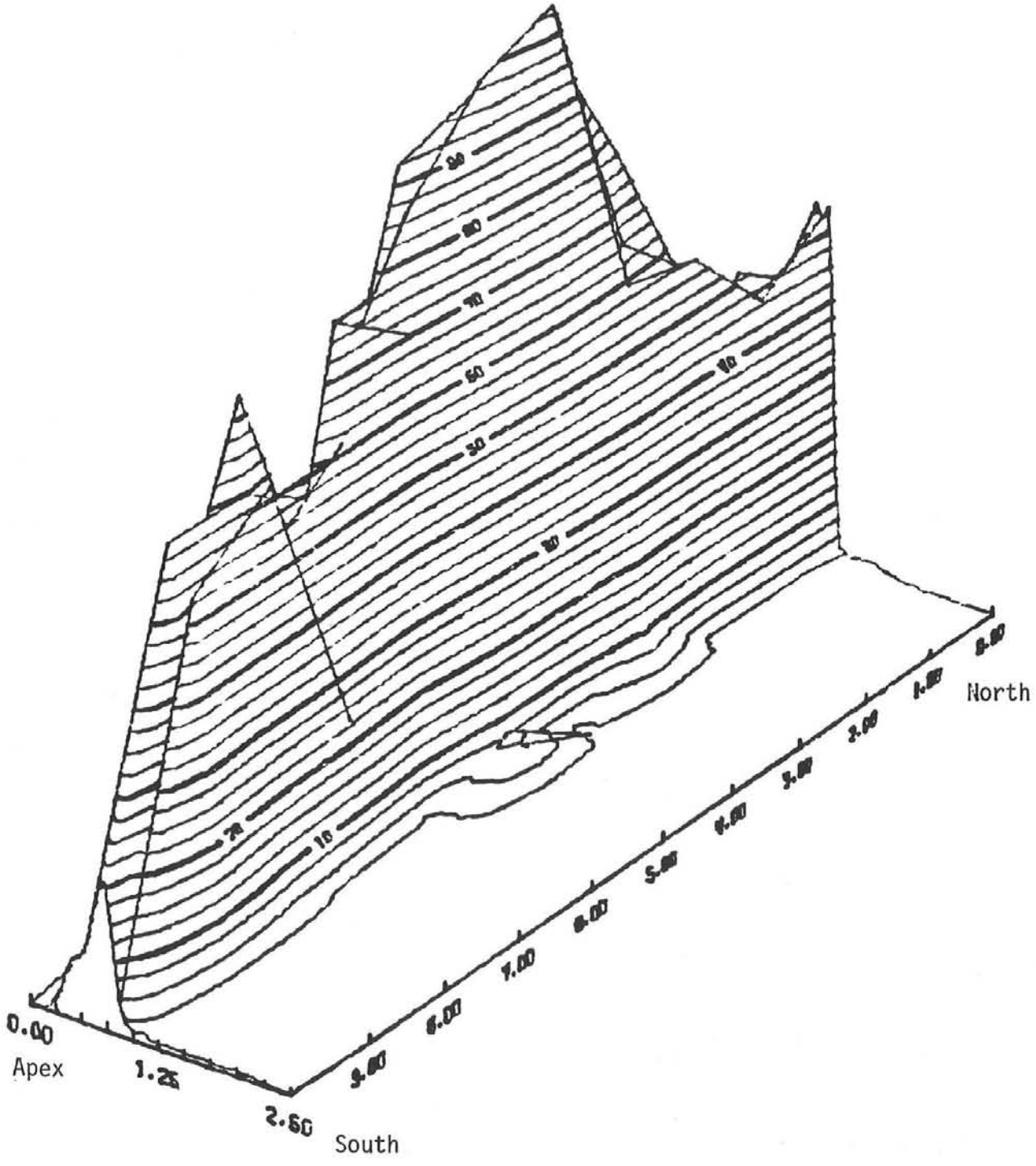

NORTH.UPSIDE.20.

Figure 6-20. Two-Dimensional Flux Map 20° Incident Angle

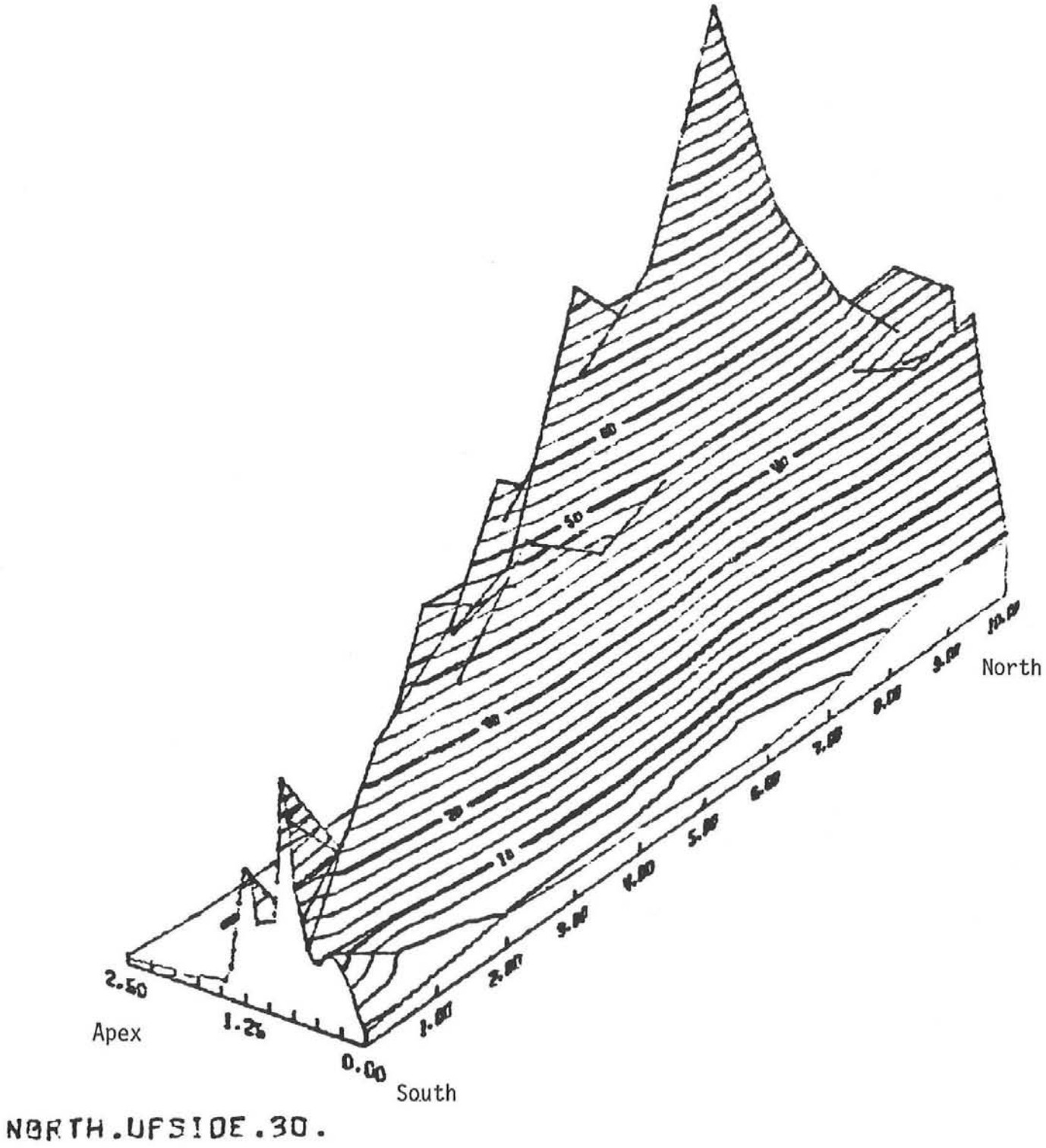

Figure 6-21. Two-Dimensional Flux Map — 30° Incident Angle

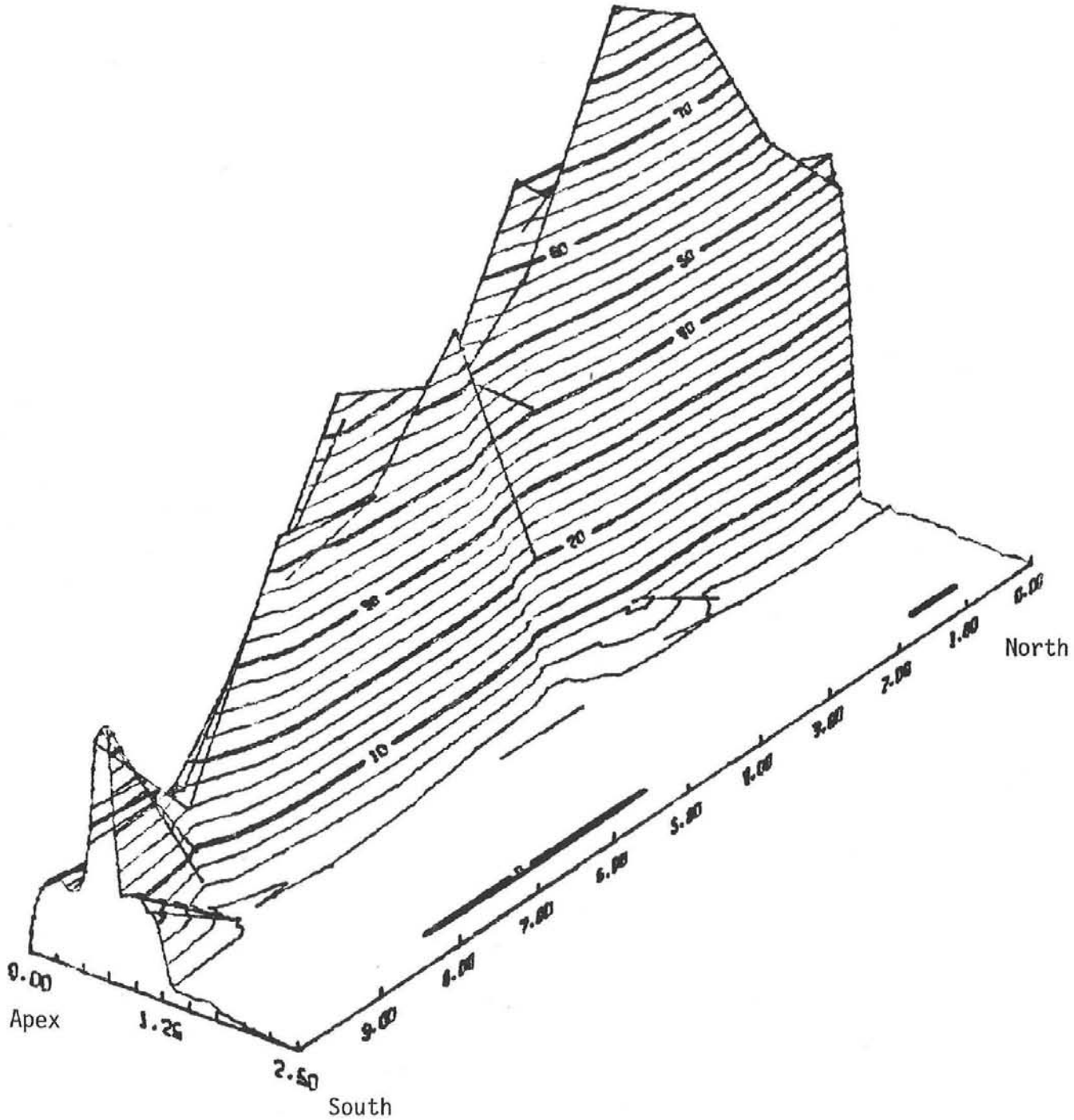

NORTH.UPSIDE.40.

Figure 6-22. Two-Dimensional Flux Map -- 40° Incident Angle

nonilluminated portion of the receiver at the southern end is increasing with incident angle, and the poorly distributed image typical of the extreme ends of the reflector surface are predominant in that section of the receiver.

The one-dimensional flux map can easily be interpreted for intercept factor. The area under the curve within the cell active surface as a fraction of the total illuminated area is the intercept factor. It should be noted that the total illuminated area is not constant along the receiver. Some light escapes at the apex of the trough and is missed by the sensor. The amount of this light varies from one receiver station to the other. On the other hand, longitudinal displacements in image result in locally concentrated sections. Since the longitudial flux variation is accounted for in the image uniformity factor, the intercept factors were evaluated on the basis of a constant total illuminated area.

All of the sensor data is normalized to 800 W/m^2 DNI using the pyheliometer data recorded with each scan. The illuminating energy on the cell is divided by a constant value which represents the total reflected energy. All values more than 2σ below the mean are rejected and the resultant data is averaged to yield intercept the factor. The resultant data is plotted in figure 6-23 for two different reflectors. As could be predicted, there is a general degradation in intercept factor as the length of the light path, and hence its sensitivity to slope error increases with increasing incident angle.

The minimum intercept factor within 2σ of the mean of a 40-scan set of data is divided by the average value to give an indication of the differences in cell performance in the series string. This is a significant limiter in the output of the concentrating photovoltaic

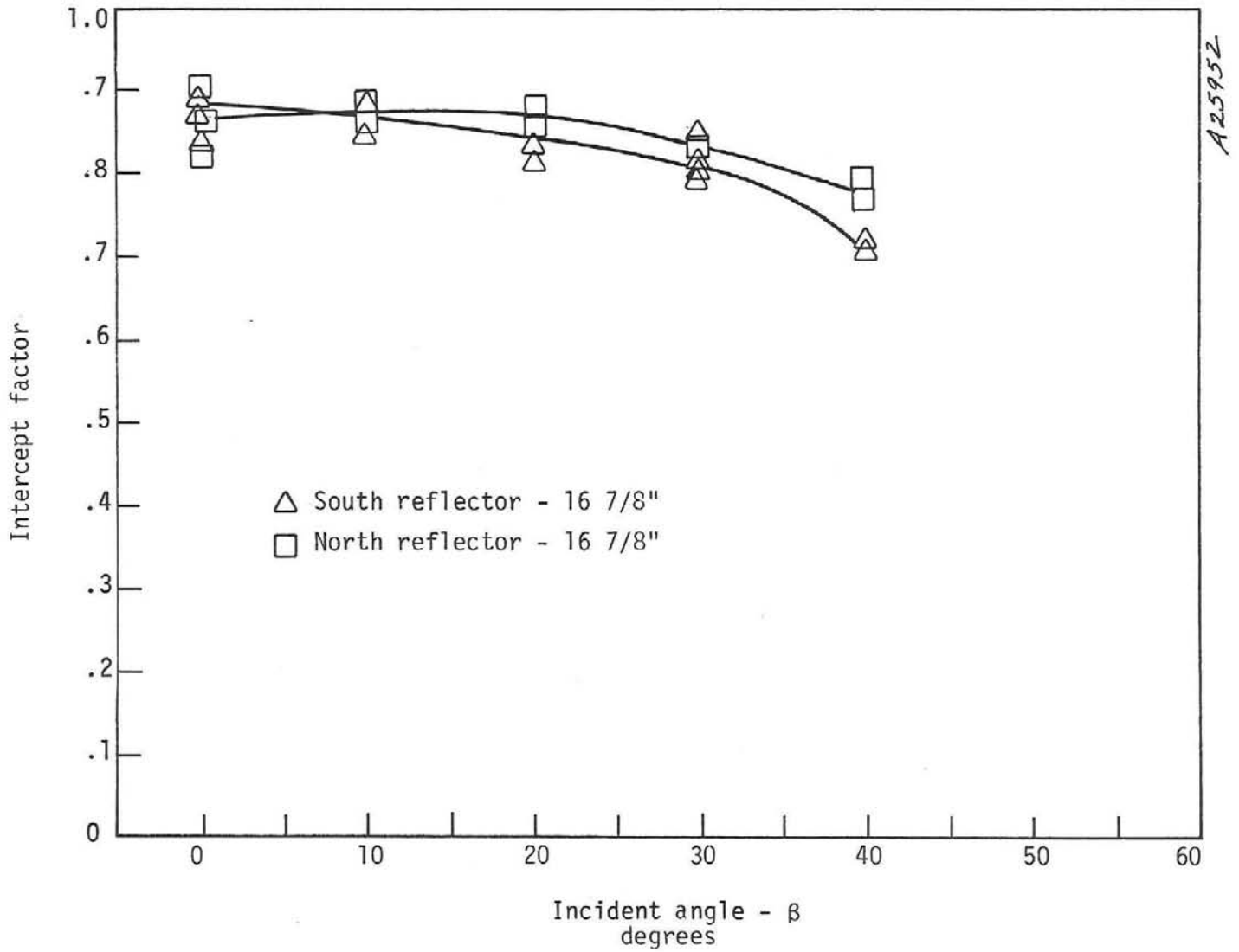

Figure 6-23. Intercept Factor

receiver even if bypass diodes are used. This function is called the image uniformity factor (F_{iu}). We would expect that this factor would have a relatively low value at normal incidence due to systematic slope errors (sheet edges, rib print through, etc.). As the systematic errors are spread out along the receiver by increasing incidence angle, we would expect the image uniformity to increase. The data supports this theory for the first 20° as figure 6-24 demonstrates. What is unexpected, however, is the down-turn in uniformity at fairly high incident angles. As the length of the light paths increase some new systematic slope error must be evolving. This effect is not understood, but is consistent in the data.

In either case, the differences between reflectors is seen to have a significant effect. The inherent slope error variability of reflector modules has as strong an effect as the dependence on incident angle. In modeling these collectors, therefore, average values and functions may have validity for statistically large fields. The application of the model for individual module performance, however, is somewhat limited.

6.6.3 Electrical Loss Factor

The effect of diode turn on in the string is a difficult factor to separate from the other components of the equation for collector performance. The cells are wired on the receiver in three parallel strings of 36 series connected cells. Each series string is divided so that half of its 36 cells are on each face of the receiver. One string is located at the south end of the receiver, one north and one middle. Figure 6-25 shows the southern string in schematic form. There is one bypass diode every three cells in all strings. In this way, we have theoretically optimized the electrical output of the collector for

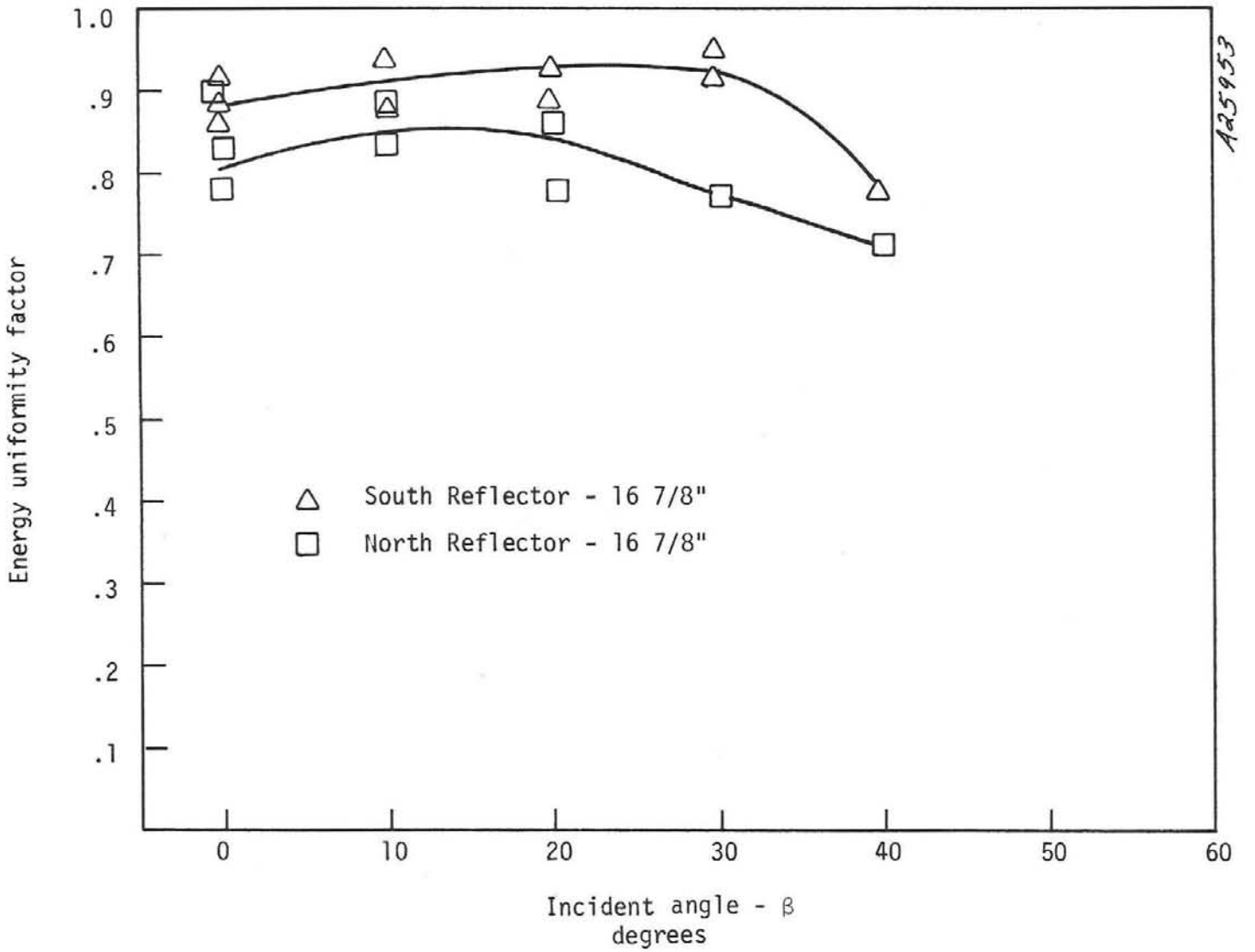

Figure 6-24. Image Uniformity Factor

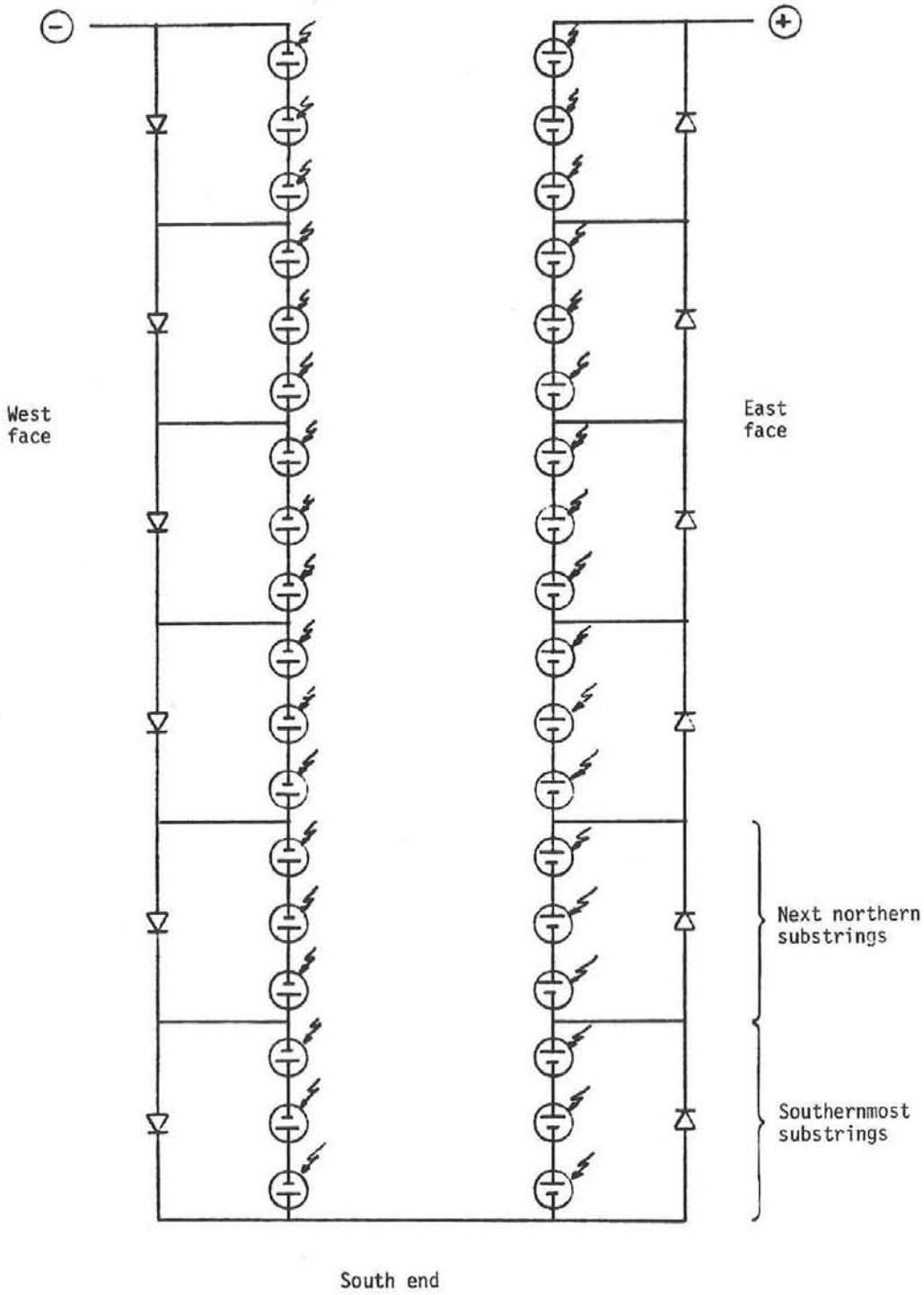

Figure 6-25. Receiver Electrical Schematic

off-normal performance. At higher incidence angles a poorly illuminated region and an unilluminated region appear in the image on the receiver. This effect is shown in figures 6-26 through 6-28. As the incidence angle is increased, this area in the image migrates north. By the time the image has moved to the 30° position of figure 6-28; the unilluminated portion of the image is on the first substring. Without diodes, the southern most cells would be limiting the whole series string. With diodes, the series string can continue to produce power.

The electrical dynamics of various substrings were evaluated in order to understand diode turn on in the partially illuminated and unilluminated portions of the image. Figures 6-29 and 6-30 show the results of these studies for a single reflector. There is no reflector to the south, so no image from an adjacent reflector is ever realized. In figure 6-30, for the "B" or west side, we see that the southern most substring diode turns on at roughly 17.5^{o} incident angle while the second diode, that of the southermost string on the "A" or East face turns on at approximately 22.5^{o} as shown in figure 6-29. The uncertainty in diode turn-on is due in part to the uncertainty in peak power point. It is not, in fact, clear that any current inverter system with peak power tracker can successfully pick the true peak power point in a single module with varying incident angle. The slightly different characteristics of reflectors in any large field, however, will cause this phenomena to be blurred enough that the peak power tracker should, in fact, be able to track peak power accurately.

The explanation for one diode turning on 5° earlier than the other when both substrings are receiving equilavent insolation is made apparent by an examination of the electrical characteristics of the

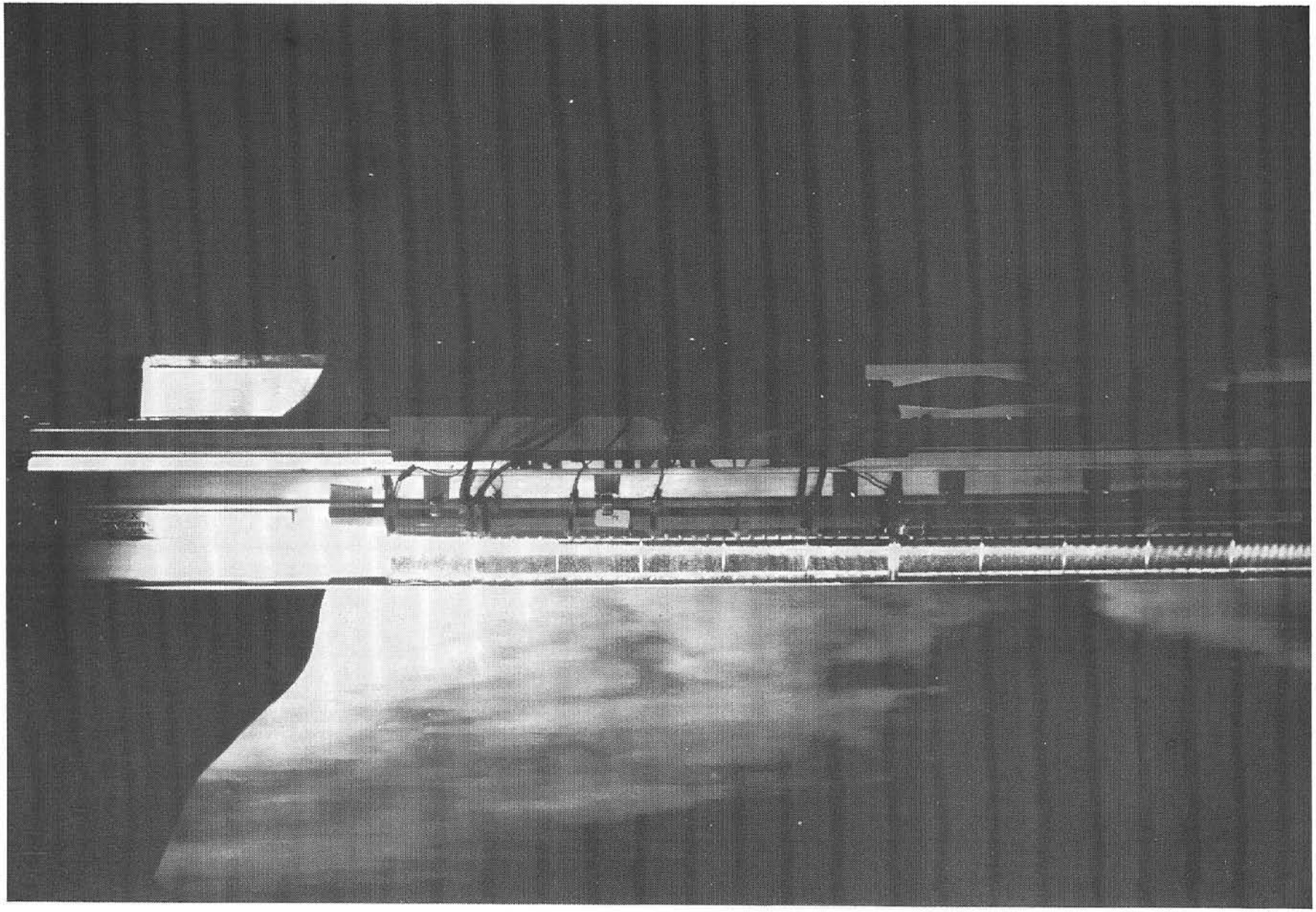

Figure 6-26. 10° Incident Angle Image

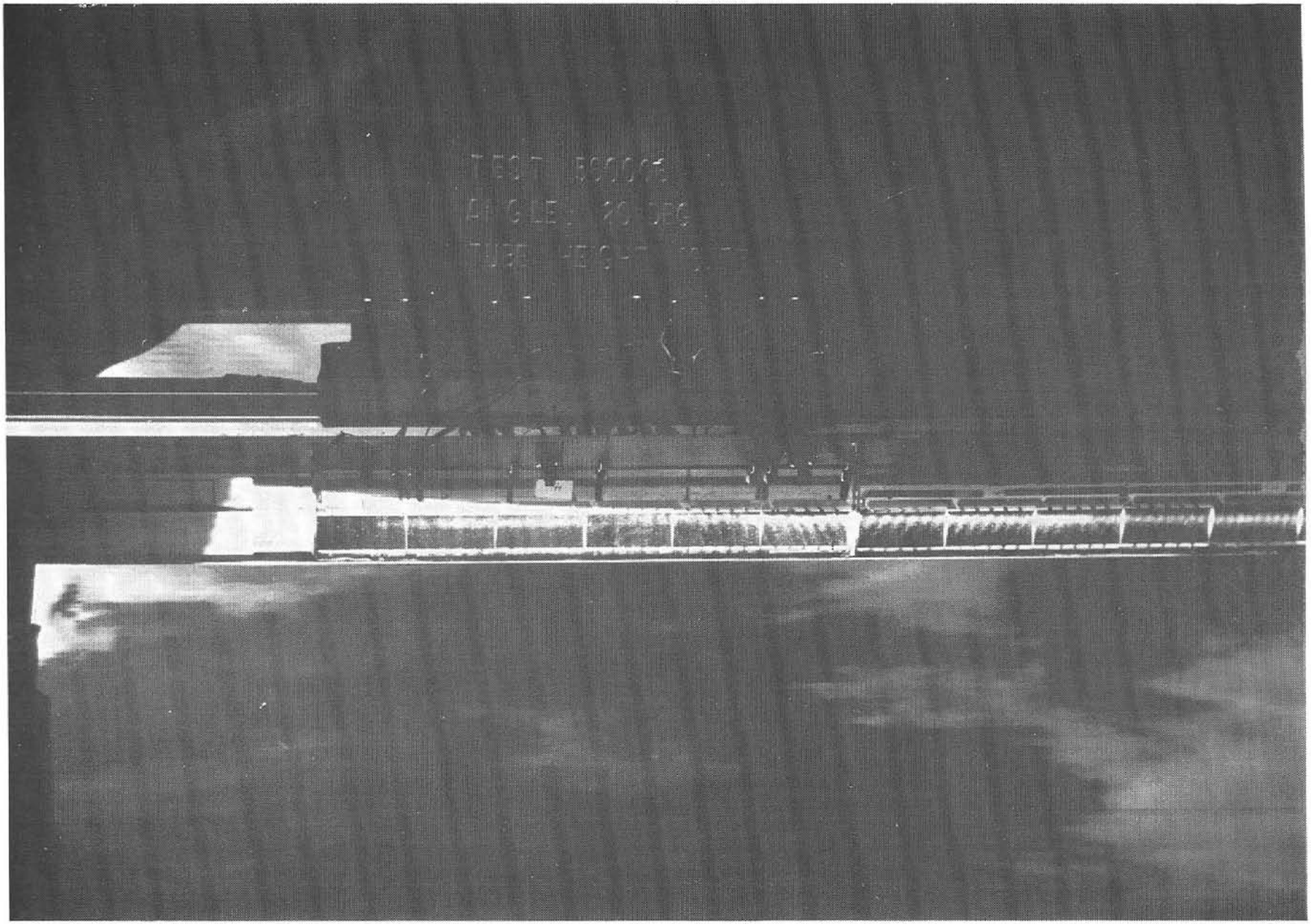

Figure 6-27. 20° Incident Angle Image

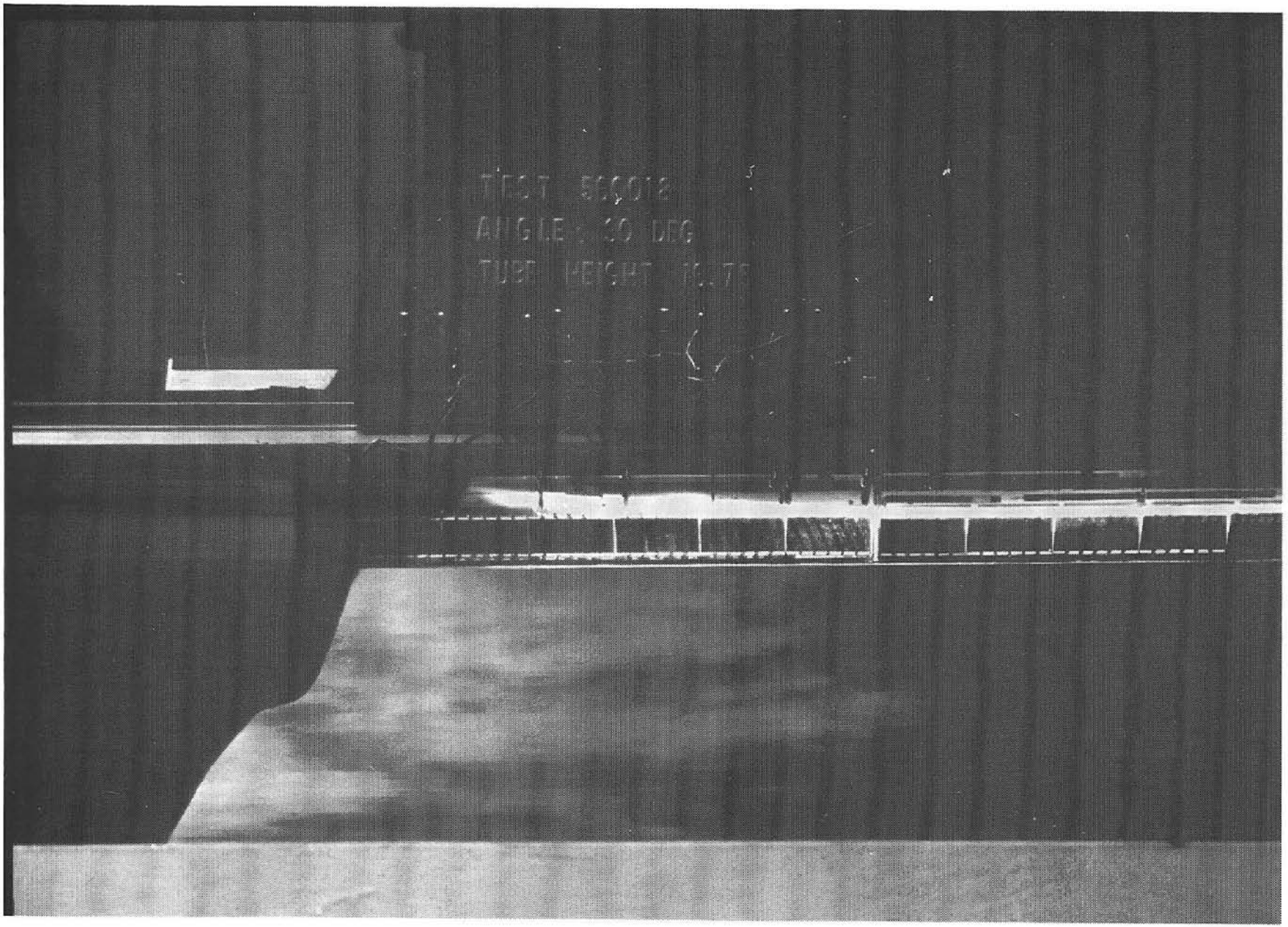

Figure 6-28. 30° Incident Angle Image

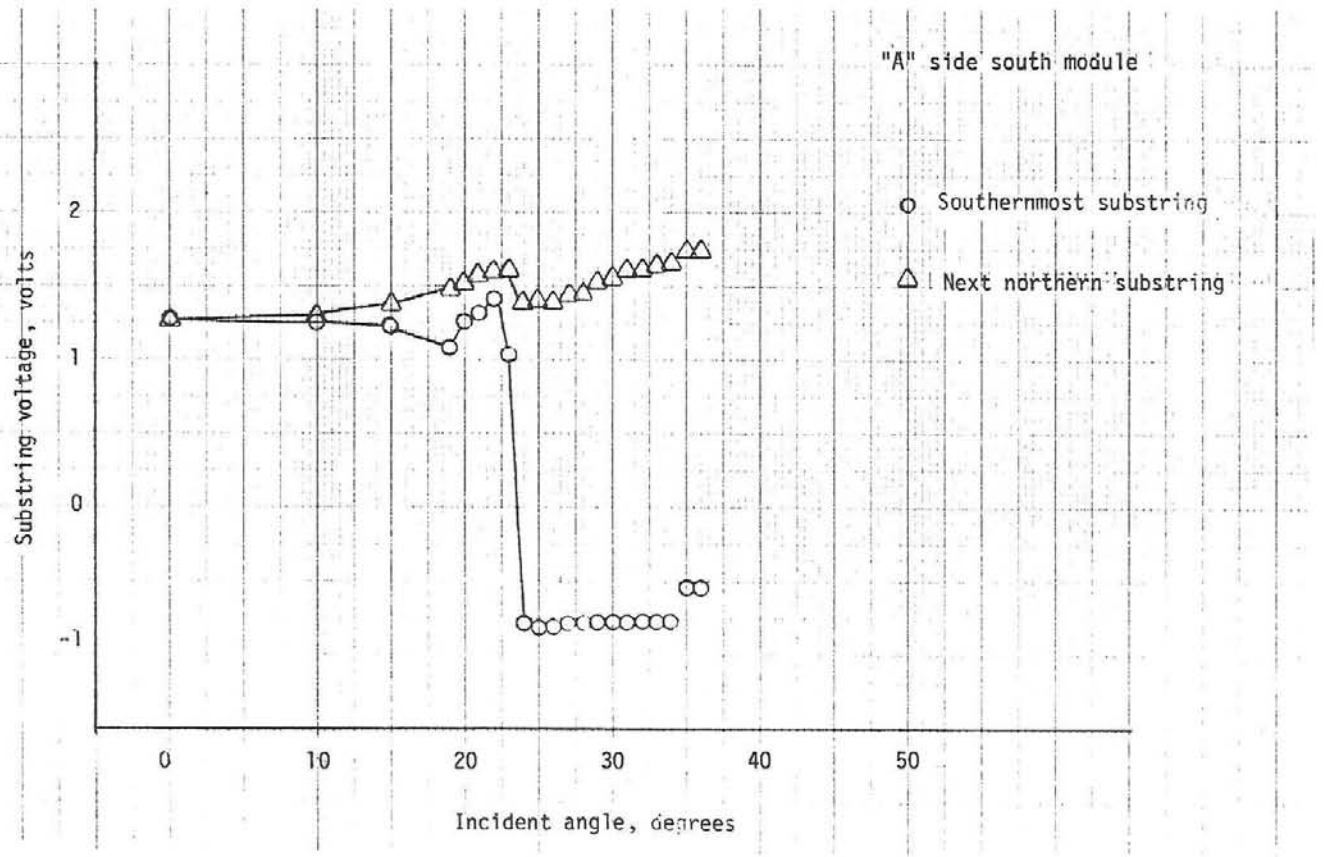

Figure 6-29. Diode Turn On Study "A" Face, South Module

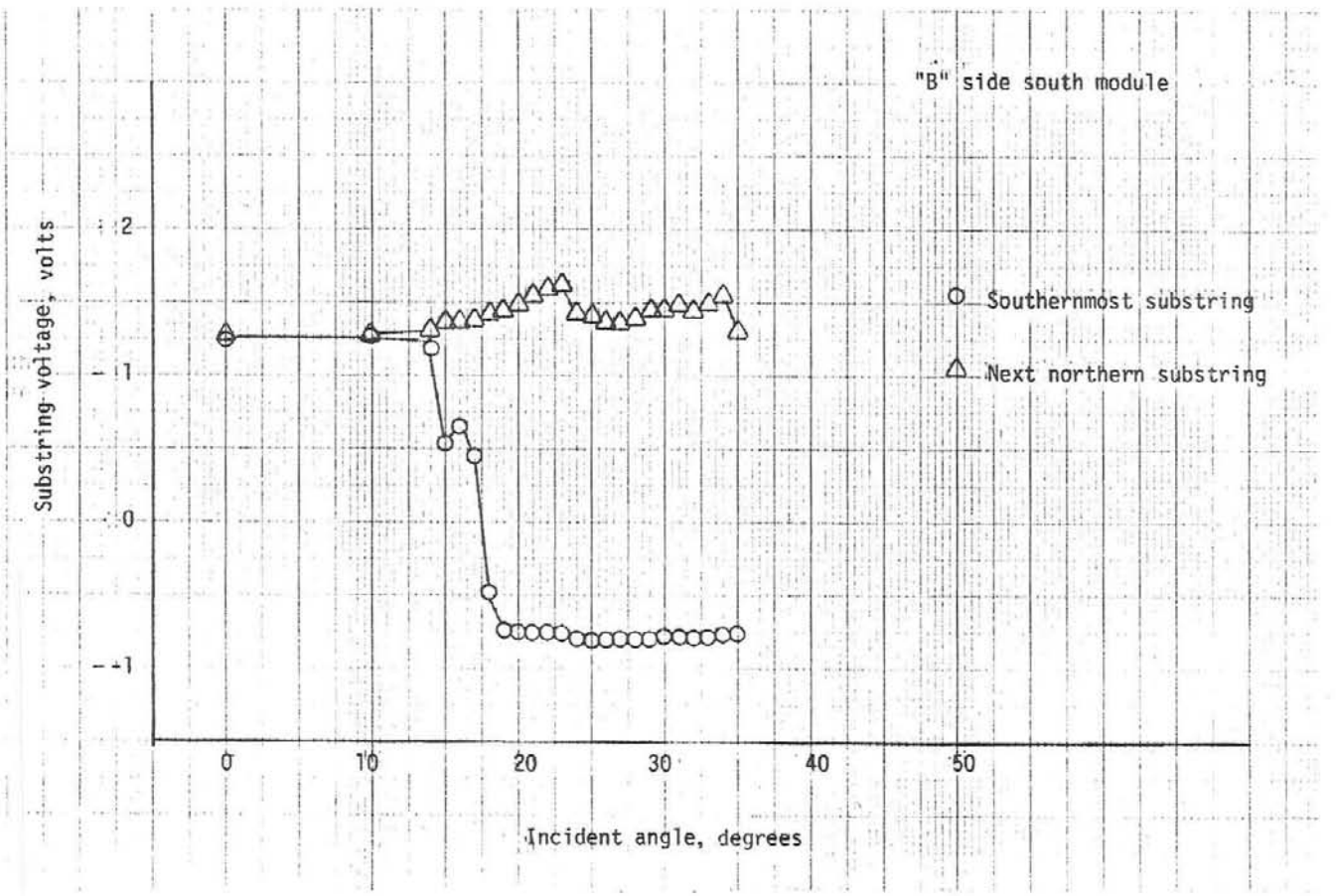

Figure 6-30. Diode Turn On Study "B" Face, South Module

system. With no shadowing of the cells as in the 0 to 10° incidence portions of the curves, there is balanced current flow in all three parallel strings on the receiver and the substrings are producing at 1.25 volts or 420 mV/cell. This is the fully illuminated peak power point. As the southern most substring is shaded, its current limiting forces the substring voltages to increase in order to maintain peak output of the entire receiver. Figures 6-31 through 6-34 show the I-V characteristics for 0°, 17°, 18°, and 20°. At 0°, some of the regular slope error patterns bring diode turn ons (the small discontinuity in the classic I-V curve form) into the peak power point region, but don't significantly affect the performance. By 17° incidence angle (figure 6-32), these regular slope errors are smeared out in the image and the trough end effects are dominating. The diode from the southern most substring on the West face is the prominent feature shown between 109 and 110 on the I-V curve. Point 109 with the diode off is still the peak power but by less than 0.1 percent. Point 110, with the diode turned on is almost as attractive to a peak power tracker. By 18° incidence angle however (figure 6-33), the diode has definitely turned on as point 111 is now a significantly lower power than point 112. In addition, the series string voltage has dropped from 16.8V to 15.1V. This accounts for the 0.75V for diode turn on and the 0.75V of cell voltage in the southwestern most substring. The rise in the operating voltage in the other substrings from 1.25V at 0° incidence to 1.45V at 18° incidence accomodates the lowered output of the southern substring before turn on and the diode loss after turn on. The substring voltage continues to rise with increasing incident angle as the east face southern substring current limits. Figure 6-34 shows the diode effect of the second diode as it current

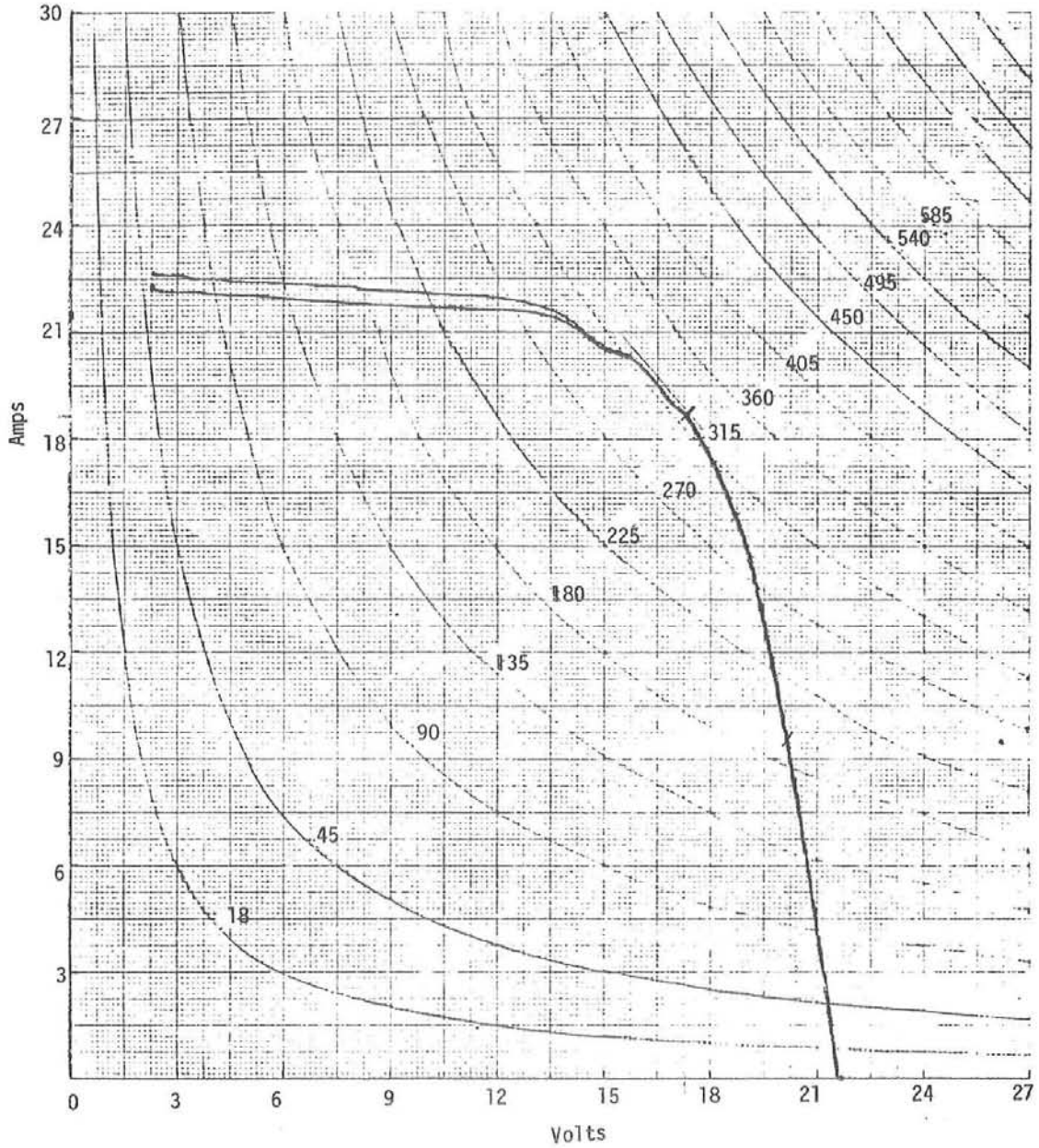

Figure 6-31. I-V Curve for 0° Incident Angle

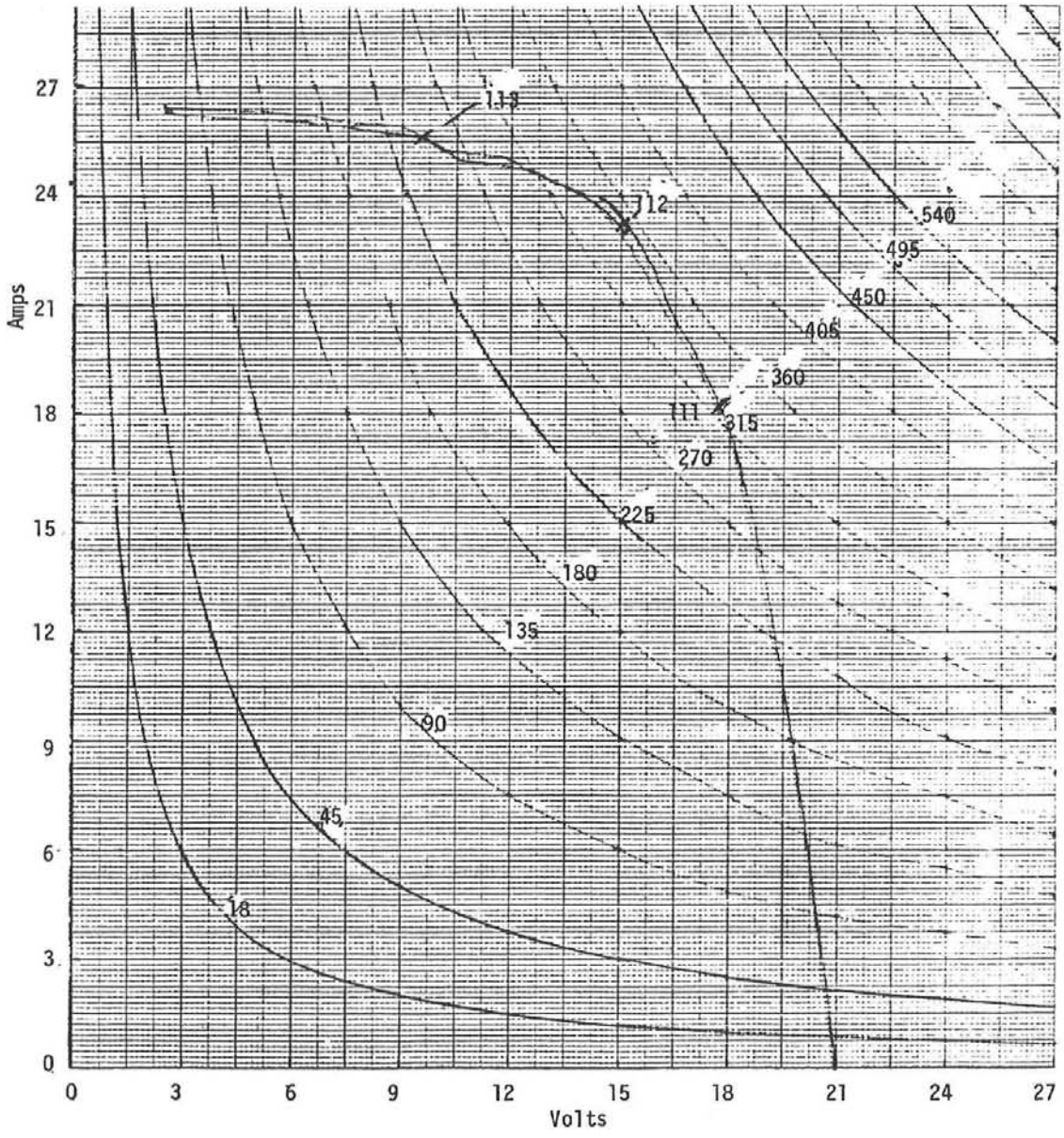

Figure 6-32. I-V Curve for 17° Incident Angle

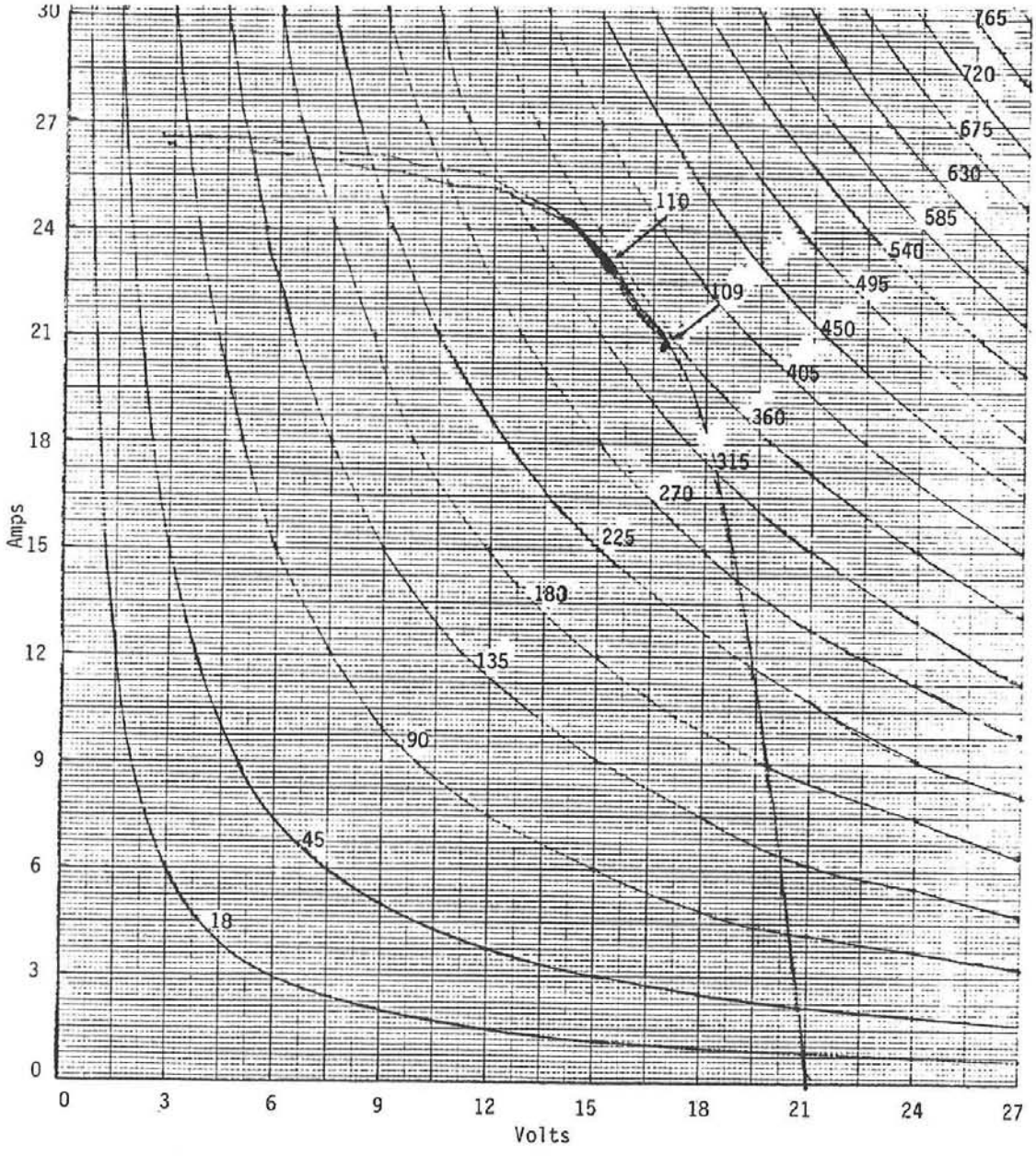

Figure 6-33. I-V Curve for 18° Incident Angle

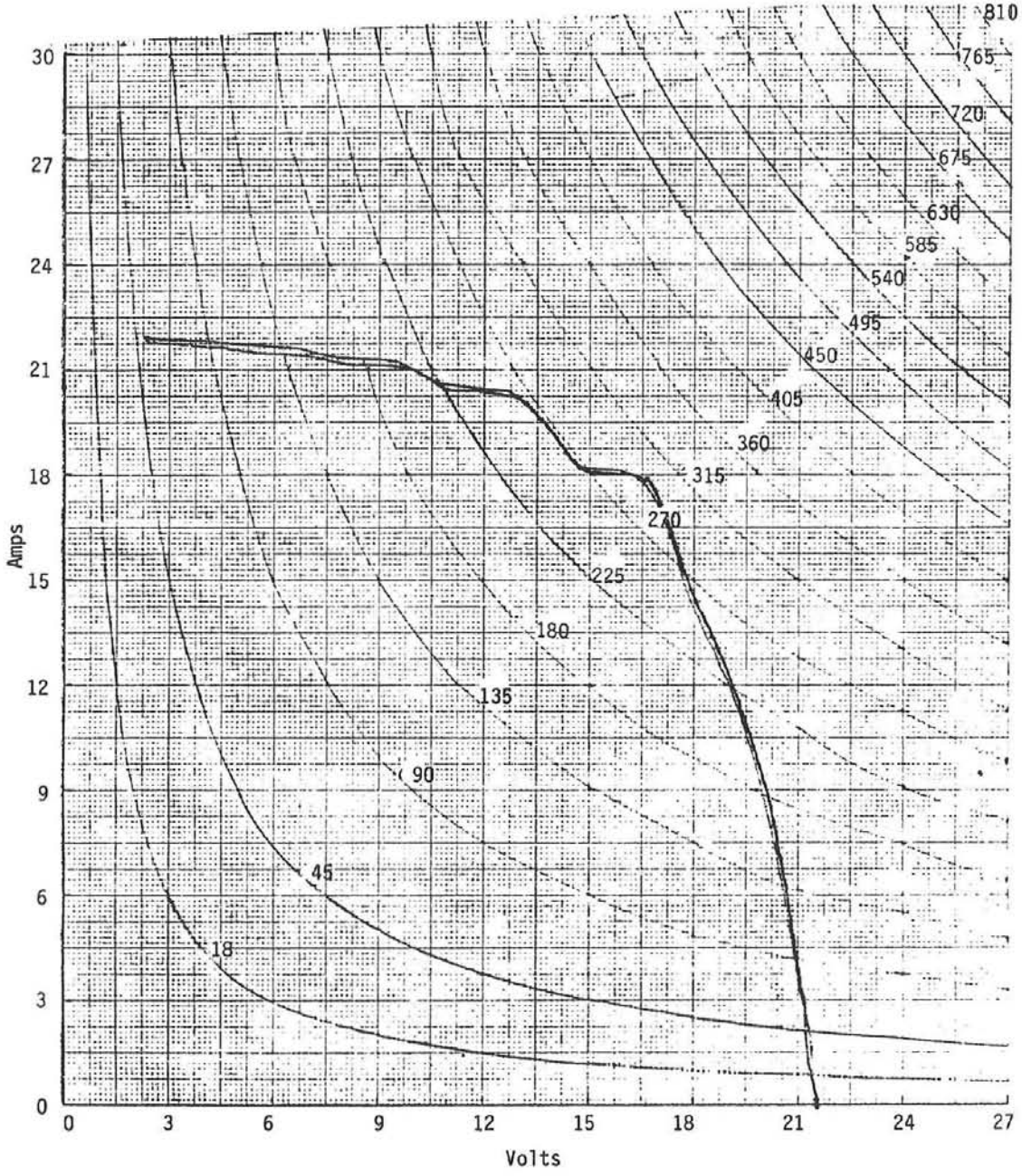

Figure 6-34. I-V Curve for 20° Incident Angle

limits the string. This second diode has a more significant effect due to the increased voltage of the illuminated substrings. The illuminated sections are well off peak power in order to produce the required series string voltage. When the second diode turns on the voltage impact on the string is a total of 4.0V or 133 mV/cell in the remaining 30 cells of the series. The resultant 550 mV/cell is close to the open circuit value of 583 mV and hence the substring must be truly dark for it to limit the series string enough to justify the diode turn on. Once two diodes within a series string are on, there cannot be any further turn-on of diodes as the required cell voltage in the illuminated substrings is greater than Voc.

This discussion of the effects is simplified as it does not consider the possibility of operating the other two illuminated series strings at a lower voltage than peak power. A brief inspection of this phenomenon will show that the two diode limit and the voltages are valid. This is due to the high fill factor of the cells. For the illuminated series string to move significantly from peak power voltage would cause a corresponding loss of power at a near unity rate. Since the shaded string is already current limited as well as voltage limited, the relatively low increase in power from that shaded string does not justify the loss of power from the illuminated strings.

Figures 6-29 and 6-30 show a further interesting point. The first two diodies to turn-off are the only diodes which turn-off. Figures 6-35 and 6-36 show the diode turn-on profiles for a reflector which has another reflector to the south to contribute irradiance. The first two diodes to turn on eventually are illuminated at higher incidence angles from the next southern trough. The next northern diode on the east face turns on

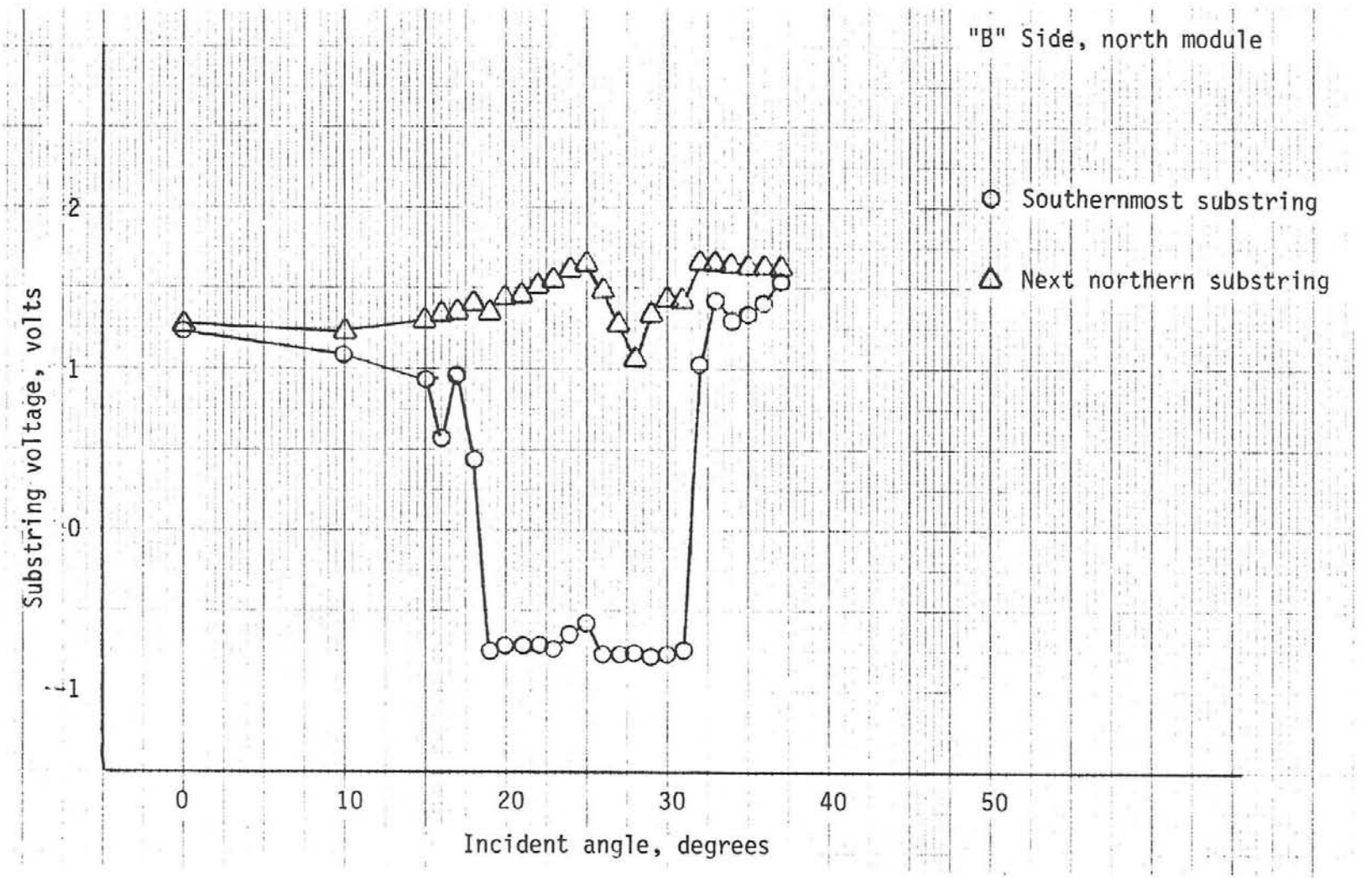

Figure 6-35. Diode Turn On Study "A" Side, North Module.

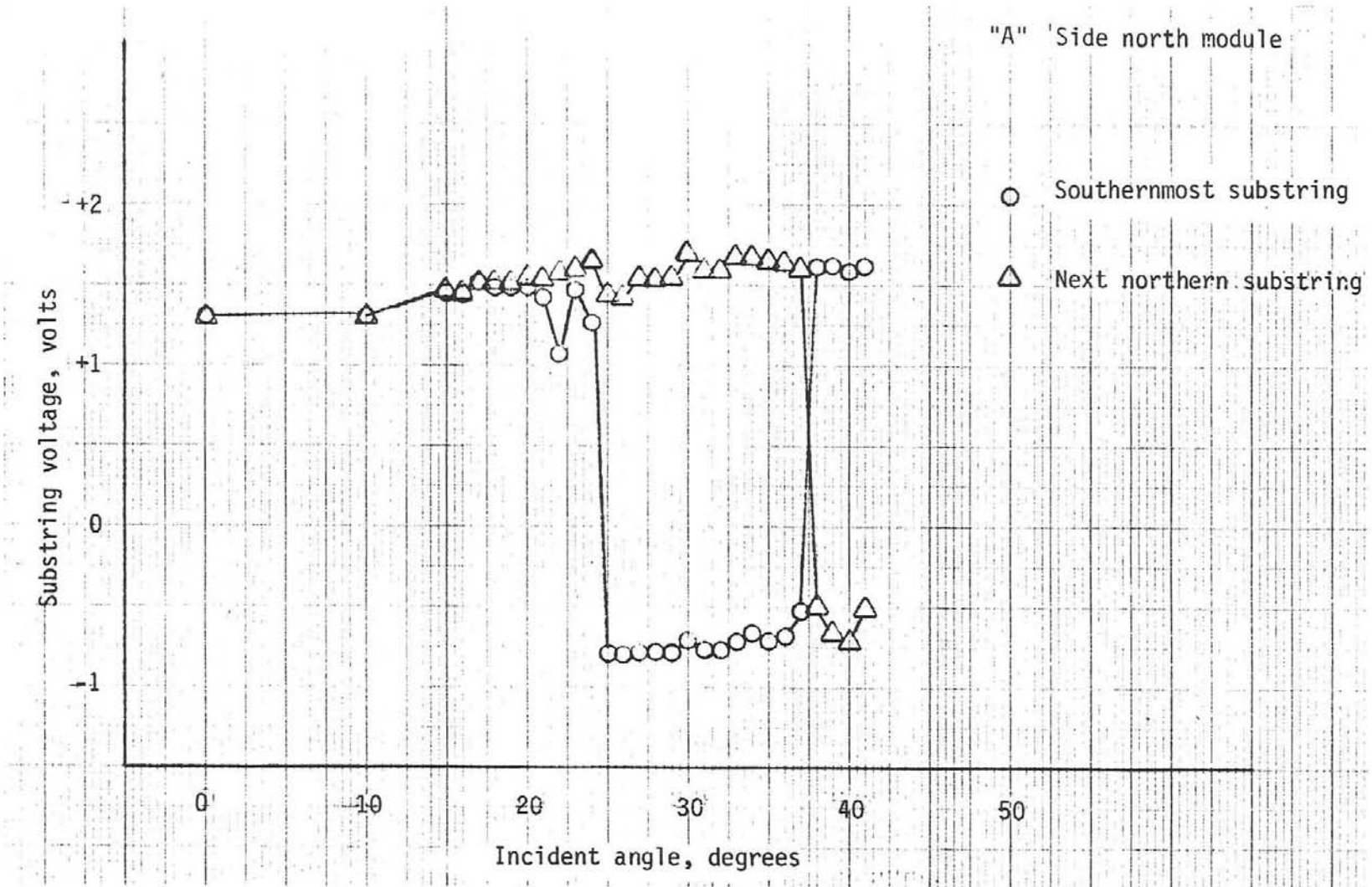

Figure 6-36. Diode Turn On Study "B" Side North Module

as its partner turns off, but the west face does not see a similar effect. Since this does not occur until approximately 38°, the absolute illumination on the cells is significantly reduced. Either the lower string output can not drive the second diode turn on or the image is so blurred that none of the substring is sufficiently current limiting the output. This effect is not totally understood, but the result in terms of the effect of diode turn on is the same in either case.

The initial diode turn on and the second diode turn on demonstrate good conformance in the two cases. The initial diode turns on at 18° and the second diode at 23°. The effect of the first diode is to drop the output by 7 percent and the effect of the second diode is a further 15 percent of the receiver output. This is not of course a square wave function on the output of the receiver however the diode can only turn on if it improves the output and its is the current limiting of the bypassed cells which causes the degredation in performance. The curve in figure 6-37 is the assessment of the electrical limitation function E (β) as determined by our analysis for large system applications where most reflectors have adjacent reflective surfaces.

The curve is generated by computer smoothing of the IV curve data generated on the single cell module tests. The effect on entire string output is included.

6.6.4 Environmental Testing

Several different environmental tests were performed at Sandia and at Acurex. The test specimens were the short sections listed in section 6.4.4. Three different cell manufacturers products were represented. The different cell modules were all built up using identical encapsulation techniques and submitted to standard test procedures.

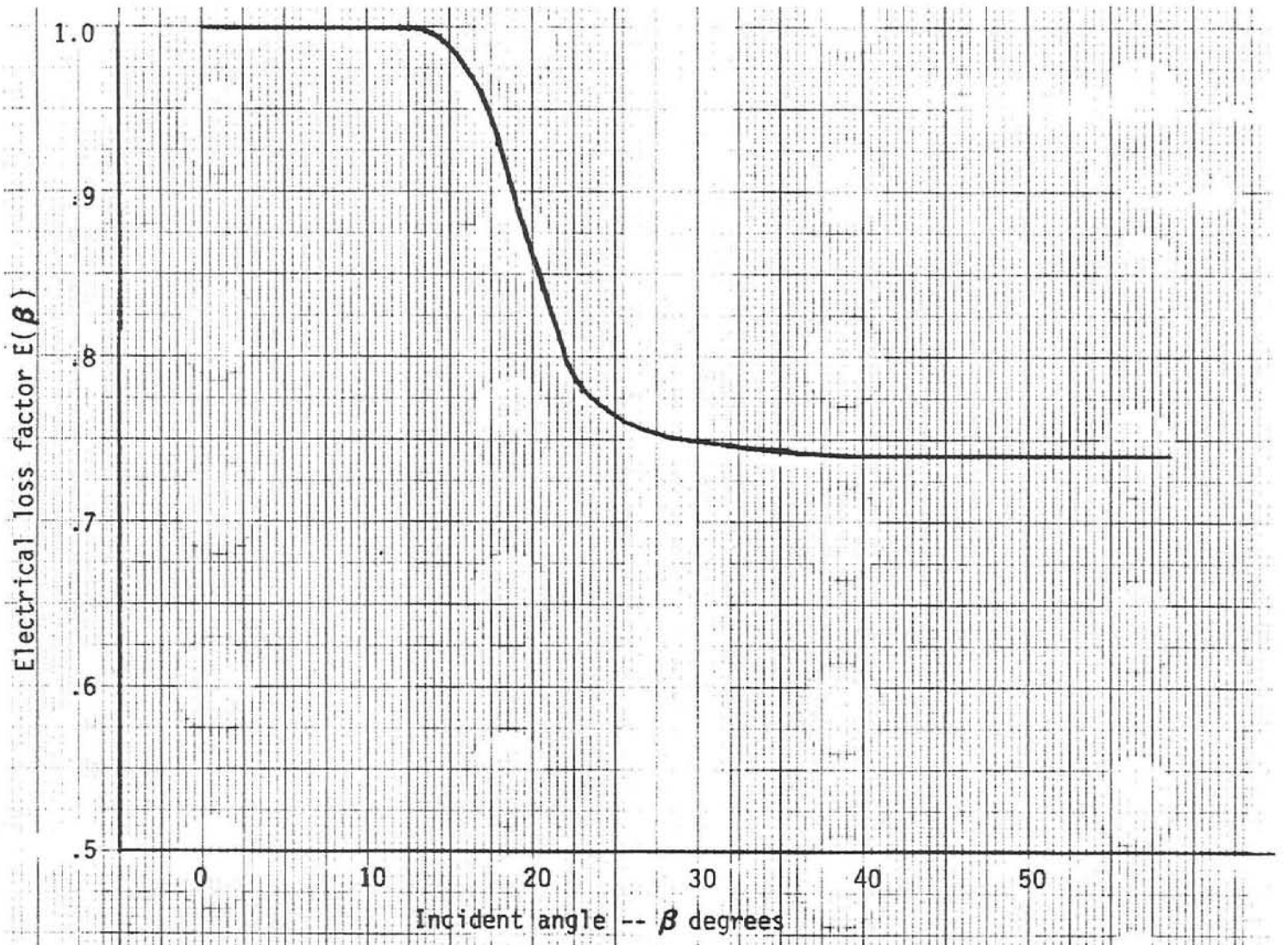

Figure 6-37. Electrical Loss Factor

The short sections were evaluated using their one-sun performance as an indication of condition. Upon receipt at Sandia, the samples were given a high potential test at 1,750 VDC. Any leakage over 50μA was considered a failure. In general, this test did not cause any module to fail. On two of the nine modules some rework was required in order to pass the initial test. No degradation beyond that point was observed. The short sections were then placed in a columator assembly on the Motorola two-axis tracker in the Sandia Photovoltaic test facility. The one sun performance of each face of each sample was carefully evaluated. This value is the reference against which each sample was subsequently rated.

The samples under went testing in three different exposure chambers at Sandia:

- UV exposure
- Thermal cycling
- Freeze thaw cycling

These tests and results are discussed briefly in the following paragraphs.

6.6.4.1 UV Exposure

The conditions of this test chamber are not completely understood and it appears that they are unreasonably harsh. The intensity of very short wavelength radiation being too high. The Applied Solar Energy Corporation modules' test sample was exposed in this chamber for 4 weeks without degradation. Due to other problems at that same interval, however, this chamber was deemed inappropriate and its use was discontinued.

6.6.4.2 Thermal Cycling

The thermal cycling or thermal shock test chamber puts the sample through 12 cycles/day of $-6^{o}C$ to $+120^{o}C$ in a dry atmosphere. The test

duration is 4 weeks simulating an extreme environment for 1 year. One sample from each cell manufacturer passed this test. They all passed without degradation except the first Spire Corporation module. No primer for the EVA was used on the cell, and that interface delaminated in thermal cycling. The delaminated sample is shown in figure 6-38. The subsequent modules supplied by Spire had the primer and did not show any degredation.

6.6.4.3 Freeze Thaw Cycling

The freeze thaw chamber submits the sample to three cycles per day of $-6^{o}C$ to $+50^{o}C$ in an atmosphere with a dew point of $5^{o}C$. Only ASEC samples were exposed to that chamber as it was determined to be a test of the encapsulant system and not the module. The sample demonstrated no degradation under test.

6.6.4.4 Full Receiver Tests

The full receivers manufactured by Acurex were also subjected to the environmental test of daily operation and of "off-axis beam destruction." These tests were conducted at Acurex and at Sandia. The most damaging testing occured at Sandia, apparently due to the higher incident radiation levels.

There were two failures exhibited by the receiver which have been corrected in subsequent versions of the receiver. The first was the escape of the apex gasket due to the differential thermal expansion of the receiver in its 10-foot length. The glass bevel was increased from 60° to 70° to better trap the gasket. In addition, the adhesive supplied with the gasket material is augmented with Proglaze RTV. This forms a more permanent adhesion to the extrusion.

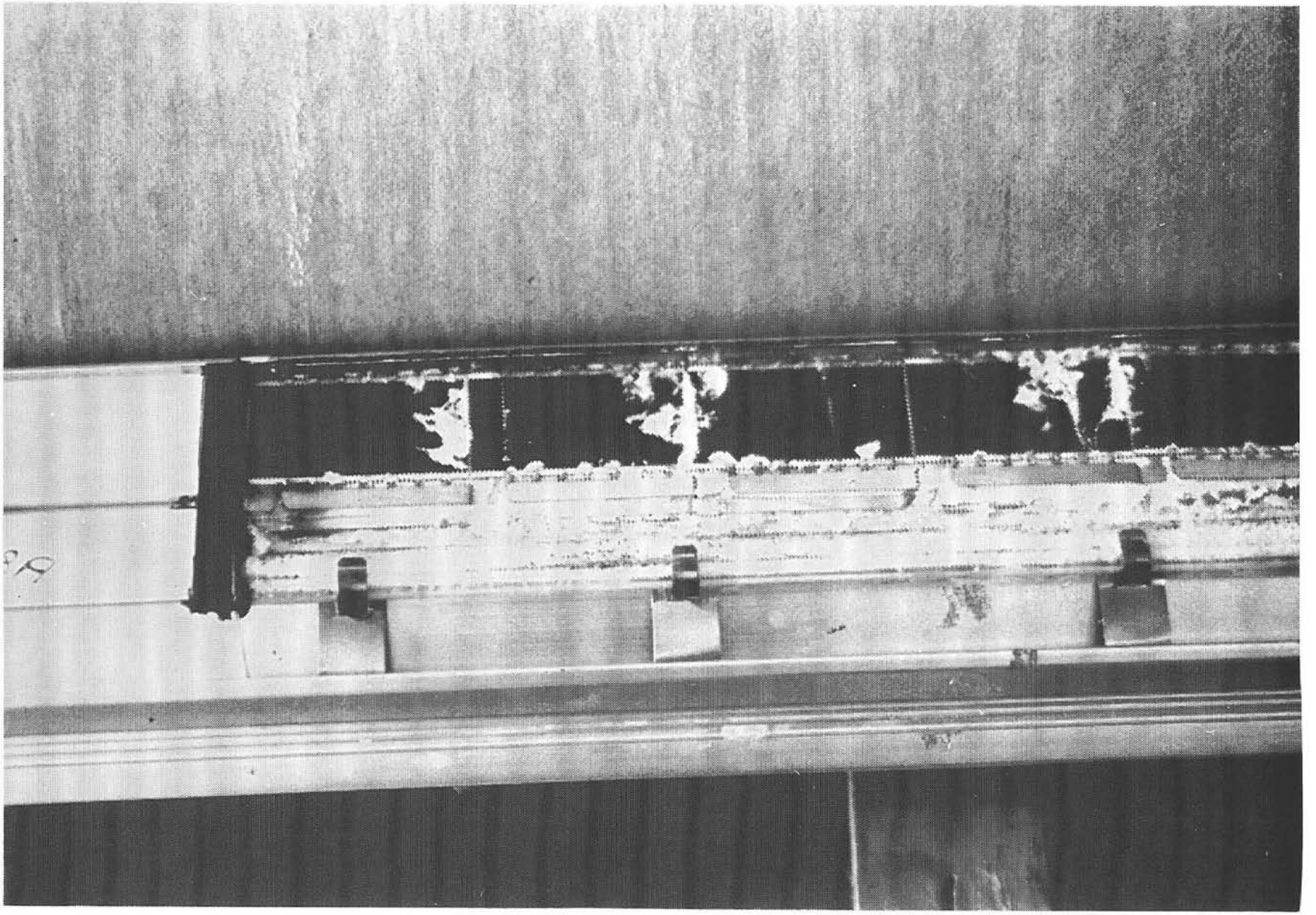

Figure 6-38. Spire Module Delaminated in Thermal Shock Cycling

The second failure mode was cracking in the cover glass material of the cell module. This was caused by thermal expansion stresses built up due to two factors. The diode, when on, was not thermally coupled to the extrusion. This caused spot heating in the glass. The back gasket was a bright orange color, which was a good absorber for the concentrated beam. When in the focus, this was also adequate to initiate thermal stress-related cracks in the glass.

The solutions to the glass cracking problems were:

1. Locate the diode farther from the glass and closer to the extrusion. In that way the diode is better cooled and the thermal stress is alieviated.
2. Modify the color of the back seal by covering it with white proglaze so it doesn't absorb the sunlight.
3. Use thermally tempered glass in the module to allow higher stress levels before crack initiation.

These three solutions have been employed in the final three modules for testing and in all subsequent receiver manufacture. The problem of the cover glass cracking is basically eliminated by these changes.

6.6.5 Apex Angle Testing

The apex angle testing was intended to confirm the computer analysis of optimum receiver configuration. The effective apex angle of the Vee type receiver is simulated by rotating the receiver about its virtual apex and reading only the appropriate half of the receiver performance. The computer analysis predicted that the optimum performance would be found at 34^{0} between the faces of the receiver. This is supported by the results shown in figure 6-39. The curves represent the performance of the half of the trough, for which gravity helps hold the

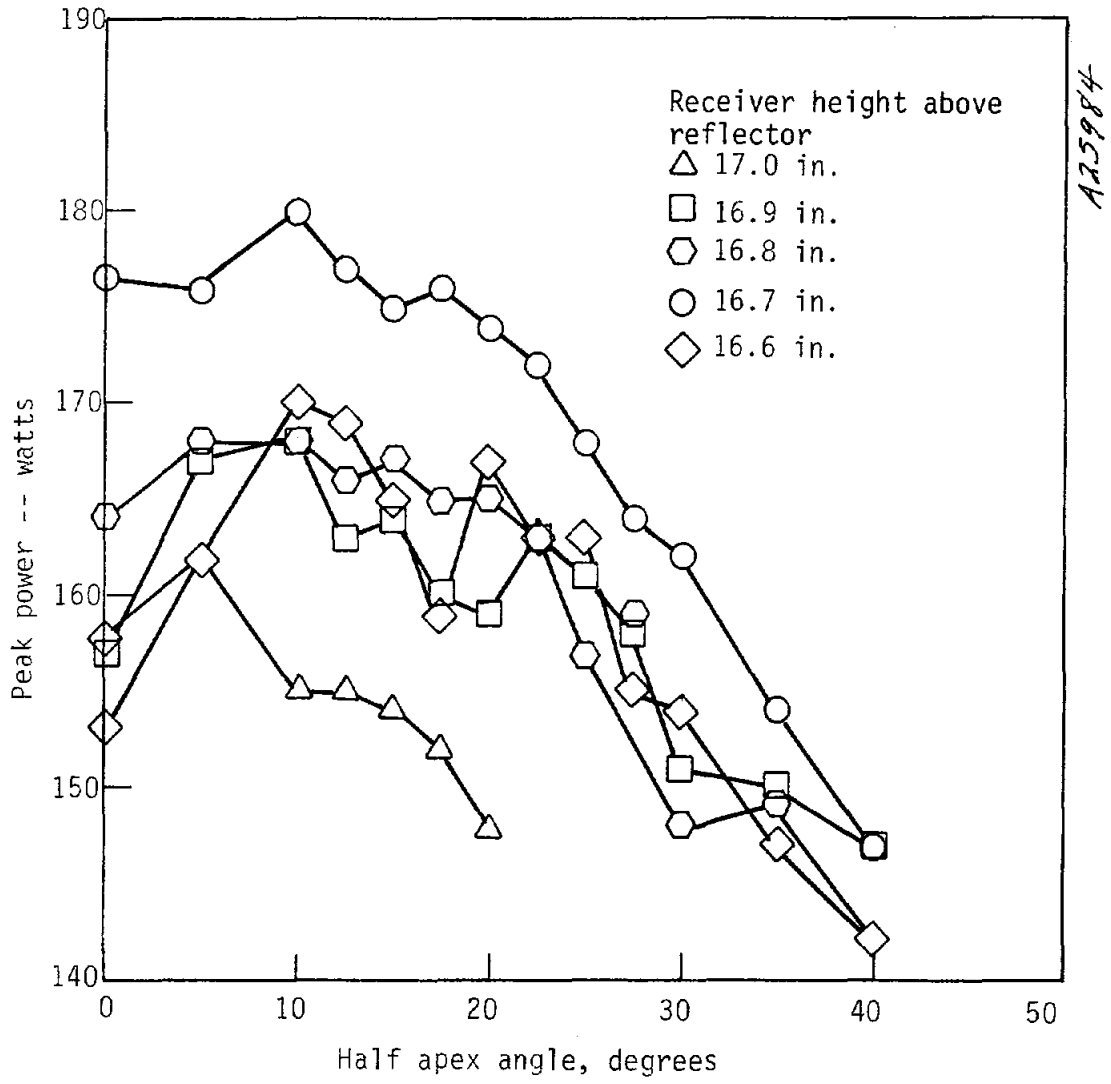

Figure 6-39. Lower Trough Half Apex Angle Optimizaton

sheet in place (the lower half of the parabola). This is the east half of the trough before noon and the west half of the trough after noon. The optimum for most receiver heights appears to be 10 to 17° apex half angle, which corresponds well with the theoretical 17°.

Figure 6-40 shows the apex angle optimization for the other half of the trough. The upper side is changed slightly, where gravity pulls the sheet out away from the rib and the paraboloid. The optimum apex angle is now 30° to 35°. The degradation for the lower half angle is much more severe than that for 30° half angle on the lower half of the trough. Therefore, it would appear that the currently used 30° half angle is in fact optimal.

The other interesting factor is the absolute magnitude of the power values. All data in both figures 6-39 and 6-40 is normalized to 800 W/m^2 and $50^{o}C$ cell temperature. Both graphs are for the same face of the receiver and the same reflector surface. The upper "distorted" face provides about 10 percent better performance than the lower "correct" face. Currently, we do not have a method for distorting both reflectors at all times.

6.6.6 Miscellaneous Testing Activities

Several other testing activities for specific areas of interest were undertaken during the course of this program and are worth reporting.

6.6.6.1 Voltage Isolation Media

During the initial evaluation of component media for use in the receiver encapsulation the critical element was deemed to be the voltage isolation media. The key parameters are durability, voltage breakdown, and thermal conductivity in the required thickness. Several different materials were investigated and a few were determined to be practical:

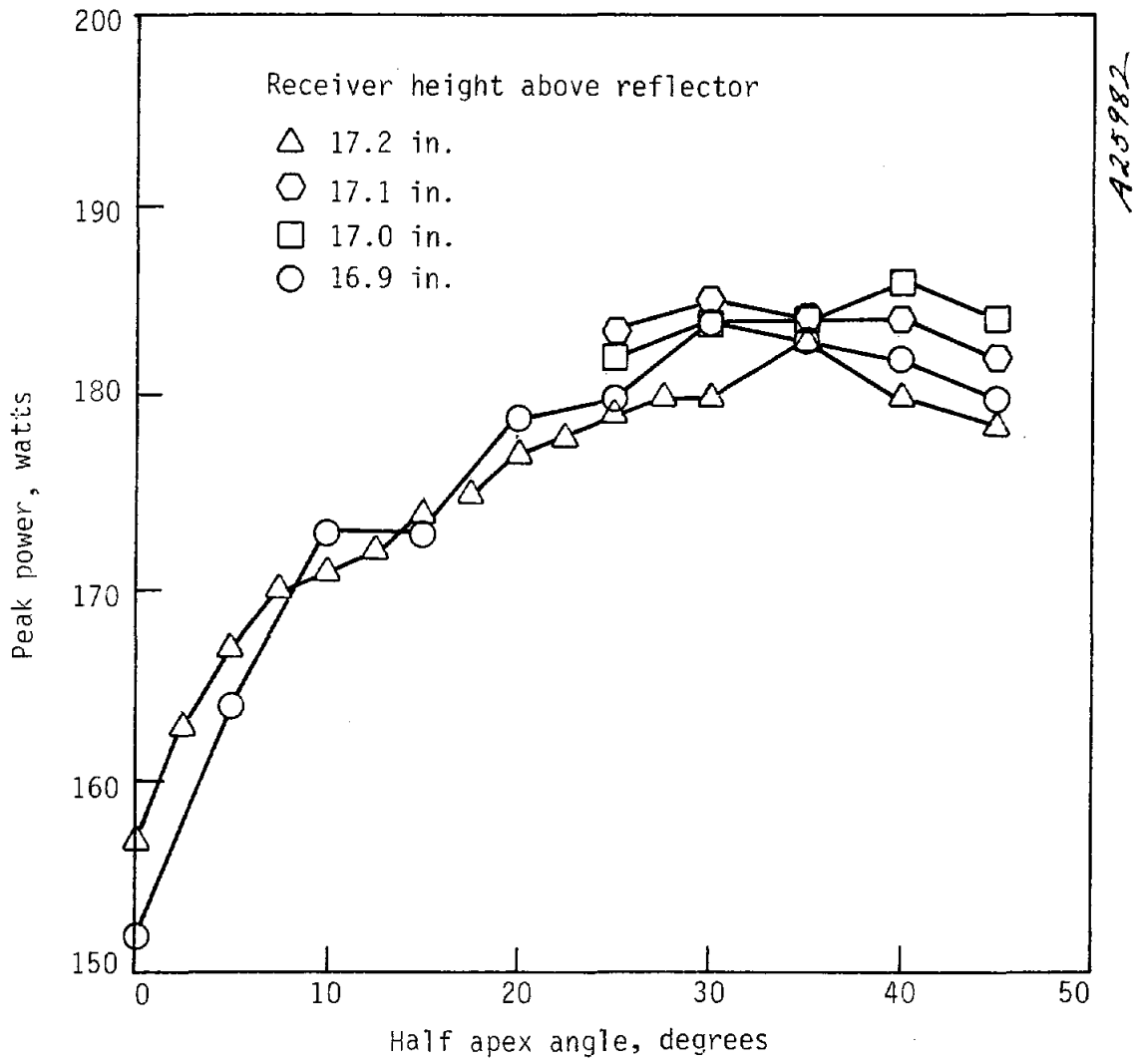

Figure 6-40. Upper Trough Half Apex Angle Optimizaton

- Plasma sprayed alumina
  - minimum thickness of 0.010 in. due to poor tolerances in application ($\pm$0.004 in.)
- Kapton tape
  - Total thickness 0.0016 in.
- Teflon tape
  - Total thickness 0.0024 in.
- Polyester type
  - Total thickness 0.0056 in.

The durability of the plasma sprayed alumina is better during the assembly stages, but its long term stability is in doubt. Thermal cycling may cause minute cracks which are voltage leakage paths. The tapes are fragile and easily damaged in assembly, but the long term stability is very good.

The theoretical analysis of thermal conductivity couldn't separate the better material. We constructed 18 sample sections on nine short extrusion lengths representing all of the possible media. These were shipped to Sandia, coupled together, and placed in the position of the receiver in an Acurex trough. Each section was instrumented with thermocouples to determine the thermal performance of the samples. The teflon tape was chosen because it turned out to have the superior capability in thermal conductivity and ease of application.

6.6.6.2 Glass Reflector Testing

The value of an increased reflective of glass, 0.92 versus 0.82 (glass versus FEK-244) or 12 percent, must be traded off against the adverse impact of the nonreflective joints between sheets. Figure 6-41 shows the relative performance of FEK and glass troughs. The FEK trough

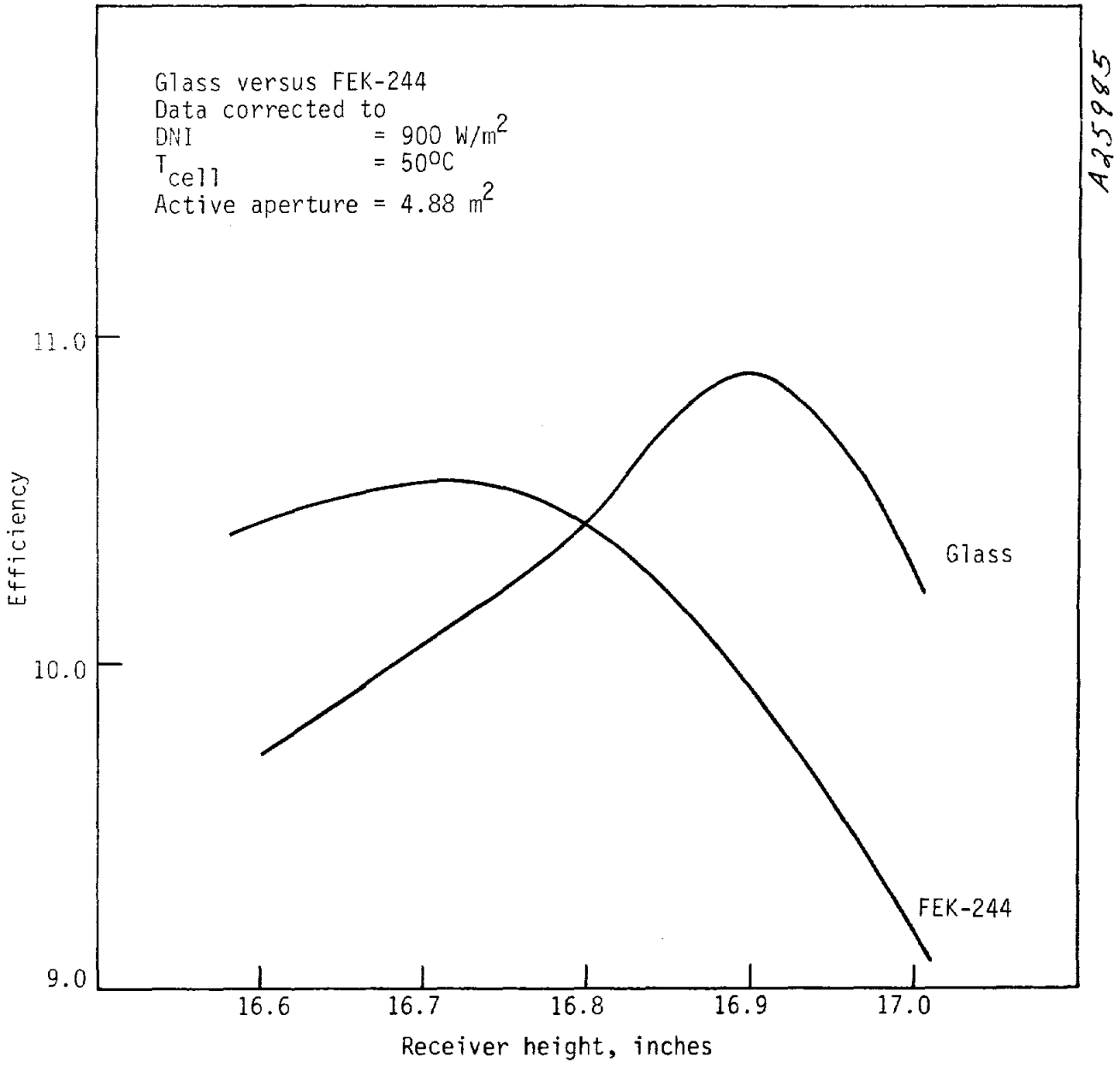

Figure 6-41. FEK Versus Glass Performance

has a shorter focal length and lower reflectivity. The 3.2 percent increase in output for glass would tend to indicate that the reduction in output due to intersheet gaps is more significant than the increased reflectivity of the mirror.

Figure 6-42 shows the results of testing with strips of FEK covering the gaps between sheets. The indicated 1.2 percent performance increase probably indicates that the FEK did not adequately fill in the dark areas in the image. This is probably due to the high longitudinal slope error in the image, as there is a 0.060 depression into which the FEK can collapse. In addition, there is typically a poor alignment between adjacent sheets — with as much as 0.020 in. to 0.030 in. alignment error. This is fairly small as a manufacturing tolerance on a 40-in. sheet, but is large on a reflective surface.

The focus was mapped using Acurex's flux mapping device to image the "dark" areas caused by the gaps. The three-dimensional maps in figures 6-43 through 6-50 show clearly these low-illumination areas. The detail maps of the gaps represent a 6 in. x 2.5 in. area and are truly proportioned. The maps of the whole side (figures 6-43 and 6-47) represent the 10 in. x 2.5 in. receiver face and are biased to exaggerate the gap areas. The gaps in the image are extremely noticeable in operation and show as definite discontinuities in the image.

6.7 CONCLUSIONS

The intent of most of the testing performed was to create a model of parabolic trough performance. The testing was designed to evaluate particular elements of the mathematical model which was presented as a trial solution. It was necessary to reduce the data into a family of

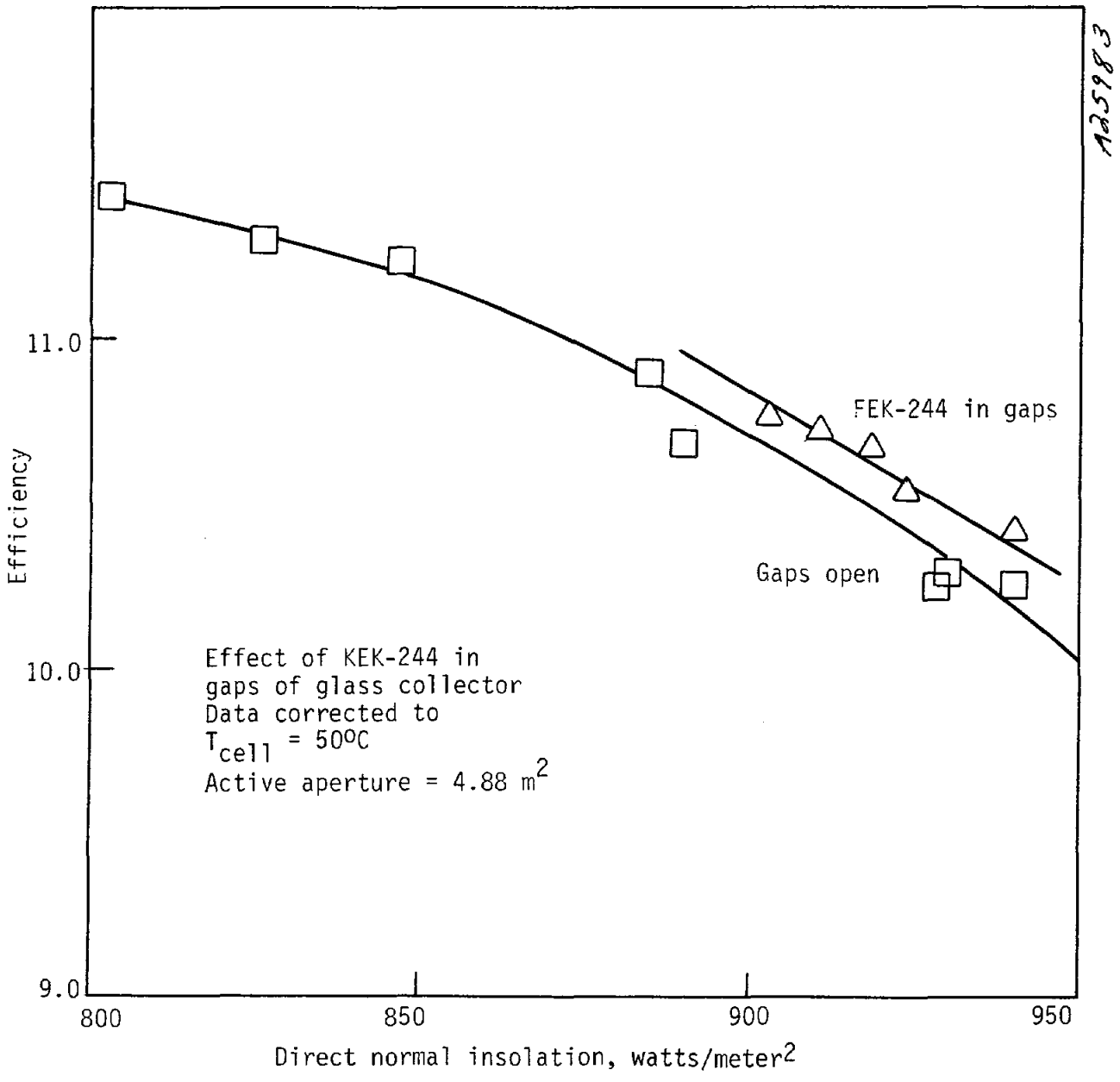

Figure 6-42. Gap Effect in Glass Reflector

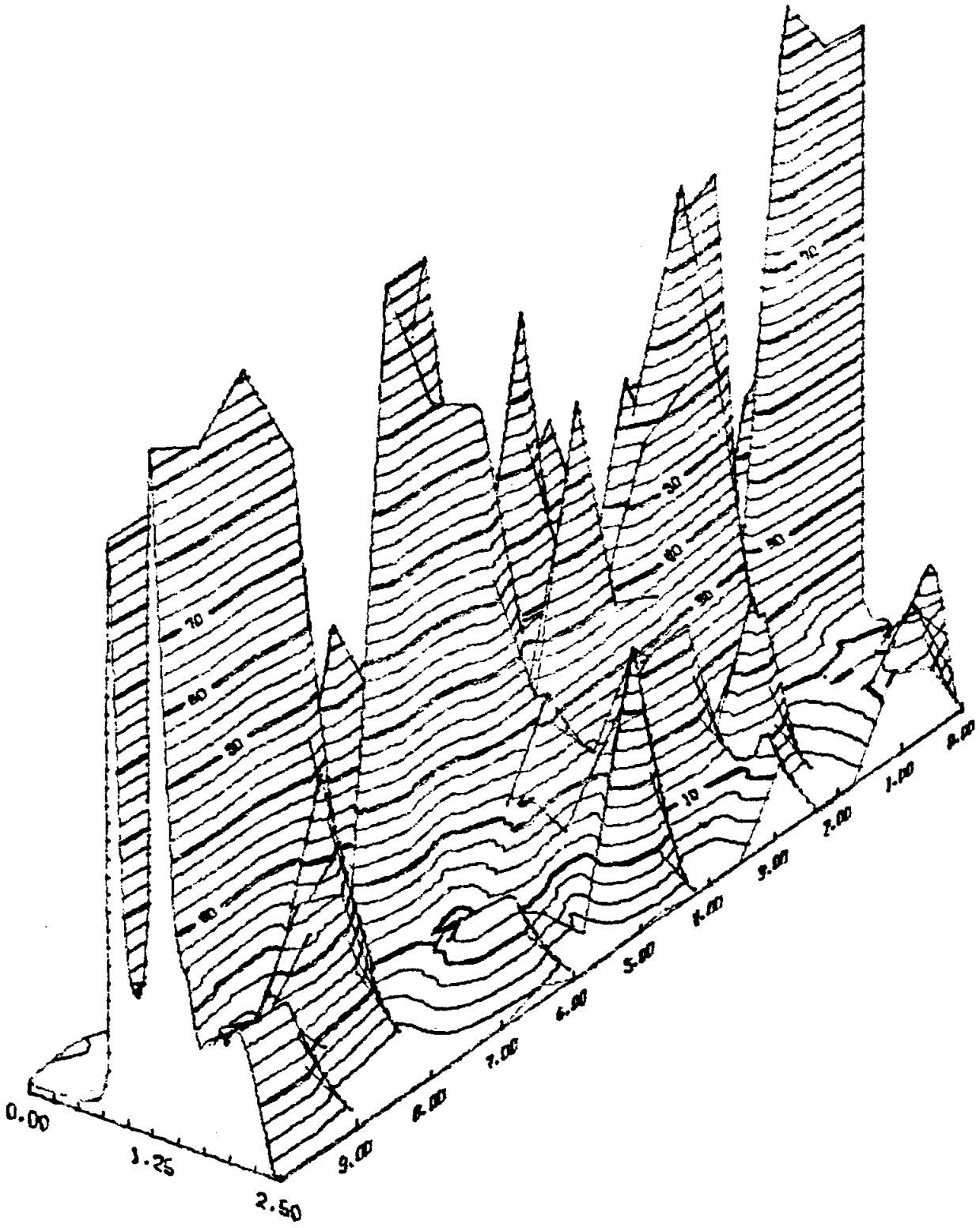

SOUTH SIDE

Figure 6-43. Flux Map -- South Face of Receiver Glass Trough

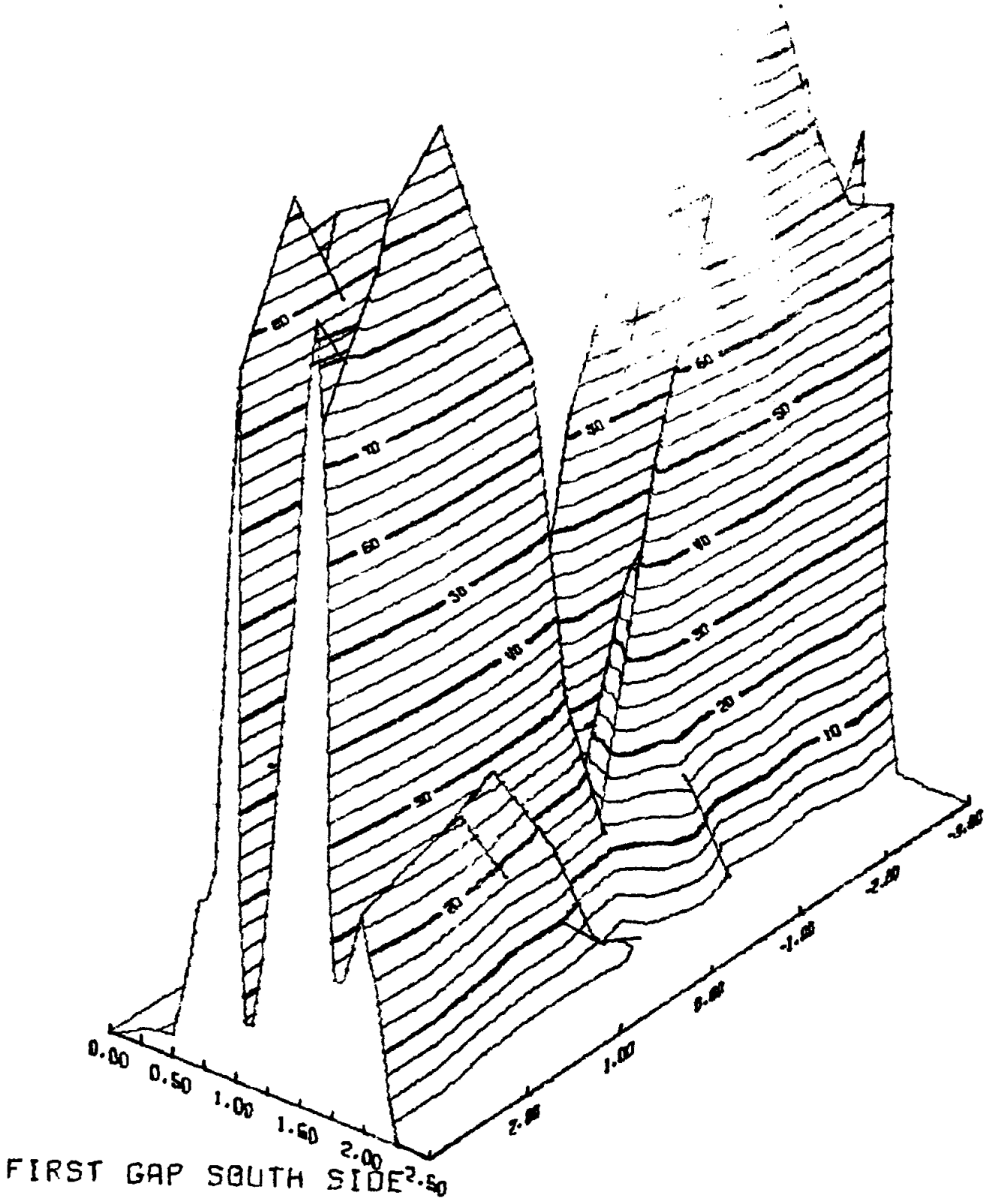

Figure 6-44. Flux Map — First Gap on South Face — Glass Trough

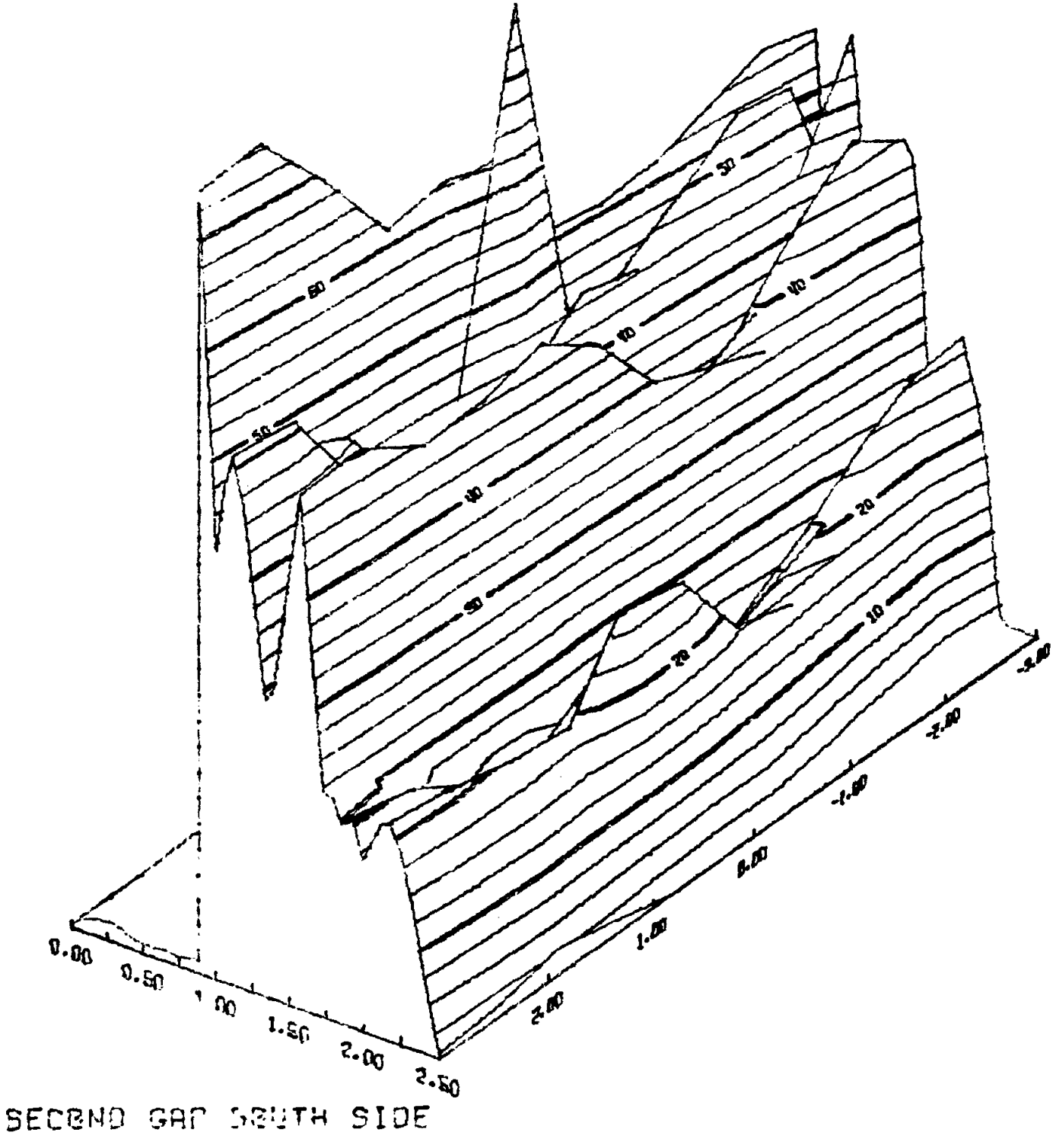

Figure 6-45. Flux Map -- Second Gap on South Face -- Glass Trough

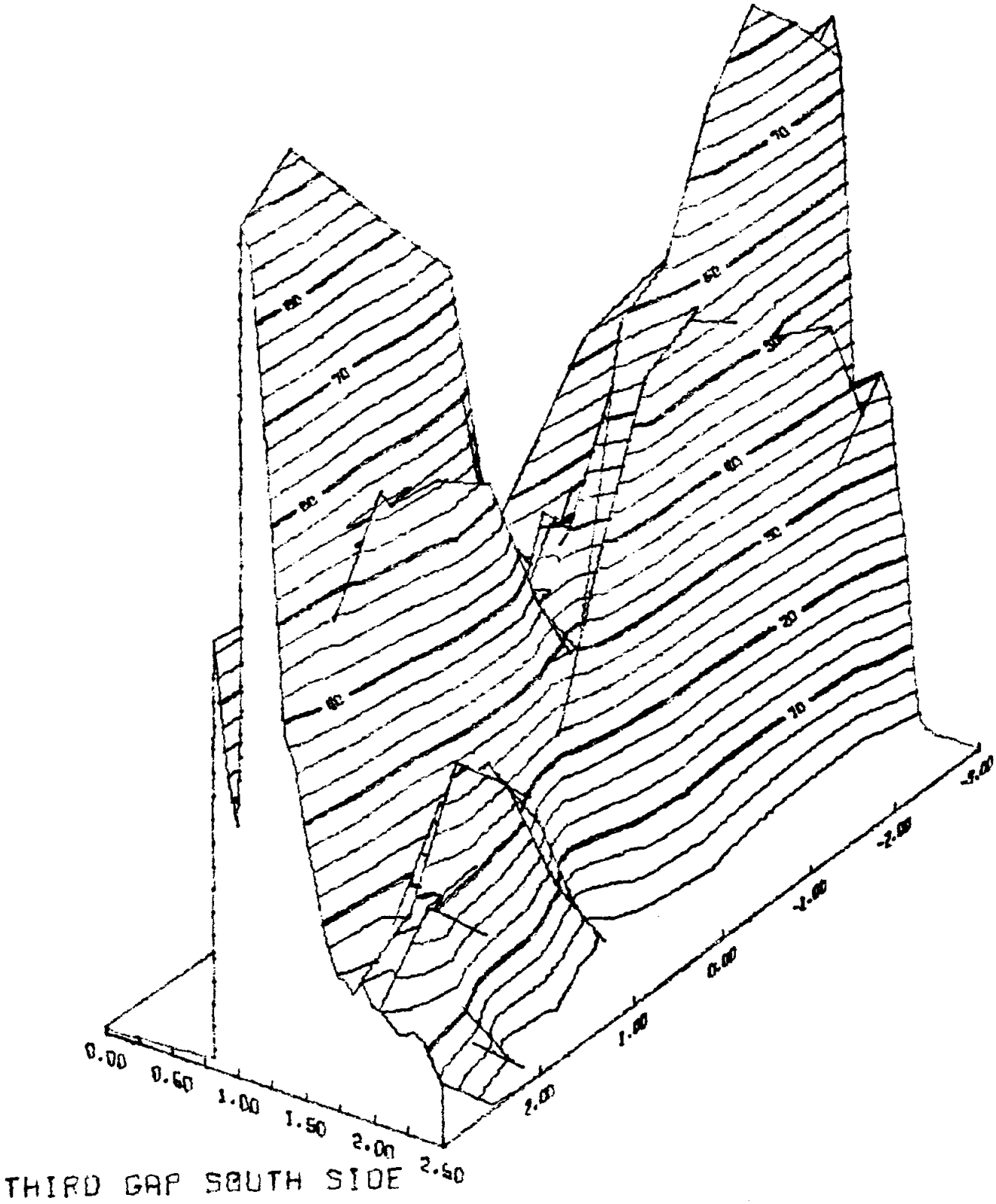

Figure 6-46. Flux Map — Third Gap on South Face — Glass Trough

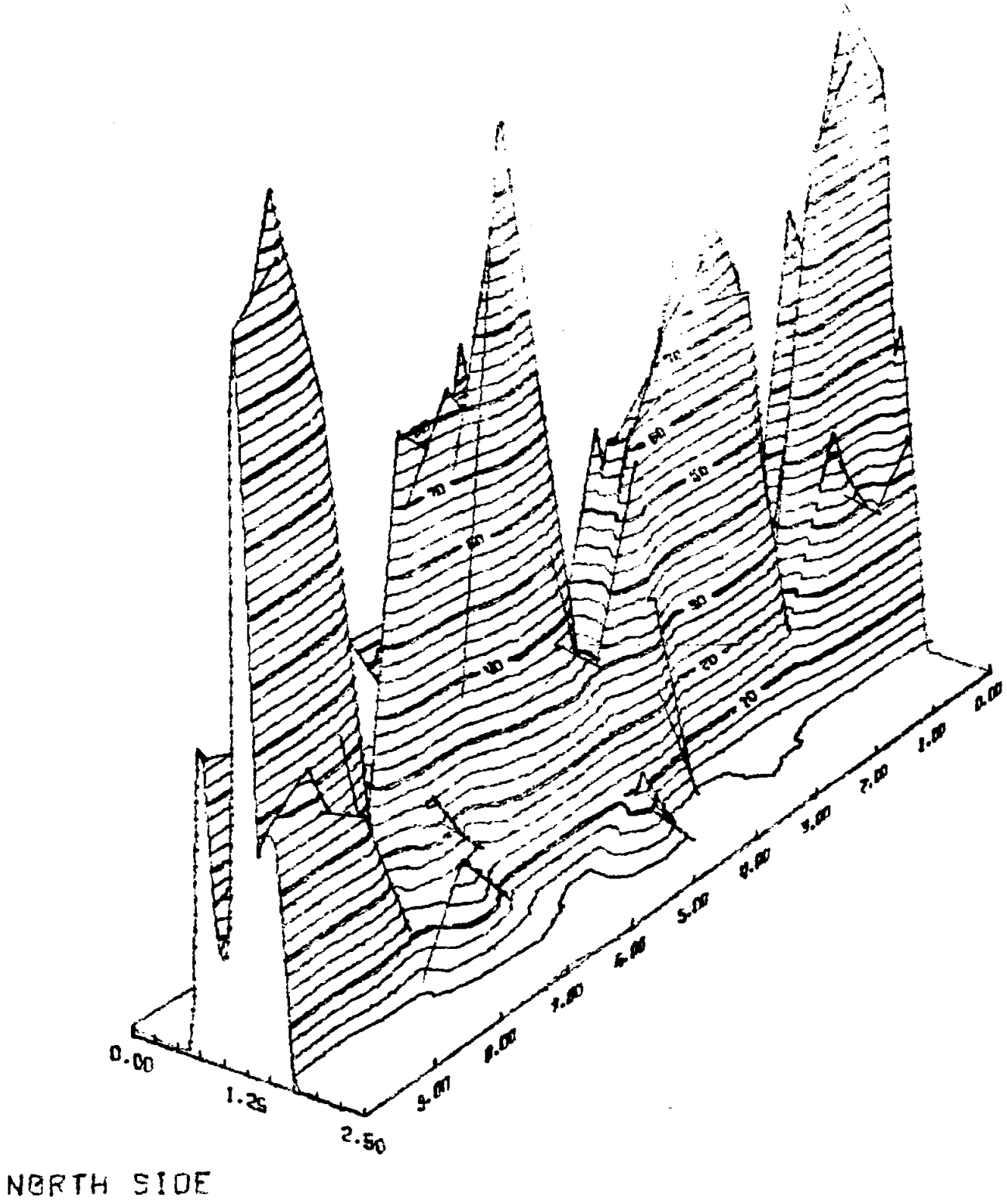

Figure 6-47. Flux Map — North Face of Receiver — Glass Trough

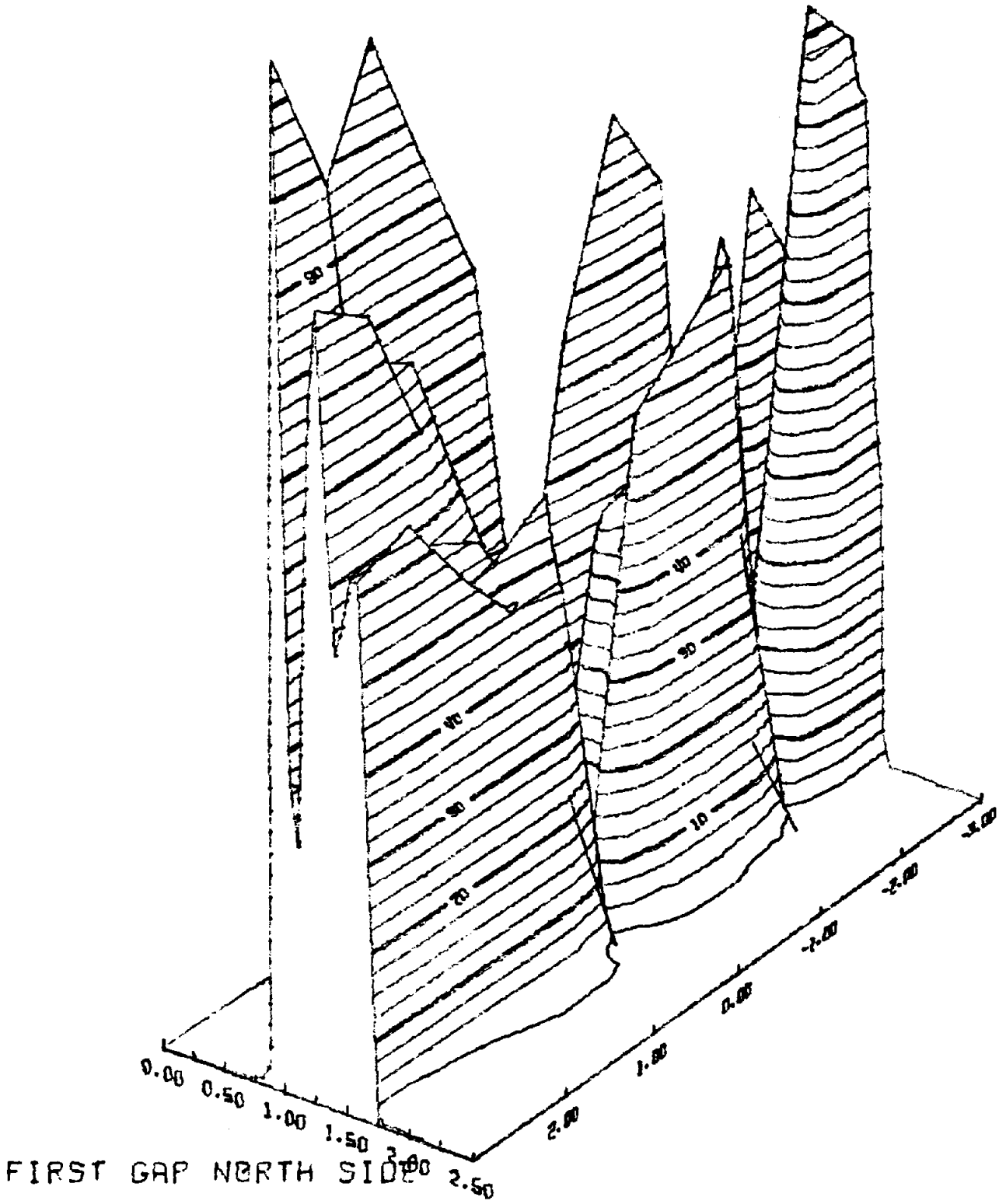

Figure 6-48. Flux Map — First Gap on North Face — Glass Trough

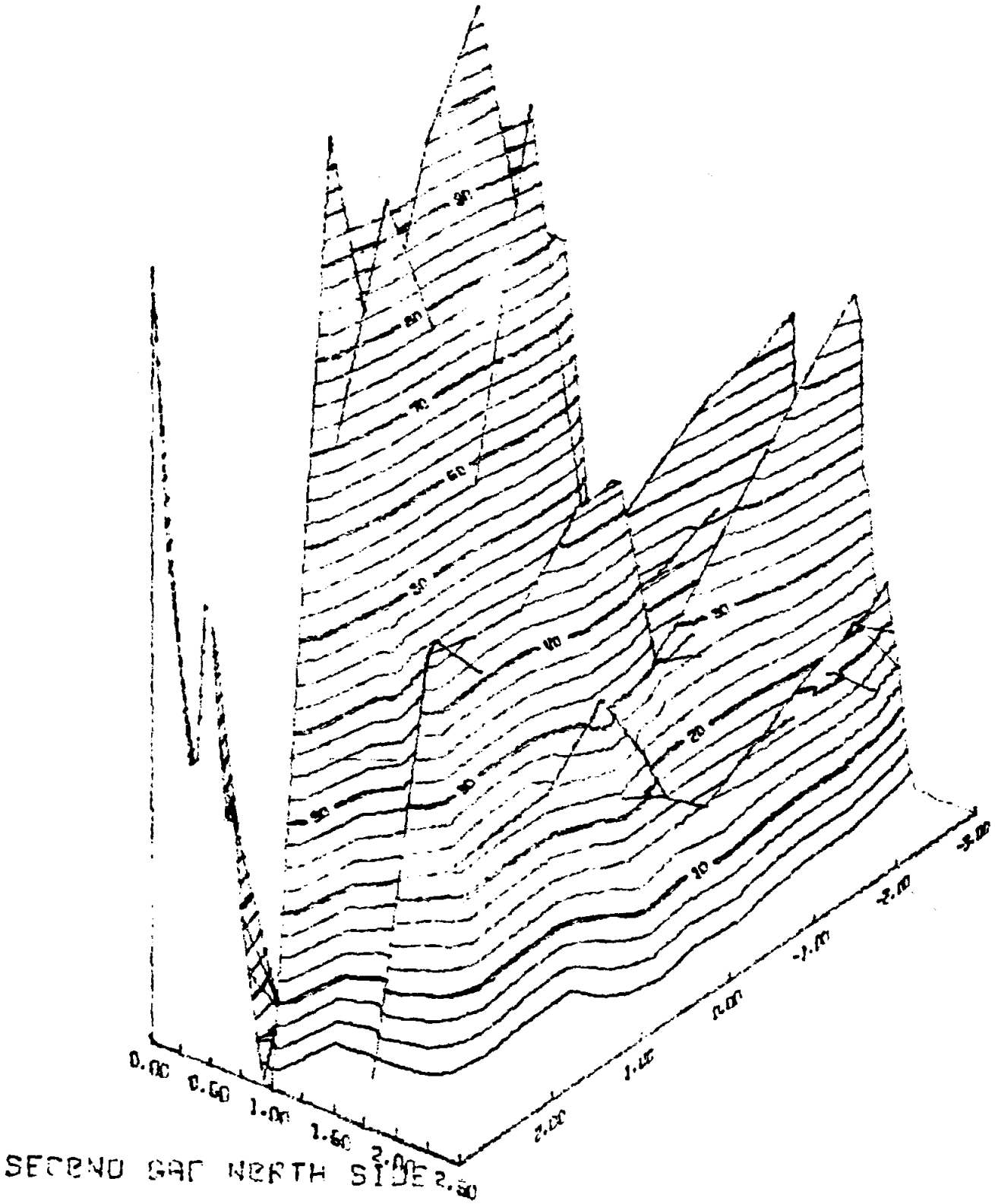

Figure 6-49. Flux Map — Second Gap on North Face — Glass Trough

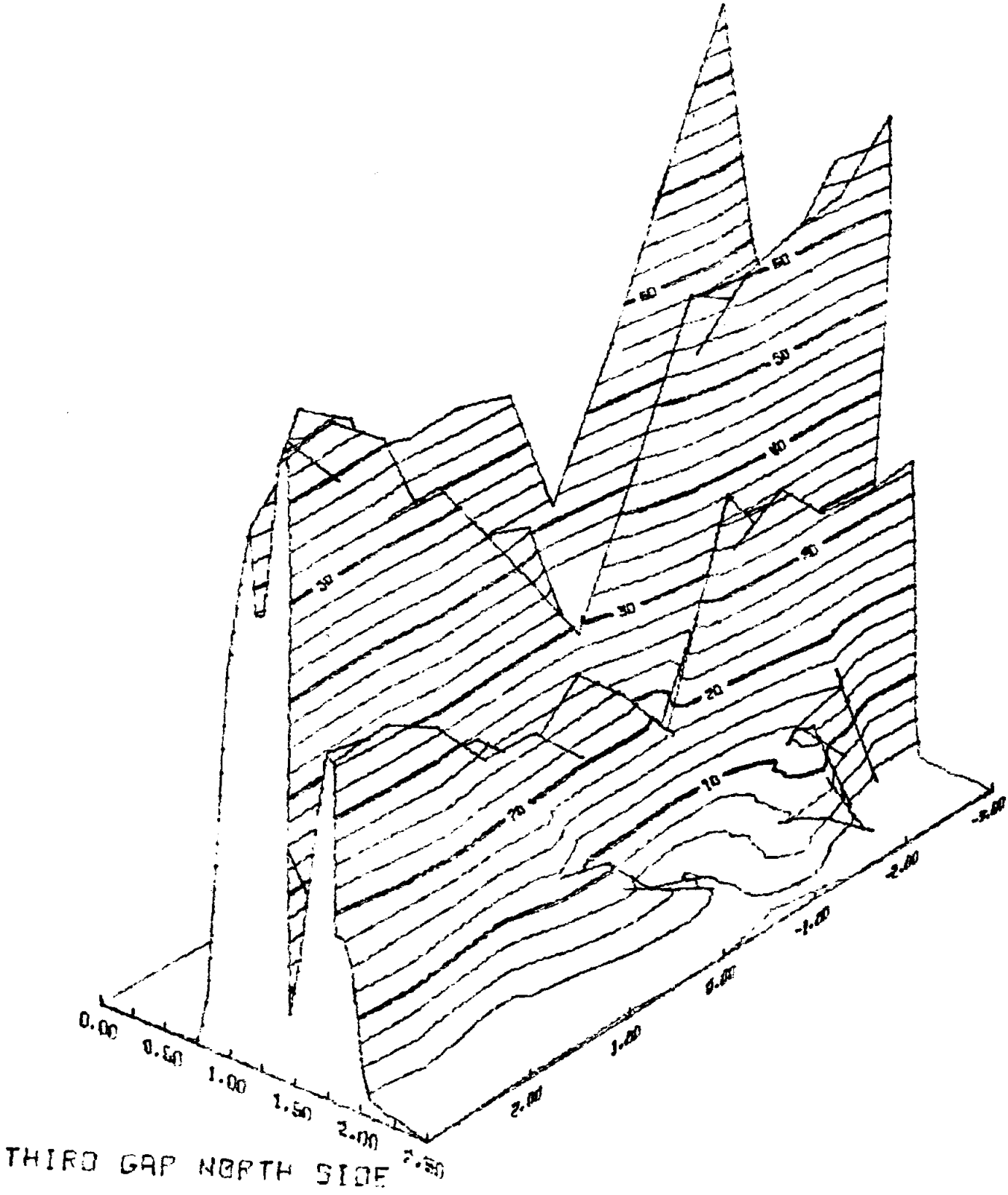

Figure 6-50. Flux Map — Third Gap on North Face — Glass Trough

curves which fit the format of the model. This effort is discussed in section 6.7.2.

In addition, another model was developed at Acurex which attempts to solve the problem of diode turn on analytically. Using constant factors for other elements of the reflector optics this code has been in use for about 2 years. We felt that some verification of that code was also required from the data gathered. The code is described in greater detail in section 6.7.1.

The two models must then be compared with actual data to evaluate their validity. This effort is discussed in section 6.6.3.

6.7.1 Analytical Model of the Parabolic Trough Performance

A model of the electrical output of the cells on the receiver has been formulated to simulate their performance under a variety of condtions. First, an illumination pattern along the receiver is computed geometrically. Using the solar radiation incident on each cell and the cell temperature, the voltages and currents are computed and summed corresponding to the actual circuit on the receiver to give the output electrical power. By activating the diodes around the least illuminated cells, the highest electrical output is determined for a given incident angle.

The receiver for each trough is made up of three parallel circuits, one each to the south, middle, and north of the collector module. Each circuit of 36 cells in series, 18 cells on each side of the receiver and a bypass diode around each group of three cells, as shown in figure 6-51. As the incident angle increases from zero, a reduction in the illumination will occur due to the end of the reflector at the end of the trough not suppling solar radiation to the end cells on the receiver. Therefore, for

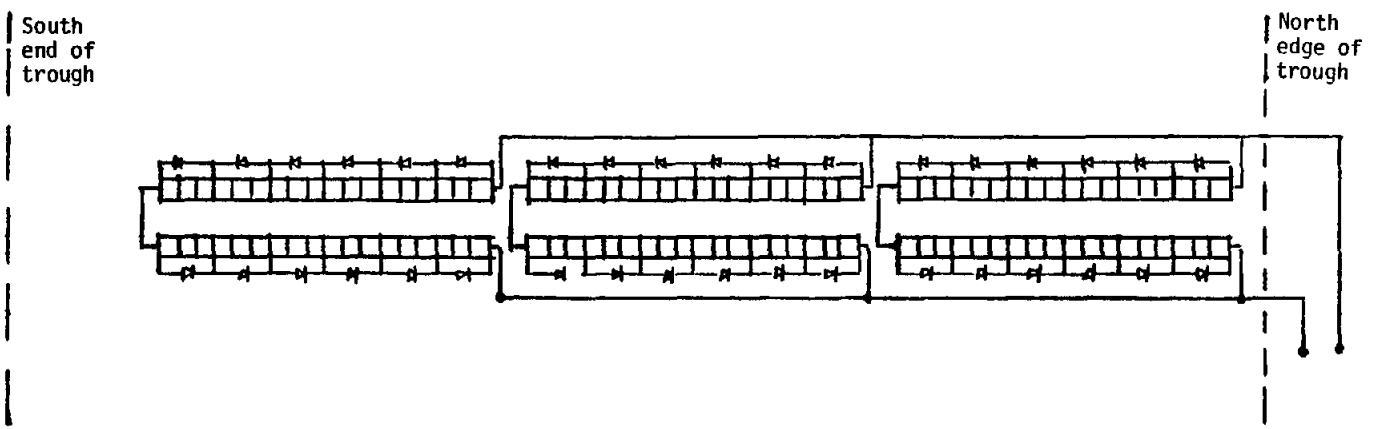

Figure 6-51. Schematic of Receiver Circuit

a given incident angle, the solar radiation incidient on the center of each cell on the receiver can be computed. This solar radiation along with the specified cell temperature can be used to compute the current and voltage for each cell using the method of Goldstein and Case to determine to I-V curve for each cell.[6-1]

The receiver performance is computed first for the partially shaded string. Since the least illuminated cell in the string will limit the current in the string, the current is taken as the smaller of (1) The current for the maximum power point for a fully illuminated cell and (2) the short-circuit current for the least illuminated cell. Using this current, the voltage rise for each cell in this string is computed and summed for the 18 cells on one side of the receiver. Since the electrical performance is assumed to be the same for both sides of the receiver, the voltage of the circuit is twice the summed voltage of the 18 cells. This voltage is assumed for the other two circuits in which the cells are fully illuminated and the current is computed from the known voltage. With the circuit voltage and currents known the output power is computed.

As a result of the reduced illumination on some cells this power may not be the maximum possible. Therefore, the calculation is repeated with the diode which contains the least illuminated cell turned on, i.e., the voltage for the diode and the three cells is -0.60 V. Using the short circuit current for the least illuminted cell which does not have the diode on or the current for the maximum power point for a fully illuminated cell (whichever is smaller), the voltages are summed as before and the output power is computed. Further diodes around partially illuminated cells are turned on with the output electrical power computed. This is repeated until the output power decreases as an additional diode

is turned on. The predicted output power is then taken as the maximum computed power. For the circuit configuration in figure 6-55, the maximum power typically is associated with either one diode or no diodes turned on and the data have verified this result.

6.7.2 Empirical Model of the PV Parabolic Trough

As mentioned earlier in section 6.1, the testing is designed to determine four elements of the modeling equation:

- $\gamma(\beta)$ -- The intercept factor as a function of incidence angle. That is, the fraction of light available at the receiver which is intercepted by the cell
- Fiu (β) -- The image uniformity factor describes the variability in the intercept factor along the receiver
- E (β) -- The electrical loss factor describes the effect of diode turn on in off-normal incidence, I^2R losses are not included and are considered insignificant
- η_{cell} (T_i, H_i) -- Cell efficiency as a function of cell temperature and direct normal insolation. This is actually cell module efficiency as it includes all effects of the encapsulation. η_{cell} is derived by solving for it in the known data.

The derivation of each of these functions is described briefly in the following paragraphs.

The intercept factor was measured during the Acurex flux maping device and interpreted as described in section 6.5.3. The image uniformity factor was measured in the same manner. The consultant equations which roughly fit the curves shown in figures 6-23 and 6-24 are equations 6-3 and 6-4.

$$\gamma(\beta) = .85873 + 1.40342 \times 10^{-3}\beta - 6.9840 \times 10^{-5}\beta^2 - 6.6139 \times 10^{-7}\beta^3 \qquad (6\text{-}3)$$

$$F_{iu}(\beta) = .869385 - 1.74214 \times 10^{-3}\beta + 2.74293 \times 10^{-4}\beta^2 - 7.589738^{-6}\beta^3 \qquad (6\text{-}4)$$

The electrical loss factor, $E(\beta)$ was determined using a specially instrumented module as described in section 6.4.4. The reduced data provided the curve of $E(\beta)$ shown in figure 6-37. The equation for that curve is shown in equation 6-5 below:

$$E(\beta) = .99470 + 9.2547\ N10^{-3}\beta - 1.1056 \times 10^{-3}\beta^2 + 1.75397 \times 10^{-5}\beta^3 \qquad (6\text{-}5)$$

The total efficiency was determined through tests in which only temperature or insolation was allowed to vary. Each cell manufacturer's product has its own performance, of course. These curves are described in equations 6-6 through 6-8 for ASEC, Solarex and Spire respectively.

ASEC

$$\eta_{cell}(T,Hi) = (1.4746794 - 4.9723322 \times 10^{-3}Hi + 6.314242 \times 10^{-6} Hi^2 - 2.6898532 \times 10^{-9}\ Hi^3)(1-.0048\ (T-50)) \qquad (6\text{-}6)$$

SOLAREX

$$\eta_{cell}(T,Hi) = (3.3360832 - 1.2767839 \times 10^{-3}\ Hi + 1.7166055 \times 10^{-5}\ Hi^2 - 7.6995882 \times 10^{-9}\ Hi^3)\ (1 - .0048(T-50)) \qquad (6\text{-}7)$$

SPIRE

$$\eta_{cell}\ (T,Hi) = (1.0619128 - 3.9751771 \times 10^{-3}\ Hi + 5.7649767 \times 10^{-6}Hi^2 - 2.7855229 \times 10^{-9}\ Hi^3)(1 - .0048\ (T-50)) \qquad (6\text{-}8)$$

The empirical model as described earlier in equation 6-8 is:

$$P_{ARR} = Hi\ A\ Cos\beta\ \rho\ F_B\ F_{RL}\ M\ (8\ (\beta)\ F_{iu}\ (\beta)\ E\ (\beta)\ \eta_{cell}\ (T-Hi) \qquad (6\text{-}9)$$

where the constant factors are:

A - aperture = 5.574 m^2/module

ρ - reflecticity = .84 for FEK-244

F_B - blockage factor = .96

F_{RL} - active receiver length factor = .90

M - cell matching factor = .96 with present sorting techniques

Therefore $A\rho F_B F_{RL} M = 3.884\ m^2$

Running through a varied selection of models at individual points, we were able to generate a comparison between performance data gathered in our test efforts and the two models presently available. These results are presented in table 6-1. All of the performance data is for ASEC cells in various reflectors at Acurex and Sandia test sites.

Table 6-1. Model Evaluation

Insolation w/m^2	Cell Temp ^oC	Incidence Angle	Theoretical Model	Empirical Model	Performance Data
670	54	0°	313.4 w	321.4 w	324.9 w
920	62	0°	399.4 w	377.0 w	383.7 w
790	52	0°	366.6 w	365.4 w	368.8 w
800	85	0°	320.4 w	310.2 w	314.6 w
760	58	20°	336.3 w	286.1 w	305.9 w
760	58	30°	269.0 w	210.7 w	213.5 w

The empirical model represents a significant improvement on the theoretical model in use until this point. That the empirical model is slightly low as a general rule is probably not a limiting deficiency as long term data will determine the absolute values and a 1 percent trend is probably not indicative of a failure of the model. In addition, the

accuracy of the data gathered is not adequate to determine 1 percent differences in performance.

Acquisition of more operational data should enable some improvement of this model. The long term operation of a large field such as Wilcox Hospital will enable us to develop an understanding of the effects when models are combined and minor intermodule difference are averaged.

REFERENCES

1. Goldstein, L. H., and G. R. Case, "PVSS — A Photovoltaic System Simulation Program User's Manual," SAND77-0814, June, 1977.

APPENDIX A

INTENSITY PROFILES FOR DIFFERENT REFLECTOR RIM ANGLES

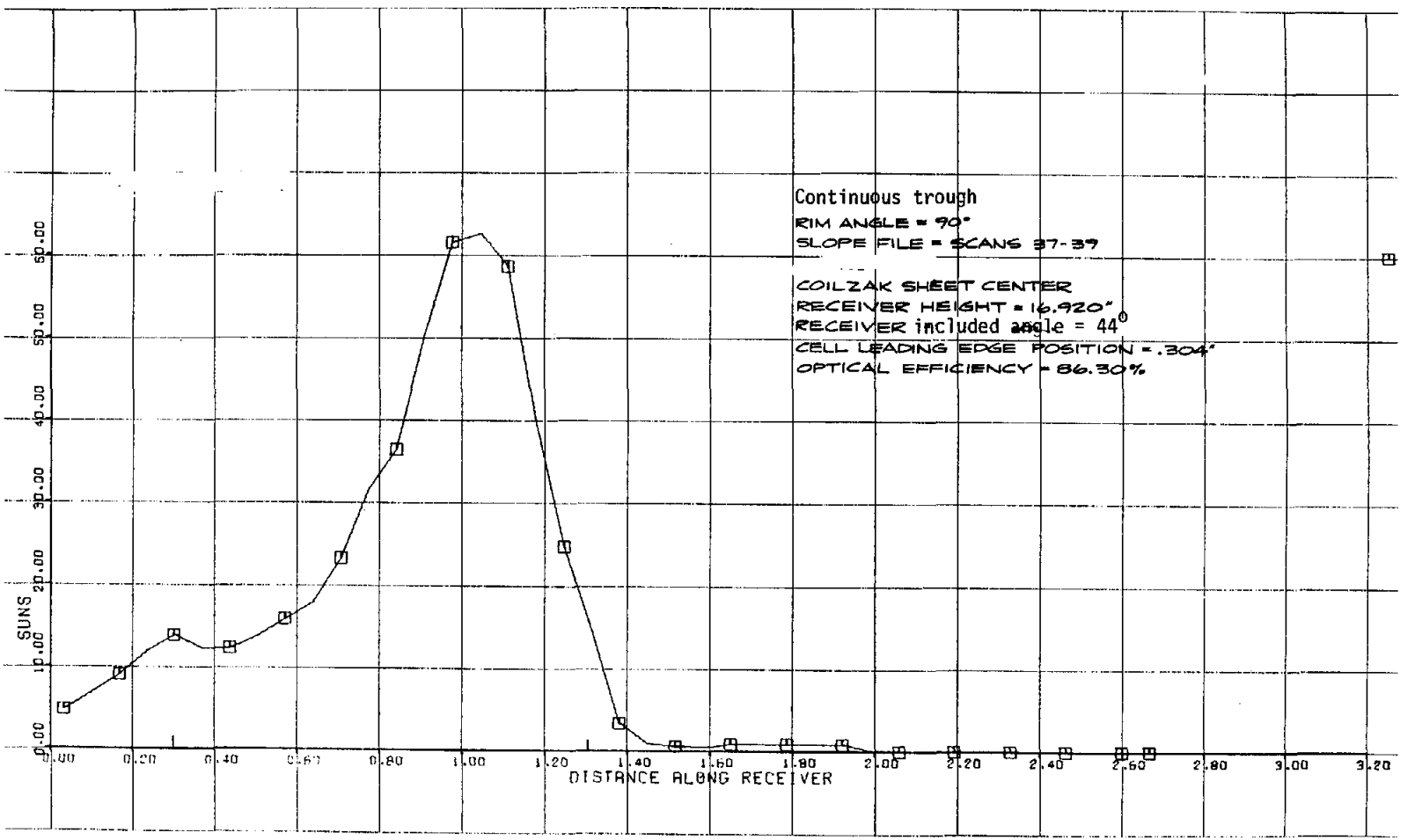
Continuous trough
RIM ANGLE = 90°
SLOPE FILE = SCANS 37-39
COILZAK SHEET CENTER
RECEIVER HEIGHT = 16.920"
RECEIVER included angle = 44°
CELL LEADING EDGE POSITION = .304"
OPTICAL EFFICIENCY = 86.30%
SUNS
0.00
10.00
20.00
30.00
40.00
50.00
60.00
0.00
0.20
0.40
0.60
0.80
1.00
1.20
1.40
1.60
1.80
2.00
2.20
2.40
2.60
2.80
3.00
3.20
DISTANCE ALONG RECEIVER

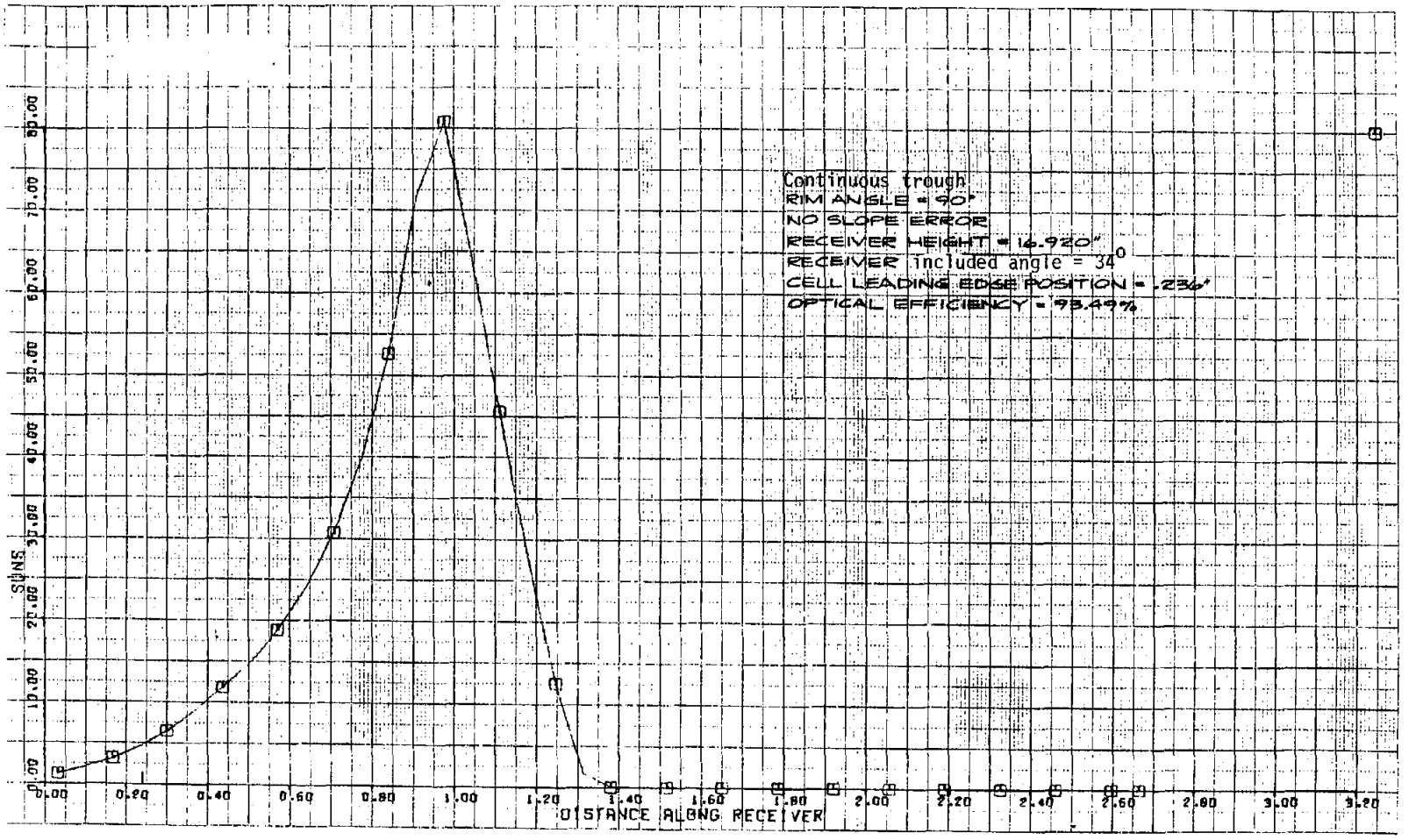
Continuous trough
RIM ANGLE = 90°
NO SLOPE ERROR
RECEIVER HEIGHT = 14.920"
RECEIVER included angle = 34°
CELL LEADING EDGE POSITION = .236"
OPTICAL EFFICIENCY = 93.49%
SUNS
0.00
10.00
20.00
30.00
40.00
50.00
60.00
70.00
80.00
0.00
0.20
0.40
0.60
0.80
1.00
1.20
1.40
1.60
1.80
2.00
2.20
2.40
2.60
2.80
3.00
3.20
DISTANCE ALONG RECEIVER

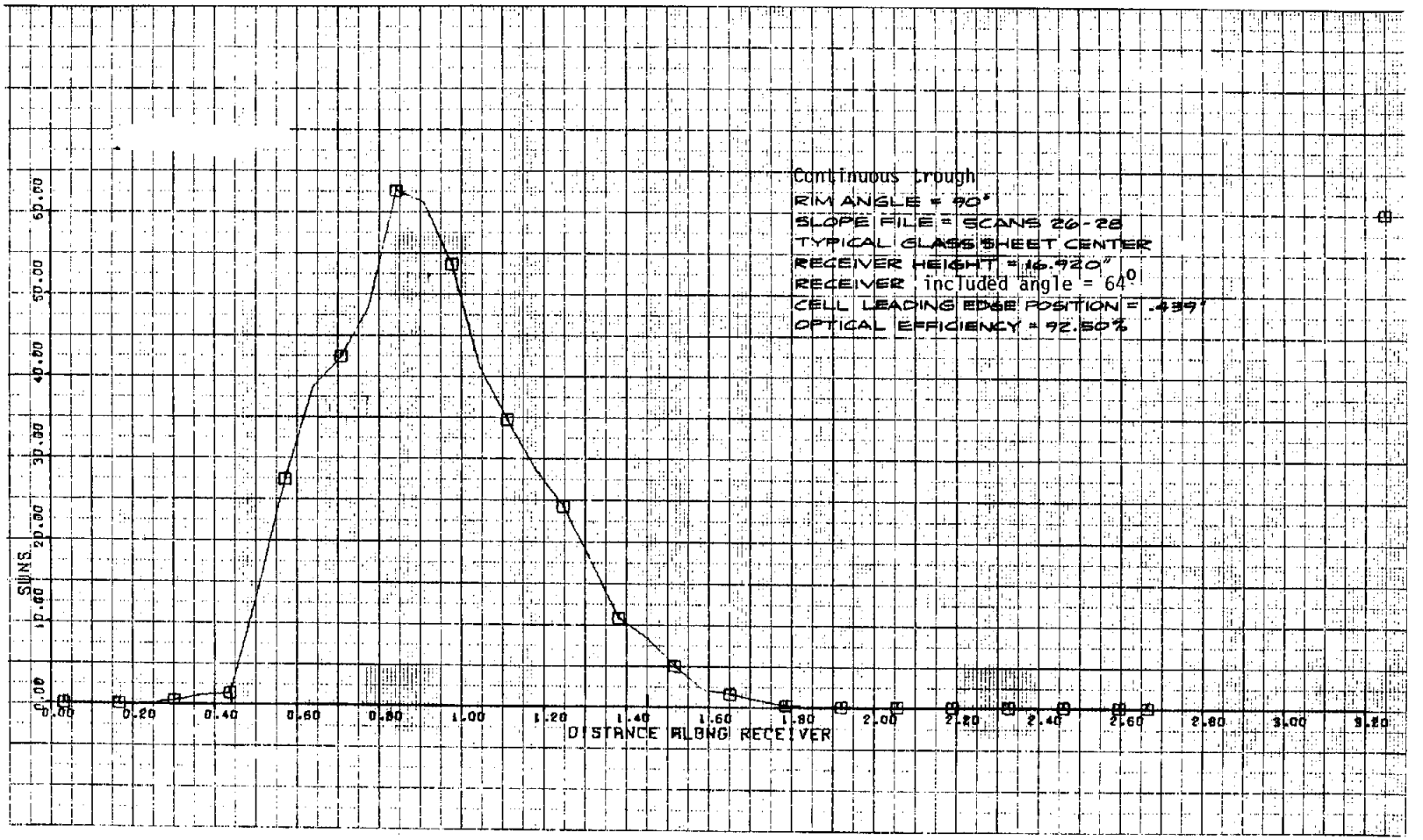
Continuous trough
RIM ANGLE = 90°
SLOPE FILE = SCANS 26-28
TYPICAL GLASS SHEET CENTER
RECEIVER HEIGHT = 16.920"
RECEIVER included angle = 64°
CELL LEADING EDGE POSITION = .439"
OPTICAL EFFICIENCY = 92.50%
SUNS
0.00
10.00
20.00
30.00
40.00
50.00
60.00
0.00
0.20
0.40
0.60
0.80
1.00
1.20
1.40
1.60
1.80
2.00
2.20
2.40
2.60
2.80
3.00
3.20
DISTANCE ALONG RECEIVER

APPENDIX B

INTENSITY PROFILES FOR DIFFERENT REFLECTOR SLOPE ERRORS

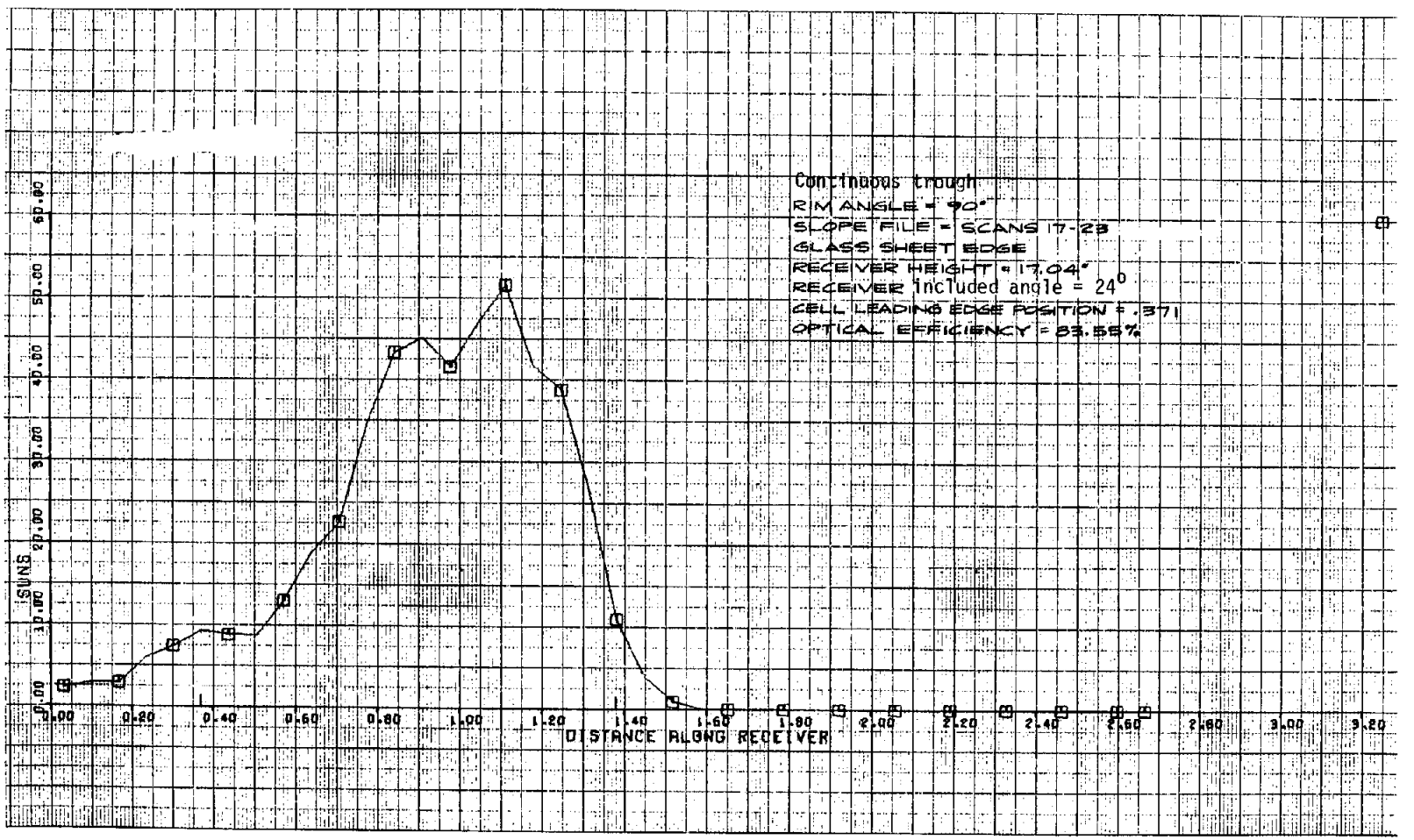
Continuous trough
RIM ANGLE = 90°
SLOPE FILE = SCANS 17-28
GLASS SHEET EDGE
RECEIVER HEIGHT = 17.04"
RECEIVER included angle = 24°
CELL LEADING EDGE POSITION = .371
OPTICAL EFFICIENCY = 83.55%
SUNS
0.00
10.00
20.00
30.00
40.00
50.00
60.00
0.00
0.20
0.40
0.60
0.80
1.00
1.20
1.40
1.60
1.80
2.00
2.20
2.40
2.60
2.80
3.00
3.20
DISTANCE ALONG RECEIVER

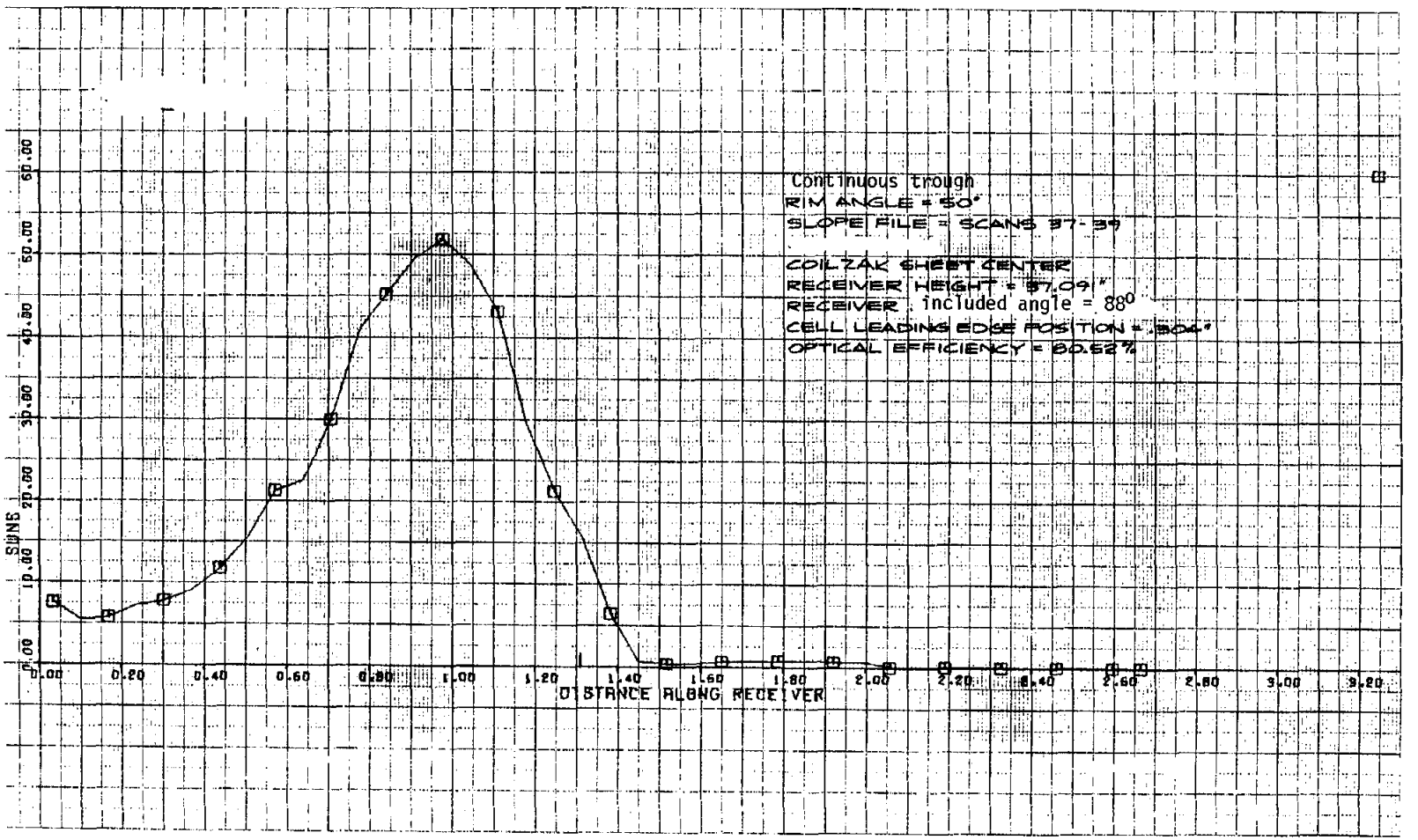
Continuous trough
RIM ANGLE = 50°
SLOPE FILE = SCANS 37-39
COILZAK SHEET CENTER
RECEIVER HEIGHT = 57.09"
RECEIVER included angle = 88°
CELL LEADING EDGE POSITION = .504"
OPTICAL EFFICIENCY = 80.52%
SUNS
0.00
10.00
20.00
30.00
40.00
50.00
60.00
0.00
0.20
0.40
0.60
0.80
1.00
1.20
1.40
1.60
1.80
2.00
2.20
2.40
2.60
2.80
3.00
3.20
DISTANCE ALONG RECEIVER

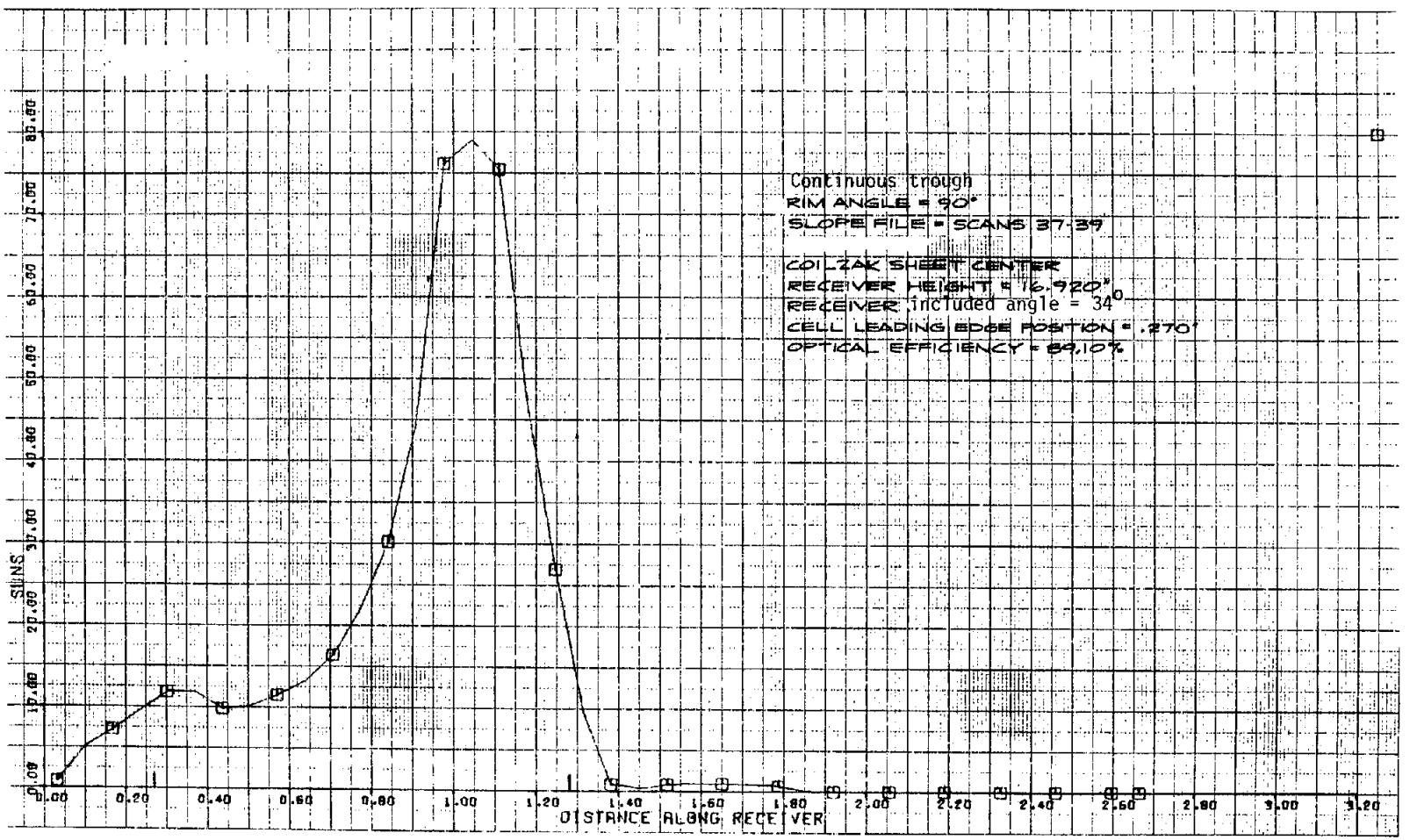
Continuous trough
RIM ANGLE = 90°
SLOPE FILE = SCANS 37-39
COILZAK SHEET CENTER
RECEIVER HEIGHT = 16.920"
RECEIVER included angle = 34°
CELL LEADING EDGE POSITION = .270'
OPTICAL EFFICIENCY = 89.10%
SUNS
0.00
10.00
20.00
30.00
40.00
50.00
60.00
70.00
80.00
0.00
0.20
0.40
0.60
0.80
1.00
1.20
1.40
1.60
1.80
2.00
2.20
2.40
2.60
2.80
3.00
3.20
DISTANCE ALONG RECEIVER

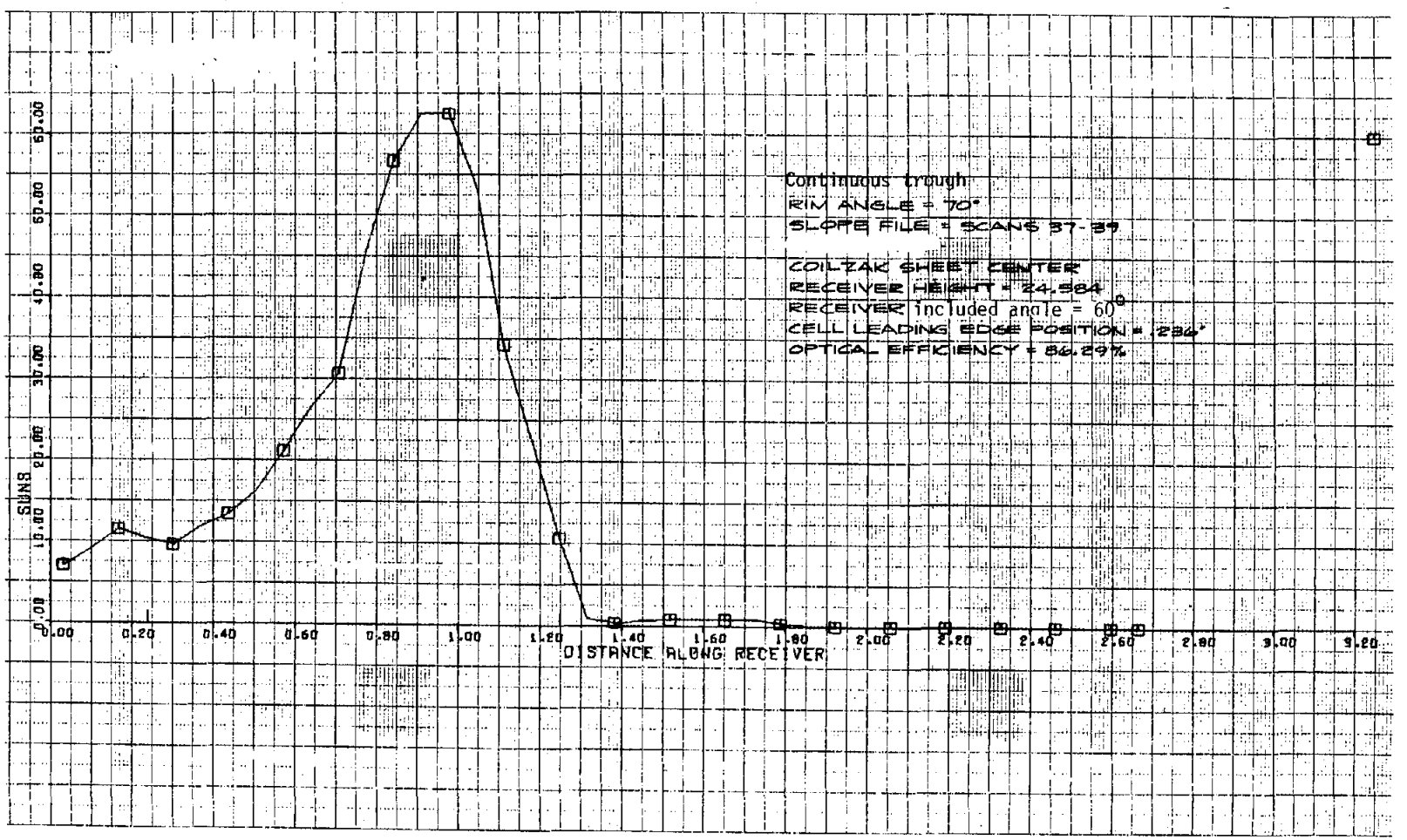
Continuous trough
RIM ANGLE = 70°
SLOPE FILE = SCANS 37-39
COILZAK SHEET CENTER
RECEIVER HEIGHT = 24.984
RECEIVER included angle = 60°
CELL LEADING EDGE POSITION = .234'
OPTICAL EFFICIENCY = 86.29%
SUNS
0.00
10.00
20.00
30.00
40.00
50.00
60.00
0.00
0.20
0.40
0.60
0.80
1.00
1.20
1.40
1.60
1.80
2.00
2.20
2.40
2.60
2.80
3.00
3.20
DISTANCE ALONG RECEIVER

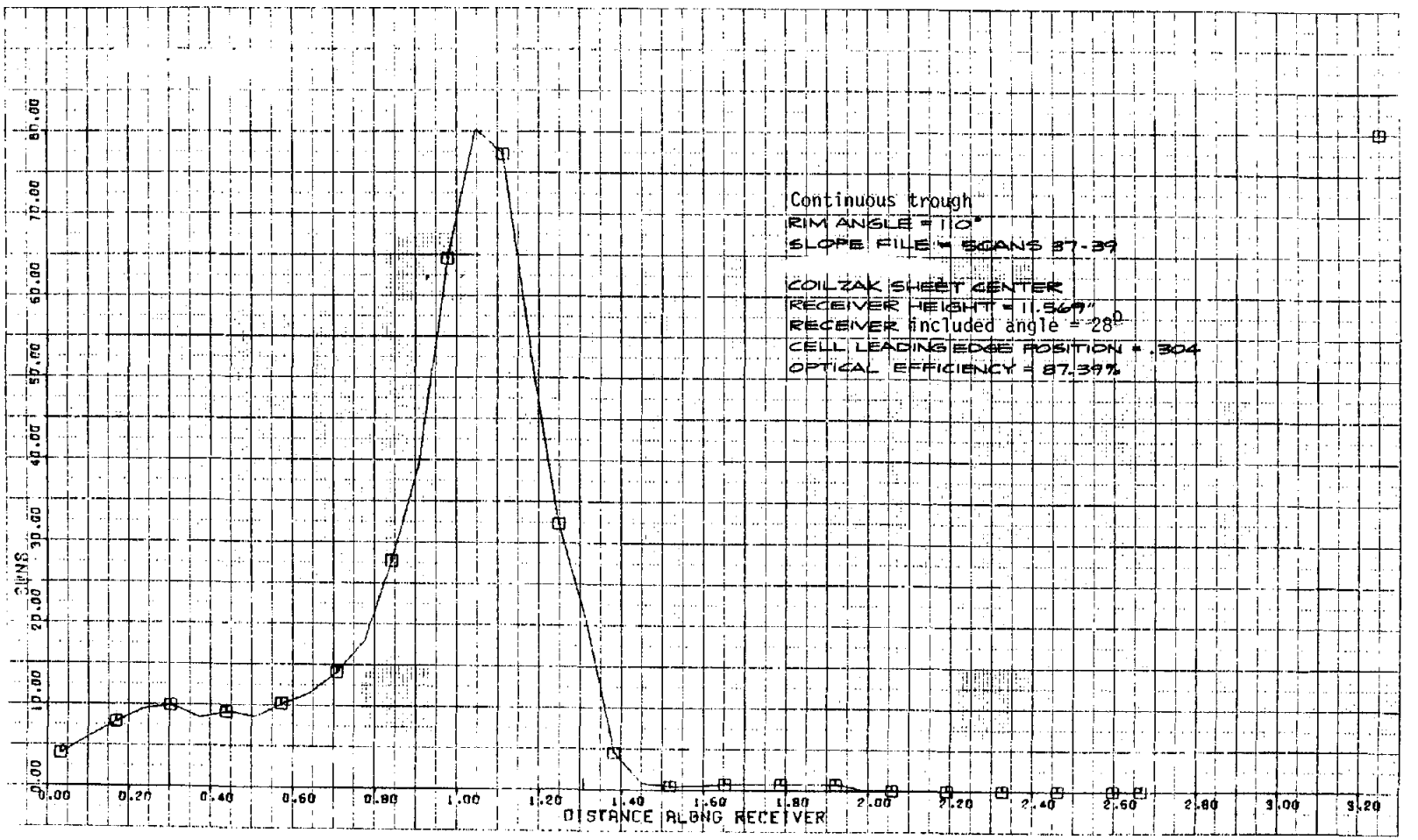
Continuous trough
RIM ANGLE = 110°
SLOPE FILE = SCANS 37-39
COILZAK SHEET CENTER
RECEIVER HEIGHT = 11.569"
RECEIVER included angle = 28°
CELL LEADING EDGE POSITION = .304
OPTICAL EFFICIENCY = 87.39%
SUNS
0.00
10.00
20.00
30.00
40.00
50.00
60.00
70.00
80.00
0.00
0.20
0.40
0.60
0.80
1.00
1.20
1.40
1.60
1.80
2.00
2.20
2.40
2.60
2.80
3.00
3.20
DISTANCE ALONG RECEIVER

APPENDIX C

NEUTRAL AXIS CALCULATION

Derive equations appropriate for a glass/steel laminate yielding:

- Neutral axis location for given thickness of glass and steel
- Required metal thickness for given glass thickness to yield neutral axis located 10 percent within the metal

Define terminology:

	Glass	Steel	Adhesive
Material thickness	t_g	t_s	t_a
Modulus of elasticity	E_g	E_s	E_a
Relative rigidity	N_g	N_s	N_a
Cross section	A_g	A_s	A_a

Steel porosity (fraction open) = X

Centroidal (neutral) axis = NA

Material properties: $E_s = 30 \times 10^6$ psi

$E_g = 11.1 \times 10^6$ psi

$E_a \cong 0$ (low compared to E_g or E_s)

Relative rigidity referenced to steel: $N_g = 0.37$

$N_s = 1.0$

$N_a = 0$

Transform laminate into equivalent homogeneous beam.

Basis:

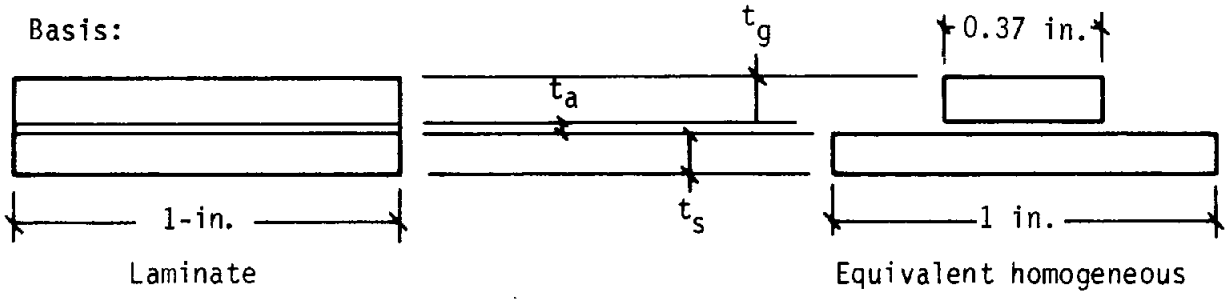

$A_g = t_g N_g$ (1 in.)

$A_s = t_s N_s$ (1 in.) (1 - x)

$A_a = t_a N_a$ (1 in.) = 0

Locate centroidal axis using top surface of glass as reference (Y top-glass = 0).

$$NA = \frac{\Sigma A_i y_i}{\Sigma A_i}$$

$$NA = \frac{1/2\ N_g t_g^2 + N_s t_s\ \ 1 - x\ \ t_g + t_a + \frac{t_s}{2}}{t_g N_g + t_s N_s\ (1 - x)} \qquad \text{(C-1)}$$

Define centroidal axis to be 10 percent within metal and solve for t_s:

$$NA = t_g + t_a + 0.1\ t_s$$
$$NA\ (1) = NA\ (2) \qquad \text{(C-2)}$$

$$t_s = \frac{0.2 t_g N_g + 0.2 t_g N_g^2 + 3.2 N_s\ 1 - x\ \ N_g t_g^2 + 2 t_a t_g N_g^{1/2}}{1.6\ N_s\ (1 - x)} \qquad \text{(C-3)}$$

Construct matrix of metal thickness required to locate NA 10 percent within metal for given glass thicknesses (t_g = 0.032, 0.040, 0.060-in.) as a function of adhesive thickness and metal porosity.

Case 1: t_g = 0.032

t_a \ x	0.10	0.20	0.30
0.003	0.027	0.029	0.031
0.009	0.030	0.032	0.034
0.015	0.034	0.036	0.038

Case 2: $t_g = 0.040$

t_a \ x	0.10	0.20	0.30
0.003	0.033	0.035	0.038
0.009	0.037	0.039	0.042
0.015	0.040	0.043	0.045

Case 3: $t_g = 0.060$

t_a \ x	0.10	0.20	0.30
0.003	0.048	0.051	0.055
0.009	0.052	0.056	0.060
0.015	0.056	0.059	0.064

Cost, availability, and long lead time for perforated metal material dictated conservative specification of metal thickness.

Metal backing procured:

Type 1: $x = 0.121$

$t_s = 0.062$

Type 2: $x = 0.121$

$t_s = 0.050$

Determine locations of NA for the various combinations of glass and metal. Use the worst case adhesive thickness t_a = 0.003.

t_s \ t_g	0.32	0.40	0.60
0.062	0.057	0.062	0.075
0.050	0.051	0.056	0.069

To present location of NA differently:

assume t_a = 0.003, x = 0.121

Glass thickness	0.032	0.040	0.060	0.032	0.040	0.060
Steel thickness	0.062	0.062	0.062	0.050	0.050	0.050
Distance NA below top glass surface	0.057	0.062	0.075	0.051	0.056	0.069
Distance NA below top steel surface	0.022	0.019	0.012	0.016	0.013	0.006
Percent of t_s NA Located below steel surface	35.	31.	19.	32.	26.	12.

APPENDIX D

CELL WIDTH OPTIMIZATION STUDY

As an early step in the effort to optimize the receiver configuration, we undertook to evaluate the optimum cell width for the proposed receiver design. The optimum was to be based on lowest system cost. For this reason, many assumptions were made as to balance of system (BOS) costs for a photovoltaic concentrator installation. These are detailed later in this appendix.

The first step in optimizing cell width was to try and understand the intensity distribution on the receiver which might result from the 3001 trough. For this effort we used the laser ray trace data from Acurex and Sandia (the two fixtures are described in section 4). The output was then convolved into the resultant image on the receiver, as demonstrated in Figure D-1. The position on the reflector of the incident ray determined its focal length and hence the distribution of its image due to the real sunshape. The images for incoming rays are spread and combined in this fashion to produce a family of intensity maps based on receiver height above the reflective surface. The maps in figure D-2 are convolved from laser ray trace data from Bruce Hansche's equipment at Sandia on an Acurex 3001 trough.

By integrating under the curves and then integrating the area which would be covered by the active surface of different cell widths, we can determine intercept factors for various cell widths. The intercept factor is the ratio of the radiant energy which falls on active surface to the total energy reflected off the trough. This calculation was performed for 60° included receiver angle. The position of the leading edge of the cell active area, i.e., the distance from the virtual apex of the Vee receiver to the active cell surface, is constrained. It is necessary to provide for environmental protection of the cell. The mechanical evaluation of this problem suggested that a single bus cell might be located as close as

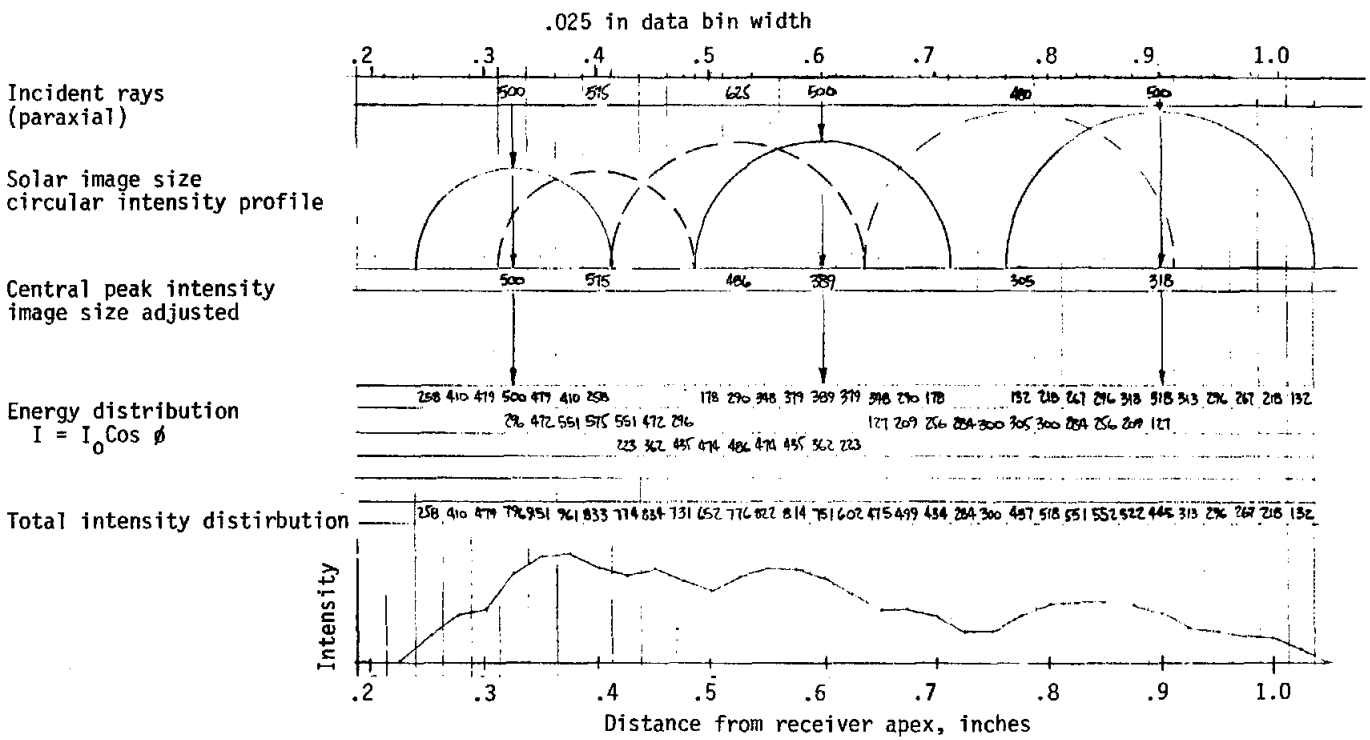

Figure D-1. Expansion of Central Ray into Solar Image

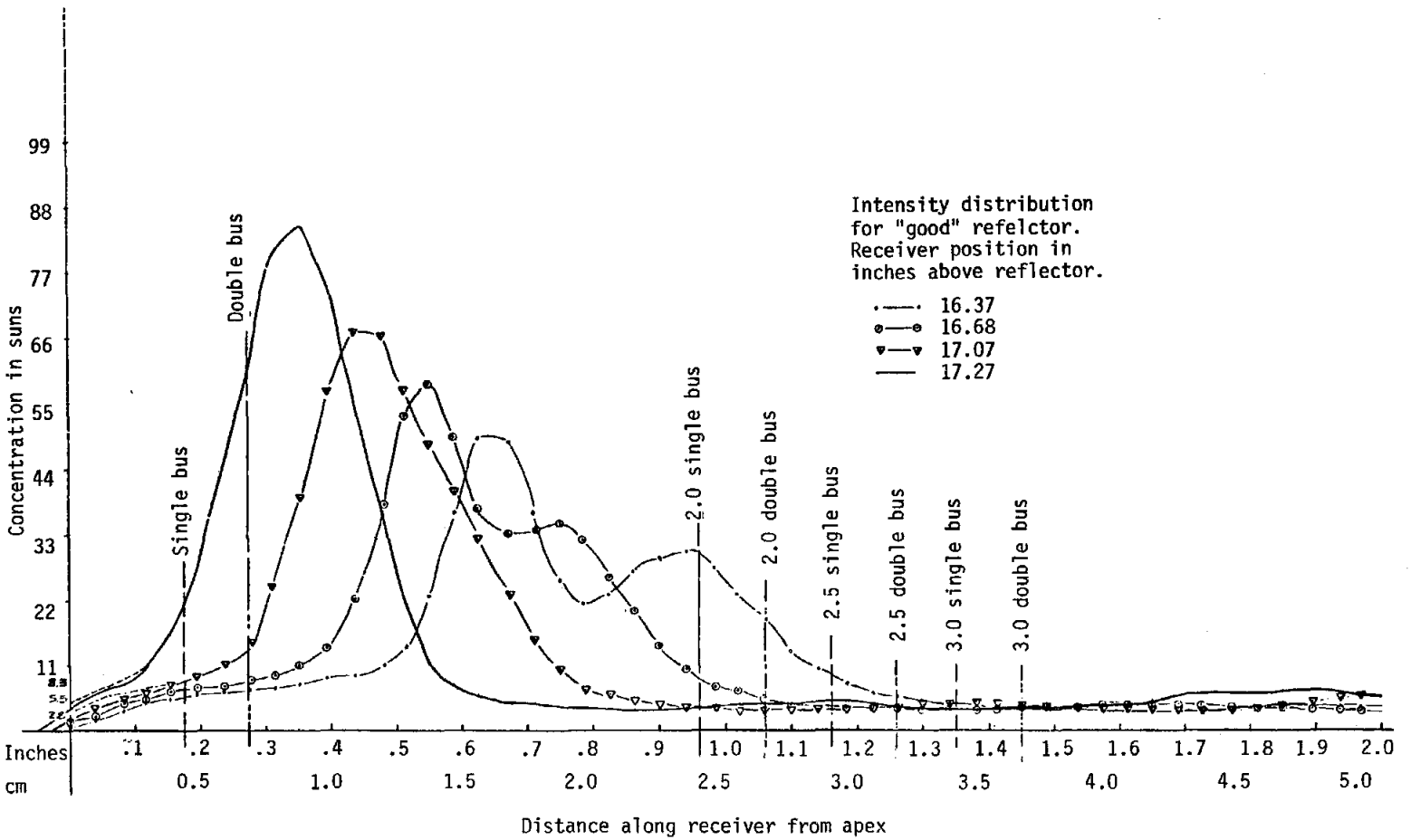

Figure D-2. Intensity Distribution from Sandia Data

0.175 in. from the virtual apex. A double bus cell with its attendant interconnect could not be placed closer than 0.275 in. to the apex. These values are indicated in figure D-2 as the limits of the leading edge of the cell. The possible cell widths and bus combinations are also listed on figure D-2. When all possible intercept factors are figured and plotted, we have a family of curves such as shown in figure D-3. As could be predicted, the 3.0 cm-wide cell has the highest intercept factor and the single bus cell position has the highest intercept factors at most receiver heights. These values have to be traded off against cost and performance of each combination.

The performance of each cell was determined by evaluations on performance done by C. Michael Garner at Sandia labs. The performance is based on the assumptions that the bulk cell area would perform identically for any size and configuration cell. The extensive losses would account for differences in performance. The extrinsic loss for each of the six candidate cells was computed for a 30 sun uniform incident radiation. The power output of a standard field of 60 kW was used as reference and the equation

$$P_F = 60 \text{ kW} = \gamma \text{ (1 -extrinsic loss) Z (number of collectors) } (H_i) \text{ (A)}$$

was used to determine the required field size for each cell configuration where

γ = Intercept factor

Z = Product of receiver block age factor, reflectivity intrinsic losses, effective receiver length, and cover glass transmittance =

H_i Isolation = 1,000 W/m^2

A = Collector aperture = 5.574 m^2

The intercept factors and extrinsic losses are included in table D-1.

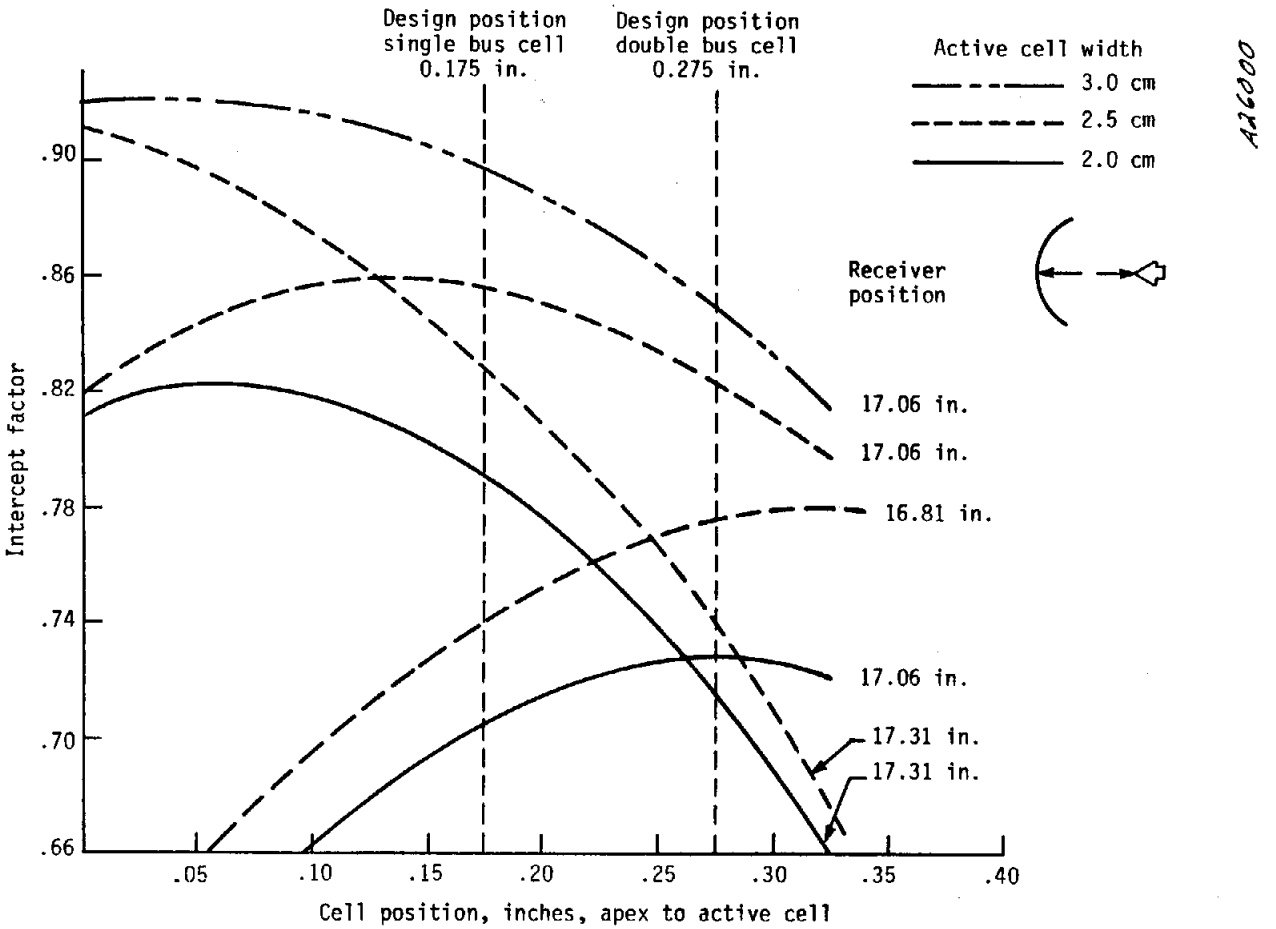

Figure D-3. Acurex Laser Ray Trace Results

The cost factor then is computed. For each cell configuration we can compute the field cost for the hypothetical 60 kW field using the equation

$$\text{cost}_{\text{field}} = [(\text{No. of Cells/Receiver})\ (\text{cost}_{\text{cell}}) + \text{cost}_{\text{reflector}}]\ (\text{No. of collectors})$$

The number of collectors is determined as described above. The cost of the reflector includes installation and is based on Acurex field construction experience. We assumed two cells/wafer for any cell size and a constant cost/wafer which was supplied by ASEC. The number of cells per receiver is two times the value $\frac{108 \text{ in.}}{\text{cell length (in.)}}$ where the cell length is determined by the following method.

Figure D-4 shows the assumptions for cell manufacture. For a 3 in. wafer, the active surface widths of 2.0, 2.5, and 3.0 cm yield six cell lengths by geometric determination. These are listed in table D-1.

The resultant costs of a 60 kW field were normalized and are included in table D-1. The choice of a 2.5 cm active width, two-bus cell is the cost optimum but the differential is fairly small. The further analysis of sensitivity to pointing error and the fact that the illumination profile is not a uniform 30 suns make the 2.5 cm double bus configuration a firm optimum.

Table D-1. Cell Size Optimization

Active cell width (cm)	2.0	2.0	2.5	2.5	3.0	3.0
Cell length (cm)	6.26	5.97	5.43	5.00	4.20	3.52
Number of buses	1	2	1	2	1	2
Cell position (in. from apex)	0.175	0.275	0.175	0.275	0.175	0.275
Receiver position (in. to relfector)	17.31	17.06	17.06	17.06	17.06	17.06
Intercept factor (γ)	0.79	0.73	0.86	0.82	0.90	0.85
Extrinsic cell loss (percent)	15.7	9.0	19.1	10.6	22.4	12.3
γ(1-Extrinsic loss)	0.66	0.66	0.70	0.73	0.70	0.75
Normalized 60 kWe field cost	1.015	1.032	1.009	1.000	1.124	1.141

At mass production level, cells are priced per wafer not by finished cell area. Hence, maximizing cell area/wafer minimizes cost. For rectangular cells we cut two from each wafer:

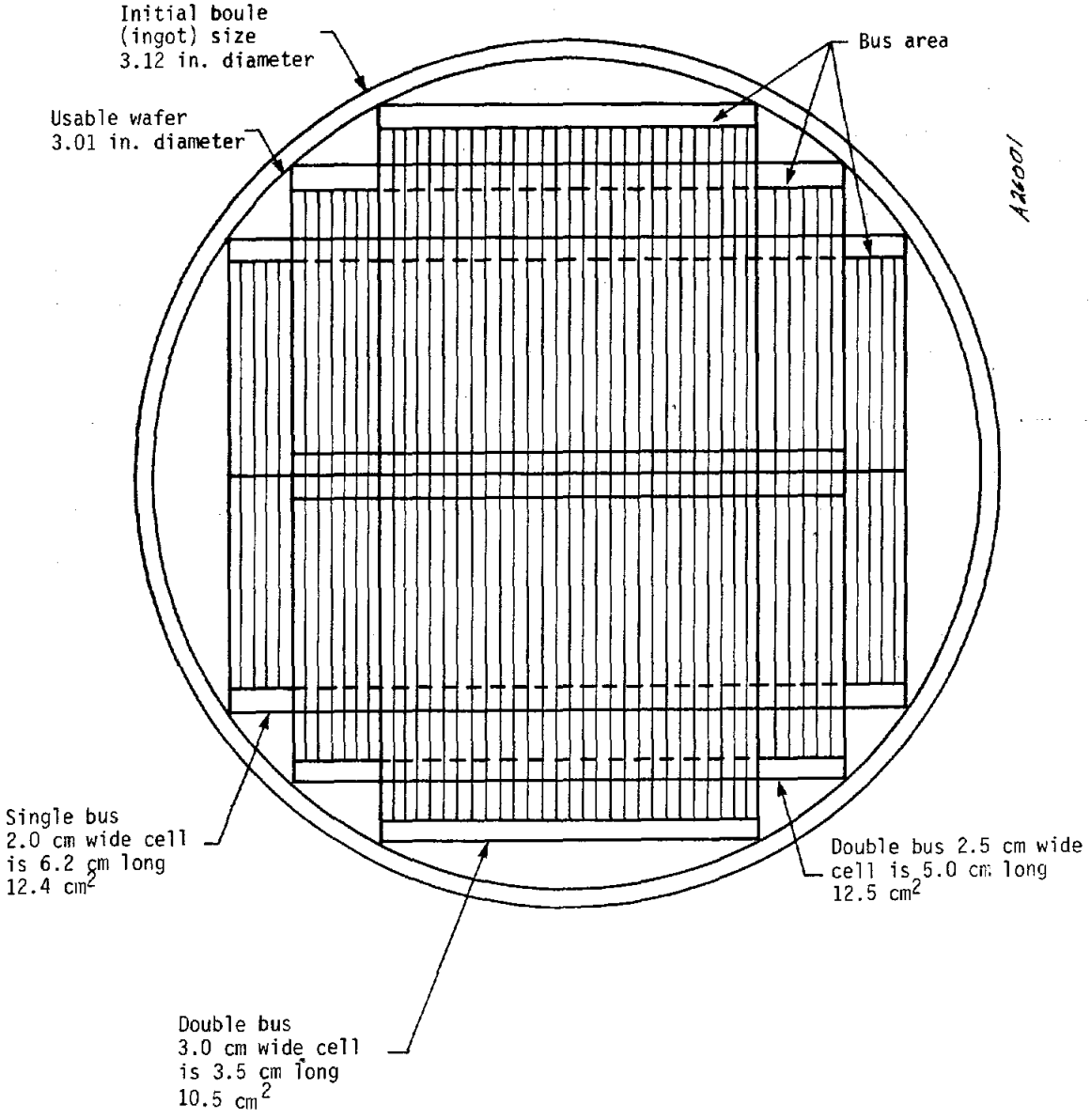

Figure D-4. Cell Size Economics

APPENDIX E

UNCERTAINTY ANALYSIS

An uncertainty analysis of the data gathering technique for the η_{array} versus coolant temperature tests must start with the derivation of:

$$\eta_{arc}\ (T) = \frac{P_{array}\ (T)}{DNI*A} \text{ or } \frac{I_{max.power}\ (T).V_{max.power}\ (T)}{DNI*A}$$

where A is the module aperture and is considered constant for all measurements.

To understand the uncertainty in the equation, we must first evaluate the effect of each of the variables on the efficiency. The sensitivity coefficients are formed with:

$$\frac{d\eta}{DI} = \frac{V_{mp}}{DNI*A}$$

$$\frac{d\eta}{dV} = \frac{I_{mp}}{DNI*A}$$

$$\frac{d\eta}{dT} = \frac{dp}{dT}\ \frac{1}{DNI*A}$$

$$\frac{d\eta}{dDNI} = \frac{P_{array}}{DNI^2*A}$$

and the efficiency uncertainty is given by:

$$\delta\eta = \left[\left(\frac{I_{mp}}{DNI*A}*\delta V_{mp}\right)^2 + \left(\frac{V_{mp}}{DNI*A}*\delta I_{mp}\right)^2 + \left(\frac{P_{array}}{DNI^2*A}*\delta DNI\right)^2 + \left(\frac{dp}{dT}*\frac{1}{DNI*A}*\delta T\right)^2\right]^{1/2}$$

In this approach the uncertainty due to tracking error is included in the estimate of uncertainty assigned to $V_{max.power}$ and $I_{max.power}$. Based on tests at the PASTF the uncertainty in $\delta\eta$ is found to be on the order of $\pm 5\%$ of the measured η value*.

These values are presented on figure 6-8.

*See Sandia Division 4724 Memorandum by D. L. King and D. E. Arvizu "Estimating Uncertainty in module or array efficiency values as measured during an I-V sweep at the PASTF".

DISTRIBUTION

Acurex Corporation (2)
Attn: George Sutton
Bob Spencer
485 Clyde Avenue
Mountain View, CA 94042

Aerospace Corporation
Attn: Ed Simburger
2350 El Segundo Blvd.
El Segundo, CA 90266

Applied Solar Energy Corp. (3)
Attn: Steve Olah
Frank Ho
Ken Ling
15251 E. Don Julian Road
City of Industry, CA 91746

Arizona State University (2)
Attn: Charles Backus
Robert Sanderson
College of Engineering
Tempe, AZ 85281

Battelle
Attn: Don Carmichael
505 King Avenue
Columbus, OH 43201

BDM Corporation (3)
Attn: Tim Lambarski
Wayne Kauffman
Bill Schwinkendorf
1801 Randolph Road SE
Albuquerque, NM 87111

Chevron Research (2)
Attn: John Cape
R. Creek
576 Standard Avenue
Richmond, CA 94802

Cyro Industries
697 Route 46
Clifton, NJ 07015

U. S. Dept of Energy (2)
ALO
Attn: James Morley
Ethan Walker
P. O. Box 5400
Albuquerque, NM 87115

U. S. Dept of Energy (7)
Division of PV Energy Systems
Attn: M. B. Prince (5)
L. A. Barrett
A. Scollaro
1000 Independence Ave. SW
Washington, DC 20585

E-Systems (2)
Attn: Mark O'Neill
A. J. McDanal
P. O. Box 226118
Dallas, TX 75266

General Electric Co.
Attn: Ron Hodge
P. O. Box 527
King of Prussia, PA 19406

International Rectifier
Attn: Harold Weinstein
235 Kansas Street
El Segundo, CA 91214

Intersol Power Corporation
Attn: John Sanders
7400 W. Radcliff Avenue
Littleton, CO 80123

Jet Propulsion Lab (2)
Attn: K. Shimada
R. Ferber
4800 Oak Grove Drive
Pasadena, CA 91109

Martin Marietta (4)
Attn: S. Broadbent
M. Imamura
D. Hughes
J. Baumann
P. O. Box 179
Denver, CO 80201

Microwave Associates
Attn: Jonathon Chapple-Sokol
South Avenue MS-116
Burlington, MA 01803

3M
Attn: Sanford Cobb
Industrial Optics
235 2D15
3M Center
St. Paul, MN 55144

Motorola
Attn: Keith Kingston
GED
8201 E. McDowell
Scottsdale, AZ 85252

NASA, HQ
Attn: John Loria
Code RET-1
Washington, DC 20546

New Shelter Home Magazine
9317 Shoshone
Albuquerque, NM 87111

Oak Ridge National Lab
Attn: Steve Kaplan
P. O. Box X
Oak Ridge, TN 37830

Oklahoma University
571 South University Blvd.
Norman, OK

Photowatt (2)
Attn: William Taylor
Mike Keeling
2414 W. 14th Street
Tempe, AZ 85281

Power Hybrids
Attn: Jeff Meyer
1742 Crenshaw Blvd.
Torrance, CA 90501

PRC
Attn: E. Stirewalt
5201 Leesburg Pike
Suite 400
Falls Church, VA 22070

Purdue University (2)
Attn: Richard Schwartz
Mark Lundstrom
Electrical Engineering Dept.
West Lafayette, IN 47907

Ray Bahm & Associates
Attn: Ray Bahm
2513 Kimberly Court NW
Albuquerque, NM 87130

Research Triangle Institute
Attn: Mayrant Simons
Box 12194
Research Triangle Park, NC 27709

SERI (3)
Attn: Gene Blakeslee
Lee Cole
John Benner
1617 Cole Blvd.
Golden, CO 80401

SERI, Library (2)
1536 Cole Blvd., Bldg. #4
Golden, CO 80401

Southern Cal Edison
Attn: Spencer Carlisle
2244 Walnut Grove Ave.
Rosemead, CA 91770

Spectrolab
Attn: Brian Elm
12500 Gladstone Avenue
Sylmar, CA 91342

Spire (3)
Attn: S. Tobin
M. Nowlan
R. Little
Patriots Park
Bedford, MA 01730

Star Light Energy
Attn: J. Furber
1717 18th Street NW
Washington, DC 20009

Strategies Unlimited
201 San Antonio Circle
Suite 205
Mountain View, CA 94040

Solar Works
Attn: Paul Wilkins
Route 2, Box 274
Santa Fe, NM 87501

Thermo Electron
Attn: Ron Scharlack
45 First Avenue
Waltham, MA 02154

UNM/NMERI
Attn: G. Leigh
Campus Box 25
Albuquerque, NM 87131

Varian & Associates (2)
Attn: Peter Borden
N. Kaminar
611 Hansen Way K-219
Palo Alto, CA 94303

Wright Patterson AFB
Attn: Jack Geis
AFWAL/POOC
Wright Patterson AFB, OH

Wyle Labs (2)
Attn: Dave Christenson
George Meares
7800 Governors Drive West
Huntsville, Al 35807

Alliance Tool Corp.
Attn: Helmut Walter
1300 Mt. Read Blvd.
Rochester, NY 14606

2146 M. Garner
2146 B. Hanson
2146 B. Nasby
2146 J. Rodriguez
2146 B. Rose
2146 H. Weaver
4700 E. Beckner
4720 D. Schueler
4721 H. Gerwin
4721 W. Schimmel
4723 E. Burgess
4724 D. Arvizu
4724 L. Beavis
4724 E. Boes
4724 C. Chiang
4724 M. Edenburn
4724 D. King
4724 A. Maish
4724 M. Rios
5133 R. Chaffin
5133 J. Wiczer
5811 R. Assink
3141 L. J. Erickson (5)
3151 W. L. Garner (3)
3154-3 C. H. Dalin (25)
for DOE/TIC (Unlimited Release)

★U.S. GOVERNMENT PRINTING OFFICE: 1982-0-576-021/553